

Department of Earth Science and Engineering
Imperial College London

MACHINE LEARNING AND SIMULATION FOR
THE OPTIMISATION AND CHARACTERISATION
OF ELECTRODES IN BATTERIES

Andrea Gayón Lombardo

Supervisor: PROF. NIGEL P. BRANDON
Co-supervisors: PROF. STEPHEN J. NEETHLING
DR SAMUEL J. COOPER

SUBMITTED IN PARTIAL FULFILMENT OF THE REQUIREMENTS FOR THE DEGREE
OF
DOCTOR OF PHILOSOPHY IN ENGINEERING AND
THE DIPLOMA OF IMPERIAL COLLEGE LONDON

LONDON
JUNE 15, 2021



I hereby declare that all of the work presented in this thesis – except that which is appropriately acknowledged and referenced as such – is my own, and that it has not been submitted in fulfilment of the requirements of any other degree at Imperial College London.

Andrea Gayón Lombardo

June 15, 2021

The copyright of this thesis rests with the author and is made available under a Creative Commons Attribution Non-Commercial No Derivatives licence. Researchers are free to copy, distribute or transmit the thesis on the condition that they attribute it, that they do not use it for commercial purposes and that they do not alter, transform or build upon it. For any reuse or redistribution, researchers must make clear to others the licence terms of this work.

Abstract

The performance of electrochemical energy storage (EES) and energy conversion (EC) technologies is closely related to their electrode microstructure. Thus, this work focuses on the development of two novel computational models for the characterisation and optimisation of electrodes for three devices: Redox Flow batteries (RFBs), Solid Oxide Fuel Cells (SOFCs), and Lithium-ion batteries (LIBs).

The first method introduces a Pore Network Model (PNM) for simulating the coupled charge and mass transport processes within electrodes. This approach is implemented for a vanadium RFB using different commercially available carbon-based electrodes. The results from the PNM show non-uniformity in the concentration and current density distributions within the electrode, which leads to a fast discharge due to regions where mass-transport limitations are predominant. The second approach is based on the stochastic reconstruction of synthetic electrode microstructures. For this purpose, a deep convolutional generative adversarial network (DC-GAN) is implemented for generating three-dimensional n-phase microstructures of a LIB cathode and a SOFC anode. The results show that the generated data is able to represent the morphological properties and two-point correlation function of the real dataset. As a subsequent process, a generation-optimisation closed-loop algorithm is developed using Gaussian Process Regression and Bayesian optimisation for the design of microstructures with customised properties. The results show the ability to perform simultaneous maximisation of correlated properties (specific surface area and relative diffusivity), as well as an

optimisation of these properties constrained by constant values of volume fraction.

Overall, this work presents a comprehensive analysis of the effect of the electrode microstructure in the performance of different energy storage devices. The introduction of a PNM bridges the gap between volume-averaged continuum models and detailed the pore-scale models. The main advantage of this model is the ability to visually show the concentration and current distributions inside the electrode within a reasonably low computational time. Based on this, this work represents the first visual showcase of how regions limited by low convective flow affect the rate of discharge in an electrode, which is essential for the design of optimum electrode microstructures. The implementation of DC-GANs allows for the first time the fast generation of arbitrarily large synthetic microstructural volumes of n-phases with realistic properties and with periodic boundaries. The fact that the generator constitutes a virtual representation of the real microstructure allows the inclusion of the generator as a function of the input latent space in a closed-loop optimisation process. For the first time, a set of visually realistic microstructures of a LIB cathode with user-specified morphological properties were designed based on the optimisation of the generator's latent space. The introduction of a closed-loop generation-optimisation approach represents a breakthrough in the design of optimised electrodes since it constitutes a first approach for evaluating the microstructure-performance correlation in a continuous forward and backward process.

To my parents, Esther Lombardo Aburto and Eduardo Gayón Vera

To my lovely family

I sell here, Sir, what all the world desires to have — POWER

- Matthew Boulton, at the Boulton-Watt works (1776)

Acknowledgements

First, I would like to thank my supervisors Nigel P. Brandon, Samuel J. Cooper and Stephen J. Neethling for their continuous support and guidance throughout my PhD. Steve, thank you for your constant help to develop the pore network model, and for teaching me new programming languages. But mainly thank you for your kindness and patience when discussing complex topics of transport phenomena and numerical methods. Sam, thank you for the countless conversations and constructive discussions we had over the past years. Particularly thank you for encouraging me to submerge in the area of machine learning. Your constant enthusiasm and feedback pushed me to become a better researcher. Nigel, thank you for being my mentor and a role-model in the academic and professional life. Your working ethics, your kindness to help students and your passion for sharing knowledge have deeply inspired me. But most importantly, thank you for believing in me and providing me the support to work independently in the projects of my interest.

I would like to thank my parents Esther and Eduardo for being my source of inspiration, and supporting me in every decision that I have made. Despite the distance, I know that you are always with me in every step, encouraging me to become the best version of myself. I also want to thank my sisters, Erika and Maria, for always being there for me and for their love and lifelong support. I want to thank my grandparents Esther and Horacio for their constant support, inspiration and words of encouragement, even in the most difficult times. I would also like to

give special thanks to Dr. Humberto Hinojosa for his continuous support throughout my career.

I want to give special thanks to the friends that I consider part of my family: to Bego and Mariana for being the best friends I could ask for, and for always being there for me through good and bad moments; to Adrian for becoming my family in London and always keeping me positive despite difficult times; to Dani, Antonio, Eduardo, and Miguel for all the moments that we shared and for creating memories that will last forever. I want to thank Veronica for her kindness and advice, and for making her house a second home for me. I also want to thank the friends that have made this journey a very special one. Particularly, I want to thank Rid and Felipe, for their support and motivation, for all the amazing time spent together in London and for making my experience at Imperial College one of the best. I want to thank Ola, Doris, Ben, Francesco, Catalina, Sam and Kartik for their support and for making these years very enjoyable.

Finally, I would like to thank the Mexican National Council of Science and Technology (CONACYT) and the Secretary of Energy (SENER) for funding this work.

Contents

Abstract	
Acknowledgements	
List of Figures	iv
List of Tables	viii
Nomenclature	x
1 Introduction	1
1.1 Motivation	1
1.2 Overview of EES and EC technologies	4
1.2.1 Solid Oxide Fuel Cells	4
1.2.2 Lithium-ion batteries	5
1.2.3 Redox Flow Batteries	7
1.3 Objectives	9
1.4 Thesis structure	10
2 Background	18
2.1 Modelling porous materials	18
2.1.1 Continuum models	19
2.1.2 Direct Numerical Simulations as pore-scale models	24
2.1.3 Pore Network Models	32
2.2 Stochastic reconstruction of porous materials	40
2.2.1 Stochastic reconstruction of electrodes for electrochemical systems	42
2.2.2 Introduction to Machine Learning	45
2.2.3 Generative Models	49
3 A Pore Network Model for electrochemical energy storage devices	71
3.1 Abstract	71
3.2 Background	72
3.2.1 Transport modelling through porous media	72
3.3 Model development	75
3.3.1 Fluid transport	76
3.3.2 Mass transport	77
3.3.3 Charge transport	80

3.4	Boundary conditions	82
3.4.1	Boundary conditions for flow transport	82
3.4.2	Boundary conditions for species transport	82
3.4.3	Boundary conditions for charge transport	83
3.5	Iterative algorithm	83
3.6	Results and discussion	86
3.6.1	Verification of the Explicit Euler Scheme	86
3.6.2	Implementation of the proposed framework in a VRFB	88
3.7	Conclusions	92
4	PNM implementation for carbon-based VRFB electrodes	98
4.1	Abstract	98
4.2	Background	99
4.3	Pore Network Model implementation for Toray 090 from XCT	101
4.3.1	Boundary conditions	104
4.3.2	Purely convective-diffusive transport	105
4.3.3	Convection, diffusion, migration and electrochemical reaction	107
4.3.4	Comparison of pore-scale models in terms of computational expense	114
4.4	Case studies: implementation of PNM for SGL 29AA, Freudenberg, ELAT-H	115
4.4.1	SGL29AA	115
4.4.2	Freudenberg	120
4.4.3	ELAT-H	122
4.5	Conclusions	126
5	Generative Adversarial Networks for the reconstruction of three-dimensional multi-phase electrode microstructure	132
5.1	Abstract	132
5.2	Background	133
5.3	Generative Adversarial Networks	136
5.4	Microstructural data	137
5.4.1	Sample details	138
5.4.2	Image data	138
5.5	Method	140
5.5.1	Pre-treatment of the training set	140
5.5.2	GAN Architecture and Training	142
5.5.3	Microstructural characterisation parameters	144
5.6	Results	147
5.6.1	Lithium-ion cathode results	150
5.6.2	SOFC anode results	153
5.6.3	Representativity	156
5.6.4	Generating larger volumes	157
5.6.5	Computational expense	158
5.6.6	Mode collapse	159
5.6.7	Periodic boundaries	160
5.7	Discussion	161
5.8	Conclusions	165

6	Gaussian Processes and Bayesian optimisation for the design of microstructures with optimum properties	175
6.1	Abstract	175
6.2	Introduction	176
6.2.1	Generative Adversarial Networks	179
6.2.2	Introduction to Gaussian Process regression	181
6.2.3	Bayesian Optimisation with Gaussian Processes	185
6.3	Method	187
6.3.1	Microstructural image data and pre-processing	187
6.3.2	Closed-loop Generation-optimisation process	187
6.3.3	Case study: Optimisation of a 3D Li-ion cathode	191
6.4	Results and Discussion	194
6.4.1	Optimisation of microstructural and transport properties	194
6.4.2	Analysis and visualisation of the microstructural properties as a function of the latent space	211
6.5	Conclusions	214
7	Conclusions and further work	223
7.1	Summary and conclusions	224
7.1.1	Chapter 3: A Pore Network Model for electrochemical energy storage devices	224
7.1.2	Chapter 4: PNM implementation for various VRFB electrodes	224
7.1.3	Chapter 5: Generative Adversarial Networks for the reconstruction of three-dimensional multi-phase electrode microstructure	225
7.1.4	Chapter 6: Gaussian Processes and Bayesian optimisation for the design of microstructures with optimum properties	226
7.2	Further work	227
7.3	Dissemination	228
7.3.1	Papers	228
7.3.2	Oral presentations	229
7.3.3	Poster presentations	230
	Appendices	253
A	Flow chart of PNM iterative process	254
B	Publications	256
B.1	Publication 1	256
B.2	Publication 2	256

List of Figures

1.1	Schematic diagram of a solid oxide fuel cell (SOFC) showing the electrolyte, the H ₂ electrode (<i>i.e.</i> anode), the O ₂ electrode (<i>i.e.</i> cathode) with their respective reactions, and the arrows representing the direction of electron and ion flow. ³⁸	5
1.2	Schematic diagram of a Lithium-ion cell composed of a LiCoO ₂ cathode and a graphite anode. The green arrows represent the transport of electrons during charge, as well as the Li ⁺ ions traveling from the cathode through the electrolyte (composed fo LiPF ₆ solvent) and inserted into the anode. The opposite process occurs during discharge and is shown with the black arrows. ⁴²	7
1.3	Schematic diagram of a Vanadium Redox Flow battery (RFB) showing the flow of electrodes and electrolyte during charge (solid arrow) and discharge (dashed arrow). The VRFB uses a V ²⁺ /V ³⁺ redox couple as the negative pair and a V ⁵⁺ /V ⁴⁺ redox couple as the positive pair. ⁴⁵	8
2.1	Schematic diagram of a PEM fuel cell showing the electrolyte, the H ₂ anode, the O ₂ cathode, the catalyst layers, the GDL and the PEM membrane, and the arrows representing the direction of electron and ion flow. ⁴⁸	28
2.2	Reconstruction of the Fontainebleau sandstone using the two-point correlation function (S_2) obtained from one slice. The system size is 128 × 128 × 128 pixels, and one pixel is equal to 7.5. The figure on the left shows the pore space as white and opaque, and the grain phase as black and transparent. The figure on the right shows a 3D perspective of the reconstruction. ⁸⁷	41
2.3	The figure on the left shows a reconstruction of a boron carbide/aluminum composite, where the black phase represents boron carbide with $\phi_1 = 0.647$, and the white phase constitutes aluminum with $\phi_2 = 0.353$. The figure on the right shows the TPCF plot of the aluminum phase. ⁹¹	42
2.4	Reconstructed anode microstructures sintered at (a) 1300 °C, (b) 1350 °C and (c) 1400 °C. Green: Ni, blue: YSZ, transparent gray: pore. ⁹³	44
2.5	Graphic representation of a logistic function as a neural network	46
2.6	Three layer neural network	47
3.1	Electrochemical and geometric properties of the pore network model.	75

3.2	Comparison of simulated explicit Euler scheme (dots) and analytical solution (solid line) for convective-diffusive-migration-reactive flow in MCM transport for 8 pores connected in series.	88
3.3	Plots showing graphical validation of cell discharge at $400 \text{ A} \cdot \text{m}^2$ compared with literature results [55].	92
4.1	Segmented reconstructed image of Toray 090 from XCT data	101
4.2	Pore size distribution histogram representing the pore network extracted from an X-CT image of a Toray 090 sample with dimensions $441 \times 215 \times 546 \mu\text{m}$. ⁸	102
4.3	Overview of pore network extraction and operation: (a) X-CT segmented image, (b) pore fractions with inserted pore network, (c) standalone pore network, (d–f) 3D example of simulation. ⁸	103
4.4	Decoupled steady-state (a) pressure, and; (b) flow distributions. ⁸ .	106
4.5	Permeation of V(II) through a PNM representing a section of Toray 090. The 3D images proceed in 1 s steps starting from 0 s (a). ⁸ . . .	107
4.6	(a) Current density; and, (b) state of charge variation with time at various electrode potential drops. ⁸	108
4.7	Current distribution at various electrode potentials (a) -0.24 V , (b) -0.21 V , (c) -0.19 V and (d) -0.15 V (at 50% state of charge). ⁸ . .	109
4.8	(a) Current distribution (at -0.21 V electrode potential and state of charge 50%), and; (b) concentration (purely convective-diffusive regime) distribution after 4 s. ⁸	110
4.9	Transient concentration distribution with electrochemical reaction at an electrode potential of -0.21 V for Toray 090. The 3D images proceed in 1 s steps starting from 0 s (a) to 8 s (f). ⁸	111
4.10	Transient current density distribution with electrochemical reaction with electrode potential of -0.21 V . The 3D images proceed in 1 s steps starting from 0 s (a) to 8 s (f). ⁸	112
4.11	Comparison of concentration distribution at 5 s in (a) a purely convective-diffusive transport system and, (b) a convective-diffusive transport system with electrochemical migration. Green rings highlight the regions where convective flow is limited. ⁸	114
4.12	Segmented reconstructed image of SGL29AA	116
4.13	Overview of pore network extraction of SGL29AA: (a) X-CT segmented image of SGL, (b) pore fractions in segmented image obtained using Avizo software, (c) standalone pore network extracted using the Maximal Ball algorithm ¹⁰	117
4.14	Permeation of V(II) through a PNM representing a section of SGL29AA. The 3D images proceed in 1 s steps starting from 0 s (a).	118
4.15	Transient concentration distribution with electrochemical reaction at an electrode potential of -0.21 V for SGL29AA. The 3D images proceed in 1 s steps starting from 0 s(a) to 8 s(f)	119
4.16	Segmented reconstructed image of Freudenberg electrode	120
4.17	Overview of pore network extraction of Freudenberg: (a) X-CT segmented image, (b) pore fractions in segmented image, (c) standalone pore network	120

4.18	Permeation of V(II) through a PNM representing a section of Freudenberg. The 3D images proceed in 1 s steps starting from 0 s (a). . . .	122
4.19	Transient concentration distribution with electrochemical reaction at an electrode potential of -0.21 V for Freudenberg. The 3D images proceed in 1 s steps starting from 0 s(a) to 8 s(f)	123
4.20	Segmented reconstructed image of ELAT-H carbon cloth	124
4.21	Overview of pore network extraction of ELAT-H: (a) X-CT segmented image, (b) pore fractions in segmented image, (c) standalone pore network	124
4.22	Transient concentration distribution with electrochemical reaction at an electrode potential of -0.21 V for ELAT-H. The 3D images proceed in 1 s steps starting from 0 s(a) to 8 s(f)	125
4.23	Transient concentration distribution with electrochemical reaction at an electrode potential of -0.21 V for ELAT-H. The 3D images proceed in 1 s steps starting from 0 s(a) to 8 s(f)	127
6.1	Gaussian Process as surrogate model $\hat{f}(\mathbf{x})_{\mathcal{GP}}$ to map the correlation between the latent space \mathbf{z} and the estimated properties \mathbf{y}	189
6.2	Closed-loop generation-optimisation process: implementation of a Bayesian optimisation algorithm to optimise the morphological and transport properties \mathbf{y} of the generated microstructure as a function of the latent space \mathbf{z} of the Generator.	191
6.3	Estimated SSA of 30 generated samples at points 0, 50, 150, 350 and 500 during the maximisation process. The inserted figure shows the complete unconstrained maximisation of SSA of NMC phase for 500 iterations.	195
6.4	Comparison between the estimated SSA_{NMC} , $D_{\text{rel,pore}}$ and ϕ_{NMC} at iteration 0 and 500 for 30 generated samples	196
6.5	Estimated SSA_{NMC} as a function of ϕ_{pore} using different correlations compared to the image-based estimated values of the generated microstructures with different ϕ_{pore}	197
6.6	Estimated $D_{\text{rel,pore}}$ of 30 generated samples at each 100 points during the maximisation process. The inserted figure shows the complete unconstrained maximisation of $D_{\text{rel,pore}}$ for 400 iterations. . .	199
6.7	Comparison of the estimated SSA_{NMC} , $D_{\text{rel,pore}}$, ϕ_{pore} , and τ_{b} for iteration 0 and 400 of the unconstrained maximisation process of $D_{\text{rel,pore}}$	199
6.8	Results of estimated SSA_{NMC} and $D_{\text{rel,pore}}$ as a function of the iterations number for different values of β : a) $\beta = 0.25$, b) $\beta = 0.5$, c) $\beta = 0.75$	202
6.9	Results of estimated SSA_{NMC} and ϕ_{NMC} as a function of the iterations number for the SSA_{NMC} maximisation process constrained by a constant ϕ_{NMC} . The results show a confidence interval of 95%. . .	204
6.10	Results of estimated $D_{\text{rel,pore}}$, ϕ_{pore} and ϕ_{CBD} as a function of the iterations number for the $D_{\text{rel,pore}}$ maximisation process constrained by a constant ϕ_{pore} . The results show a confidence interval of 95%. . .	205

6.11	Results of the estimated $D_{\text{rel,pore}}$ as a function of the iterations number for the three directions x , y and z for the unconstrained maximisation of $D_{\text{rel,pore},x}$. The results show a confidence interval of 95%.	207
6.12	Results of estimated $D_{\text{rel,pore}}$ of 30 microstructure samples generated at four points during the unconstrained maximisation process of $D_{\text{rel,pore},x}$.	207
6.13	Results of the estimated $D_{\text{rel,pore}}$ as a function of the iterations number for the three directions x , y and z for the maximisation of $D_{\text{rel,pore},x}$ constrained by a constant value of $D_{\text{rel,pore},y}$ and $D_{\text{rel,pore},z}$. The results show a confidence interval of 95%.	208
6.14	Results of estimated $D_{\text{rel,pore}}$ of 30 microstructure samples generated at four points during the maximisation process of $D_{\text{rel,pore},x}$ constrained by a constant value of $D_{\text{rel,pore},y}$ and $D_{\text{rel,pore},z}$.	208
6.15	Porosity as a function of the electrode length along the direction to be optimised.	210
6.16	Unconstrained maximisation of the relative diffusivity of the pore phase $D_{\text{rel,pore}}$ for an image of size 128^3 voxels.	212
6.17	Two principal components of the 64-dimensional latent space as a function of different microstructural and transport properties: a) porosity (ϕ_{pore}), b) Specific surface area of the NMC phase (SSA_{NMC}), c) relative diffusivity of the pore phase along the x direction ($D_{\text{rel,pore},x}$), d) relative diffusivity of the pore phase ($D_{\text{rel,pore}}$)	213
A.1	Flow chart graphically outlining the numerical algorithm.	255
B.1	Paper front page	257
B.2	Paper front page	258

List of Tables

3.1	Physical parameters for the mass transport equation (eq. 3.3) from literature	89
3.2	Parameters of pore-network model for OpenPNM system	90
4.1	Toray 090 sample electrode dimensions.	102
4.2	Permeability data ($\times 10^{12} \text{m}^2$) of a sample of Toray 090 calculated from pore network model using different viscosities ^{6,11} , compared with literature ¹²	103
4.3	SGL29AA sample electrode dimensions.	116
4.4	Freudenberg sample electrode dimensions.	121
4.5	ELAT-H sample electrode dimensions.	123
5.1	Key details about the two open-source, segmented, nano-tomography datasets	139
5.2	Dimensionality of each layer in the GAN architecture for each porous material (layers, dimensions, optimiser, input image size, number of training samples) See Figure 5.1	143
5.3	Results of volume fractions, specific surface areas, triple-phase boundary densities and relative diffusivities calculated from the real and generate datasets. The black phase corresponds to the pores, white phase corresponds to the binder and grey phase corresponds to the NMC-532.	151
5.4	Detailed description of the normalised TPCF for the Li-ion cathode along the three directions for each of the three phases (pores, NMC and binder)	153
5.5	Results of volume fractions, specific surface areas, triple-phase boundary densities and relative diffusivities calculated from the real and generate datasets. The black phase corresponds to the pores, white phase corresponds to the ceramic (<i>i.e.</i> YSZ) and grey phase corresponds to the metal (<i>i.e.</i> Ni).	154
5.6	Detailed description of the normalised TPCF for the SOFC anode along the three directions for each of the three phases (pores, Ni and YSZ)	156
6.1	Dimensionality of each layer in the GAN architecture for each porous material (layers, dimensions, optimiser, input image size, number of training samples)	188
6.2	Equivalent diameter and sphericity of Li-ion microstructures samples during SSA_{NMC} unconstrained maximisation	198

6.3 Equivalent diameter and sphericity of Li-ion microstructures samples during SSA_{NMC} maximisation constraining ϕ_g 205

Nomenclature

Acronyms

AAD	Absolute average deviation
CFP	Carbon fibre paper
CV	Control volume
DNS	Direct numerical simulation
EC	Electrochemical conversion
EES	Electrochemical energy storage
FDM	Finite difference method
FEM	Finite element method
FVM	Finite volume method
GAN	Generative Adversarial Network
GP	Gaussian Process
LBM	Lattice Boltzmann method
LIB	Lithium-ion battery
MCM	Mixed-cell method
PNM	Pore Network Model
REV	Representative Elementary volume
RFB	Redox flow battery
SOC	State of charge
SOFC	Solid Oxide Fuel Cell
SPH	Smooth particle hydrodynamics
VRFB	All-vanadium redox flow battery

Latin Symbols

N	Mass flux, [$\text{kg s}^{-1} \text{m}^{-2}$]
\mathbf{u}	Velocity, [m s^{-1}]
A	Cross sectional area, [m^2]

C, c	Concentration, [mol m^{-2}]
D^{eff}	Effective diffusivity, [$\text{m}^2 \text{s}^{-1}$]
d_f	Fibre diameter, [m]
E	Electrode potential, [V]
E_{eq}	Equilibrium potential, [V]
F	Faraday constant, [A s mol^{-1}]
g	Hydraulic conductivity, [$\text{m}^3 \text{s}^{-1} \text{Pa}^{-1}$]
J_0	Exchange current density, [A m^{-2}]
J_{BV}	Current density from Butler-Volmer, [A m^{-2}]
J_{ct}	Transfer current density, [A m^{-2}]
J_{ext}	External current density, [A m^{-2}]
K	Permeability, [m^2]
k_a	Standard reaction rate constant, [m s^{-1}]
k_{CK}	Kozeny-Carman constant, –
L	Half-cell width/Electrode thickness, [m]
l	Throat length, [m]
L_{avg}	characteristic length scale, [m]
P	Pressure, [Pa]
Q	Flow rate, [$\text{m}^3 \text{s}^{-1}$]
R	Universal gas constant, [$\text{J mol}^{-1} \text{K}^{-1}$]
S_A	Active surface area, [m^2]
SSA	Specific surface area, [$\text{m}^3 \text{m}^{-2}$]
t	time, [s]
t_p	transference number of the positive ion, –
U_{avg}	characteristic velocity, [m s^{-1}]
v_{av}	Average electrolyte velocity, [m s^{-1}]

Greek Symbols

α_+	cathodic transfer coefficient, –
α_-	anodic transfer coefficient, –
Δ	difference, –
η	Overpotential, [V]
κ_s	solid phase conductivity, [$\text{\$/m}$]
μ	mean value, –
μ	viscosity, [Pa s]

μ_p	reduced electrochemical potential, [J mol ⁻¹]
ν	kinematic viscosity, [m ² s ⁻¹]
ν'_{ir}	effective stoichiometric matrix for irreversible reactions, –
ϕ	phase volume fraction, –
ϕ_e	electrolyte potential, [V]
ϕ_s	solid phase potential, [V]
ρ	density, [kg m ⁻³]
σ	ionic conductivity, [§/m]
τ	tortuosity, –
ε	porosity, –

Subscripts & Superscripts

$\langle \rangle$	volume averaged value
a	anodic
c	cathodic

Chapter 1

Introduction

1.1 Motivation

The global increase in the energy demand in recent years, along with a pressing need to reduce greenhouse gas emissions has led to the large-scale installation of renewable energy sources, mainly wind and solar.¹ Due to the intermittency and unreliability that these sources present, energy storage technologies are considered essential as back-up capacity to stabilise the grid. Although pumped hydro currently handles the vast majority of the required capacity², electrochemical energy storage (EES) and energy conversion (EC) technologies offer a potential alternative given by their rapid response and distributed deployability. Additionally, the road-maps for decarbonising transport systems propose the partial or total electrification of vehicles by 2050.³ This is therefore expected to boost the production of electric vehicles in the coming years, which will require a mass production of batteries. Over the past 10 years significant research has been focused on technological improvements of EES, which has resulted in a significant drop in the cell and pack prices for LIBs: from 668\$/kWh in 2013 to 137\$/kWh in 2020.⁴ Nevertheless, the high production costs of EES and EC technologies must be further decreased in order to meet the aggressive cost targets required for their widespread commercialisation.¹ One proposed pathway for increasing the returns over the production costs involves developing higher capacity EES systems. This would require an improvement in the cell architecture, as well as the design and optimisation of electrode microstructures.⁵ Understanding the effect of electrode microstructures in order to improve the performance of EES systems is the primary

motivation of this work.

Electrodes constitute one of the main components of EES and EC technologies since they represent the sites where the major transport processes and reactive mechanisms occur.⁶ Thus, any limitation at the electrode level represents an impact in the battery performance. Research around electrode materials with slow degradation, low cost and high energy density is important for the improvement of these technologies.^{7,8} Nevertheless, a significant correlation exists between the battery performance and the electrode morphology at the micro and nano scales.^{7,9,10} Therefore the quantification of electrode microstructure is crucial for understanding the structure-performance relationship and therefore essential for the design of optimal electrodes which will improve the battery performance.^{9,11}

Recent advances in micro and nano imaging techniques (*i.e.* X-ray computed tomography (X-CT), Focused Ion Beam coupled with Scanning Electron Microscope (FIBSEM)) have enabled the characterisation of electrodes in terms of their microstructural parameters.¹² These techniques have allowed the acquisition of detailed and high-resolution three-dimensional images of electrode materials.¹³ Microstructural and transport properties can be estimated over these 3D tomographic images by solving the flow and transport equations directly at the pore-scale.^{9,12} These direct numerical simulations (DNS) provide insights of the effect into the porous structure in the various transport processes (*i.e.* diffusion, convection and migration) and electrochemical reaction predominant within the electrode.⁸ This is key for understanding the correlation between the porous microstructure and the battery performance.^{14,15} However, despite the advantages of DNS, they can be computationally expensive, unrepresentative and difficult to validate. As an inexpensive alternative for simulating the transport processes within the whole electrode, continuum-scale, multi-physics models have been presented in the literature.⁵ A set of microstructural properties such as specific surface area, volume fractions, tortuosity and permeability can be determined from tomographic images. These properties are homogenised throughout the extent of the whole electrode and used as parameters of design for the continuum models. Although these models can be validated based on experimental data of the whole

cell, they sometimes risk over-simplifying the complex electrode morphology.^{16–18}

To date, most research has primarily focused on analysing the microstructure - performance relationship from a forward perspective.¹¹ In this process, an experimentally generated electrode is characterised in terms of its microstructural properties, and a model is further implemented to quantify its expected overall performance (pore-scale or continuum model). Although this forward step is insightful, the reversibility of the microstructure-performance process is required to enable the implementation of an optimisation algorithm to aid the design of improved electrodes. In this context, finding the probability distribution function (pdf) that fully defines the microstructural space is crucial for the design and optimisation process.¹⁹ For this purpose, the stochastic reconstruction of porous media has been implemented in order to manipulate the geometric representation of the microstructure so as to achieve different properties. This stochastic modelling of porous media allows the generation of synthetic realisations based on the statistical properties of the porous microstructure. Stochastic models have been implemented to generate an arrangement of particles or pores based on idealised geometric shapes such as spheres.^{20–25} These models adjust a pdf to the experimental particle or pore size distribution and spread a set of spheres in a confined space according to this function. Other authors have implemented simulated annealing techniques to reconstruct three-dimensional microstructures based on a two-point correlation function^{23,26–32}. Alternative algorithms implement sphere packing and growth methods as well as particle-based simulations to mimic the fabrication process of electrodes and relate them to their respective microstructure.^{33–36} These models however, have proved to be computationally expensive and specific for a particular type of electrode materials.

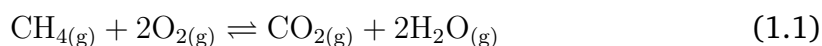
Based on this, understanding the correlation between the complex micro-scale spatial arrangement of electrodes and the resulting transport and reactive processes within them is critical for the design of improved electrodes for high capacity EES systems. The present work will focus on developing a series of models that can bridge the gap between the microstructure-performance relation as a closed-loop optimisation process.

1.2 Overview of EES and EC technologies

This section presents a brief overview of the main EES and EC technologies studied in this work: Solid Oxide Fuel Cells, Lithium-ion batteries and Redox Flow Batteries. For the purpose of this work, these systems will be analysed in terms of their electrode configuration, their microstructural properties and the transport processes that occur within the electrode during operation.

1.2.1 Solid Oxide Fuel Cells

Solid Oxide Fuel Cells (SOFCs) are a type energy conversion technology classified as a high-temperature electrolyser-fuel-cell.⁹ They are composed of a dense solid oxide material used as electrolyte which is sandwiched between two porous electrodes: the anode and the cathode. In SOFCs, the solid electrolyte is used to conduct negative oxygen ions from the cathode to the anode. These systems operate in a range between 600 – 1000 °C to allow internal reforming of hydrocarbon fuels (*e.g.* methane, propane, butane), and have a total electrical efficiency between 45 – 60%.³⁷ The overall reaction is defined as:



The most commonly used materials as SOFC components are Yttria Stabilized Zirconia (YSZ) for the electrolyte and Ni-YSZ cermet for the H₂ electrode (*i.e.* anode).⁹ The O₂ electrode (*i.e.* cathode) is currently made of Mixed Ionic Electronic Conductors (MIECs) such as Lanthanum Strontium Cobalt (LSC) or Lanthanum Strontium Cobalt Ferrite (LSCF). A schematic diagram of a solid oxide fuel cell (SOFC) with its components is shown in figure 1.1.

Although fuel cells have increased in popularity in the past years, there are still certain hurdles that need to be overcome before their mass adoption. Research has mainly focused on the development of low-temperature SOFCs to reduce costs related to operation and degradation.³⁷ Additionally, despite the stable operation achieved with various fuels, the need for a fuel pre-processing step increases the operational costs and reduces the efficiency. Thus, the development of SOFCs in which the fuel can be directly fed into the anode chamber have become a prior-

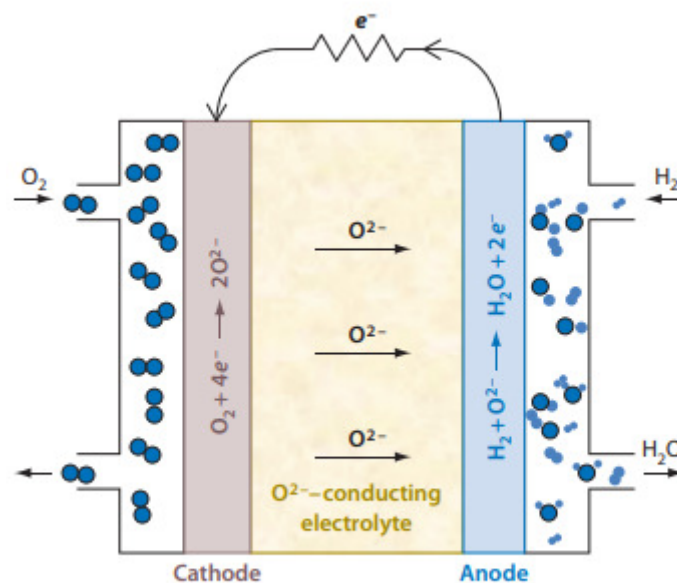


Figure 1.1: Schematic diagram of a solid oxide fuel cell (SOFC) showing the electrolyte, the H_2 electrode (*i.e.* anode), the O_2 electrode (*i.e.* cathode) with their respective reactions, and the arrows representing the direction of electron and ion flow.³⁸

ity, in order to allow a maximum transfer of chemical energy to electrical energy.³⁷

The electrode microstructure is known to play a major role in the global cell performances by controlling the rates of the electrochemical reactions.^{9,39} Given the large variety of electrode manufacturing processes, a wide range of electrodes can be produced and adapted to each application (*i.e.* fuel cell, steam electrolysis, reversible system).⁹ Therefore, improvements in the electrode microstructure are expected to lead to more efficient SOFCs for each particular application. This work implements a stochastic reconstruction technique to generate synthetic SOFC electrodes as means to further optimise the microstructure for different applications.

1.2.2 Lithium-ion batteries

Lithium-ion batteries (LIBs) constitute the leading energy storage technology for portable applications and electric vehicles. Additionally, these technologies have been recently implemented as back-up capacity for balancing the grid.⁴⁰ Similar to other EES systems, LIBs are constituted by four main components: an anode,

a separator, a liquid electrolyte and a cathode. The functioning principle of LIBs is based on the reversible reaction that allows the movement of lithium ions from the anode, through a liquid electrolyte and into the cathode during discharge, and the opposite process charging.

In terms of LIBs components, these systems use an intercalated lithium compound as the cathode material and typically graphite at the negative electrode. An intercalation cathode is a solid network which can store and release *guest* ions reversibly. In a Li-ion battery, Li^+ is the guest ion and the host network compounds are metal chalcogenides, transition metal oxides, and polyanion compounds. These intercalation compounds can be classified according to their crystal structure as: layered (e.g. LiTiS_2 , LiCoO_2 , $\text{LiNi}_{0.33}\text{Mn}_{0.33}\text{Co}_{0.33}\text{O}_2$, $\text{LiNi}_{0.8}\text{Co}_{0.15}\text{Al}_{0.05}\text{O}_2$), spinel (LiMn_2O_4), olivine (LiFePO_4). Typically, intercalation cathodes have a specific capacity ranging between 100 – 200 mAh/g and average voltage of 3 – 5 V *vs.* Li/Li^+ .⁴¹ Figure 1.2 shows a schematic diagram of a LIB composed of a LiCoO_2 cathode and graphite anode.

The most commonly used anode materials consist of graphite due to its low cost, abundant availability, high Li diffusivity, high electrical conductivity, and low volume changes during lithiation/delithiation. Other anode materials can be implemented such as LTO, Si, Ge and Sn; however, the last three almost double their size during cycling, which leads to a fast degradation. In this context it is important to mention that anode materials are implemented instead of Li metal to avoid the formation of dendrites which can cause short circuiting and a thermal run-away reaction on the cathode.⁴¹

Despite the significant advances in LIBs, a series of hurdles still remain regarding safety, energy and power density, durability and safety.⁴⁰ One of the main challenges involves elucidating the optimum electrode design for specific operating conditions. A comprehensive understanding of the physical and electrochemical processes at the micro-scale has been proposed by Lu *et al.* as a way to rationalise the microstructural design (e.g. porosity, thickness and mass loading)

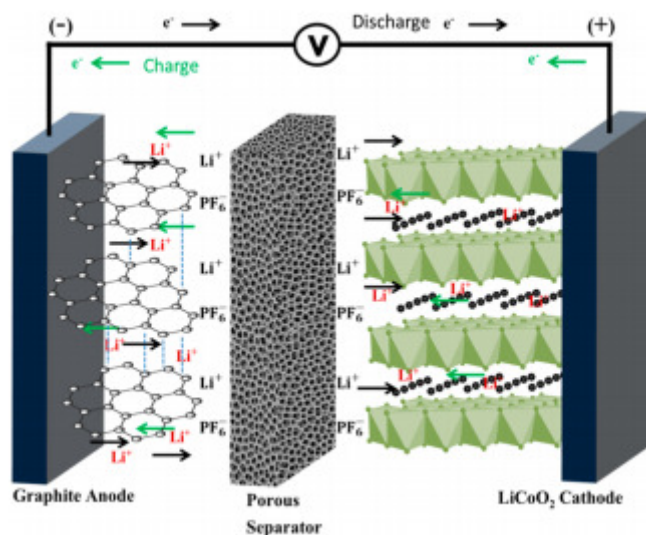


Figure 1.2: Schematic diagram of a Lithium-ion cell composed of a LiCoO_2 cathode and a graphite anode. The green arrows represent the transport of electrons during charge, as well as the Li^+ ions traveling from the cathode through the electrolyte (composed of LiPF_6 solvent) and inserted into the anode. The opposite process occurs during discharge and is shown with the black arrows.⁴²

for different applications.⁴⁰ In this context, the present work seeks to address this question of determining the optimum electrode design for different applications through the implementation of various computational techniques.

1.2.3 Redox Flow Batteries

Redox flow batteries (RFBs) have been proposed for large-scale stationary energy storage applications. In these systems, the energy is stored as, and released, by changing the oxidation states of ionic species dissolved in electrolyte solutions.⁴³ The electrolytes are stored in external containers and pumped through electrochemical cells, or electrochemical reactors, which convert chemical energy directly to electricity on demand. The power density is determined by the size and design of the electrochemical cell whereas the energy density or output depends on the size of tanks.³⁷

To date, various redox couples have been investigated in RFBs, such as Fe-Ti, a Fe-Cr, and a polyS-Br; however the vanadium redox flow battery (VRFB) has been developed the furthest. The VRFB uses a $\text{V}^{2+}/\text{V}^{3+}$ redox couple as the negative pair and a $\text{V}^{5+}/\text{V}^{4+}$ redox couple as the positive pair.^{37,44} Figure 1.3

presents a schematic diagram of a VRFB during charge and discharge.⁴⁵ The main advantage of this battery is the use of ions of the same metal on both sides, which reduces the species crossover. In other type of RFBs, the crossover causes irreversible degradation of the electrolytes and consequently a capacity loss. Future RFBs are expected to use engineered molecules or complexes, since this approach enables one to shift the standard reduction potential to a more desirable potential.¹ Additionally, the implementation of non-aqueous electrolytes has been pursued since they enable a broader window of electrochemical stability. However, non-aqueous electrolytes also present significant disadvantages, such as higher solvent costs, higher viscosities, and lower ionic conductivities.¹

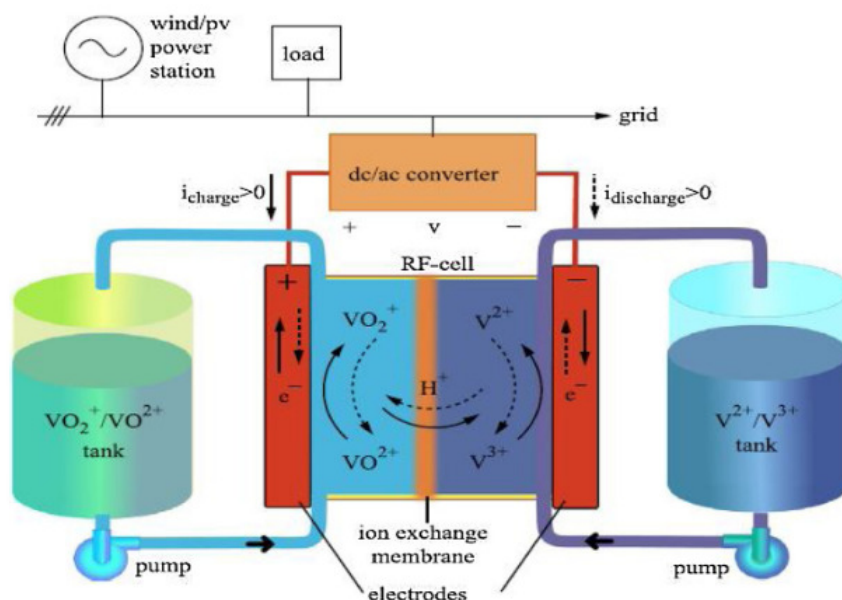


Figure 1.3: Schematic diagram of a Vanadium Redox Flow battery (RFB) showing the flow of electrodes and electrolyte during charge (solid arrow) and discharge (dashed arrow). The VRFB uses a V²⁺/V³⁺ redox couple as the negative pair and a V⁵⁺/V⁴⁺ redox couple as the positive pair.⁴⁵

In terms of the cell configuration, the reactor costs constitute the main fraction of the total capital cost of the system. Thus, maximising the power density at reasonable energy efficiencies has been proposed as a pathway for reducing costs.⁴³ Since the electrolyte is pumped into the system during cycling, high current and power densities can be achieved due to the convective flow of electrolyte through the porous electrode. Nonetheless, the pumping power required to flow the electrolyte into the system is a parasitic loss that must be accounted for.⁴³ In

this context, an improvement of the cell architecture, flow channel configuration and electrode microstructure are factors that can lead to a higher power system. Therefore, a deep understanding of the transport processes within the cell is essential for their improved design. In this work, a particular focus is given to analysing the coupled flow, mass and charge transport processes within the electrodes as means to understanding the effect of the microstructure in the cell performance.

1.3 Objectives

The central objective of this work is the characterisation and optimisation of electrode microstructures for energy storage devices. A series of computational methods are developed in order to shed light on our current understanding of the effect of the electrode microstructure on the battery performance. Due to the nature of the different electrodes used for the three systems analysed in this work (*i.e.* SOFCs, RFBs, Li-ion batteries), in terms of their microstructure and properties, different computational methods were required. These methods involve the development of a pore network model, the implementation of deep generative algorithms and the use of Bayesian optimisation to enable the design of improved electrodes.

As previously stated, the design of optimised electrodes involves a two-way reversible process that can correlate microstructure with performance. As it stands, both processes present limitations: the forward step is limited by computational expense while the backward step is constrained by the non-existence of a probability distribution function that fully defines the microstructural geometric space. As a way of overcoming these limitations, this project aims to target them as separate processes which can then be combined into an optimisation problem. This work was therefore structured into three stages, each of which has been assigned with particular objectives:

1. Objective 1: The development of a computationally inexpensive model that can efficiently correlate the electrode morphology with the overall system performance. To achieve this, a Pore Network Model (PNM) is presented.^{46,47} This model aims to achieve the full integration of the predominant transport processes that pre-determine the cell performance, (*i.e.* velocity, mass and

charge transport), along with the electrochemical reaction occurring at the electrode, within one computational model.⁶

2. Objective 2: The generation of a model that can learn the probability distribution function (pdf) that defines an electrode microstructure.¹⁹ This involves the stochastic reconstruction of the real microstructure through the implementation of Generative Adversarial Networks (GANs).^{48–50} With this approach, a differentiable function, namely the Generator, represented by a fully convolutional neural network is able to implicitly capture the pdf that characterises the electrode. This algorithm is implemented for the fast generation of synthetic three-dimensional three-phase microstructures.
3. Objective 3: Perform an optimisation of the electrode microstructure based on a structure-property evaluation. In this step, a transport simulation is implemented over the generated microstructures to evaluate the microstructural and transport properties of the electrodes. A Gaussian Process Regression is then used as a surrogate function to map the latent space of the generator with the calculated properties.^{51–53} Finally a Bayesian Optimisation approach based on sequential adaptive sampling is proposed in order to optimise the latent space to achieve microstructures with optimised properties.^{54,55}

1.4 Thesis structure

This dissertation is structured in such a way that each chapter is self-contained and can be considered as a separate entity, but the context of the document allows each chapter to build from the previous one. Each chapter contains an introduction section with the necessary literature review to present the motivation behind the work contained in that chapter. Subsequently, the results, discussion and conclusions of each chapter are included, addressing the main findings and contributions.

In order to provide a structure to the computational approaches presented in this work, this thesis is organised into the following chapters:

Chapter 2 contains the theoretical background behind the motivation of this work, and to the research questions that this project seeks to answer.

Chapter 3 outlines the theory behind the development of a pore network model (PNM) as a computationally efficient algorithm to simulate the transport processes and electrochemical reaction within electrodes.

Chapter 4 presents a case study that consists on the implementation of the PNM for a set of carbon-based electrodes in a redox flow battery.

Chapter 5 introduces a computational method based on Generative Adversarial Networks for the stochastic reconstruction of electrode microstructures.

Chapter 6 presents a closed-loop generation-optimisation approach for the design of electrode microstructures with optimum user-specified properties.

Finally, Chapter 7 outlines the main conclusions and contributions of this work and presents the key points that set the basis for future projects.

References

- [1] M. L. Perry and A. Z. Weber, “Advanced Redox-Flow Batteries: A Perspective,” *Journal of The Electrochemical Society*, vol. 163, no. 1, pp. A5064–A5067, 2016.
- [2] D. Rastler, “Electricity energy storage technology options: a white paper primer on applications, costs, and benefits,” 2010.
- [3] Department of Transport, “Decarbonising transport, Setting the Challenge,” tech. rep., Department of Transport, 2020.
- [4] Bloomberg NEF, “Battery Pack Prices Cited Below \$100/kWh for the First Time in 2020, While Market Average Sits at \$137/kWh,” 2020.
- [5] H. W. Wu, “A review of recent development: Transport and performance modeling of PEM fuel cells,” *Applied Energy*, vol. 165, pp. 81–106, 2016.
- [6] A. Gayon Lombardo, B. A. Simon, O. Taiwo, S. J. Neethling, and N. P. Brandon, “A pore network model of porous electrodes in electrochemical devices,” *Journal of Energy Storage*, vol. 24, p. 100736, 2019.
- [7] M. H. Chakrabarti, N. P. Brandon, S. A. Hajimolana, F. Tariq, V. Yufit, M. A. Hashim, M. A. Hussain, C. T. Low, and P. V. Aravind, “Application of carbon materials in redox flow batteries,” *Journal of Power Sources*, no. 253, pp. 150–166, 2014.
- [8] A. Gupta, J. H. Seo, X. Zhang, W. Du, A. M. Sastry, and W. Shyy, “Effective Transport Properties of LiMn₂O₄ Electrode via Particle-Scale Modeling,” *Journal of The Electrochemical Society*, vol. 158, no. 5, p. A487, 2011.
- [9] H. Moussaoui, J. Laurencin, Y. Gavet, G. Delette, M. Hubert, P. Cloetens, T. Le Bihan, and J. Debayle, “Stochastic geometrical modeling of solid oxide cells electrodes validated on 3D reconstructions,” *Computational Materials Science*, vol. 143, pp. 262–276, 2018.
- [10] G. Hinds and E. Brightman, “In situ mapping of electrode potential in a PEM fuel cell,” *Electrochemistry Communications*, vol. 17, no. 1, pp. 26–29, 2012.
- [11] Y. Zhang, M. Yan, Y. Wan, Z. Jiao, Y. Chen, F. Chen, C. Xia, and M. Ni, “High-

- throughput 3D reconstruction of stochastic heterogeneous microstructures in energy storage materials,” *npj Computational Materials*, vol. 5, no. 1, 2019.
- [12] S. J. Cooper, A. Bertei, D. P. Finegan, and N. P. Brandon, “Simulated impedance of diffusion in porous media,” *Electrochimica Acta*, vol. 251, pp. 681–689, 2017.
- [13] M. J. Blunt, *Multiphase Flow in Permeable Media: A Pore-Scale Perspective*. Cambridge: Cambridge University Press, 1 ed., 2017.
- [14] G. Qiu, A. S. Joshi, C. R. Dennison, K. W. Knehr, E. C. Kumbur, and Y. Sun, “3-D pore-scale resolved model for coupled species/charge/fluid transport in a vanadium redox flow battery,” *Electrochimica Acta*, vol. 64, pp. 46–64, mar 2012.
- [15] G. Qiu, C. R. Dennison, K. W. Knehr, E. C. Kumbur, and Y. Sun, “Pore-scale analysis of effects of electrode morphology and electrolyte flow conditions on performance of vanadium redox flow batteries,” *Journal of Power Sources*, vol. 219, pp. 223–234, 2012.
- [16] A. A. Shah, R. Tangirala, R. Singh, R. G. A. Wills, and F. C. Walsh, “A Dynamic Unit Cell Model for the All-Vanadium Flow Battery,” *Journal of The Electrochemical Society*, vol. 158, pp. A671–A677, jun 2011.
- [17] Y. A. Gandomi, D. S. Aaron, T. A. Zawodzinski, and M. M. Mench, “In Situ Potential Distribution Measurement and Validated Model for All-Vanadium Redox Flow Battery,” *Journal of The Electrochemical Society*, vol. 163, no. 1, pp. A5188–A5201, 2016.
- [18] J. Newman, “Optimization of Porosity and Thickness of a Battery Electrode by Means of a Reaction-Zone Model,” *Journal of The Electrochemical Society*, vol. 142, no. 1, pp. 97–101, 1995.
- [19] A. Gayon-Lombardo, L. Mosser, N. P. Brandon, and S. J. Cooper, “Pores for thought: generative adversarial networks for stochastic reconstruction of 3D multi-phase electrode microstructures with periodic boundaries,” *npj Computational Materials*, vol. 6, no. 1, pp. 1–11, 2020.
- [20] G. Matheron, *Random sets and integral geometry*. Wiley New York, 1975.

- [21] J. Serra, "The Boolean model and random sets," *Computer Graphics and Image Processing*, vol. 12, no. 2, pp. 99–126, 1980.
- [22] D. Jeulin, "Random texture models for material structures," *Statistics and Computing*, vol. 10, no. 1, pp. 121–132, 2000.
- [23] C. L. Yeong and S. Torquato, "Reconstructing random media," *Physical Review E - Statistical Physics, Plasmas, Fluids, and Related Interdisciplinary Topics*, vol. 57, no. 1, pp. 495–506, 1998.
- [24] S. Torquato, *Random heterogeneous materials: microstructure and macroscopic properties*. Springer Science & Business Media, 1 ed., 2013.
- [25] P. A. Rikvold and G. Stell, "Porosity and specific surface for interpenetrable-sphere models of two-phase random media," *The Journal of Chemical Physics*, vol. 82, no. 2, pp. 1014–1020, 1985.
- [26] B. Lu and S. Torquato, "N-Point Probability Functions for a Lattice Model of Heterogeneous Media," *Physical Review B*, vol. 42, no. 7, pp. 4453–4459, 1990.
- [27] C. L. Yeong and S. Torquato, "Reconstructing random media. II. Three-dimensional media from two-dimensional cuts," *Physical Review E - Statistical Physics, Plasmas, Fluids, and Related Interdisciplinary Topics*, vol. 58, no. 1, pp. 224–233, 1998.
- [28] C. Manwart, S. Torquato, and R. Hilfer, "Stochastic reconstruction of sandstones," *Physical Review E - Statistical Physics, Plasmas, Fluids, and Related Interdisciplinary Topics*, vol. 62, no. 1 B, pp. 893–899, 2000.
- [29] N. Sheehan and S. Torquato, "Generating microstructures with specified correlation functions," *Journal of Applied Physics*, vol. 89, no. 1, pp. 53–60, 2001.
- [30] L. M. Pant, *Stochastic characterization and reconstruction of porous media*. PhD thesis, University of Alberta, 2016.
- [31] Y. Jiao, F. H. Stillinger, and S. Torquato, "Modeling heterogeneous materials via two-point correlation functions: Basic principles," *Physical Review E - Statistical, Nonlinear, and Soft Matter Physics*, vol. 76, no. 3, pp. 1–37, 2007.

- [32] Y. Jiao, F. H. Stillinger, and S. Torquato, "Modeling heterogeneous materials via two-point correlation functions. II. Algorithmic details and applications," *Physical Review E - Statistical, Nonlinear, and Soft Matter Physics*, vol. 77, no. 3, pp. 1–35, 2008.
- [33] M. M. Forouzan, C. W. Chao, D. Bustamante, B. A. Mazzeo, and D. R. Wheeler, "Experiment and simulation of the fabrication process of lithium-ion battery cathodes for determining microstructure and mechanical properties," *Journal of Power Sources*, vol. 312, pp. 172–183, 2016.
- [34] I. Srivastava, D. S. Bolintineanu, J. B. Lechman, and S. A. Roberts, "Controlling binder adhesion to impact electrode mesostructures and transport," *ACS Applied Materials and Interfaces*, vol. 12, no. 31, pp. 34919–34930, 2020.
- [35] N. Siddique, A. Salehi, and F. Liu, "Stochastic reconstruction and electrical transport studies of porous cathode of Li-ion batteries," *Journal of Power Sources*, vol. 217, pp. 437–443, 2012.
- [36] N. A. Siddique and F. Liu, "Process based reconstruction and simulation of a three-dimensional fuel cell catalyst layer," *Electrochimica Acta*, vol. 55, no. 19, pp. 5357–5366, 2010.
- [37] S. P. S. Badwal, S. S. Giddey, C. Munnings, A. I. Bhatt, and A. F. Hollenkamp, "Emerging electrochemical energy conversion and storage technologies," *Frontiers in Chemistry*, vol. 2, p. 79, 2014.
- [38] R. Gorte and J. Vohs, "Catalysis in solid oxide fuel cells," *Annual review of chemical and biomolecular engineering*, vol. 2, pp. 9–30, 2011.
- [39] H. Moussaoui, R. K. Sharma, J. Debayle, Y. Gavet, G. Delette, and J. Laurencin, "Microstructural correlations for specific surface area and triple phase boundary length for composite electrodes of solid oxide cells," *Journal of Power Sources*, vol. 412, no. November 2018, pp. 736–748, 2019.
- [40] X. Lu, A. Bertei, D. P. Finegan, C. Tan, S. R. Daemi, J. S. Weaving, K. B. O'Regan, T. M. Heenan, G. Hinds, E. Kendrick, D. J. Brett, and P. R. Shearing, "3D microstructure design of lithium-ion battery electrodes assisted by X-ray nano-computed tomography and modelling," *Nature Communications*, vol. 11, no. 1, pp. 1–13, 2020.

- [41] N. Nitta, F. Wu, J. T. Lee, and G. Yushin, “Li-ion battery materials: present and future,” *Materials Today*, vol. 18, no. 5, pp. 252–264, 2015.
- [42] K. M. Abraham, “Prospects and limits of energy storage in batteries,” *The Journal of Physical Chemistry Letters*, vol. 6, no. 5, pp. 830–844, 2015.
- [43] R. M. Darling and M. L. Perry, “The Influence of Electrode and Channel Configurations on Flow Battery Performance,” *Journal of The Electrochemical Society*, vol. 161, no. 9, pp. A1381–A1387, 2014.
- [44] M. Kazacos and M. Skyllas-Kazacos, “Performance Characteristics of Carbon Plastic Electrodes in the All-Vanadium Redox Cell,” *Journal of The Electrochemical Society*, vol. 136, no. 9, pp. 2759–2760, 1989.
- [45] A. K. Rohit, K. P. Devi, and S. Rangnekar, “An overview of energy storage and its importance in indian renewable energy sector: Part i – technologies and comparison,” *Journal of Energy Storage*, vol. 13, pp. 10–23, 2017.
- [46] J. T. Gostick, “Versatile and efficient pore network extraction method using marker-based watershed segmentation,” *Physical Review E*, vol. 96, no. 2, pp. 1–15, 2017.
- [47] Q. Xiong, T. G. Baychev, and A. P. Jivkov, “Review of pore network modelling of porous media: Experimental characterisations, network constructions and applications to reactive transport,” *Journal of Contaminant Hydrology*, vol. 192, pp. 101–117, 2016.
- [48] I. Goodfellow, J. Pouget-Abadie, M. Mirza, B. Xu, D. Warde-Farley, S. Ozair, A. Courville, and Y. Bengio, “Generative Adversarial Networks,” *pre-print*, pp. 1–9. arXiv:1406.2661 [stat.ML].
- [49] I. Goodfellow, “NIPS 2016 tutorial: Generative adversarial networks,” *pre-print*, 2016. arXiv:1701.00160 [stat.ML].
- [50] I. Goodfellow, Y. Bengio, and A. Courville, *Deep Learning*. Cambridge, MA, USA: MIT Press, 2016.
- [51] X. Li, Z. Yang, L. Catherine Brinson, A. Choudhary, A. Agrawal, and W. Chen, “A deep adversarial learning methodology for designing microstructural material systems,” *Proceedings of the ASME Design Engineering Technical Conference*, vol. 2B-2018, pp. 1–14, 2018.

-
- [52] C. E. Rasmussen and C. K. Williams, *Gaussian Processes for Machine Learning*. Cambridge, MA, USA: MIT Press, 2006.
- [53] C. E. Rasmussen, *Evaluation of Gaussian Processes and other Methods for Non-Linear Regression*. PhD thesis, University of Toronto, 1997.
- [54] E. A. Del Rio Chanona, J. E. Alves Graciano, E. Bradford, and B. Chachuat, “Modifier-adaptation schemes employing Gaussian processes and trust regions for real-time optimization,” *IFAC-PapersOnLine*, vol. 52, no. 1, pp. 52–57, 2019.
- [55] E. A. del Rio-Chanona, P. Petsagkourakis, E. Bradford, J. E. A. Graciano, and B. Chachuat, “Real-time optimization meets bayesian optimization and derivative-free optimization: A tale of modifier adaptation,” *pre-print*, 2021. arXiv:2009.08819 [math.OC].

Chapter 2

Background

2.1 Modelling porous materials

Modelling flow and transport phenomena in porous media is a widely researched topic and of high interest in a variety of fields.¹⁻³ The irregular surfaces of porous materials, the possible evolution of the microstructure during operation, and the multi-scale correlation between transport and microstructural properties make these materials very complex to be mathematically described.⁴ In electrochemical systems, whether considering batteries or fuel cells, the electrodes consist of porous materials in order to achieve a high active surface area, but also need to contain percolating paths to enable a fast ionic and electronic transport, as well as maintaining sufficient mechanical integrity⁵⁻⁷ Due to the importance of electrodes in energy storage systems (EES), understanding the transport processes that occur within them as well as the effect of their microstructural properties in the battery performance is crucial to improve their durability and aid the design of more optimum systems.⁸⁻¹⁰

Previous experimental work has shown that improvements in the electrode structure at a pore-scale level can lead to an improved power density.¹¹⁻¹⁴ However, in terms of optimisation, experimental trial and error is expensive, time consuming and physically laborious.¹⁵ Therefore, it has become of high interest to implement mathematical modelling and simulation techniques to optimise and investigate electrode microstructure.

To date, no consistent approach has been defined for modelling flow and transport phenomena through porous media, making it a very disputed area among researchers, particularly in terms of correlating model accuracy with simplicity and computational expense. Several mathematical techniques have been proposed for this purpose, the most common ones being: continuum models, pore-scale direct numerical simulations (DNSs), and pore network models (PNMs).¹⁶

2.1.1 Continuum models

A wide amount of research has focused on developing macro-homogeneous models to simulate transport processes within electrodes.¹⁷⁻³⁴ These continuum models are formulated based on the assumption of a representative elementary volume (REV) over which microstructural properties such as surface area, permeability and tortuosity are volume-averaged. In these models, properties are calculated as effective transport properties and therefore are not based on the real electrode morphology.³² This over-simplification of the microstructure is related to the mathematical complexity and high computational power required for modelling flow and transport processes through porous materials. From the estimated effective properties, the velocity and pressure profiles can be estimated with phenomenological relationships, and finally the mass transport equations can be solved through numerical discretisation methods^{15,16,35}.

Flow equations

The flow and velocity profiles of a continuum system are defined by the continuity equation (2.1) and the Navier-Stokes (N-S) equation (2.2):

$$\nabla \cdot \mathbf{u} = 0 \quad (2.1)$$

$$\frac{\partial \mathbf{u}}{\partial t} + (\mathbf{u} \cdot \nabla) \mathbf{u} = -\frac{1}{\rho} \nabla P + \nu \nabla^2 \mathbf{u} \quad (2.2)$$

where \mathbf{u} represents the velocity, ρ is the density, p is the pressure ν is the kinematic viscosity of the fluid, and t is time.

Modeling the velocity and pressure profiles through porous media requires a rearrangement and simplification of the N-S equation. For this purpose, three main modifications have been proposed: the modified N-S equation^{36,37}, the Brinkmann equation^{17–21,38}, and Darcy's law^{22–28,39}. Each of them is derived from the general form of the Navier-Stokes equation (2.2) based on a set of assumptions and boundary conditions applied in selected cases.

Howes and Whitaker³⁷ developed a volume averaging technique called the modified N-S equation to overcome issues associated with the boundary conditions of the general N-S equation implemented in porous media. This equation is defined as

$$\rho \langle (\mathbf{u} \cdot \nabla) \mathbf{u} \rangle = -\nabla \langle P \rangle + \mu \nabla^2 \langle \mathbf{u} \rangle - \frac{\mu \varepsilon}{\mathbf{K}} \langle \mathbf{u} \rangle \quad (2.3)$$

where μ is the dynamic viscosity of the liquid, \mathbf{K} is the permeability tensor of the porous media and ε is the porosity^{36,37}. The quantities in angle brackets are the *volume averaged properties* defined as:

$$\langle \Psi_\phi \rangle = \frac{1}{\mathcal{V}} \int_{V_\phi} \Psi_\phi dV \quad (2.4)$$

where V_ϕ is the volume of the ϕ -phase contained within the averaging volume \mathcal{V} , and Ψ_ϕ is a continuously differentiable function associated with the ϕ -phase.³⁷

If the inertial term in equation (2.3) is ignored, *i.e.* $\rho \langle (\mathbf{u} \cdot \nabla) \mathbf{u} \rangle$, or has little effect, the modified N-S equations reduces to the Brinkmann equation^{17–21,38}, defined as:

$$0 = -\nabla \langle p \rangle + \mu \nabla^2 \langle \mathbf{u} \rangle - \frac{\mu \varepsilon}{\mathbf{K}} \langle \mathbf{u} \rangle \quad (2.5)$$

Furthermore, if the viscous term in equation 2.5 is ignored, *i.e.* $\mu \nabla^2 \langle \mathbf{u} \rangle$, the

macroscopic velocity of the electrolyte through the porous electrode expressed by Darcy's law^{22–28,39} is obtained:

$$\frac{\mu\varepsilon}{\mathbf{K}}\langle\mathbf{u}\rangle = -\nabla\langle p\rangle \quad (2.6)$$

The permeability of the porous electrode is calculated by the Kozeny-Carman equation²⁷

$$\mathbf{K} = \frac{d_f^2}{16 k_{\text{CK}}} \frac{\varepsilon^2}{(1 - \varepsilon^2)} \quad (2.7)$$

where d_f is the fibre diameter, ε is the porosity of the electrode, and k_{CK} is the Kozeny-Carman constant for a fibrous media. The k_{CK} constant is a fitting parameter that depends on the shape of the material that is not accounted for in the porosity or diameter²⁴.

Despite the fact that Darcy's law has been widely used to describe the flow through porous media due to its simplicity, it has been proved to present some limitations^{36,40} In terms of the interaction between the wall and flow regime, Darcy's law is only consistent with perfect slip at solid boundaries⁴⁰, and thus the no-slip boundary condition is non existent for Darcy's law. Furthermore, based on the definition of Darcy's number (Da) by Parvazinia *et al.*⁴⁰ as the ratio of the permeability to the equivalent diffusion length square, Darcy's law is only applicable for a value of the Darcy number $\text{Da} < 10^{-6}$, characteristic of flow through a porous media with very low permeability. If the value of Da is $1 > \text{Da} > 10^{-6}$, the inertial term in equation 2.5 cannot be overlooked and therefore Brinkmann equation must be implemented³⁶.

Transport equations

The continuum mass transport of species in a system involving the effects of convection, diffusion, dispersion, and reaction was first defined by Lichtner as:⁴¹

$$\frac{\partial}{\partial t} (\phi_{\pi_i} c_i) + \nabla \cdot \mathbf{N}_i = \sum_{r=1}^M \nu'_{ir} \frac{\partial \Xi_r}{\partial t} \quad (2.8)$$

where ϕ_π represents the volume fraction occupied by phase π ; c_i is the concentration of the i th species of phase π_i ; Ξ_r is the reaction progress density; the time derivative $\frac{\partial \Xi_r}{\partial t}$ represents the rate of the r th reaction at time t ; ν'_{ir} represents the effective stoichiometric matrix for irreversible reactions; i has the values from 1 to n , where n is the total number of species in the bulk.⁴¹ The total flux of the mass transport \mathbf{N}_i is expressed as

$$\mathbf{N}_i = \mathbf{N}_i^D + \mathbf{N}_i^v \quad (2.9)$$

where \mathbf{N}_i^D , and \mathbf{N}_i^v represent the resulting flux from diffusive and convective transport respectively, defined by

$$\mathbf{N}_i^D = -D_i \nabla c_j \quad (2.10)$$

$$\mathbf{N}_i^v = \mathbf{u}c_i \quad (2.11)$$

where D_i corresponds to the diffusion coefficient of the bulk. For modelling transport through porous media, D_i is replaced with the effective diffusivity D_i^{eff} as a function of the tortuosity and the porosity of the media (ε). The effective diffusivity is commonly related to the bulk diffusion coefficient by the Bruggeman relation⁴², defined as

$$D_i^{\text{eff}} = \varepsilon^{3/2} D_i \quad (2.12)$$

Additionally, the ratio between the convection and diffusion in porous media can be estimated by the Peclet number, defined as $\text{Pe} = v d_p / D_i^{\text{eff}}$ where d_p corresponds to the mean pore diameter.^{15,43}

In electrochemical systems, the total flux of ionic species through a porous media is given by the Nernst-Planck equation, which accounts for the transport of ionic species due to convection and diffusion as equation 2.9 but adds an additional term to account for the electrophoretic transport:

$$\mathbf{N}_i = -D_i^{\text{eff}} \nabla c_i - \frac{z_i c_i D_i^{\text{eff}} F}{RT} \nabla \phi_e + \mathbf{u} c_i \quad (2.13)$$

where ϕ_e corresponds to the electric potential in the electrolyte, F is the Faraday constant, and z_i is the charge number of species i . The right hand side of equation (2.8) corresponding to the source term due to the reaction is renamed as $R(c_i)$ and will be determined by the electrochemical reaction. For simplicity, in most electrochemical systems $R(c_i)$ is defined by the Butler-Volmer equation to determine the current density as

$$J_{\text{ct}} = j_0 \left[\exp \left(\frac{\alpha_a z F \eta}{RT} \right) - \exp \left(\frac{-\alpha_c z F \eta}{RT} \right) \right] \quad (2.14)$$

where j_0 is the exchange current density, α_a and α_c are the anodic and cathodic transfer coefficients respectively, z is the number of electrons transferred in the reaction, R is the universal gas constant, T is the absolute temperature of the system, F is the Faraday constant, η is the overpotential, defined as:

$$\eta = \phi_s - \phi_e - E^0 \quad (2.15)$$

where E^0 is the equilibrium potential, ϕ_e is the electric potential in the electrolyte, and ϕ_s is the electric potential in the solid electrode.

Continuum models based on parametric relationships could lead to an acceptable prediction of the flow and transport profiles, particularly considering the low processing time they require.³⁶ Nevertheless, these macro-homogeneous models fail to offer an understanding of the pore-scale dependence of the microstructure with continuum transport parameters. Moreover, given that the properties of the porous medium are defined as effective properties based on average values of a control volume, they do not account for the exact microstructure.⁴ Given the case in which the microstructure is homogenisable and the control volume is a Representative Elementary Volume (REV), it could be argued the model accounts for the exact microstructure. However, if the microstructure is not homogenisable, there could be some local interactions that are not captured by the chosen metrics and thus the microstructure is not fully accounted for with the averaged values.

In electrochemistry, if a more detailed model is required to understand the effect of the electrode microstructure in the battery performance, other more computationally expensive techniques are needed. These models will be briefly described in the next section.

2.1.2 Direct Numerical Simulations as pore-scale models

The increasing availability of high computing power, coupled with improvements in micro-scale characterisation techniques (*i.e.* X-ray Computed Tomography (X-CT)) has led to the implementation of complex computational models for studying flow and transport processes in porous media.³⁵ These models allow improved assessments of macroscopic transport properties by varying the pore space structure parameters.⁴ One proposed pathway for implemented a pore-scale modelling approach is by simulating directly over the pore geometry obtained from X-CT images.³⁵ This pathway is referred to as direct numerical simulation (DNS) as it performs simulations directly over the complex pore geometry obtained from X-CT images.

The porous microstructure is represented as a numerical mesh, or as a Cartesian grid, depending on the type of DNS applied.³⁵ These can be classified as a) grid-based simulations and b) particle-based methods. Grid-based methods employ the Finite Volume method (FVM), the Finite Difference method (FDM) or the Finite Element method (FEM) to solve the governing partial differential equations^{22,44}, while particle-based methods define the movement of particles through a porous space, such as the Lattice-Boltzmann method (LBM)⁴⁵ and smoothed particle hydrodynamics⁴⁶ The advantage of these models is that they can distinguish between the phases (*i.e.* solid active material and porous matrix), allowing the estimation of the effect of the porous morphology on the transport processes within the system.^{32,33} Nevertheless, these models are computationally expensive and therefore often restricted to a non-representative sub-volume of the entire electrode.¹⁵

Application of DNS to electrochemical systems

The implementation of DNS to model electrodes in electrochemical energy storage systems depends on the type of system to be modelled. In the case Li-ion batteries, the cathode is composed of three domains: the active material (in most cases composed of NMC ($\text{LiNi}_{1/3}\text{Mn}_{1/3}\text{Co}_{1/3}\text{O}_2$)), a carbon binder domain (CBD) and a porous matrix. Each domain is governed by different transport processes which allow the implementation of a modification of the transport equation 2.8. The movement of electrolyte in the porous phase is governed by diffusion and migration, as given by the following expression:⁴⁷

For Li^+ the balance equation is given by:

$$F \frac{\partial c_{\text{Li}^+}}{\partial t} + \nabla \cdot \mathbf{N}_p = 0 \quad (2.16)$$

where \mathbf{N}_p is the flux of Li ions given by:

$$\mathbf{N}_p = -t_p \sigma_{\text{Li}^+} \nabla \mu_p \quad (2.17)$$

For the negatively charged species (X^-), the balance equation is given by:

$$-F \frac{\partial c}{\partial t} + \nabla \cdot \mathbf{N}_n = 0 \quad (2.18)$$

where \mathbf{N}_n is the flux of negative ions given by:

$$\mathbf{N}_n = \frac{1}{t_p} F \tilde{D} \nabla c - (1 - t_p) \sigma_i \nabla \mu_p \quad (2.19)$$

In equations 2.17 to 2.19, c is the concentration of electrolyte salt, F is the Faraday constant, \tilde{D} refers to the ambipolar diffusion coefficient of the binary electrolyte, μ_p corresponds to the reduced electrochemical potential of positive ions in the electrolyte, σ_{Li^+} is the ionic conductivity of species in the electrolyte, and t_p represents the transference number of the positive ion (Li^+).⁴⁷

The transport processes inside the active material are defined by the solid-

state diffusion, corresponding to the movement of Lithium as described in equations 2.20 and 2.21, and the conduction of electrodes defined by equation 2.22 and 2.23.

The balance equation for transport of Li is defined as:

$$F \frac{\partial c_s}{\partial t} + \nabla \cdot \mathbf{N}_s = 0 \quad (2.20)$$

where N_s refers to the flux of lithium due to solid state diffusion, given by

$$\mathbf{N}_n = -FD_s \nabla c_s \quad (2.21)$$

The balance equation for transport of electrons is defined as:

$$\nabla \cdot \mathbf{N}_e = 0 \quad (2.22)$$

where \mathbf{N}_e is the flux of electrons due to conduction, given by

$$\mathbf{N}_e = -\sigma_e \nabla \mu_e \quad (2.23)$$

In equations 2.20 to 2.23, c_s refers to the concentration of lithium in the solid phase, D_s is the solid state diffusion coefficient in the active material, μ_e corresponds to the reduced electrochemical potential of electrons and σ_e refers to the electronic conductivity in the solid material in the conducting phase. Given that the CBD works as an electron conductor only, the transport equations due to conduction are the same as equations 2.22 and 2.23.

Based on the general mass balance equation given by eq. 2.8, the source term in the right hand side of the equation corresponds to the electrochemical reaction. This equation holds true for continuum models where the reaction is assumed to occur throughout the whole continuum space. In the case of DNS, since the model takes into account the different phases, the term for the electrochemical reaction is not considered as a source term, but rather as a boundary condition of charge transfer at the interface between the electrolyte in the porous matrix and the solid

active material. This expression for charge transfer is based on the Butler-Volmer equation, and is defined as

$$J_{\text{ct}} = j_0 \left\{ \exp \left(\frac{\alpha F}{RT} (\mu_{\text{p}} - \mu_{\text{e}} + E_{\text{eq}}) \right) - \exp \left(\frac{-(1 - \alpha) F}{RT} (\mu_{\text{p}} - \mu_{\text{e}} + E_{\text{eq}}) \right) \right\} \quad (2.24)$$

where j_0 is the exchange current density given by

$$j_0 = k_{\text{r}} c_{\text{s}}^{\alpha} c_{\text{s}}^{\alpha} (c_{\text{s}}^{\text{max}} - c_{\text{s}})^{(1-\alpha)} \quad (2.25)$$

where k_{r} is the reaction rate constant, α is the transfer coefficient for intercalation half-reaction, E_{eq} refers to the equilibrium potential at the active material/electrolyte interface, and $c_{\text{s}}^{\text{max}}$ is the maximum lithium concentration in the active material.⁴⁷

Lu *et al.*⁴⁷ perform an analysis of the interplay between battery microstructure and performance by estimating the state of lithiation within the cathode at different C-rates using a reconstructed cathode microstructure and an ideal metallic lithium ion. From this analysis, it is concluded that the heterogeneity of the particle size distribution leads to an inhomogeneous lithiation throughout the cathode, particularly as the rate of discharge increases. This inhomogeneous lithiation is mainly a result of the variation in lithium ion diffusion paths associated with the broad distribution of particle sizes. This uneven utilisation of NMC particles due to variation in local consumption of lithium ions at a microscale, leads to an uneven utilisation of the NMC particles, which overall results in a lower energy density and eventually a faster degradation.⁴⁷ Based on this analysis, it is suggested that a graded particle size distribution could potentially lead to a more even utilisation of the NMC particles and therefore an improved battery performance. This work by Lu *et al.*⁴⁷ proves the advantages of implementing a pore-scale model for simulating the coupled mass and charge transport processes in a lithium-ion cathode.

In the case of Redox Flow Batteries (RFBs), the electrode is constituted by an intertwined fibrous carbon material (in most cases carbon paper, carbon felt or

carbon cloth) where the reaction takes place at the surface of the fibre. These carbon materials are also used as gas diffusion layer (GDL) in Polymer Electrolyte Membrane (PEM) fuel cells (as shown in figure 2.1⁴⁸) and therefore in terms of non-reactive transport, modelling both systems is similar.⁴⁹⁻⁵²

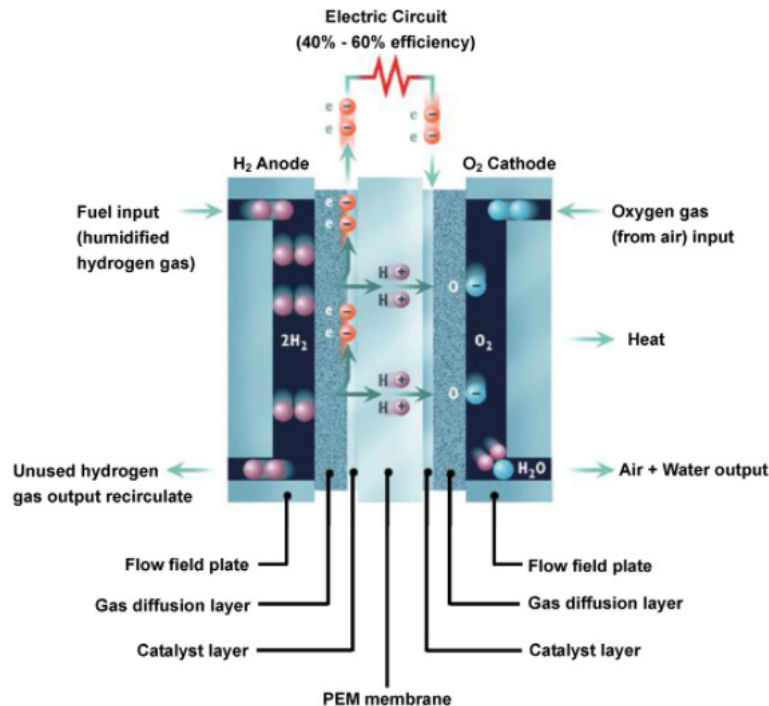


Figure 2.1: Schematic diagram of a PEM fuel cell showing the electrolyte, the H₂ anode, the O₂ cathode, the catalyst layers, the GDL and the PEM membrane, and the arrows representing the direction of electron and ion flow.⁴⁸

In both fuel cells and RFBs, the electrolyte or active species are pumped into the system, generating a pressure gradient, which leads to the existence of a velocity profile. This adds another level of complexity to the system since the velocity profile needs to be solved at a pore scale and coupled with the transport equations in order to account for the convective transport. To obtain the velocity profile, most cases implement particle based method such as LBM and SPH to solve the Navier-Stokes equation through porous media. Park *et al.*⁵³ proposed the first pore-scale model based on the LBM to analyse the flow distribution in the gas diffusion layer (GDL) of a PEM fuel cell. The Lattice Boltzmann (LB) method is applied in three dimensions to simulate the flow through the void space and investigate the effect of the tow orientation in the effective permeability of the GDL⁵³. These results encouraged other researchers^{32,33} to adopt the LBM to solve the equations of flow through porous media.

In their work, Qiu *et al.* present an analysis of the effect of the electrode morphology and electrolyte flow conditions on the cell performance of a Vanadium RFB (VRFB)^{32,33}. The LB method is employed over a reconstructed X-CT image to solve the flow field of the electrolyte inside the porous electrode. Since the velocity and pressure profiles are obtained in lattice units, the authors propose a data treatment to transform them into physical units. This method is based on matching the Reynolds (Re) (equation (2.26)) and the Euler (2.27) numbers in both lattice and physical units:

$$\left(\frac{U_{\text{avg}} L_{\text{avg}}}{\nu} \right)_{\text{LBM units}} = \left(\frac{U_{\text{avg}} L_{\text{avg}}}{\nu} \right)_{\text{Phys units}} \quad (2.26)$$

$$\left(\frac{\Delta P}{\rho U_{\text{avg}}^2} \right)_{\text{LBM units}} = \left(\frac{\Delta P}{\rho U_{\text{avg}}^2} \right)_{\text{Phys units}} \quad (2.27)$$

where L_{avg} is the characteristic length scale defined as the average pore size based on the XCT data, and U_{avg} is the characteristic velocity defined as the average velocity at the cell inlet^{32,33}. The flow field through the porous electrodes is solved by imposing boundary conditions at the physical scale. An initial velocity is specified at the cell inlet and is taken as the characteristic velocity (U_{avg}) to transform the LB units into physical units. Similarly, a prescribed pressure difference between the inlet and outlet of the flow cell is specified such that the desired flow rate is obtained. This pressure difference is then applied in the transformation of LB units into physical units, as given by equation 2.27.^{32,33}

Some authors have also shown the implementation of the LBM coupled with a finite-volume method (FVM) to solve the transport equations. Hu *et al.*⁵⁴ and Patil⁵⁵ apply a finite-volume method coupled with the LBM for solving the Darcy-Brinkman and Navier-Stokes equations.^{54,55} Qiu *et al.*, after obtaining the flow field in a porous electrode of a half-cell VRFB, implement a fully implicit 3D FVM to solve the charge and species transport equations in the domain. The transport of vanadium species in the positive reaction ($V_{\text{IV}}/V_{\text{V}}$) in the electrolyte is given by a convective, diffusive and electrophoretic term, defined as:

$$\frac{\partial c_i}{\partial t} + \mathbf{u} \cdot \nabla c_i = D_i \nabla^2 c_i + \nabla \cdot \left[\frac{z_i c_i D_i}{RT} \nabla \phi_e \right] \quad (2.28)$$

where c_i is the concentration of vanadium species i (*i.e.* V_{IV}/V_V), D_i is the diffusivity of species i in the electrolyte, ϕ_e the electric potential in the electrolyte, z_i is the charge number of species i , and \mathbf{u} is the velocity of the electrolyte. The balance equation for charge transport in the electrolyte is defined as:

$$\nabla \cdot \left[\left(\frac{F^2}{RT} \sum z_i^2 D_i c_i \right) \nabla \phi_e + F \sum z_i D_i \nabla c_i \right] = 0 \quad (2.29)$$

The balance equation for conservation of charge at the solid electrode constituted of carbon fibres is defined as:

$$\nabla \cdot (\kappa_s \nabla \phi_s) = 0 \quad (2.30)$$

where κ_s is the conductivity of the solid phase and ϕ_s is the electric potential in the solid phase.

Since this model is a pore-scale model, the electrochemical reaction is not accounted for in the balance equation given by eq. 2.28. The electrochemical reaction occurs at the interface between the electrolyte and the carbon fibres, and therefore is considered as a flux boundary condition at this interface. The reaction is described by Butler-Volmer equation applied to the V_{IV}/V_V system as:

$$N_{IV} \cdot \hat{n} = -N_V \cdot \hat{n} = k (c_{IV}^s)^{\alpha_c} (c_V^s)^{\alpha_a} \left[\exp \left(\frac{\alpha_a F \eta}{RT} \right) - \exp \left(\frac{-\alpha_c F \eta}{RT} \right) \right] \quad (2.31)$$

where N_{IV} and N_V are the flux of V_{IV} and V_V respectively, c^s is the concentration of species at the surface, α_a and α_c are the anodic and cathodic transfer coefficients respectively, k is the standard reaction rate constant, and η is the overpotential, defined as:

$$\eta = \phi_s - \phi_e - \left[E^0 + \frac{RT}{F} \ln \left(\frac{c_V}{c_{IV}} \right) \right] \quad (2.32)$$

where E^0 is the equilibrium potential.^{32,33} By solving the coupled charge and species transport equation in the domain, it is possible to obtain the cell voltage, current density and overpotential fields at a pore-scale.^{32,33}

An uneven distribution of species is seen, where a steep concentration gradient is predominant close to the current collector. This higher rate of electrochemical reaction is explained by an increased in overpotentials at the surface of the carbon fibres near the current collectors. Although this gradient is also seen in continuum models,^{22,34} a more detailed analysis of the species transport is seen at the pore scale results. The local effects of the carbon fibres is seen in the overpotential distribution along the electrode: the overpotential is higher on the fibres closer to the current collectors, and tends to decrease along the length of the fibres. A local distribution of overpotential also shows that at the regions where the highest concentration gradients are observed, the overpotentials are smaller. This indicates that higher overpotentials are obtained at the regions where reactants are available immediately near the surface of the electrode fibres.³² Additionally, the pore-scale simulation shows an uneven concentration of species within the electrodes, which leads to regions of higher consumption of species and therefore higher current density than others. This is a result of the random distribution of the carbon fibres, which results in an uneven utilisation of the electrode.³² The variation in local distribution of species concentration and overpotentials lead to a lower capacity than the theoretical estimation. Additionally, this leads to a faster capacity fade during discharge due to the fast consumption of species in some regions which are not replenished at the same rate.¹⁵ This analysis provides a detailed understanding of the effect of the microstructure in the transport processes within the electrode of a VRFB and proves the usefulness of implementing a pore-scale model for establishing a microstructure-performance correlation.^{32,33}

From the analysis presented in the previous sections, it is shown that both continuum and pore-scale models are insightful and have thus far contributed to understanding the effect of porous electrodes properties in the performance of electrochemical systems. Continuum models allow the simulation of the integrated system where the interplay between the anode, cathode and the

membrane can be simulated. Moreover, the effect of additional parameters such as flow channel configuration, pumping power, and species crossover at the membrane among others can be considered.^{22,34} In these models, the electrode is considered a continuum where the microstructural properties are homogenised and therefore simulating the coupled charge and transport equations is computationally inexpensive. Contrarily, pore-scale models present a detailed analysis of the effect of the microstructure in various transport processes within the electrode. The simulation of local concentration, current density and overpotential distributions allows the estimation of an uneven utilisation of the electrode due to the configuration of the electrode morphology (*i.e.* particle size distribution or fibre alignment). This unevenness in distributions can be allegedly one of the causes for overall degradation or capacity fade, which proves the advantage of implementing a pore-scale simulation over the microstructure. Nonetheless, these models are limited to a non-representative sub-volume of the whole electrode, and are computationally expensive (require the use of supercomputers for speeding up convergence).^{32,33}

Based on this comparison, it is clear that a trade-off between accuracy and computational expense must be considered when selecting the type of model to describe a particular system. Based on this assertion, it has become of interest to present a model with the ability to bridge the gap between a continuum scale description of electrodes and the detailed, but computationally restricted view offered by most pore-scale models.¹⁵ In this respect, Pore Network Models have been presented as a potential alternative that can capture the electrode morphology and solve the flow and transport equations in a computationally inexpensive way.

2.1.3 Pore Network Models

Pore Network Models (PNMs) are defined as an assembly of nodes (pores) connected by bonds (throats), represented by simple geometries, *i.e.* usually pores are spherical and throats are cylindrical. This geometric approximation of the porous structure greatly reduces the computational complexity of the flow and transport equations. The general algorithm for solving the flow and transport in a network is defined by various authors^{4,56-58} and comprises the following steps: a) estab-

lishing pressure boundary conditions at the network to solve the flow equation for obtaining the pressure and velocity fields at the throats and pores, b) applying the computed velocity field obtained into solving the transport equations to obtain the concentration field within the pore space.

Flow equations for PNM

In a PNM, the flow through each throat connecting two pores is analogous to the analytical solution of the steady-state N-S equation (2.2) for the flow through a cylindrical pipe. The formulation of the flow equation follows the assumption of a single-phase, Newtonian, incompressible fluid in the bulk, with creeping flow ($Re \ll 1$). The pressure and velocity fields are obtained by assuming a single pressure value per node, and enforcing the momentum balance over each pore^{56,59}, as given by equation (2.33)

$$\sum_{j=1}^{N_{th}} q_{ij} = \sum_{j=1}^{N_{th}} g_{h,ij} (P_i - P_j) = 0 \quad (2.33)$$

where P_i is the pressure at pore i , q_{ij} is the flow between pores i and j , $g_{h,ij}$ is the hydraulic conductivity of the throat connecting pore i to j , and N_{th} is the number of throats connected to pore i .¹⁵

The hydraulic conductivity ($g_{h,ij}$) is defined as a factor that represents the resistance in the flow of electrolyte between neighbouring pores imposed by the connecting throat. It is dependent on the size and length of the throat and varies depending on the shape of the throat's cross-sectional area.^{49,60,61} To explain with further detail the meaning of $g_{h,ij}$, the momentum balance between two pores is illustrated as analogous to the analytical solution of the steady state Navier-Stokes equation for the flow in a pipe with circular cross-section⁶⁰. The total flow through the cylinder is computed by integrating the velocity field and the cross-sectional area over the cylinder radius. This leads to the Hagen-Poiseuille equation (2.34):

$$Q = \int_0^R 2\pi r v(r) dr = \frac{\pi R^4}{8\mu} \nabla P \quad (2.34)$$

Based on the solution to equation (2.34), the *hydraulic conductivity* (g_h) be-

tween pores i and j in a cylindrical throat is defined as:

$$g_{h,ij} = \frac{\pi R^4}{8\mu} \cdot \frac{1}{L} \quad (2.35)$$

According to Gostick *et al.*⁴⁹, the total hydraulic conductivity between two adjacent pores, i and j , connected by a throat, is expressed as the conductivity of half of pore i and j , and the conductivity of the throat. Thus, the net conductivity between i and j , $g_{h,ij}$ is expressed based on the resistor theory as

$$\frac{1}{g_{h,ij}} = \frac{1}{g_{p,i}} + \frac{1}{g_{h,t}} + \frac{1}{g_{p,j}} \quad (2.36)$$

This same approach proposed by Gostick *et al.*⁴⁹ has been used by other authors to compute the PNM of the gas diffusion layer in a PEM fuel cell^{50,61}

The resulting system of linear equations obtained with expression (2.33) is solved to obtain the pressure field. Given the prescribed boundary pressures on each side of the network (*i.e.* P_{in} and P_{out}) the pressure in each pore is calculated. At a continuum scale, the macroscopic flow rate Q_T can be obtained by summing the flux over the boundary pores of the network along the main flow direction. Q_T follows Darcy's law, thus the permeability can be determined through back-calculation with equation (2.37), where K is the bulk permeability; A is the cross-sectional area of the network in the direction orthogonal to the main flow; L is the length of the network in the main direction of the flow; and P_{in} and P_{out} represent the inlet and outlet pressures at the boundaries respectively.^{4,49,56-59,62}

$$Q_T = -\frac{KA(P_{in} - P_{out})}{\mu L} \quad (2.37)$$

Based on this equation, it is clear that the value of the permeability in the network will be dependent on the geometry of the pores and throats given by the hydraulic conductivity, the cross-sectional area and length of the network at a macroscopic level. Thus, an iterative approach is necessary where these geometric parameters are obtained initially from statistical distribution of experimental data, and are fitted so that the calculated flow field presents a permeability similar to the one obtained experimentally.^{49,62}

Mixed Cell Method for transport in PNM

Analogous to the expression obtained in section 2.1.3 for the momentum balance over each pore (equation 2.33), the transport equation is derived from the convection-diffusion-reaction (CDR) equation by imposing the species mass balance per node (Mehmani2014). The CDR transport equation defined in eq. (2.8) is applied in the form of volumetric integral to solve the mass balance at each pore:

$$\int \int \int \frac{\partial C_i}{\partial t} dV = - \int \int C_i v \cdot n dS + \int \int D_m \nabla C_i \cdot dS + \int \int \int R_i dV \quad (2.38)$$

Based on equation (2.38), the *Mixed Cell Method (MCM)* proposed by various authors^{56,59,62–64} is obtained. The MCM assumes a single concentration in each pore, which implies a perfect mixing of species within each node. Thus, the balance of species at node i is given by

$$V_{p_i} \frac{dc_i}{dt} = \sum_{j=1}^{N_{th,q<0}} c_i q_{ij} + \sum_{j=1}^{N_{th,q>0}} c_j q_{ij} + \sum_{j=1}^{N_{th}} D_m a_{ij} \frac{\Delta c_{ij}}{l_{ij}} + R(c_i) \quad (2.39)$$

where V_p is the pore volume, c_i the pore concentration, D_m the molecular diffusivity, $R(c_i)$ the reaction term, q_{ij} , l_{ij} and a_{ij} correspond to the flow rate, length and cross-sectional area of the throat connecting pores i and j respectively.⁵⁶

The throat flow rates are obtained by solving the momentum balance equation (2.33). For the calculation of the throat cross-sectional areas in the diffusive term of equation (2.39) some authors assume cylindrical, equilateral triangle or square tubes with equivalent throat conductivities^{4,56}. Gostick *et al.*⁴⁹ introduce a new methodology analogous to the hydraulic conductivity from equation (2.33), referred to as *diffusive conductivity* which is defined for a given conduit as

$$g_d = \frac{c_i D_{AB} (2b)^2}{L} \quad (2.40)$$

where D_{AB} is the diffusion coefficient of species A in static media B , $2b$ and L are the width and the length of the conduit respectively. The net diffusive conductivity g_d is obtained through the application of the resistor theory for diffusion through each half pore and throat, similar to equation (2.36).⁴⁹ In order to verify the chosen network geometry applied in the calculation of the diffusive conductivity g_d (equation (2.40)), the effective diffusivity of the network is calculated and compared with experimental data of effective diffusivity for various fibrous materials.⁴⁹

Despite the fact that the MCM formulation from equation (2.39) for the solution of the mass transport in each pore assumes perfect mixing, it has been proved by Acharya *et al.*⁶³ that this assumption is reliable for flow at low Peclet numbers, which is the case of the systems studied in this work. Other methodologies for PNM of solute transport have been proposed by Mehmani *et al.*⁵⁶ called streamline-splitting method (SSM) and superposing transport method (STM), nevertheless in this work only the MCM method will be analysed.⁵⁶

Reactive transport in PNM

The solution of the MCM equation (2.39) which also accounts for the reactive transport has been analysed by various authors, who propose different methodologies for estimating the concentration change due to the reaction.

Li *et al.*⁶² present a PNM to simulate the reaction of kanolite and anorthite during carbon sequestration. The MCM equation is solved to represent the processes of diffusion, convection and aqueous reaction at each individual pore. The change of concentration due to reaction, represented as the last term of equation (2.39), takes a different form for each component based on the stoichiometry of the reaction. For instance, the source term $R(c_i)$ for Ca^{2+} is given by

$$R(Ca^{2+}) = r_{C,A} \cdot A_{A,T} \quad (2.41)$$

where $r_{C,A}$ corresponds to the reaction rate of anorthite, and $A_{A,T}$ refers to the total surface area of anorthite.⁶² This same model of representing the reactive

term in the MCM equation was applied by Kim *et al.*⁶⁴ to simulate the reaction of kanolite and anorthite in a PNM during carbon sequestration. The results from these works show that large anorthite reaction rates arising from highly acidic boundary fluid leads to higher order of magnitude spatial variations in concentrations and reaction rates, which are poorly represented by averaged concentrations that ignore pore-scale heterogeneities. Additionally, under these conditions, the equilibrium relationships obtained at a pore-scale are unable to hold at the continuum scale, therefore an estimation of these values with a continuum model would introduce large errors and scaling effects are significant.⁶²

Following the same method, Raouf *et al.*^{65,66} present a simulation of a Biogeochemical Reaction represented by a PNM. A sequential approach is applied for the concentrations distribution in each pore, in which first the convection-diffusion transport is solved for each time step, and then the reactive step is integrated in the MCM equation at each time step. The reactive term which represents the sum of all the reactions affecting concentration of a given species involved in the process is given by

$$R^l = \sum_{m=1}^{N_{re}} a^{l,m} \cdot r^l \quad (2.42)$$

where N_{re} is the number of reactions, r^l represents the rate of reactions obtained with reaction rate laws, and $a^{l,m}$ represents the stoichiometric coefficient of species l in reaction m .⁶⁵

Acharya *et al.*⁵⁷ present a time-stepping methodology for the solution of the MCM equation, accounting only for the convective and reactive terms. The concentration at each pore in the PNM is solved explicitly through the discretised form of equation (2.39) (without the diffusive term) as

$$c(i, t + \Delta t) - c(i, t) + k[c(i, t + \Delta t)]^P - k[c(i, t)]^P = \frac{\Delta t}{V_{p_i}} \left[\sum_{j=1}^{N_{th,q<0}} c(i, t) q_{ij} + \sum_{j=1}^{N_{th,q>0}} c(j, t) q_{ij} \right] \quad (2.43)$$

In this equation, the last two terms of the left hand side correspond to the effect of concentration change due to the reaction, while the right hand side of the equation represents the term due of convective mass transport.

The reactive term can be solved by directly including the reactions in the equation, such as the methodology followed by Li *et al.*⁶², Kim *et al.*⁶⁴ and Raoof *et al.*⁶⁵ Mehmani *et al.*⁵⁸ follow the time-step methodology of equation 2.43, for a PNM model applied in carbon sequestration. Nevertheless, Mehmani *et al.*⁵⁸ apply an *operator-splitting* approach which decouples the convective and reactive part of the transport equations. In the *operator-splitting* approach, the convective term is solved explicitly using finite differences, while the reactive term is solved analytically.⁵⁸

The *operator-splitting* method is also implemented by Tansey *et al.*⁵⁹ for the solution of convective, diffusive and reactive transport in a PNM applied for estimating the heterogeneous reactive transport and matrix dissolution at a pore scale for carbon sequestration. The authors perform a time-stepping algorithm similar to the one presented by Mehmani *et al.*⁵⁸ but also include the diffusive term. The reactive term $R(c_i)$ is solved explicitly at each pore, in which an intrapore concentration gradient is considered through the estimation of a mass transfer coefficient. This *operator-splitting* method implies a numerical error, which is not accounted for by the authors, nevertheless simplifies the procedure of solving the MCM equation explicitly with the reactive term included in the equation.^{58,59} The results from this work allow the estimation of the transient dissolution regimes of matrix acidising, the effect of the flow rate on the mass transfer, and the effect of the pore size in the rate at which acid can be delivered to the reactive surface.⁵⁹ Overall, these works implement PNMs to estimate the coupled convective, diffusive and reactive transport at a pore-scale. It is shown that although PNMs are simplifications of the actual microstructure, these models are able to accurately predict reaction rates, an optimal Damköhler number (rate of precipitation to rate of convection), and the existence of preferential flow pathways through the porous matrix due to a higher permeability along these paths, which cannot be predicted with continuum models.^{58,59,62}

In the present work, a PNM is developed to simulate the coupled mass and charge transport in electrodes for EES systems. The *operator-splitting* approach is implemented to decouple the convective and reactive parts of the transport equation, as will be further explained in chapter 3. Since the reactive term corresponds to the electrochemical reaction, it is coupled with the charge transport equation. Thus, it requires to be solved iteratively in order to calculate the concentration of species at each pore for every time-step in the dynamic simulation.¹⁵

This section has reviewed the different approaches commonly implemented in the literature to model transport process through porous media, namely continuum models, direct numerical simulations and pore network models. These approaches analyse the microstructure-performance relationship from a forward perspective and quantify the effect of the porous media in the overall system. Although insightful, these models do not account for the reversible process that can enable the optimisation of the microstructure. For this purpose, the stochastic reconstruction of porous media has been suggested and implemented by various authors in order to estimate the pdf that defines the microstructure. These methods of stochastic reconstruction of porous media will be reviewed in the following section.

2.2 Stochastic reconstruction of porous materials

As stated in the previous section, advances in high-resolution X-ray computed tomography (XCT) scanning techniques as well as an increase in computational power have allowed researchers to develop complex multiphysics models that can describe the transport processes in porous media. These numerical solutions of flow and transport equations based on three-dimensional XCT images enable the estimation of relevant microstructural properties such as permeability, diffusivity, specific surface area and porosity.⁶⁷⁻⁷⁰ However, since variations in pore shape and morphology are intrinsic features of the porous media, it is essential to develop pore structure models that can predict these microstructural properties based on geometric and topological descriptors of the complex microstructure.⁷¹ In this respect, a key challenge remains to find probabilistic representations of a microstructural dataset which contain the geometric and topological “essence” of the microstructure, such that synthetic volumes can be reconstructed with equivalent properties and a physical resemblance to the real material.

For this purpose, the stochastic generation of porous media based on statistical properties of porous microstructures or from XCT images has been proposed⁷²⁻⁷⁴. A first approach for generating three-dimensional porous media was introduced by Quiblier *et al.*⁷⁵ based on the work of Joshi⁷⁶ for the synthetic generation of two-dimensional images. The stochastic model implements a technique based on thresholding of random Gaussian fields: within a predefined volume, a binary number (*i.e.* 0 or 1) is randomly generated to indicate whether the point belongs to the solid matrix or to the void. The “disorder” of the random generation is limited by the porosity and the two-point correlation function of the porous media, defined as the the probability for a random point $P + H$ to belong to phase ϕ_i (*i.e.* solid matrix of pore phase) when point P belongs to phase ϕ_i .⁷⁵ Despite the wide application of this method^{77,78}, it is proved that for the generation of grains or packed particles, this method fails to accurately reproduce certain transport properties such as the Knudsen diffusivity. This indicates that, unlike the case of reconstructing simple sandstones, matching the porosity and two-point correlation function alone is not always adequate when attempting to accurately represent the structure of some porous materials. In these cases, higher order

statistical properties of the material, such as the chord length distribution of the solid and pore phase must be also satisfied.⁷⁹

Object-based models have been introduced to generate arrangements of granular materials using characteristic geometric shapes, such as spheres. In the classical Boolean model, the centers of the grains are distributed and grown in a confined space through a random process that allows grains to overlap.^{80,81} More complex Boolean models have been developed to define the interaction between grains and extend their application to non-spherical particles^{82–84}, such as the one presented by Rikvold and Stell⁸⁵, in which the level of penetration between spheres is defined by a hardness parameter where a value of one means the spheres are mutually impenetrable, and a value of zero reduces them to fully penetrable. Additional methods based on simulated annealing have been implemented to reconstruct two and three-dimensional heterogeneous materials from two-point correlation functions (TPCF) or higher-order statistical information, as shown in Figure 2.2 for the reconstruction of a Fontainebleau sandstone.^{83,86–89}

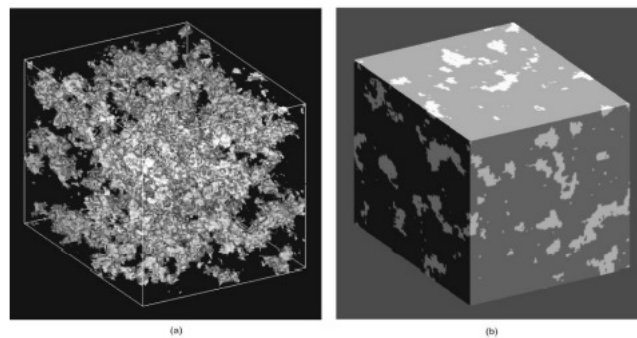


Figure 2.2: Reconstruction of the Fontainebleau sandstone using the two-point correlation function (S_2) obtained from one slice. The system size is $128 \times 128 \times 128$ pixels, and one pixel is equal to 7.5. The figure on the left shows the pore space as white and opaque, and the grain phase as black and transparent. The figure on the right shows a 3D perspective of the reconstruction.⁸⁷

The simulated annealing algorithm implemented as a pixel-based model involves the gradual transformation of a high-energy configuration of pore and void pixels distributed in space into a state of minimum energy. This "energy" is usually defined as the sum of the squared deviations between n-point correlation functions of the real data and the calculated correlation function of the generated porous media.⁷¹ Jiao *et al.*^{90,91} implemented simulated annealing by extending the

work of Yeong *et al.*^{83,87} to present an isotropy-preserving algorithm to generate realisations of materials from their two-point correlation functions (TPCF), as is illustrated in Figure 2.4.

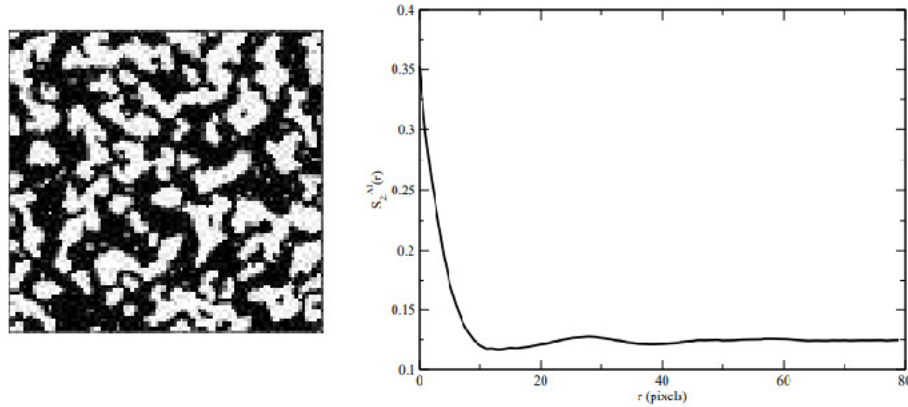


Figure 2.3: The figure on the left shows a reconstruction of a boron carbide/aluminum composite, where the black phase represents boron carbide with $\phi_1 = 0.647$, and the white phase constitutes aluminum with $\phi_2 = 0.353$. The figure on the right shows the TPCF plot of the aluminum phase.⁹¹

The aforementioned works show that the reconstruction of microstructure relies on two-point or higher-order statistical information to obtain a prior distribution that define the spatial properties of the porous media.^{2,92–97} Although most of these methods were developed for two-phase media in geological systems, their implementation has been extended to electrodes in electrochemical systems.

2.2.1 Stochastic reconstruction of electrodes for electrochemical systems

The optimisation of electrochemical energy storage technologies is required for the development of improved electrodes. Thus, a recent interest has surged for generating synthetic microstructure in order to aid the design of optimised electrodes. Whether considering Solid Oxide Fuel Cells (SOFCs) or Lithium-ion batteries, these materials are typically constituted by three phases, which increase the level of complexity for their synthetic reconstruction compared to two-phased materials, as previously described in section 2.2.

Solid Oxide Fuel Cells electrodes

Based on the work of Yeong *et al.*^{83,87}, Suzue *et al.*⁹³ used the TPCF of a two-dimensional phase image of a SOFC composite anode to reconstruct a three-dimensional microstructure of this material, as shown in figure X. As an extension of this work, Baniassadi *et al.*⁹⁸ added a combined Monte Carlo simulation with a kinetic growth model to generate three-dimensional three-phase synthetic realisation of a SOFC electrode. A common approach implemented among authors for the generation of synthetic SOFC electrodes is the truncated pluri-Gaussian simulation. Moussaoui *et al.*⁷⁴ implement a combined model based on sphere packing and truncated Gaussian random field. These models use conditional simulations of Gaussian variables thresholded based on a truncation rule that allows the spatial dependence of variables to be modelled.^{99,100} Additional authors have implemented pluri-Gaussian random fields to model the three-phase microstructure of SOFC electrodes and establish correlations between the microstructure and model parameters^{5,101,102}. One advantage of this method is the ability to correlate the pluri-Gaussian function with properties such as phase volume fraction, directionality of the phases and for the generation of graded microstructure.⁵ Alternative algorithms for reconstruction of porous electrodes are based on their experimental fabrication techniques. Siddique *et al.*¹⁰³ developed a stochastic algorithm inspired on the process of nucleation and grain growth for reconstructing a three-dimensional fuel cell catalyst layer. In a similar way, a common approach for generating synthetic microstructure of SOFC electrodes involves the random packing of initial spheres or “seeds”, followed by the expansion of such spheres to simulate the sintering process.¹⁰⁴⁻¹⁰⁷

Lithium-ion battery electrodes

In the area of Li-ion batteries one of the main challenges consists on imaging the three phases of the domain, since the carbon-binder domain (CBD) is hard to identify using XCT techniques. For this reason, some authors have implemented computational models to adhere a synthetic carbon-binder domain (CBD) into XCT three-dimensional images of the NMC/pore phases.^{108,109} An analysis of transport properties such as tortuosity and effective electrical conductivity

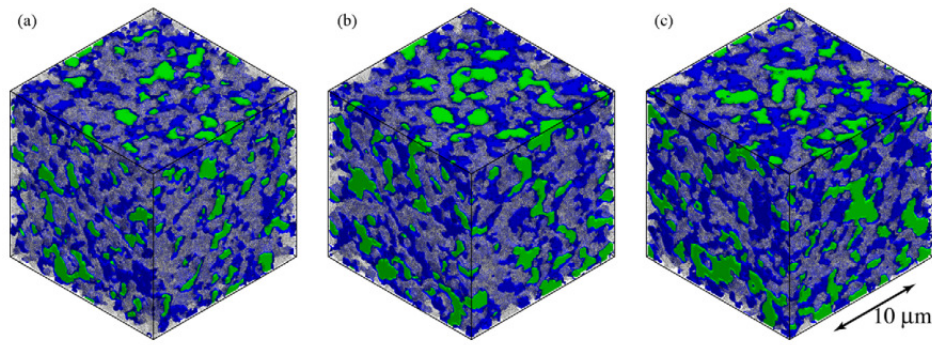


Figure 2.4: Reconstructed anode microstructures sintered at (a) 1300 °C, (b) 1350 °C and (c) 1400 °C. Green: Ni, blue: YSZ, transparent gray: pore.⁹³

prove the significant impact of different CBD configurations on the electrode performance. Other authors have implemented physics-based simulations or models based on the experimental synthesis techniques to predict the morphology of three-phase electrodes. Siddique *et al.*¹¹⁰ extended their previous work on stochastic generation of a fuel cell catalyst and implemented an algorithm of nucleation and growth to reconstruct a three-dimensional three-phase LiFePO_4 cathode. Additionally, Forouzan *et al.*¹¹¹ developed a particle-based simulation that involves the superposition of CBD particles, to correlate the fabrication process of Li-ion electrodes with their respective microstructure. Srivastava *et al.*¹¹² simulated the fabrication process Li-ion electrodes by controlling the adhesion of active material and CBD phases. Their physics-based dynamic simulations are able to predict with accuracy the effect of microstructure in transport properties.⁷

The techniques previously mentioned are important contributions to the stochastic reconstruction of electrode microstructure. Nevertheless, some of them have proved to be computationally expensive, and are restricted to a particular type of material, therefore cannot be used as general methods for fast generation of synthetic microstructure. Recent advances in deep learning techniques have led to the development of deep generative models, which have been proposed as efficient methods for the stochastic generation of three-dimensional two-phase porous media. The advantage of these methods is their ability to provide fast sampling of high-dimensional and intractable density functions without the need for an *a priori* model of the probability distribution function to be specified^{7,113}. These methods will be introduced in the following section.

2.2.2 Introduction to Machine Learning

Before introducing the concept of deep generative models, a brief overview of machine learning and deep learning techniques will be presented in this section. Machine Learning surged as research area out of the field of Artificial Intelligence based on the ideal of creating intelligent machines that can mimic the human brain. This, in conjunction with the unprecedented existence of *big data*, led to an increasing need of algorithms capable of classifying data, understanding patterns, making correlations and performing predictions. The most popular definition of Machine Learning was proposed by Tom Mitchell¹¹⁴ as:

A computer program is said to learn from experience E with respect to some task T and some performance measure P , if its performance on T , as measured by P , improves with experience E .

The mathematical process of learning is based on a training set \mathbf{x} , which can be composed of data such as images (2D or 3D), defined by the probability distribution function (pdf) p_{data} (i.e. $\mathbf{x} \sim p_{\text{data}}(\mathbf{x})$). The purpose of the learning process is to create a parametric pdf $p_{\text{model},\theta}$ to approximate p_{data} by iteratively adjusting its parameters θ . In most cases, this data is high-dimensional and therefore $p_{\text{model},\theta}$ needs to be complex enough to represent the multi-modal training set.¹¹⁵

Learning algorithms can be classified into two categories: supervised and unsupervised learning. Supervised learning, also called predictive learning, performs a mapping from inputs \mathbf{x} to outputs y , given a labeled set of input-output pairs $D = \{(\mathbf{x}_i, y_i)\}_{i=1}^N$, where D is the training set and N is the number of training samples. Each input \mathbf{x}_i is a D -dimensional vector, and the response variable y_i can be a categorical value from a finite set ($y_i \in \{1, \dots, C\}$), or a scalar ($y_i \in \mathbb{N}$). In this algorithm, the training data is labelled, so the task of the computer is to predict the labels of new data. The most common types of supervised learning are *classification* and *regression*. In unsupervised learning, also called descriptive learning, the training data is unlabeled, so the training set only consists on a set $D = \{\mathbf{x}_i\}_{i=0}^N$. In this case the algorithm learns based on measures of similarities

among the data sets. The most commonly used types of unsupervised learning are *clustering* and *dimensionality reduction*.¹¹⁵

Artificial Neural Networks for supervised learning

One of the most widely used methods for supervised learning problems are neural networks. These are developed based on the physiology of the brain, as a series of interconnected neurons that are activated upon training. The simplest neural network architecture consists of a single *perceptron* (or single neuron) introduced by Rosenblatt¹¹⁶ as a *threshold logic unit* (TLU) to perform simple binary classification operations. The TLU takes in a vector of inputs (x_0, x_1, x_2) , each associated with a weight (w_0, w_1, w_2) , then computes the weighted sum of these inputs ($z = w_0x_0 + w_1x_1 + w_2x_2 = w^T x$), and applies the Heaviside step function to z in order to output the result $h_w(x) = \text{step}(z) = \text{step}(w^T x)$. If the result exceeds a threshold, the step function outputs a positive class (i.e. $h_w(x) = 1$), or else, it outputs a negative class (i.e. $h_w(x) = 0$). By replacing the Heaviside step function with a sigmoid function, defined by equation 2.44, the problem becomes a binary classification exactly like a logistic regression problem, where the weights w_j are defined as the fitting parameters θ_j of the network.

$$g(z) = \frac{1}{1 + e^{-z}} \quad (2.44)$$

This single neuron architecture shown in Figure 2.5 can represent simple logical functions, such as AND, NOR, OR; however, to represent more complex functions, additional neurons are required, as well as interconnectivity between them.

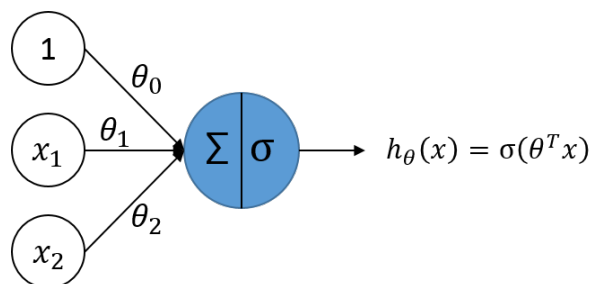


Figure 2.5: Graphic representation of a logistic function as a neural network

By definition, a neural network is composed of at least three layers: an input layer, a hidden layer, and an output layer, as shown in Figure 2.6. According to the *Universal Approximation Theorem*¹¹⁷, a neural network with at least one hidden layer can approximate arbitrarily well any function from any finite dimensional space to another given that the network has enough neurons. The number of hidden layers can increase according to the complexity or depth of the problem, which leads to the area of *deep learning*.

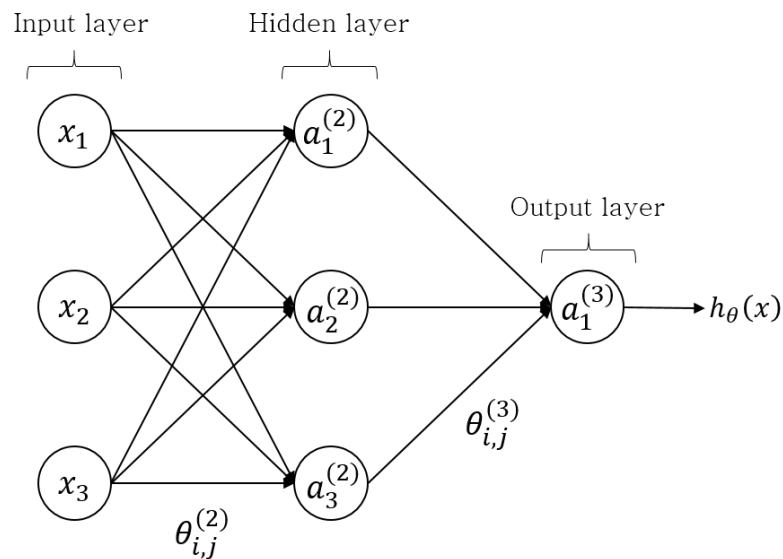


Figure 2.6: Three layer neural network

Deep learning methods have revolutionised the state-of-the-art machine learning methods by allowing computational models composed of multiple processing layers to learn representations of data with many levels of abstraction.¹¹⁸ These multiple layers are composed of simple modules that perform non-linear operations each and transform the representation at one level into a higher and more abstract representation. This composition with enough non-linear transformations allows very complex functions to be learned. Due to this multi-layer configuration, deep learning is able to discover intricate structures in high-dimensional data and thus its applications extend from image and speech recognition to object, detection, drug discovery and genomics.¹¹⁸

One of the major breakthroughs in deep learning that has allowed the efficient training of large datasets is the development of the backpropagation algo-

rithm.^{118–121}. Backpropagation allows to compute the gradients of a loss function $J(\theta)$ with respect to the parameters of the multi-layer network based on the chain rule. A stochastic gradient descent technique (SGD) is then implemented to optimise the parameters of the neural network.¹²² During each optimisation step t , parameters θ_{t+1} are updated by moving θ_t one step towards the direction of steepest descent, or optimal conditions (*i.e.* towards θ^*), where the direction is given by the gradient of the loss function $J(\theta)$ with respect to θ , and the step size or learning rate is given by α . The equation that defines the SGD process is given by

$$\theta_{t+1} = \theta_t - \alpha \nabla_{\theta} J(\theta) \quad (2.45)$$

In this stochastic process, a small set of examples, or so called batches, gives a noisy estimate of the average gradient over all samples.¹²² This is an iterative process until the loss function $J(\theta)$ is minimised.

A further development in deep learning that has been widely applied in the computer vision community are convolutional neural networks. These have been applied with great success to the detection, segmentation and object recognition in images. Convolutional neural networks are structured in layers which are organised in feature maps. Each layer is connected to local regions in the feature maps of the previous layer through a moving kernel of parameters or filter. Mathematically, this filtering operation by a feature map is a convolution, which give these networks their name. The local weighted sum is then passed through a non-linear function (*i.e.* sigmoid) and the result is passed to the next layer. Convolutional neural networks are able to detect features such as edges and local statistics of images or signals through the filtering process, with a small number of parameters. This makes the learning process more efficient and allows processing of 2D and 3D images. A stacking of various convolutional layers follows the hierarchical nature of deep neural networks, and therefore higher-level features in deeper layers are obtained by lower-level ones.¹¹⁸ This is important in image recognition, since local combinations of edges form motifs, motifs form parts and parts are assembled into objects.¹¹⁸

The non-linear transformation performed over the input data by fully con-

nected layers convolutional operations is given by a set of linear operations (weighted sum) combined with non-linear activation functions. The most well-known type of activation function is the sigmoid function, defined by equation 2.44, or sigmoid-type functions. Nonetheless, in some cases for very deep neural networks, these functions encounter a vanishing gradient problem in the backpropagation step during training. To avoid the vanishing gradient, Rectified Linear Unit (ReLU) activation function can be implemented to allow gradients of sufficient magnitude to be backpropagated. Regardless of the significant improvement, in some cases when the input is negative even the ReLU function presents vanishing gradients. For this reason Leaky ReLU function can be implemented, where the value of the function for negative numbers has a slight but positive slope, avoiding a zero-gradient value.¹²³

These advances in deep learning algorithms have led to the development of complex methods that can represent probability distribution functions of high-dimensionality data called generative models. Despite their relatively recent development, their application has extended in various areas, from computer vision to time-series prediction. In this work a generative model is, for the first time, implemented for the design of electrode microstructure for energy storage technologies.

2.2.3 Generative Models

Generative models are implemented to learn and approximate high-dimensional probability distribution functions based on a training set of data or images, from which new realisations can be sampled. For simplicity, this work will address only the type of generative models that work by the principle of maximum likelihood.^{124,125} The purpose of maximum likelihood is to define a model, parametrised by θ , that estimates a probability distribution function. Based on a training set \mathbf{x} that contains m training samples, the likelihood is defined as the probability that the model assigns to the training data: $\prod_{i=1}^m p_{\text{model}}(x^{(i)}; \theta)$. The objective of maximum likelihood is to estimate the values of θ of the model that maximise the likelihood of the training data. Thus, the maximum likelihood is defined as

$$\theta^* = \arg \max_{\theta} \prod_{i=1}^m p_{\text{model}}(x^{(i)}; \theta) \quad (2.46)$$

To simplify the derivatives of the likelihood with respect to the models, it is better to work in the log space, so that the product operator is changed to a the sum. Therefore, the function to be maximised is the log-likelihood, defined as

$$\theta^* = \arg \max_{\theta} \sum_{i=1}^m \log p_{\text{model}}(x^{(i)}; \theta) \quad (2.47)$$

Another way of estimating the distribution of the dataset p_{data} is by calculating the divergence between this pdf and the one of the model p_{model} . A common method which is equivalent to maximising the log-likelihood consists in minimising the Kullback-Leibler (KL) divergence between the data and the model:

$$\theta^* = \arg \min_{\theta} D_{KL}(p_{\text{data}}(x) || p_{\text{model}}(x; \theta)) \quad (2.48)$$

Given that p_{data} is unknown, the training set of m samples that come from this pdf are used to define an empirical distribution \hat{p}_{data} to approximate p_{data} . Therefore, minimising the D_{KL} between \hat{p}_{data} and p_{model} is the same as maximising the log-likelihood of p_{model} . D_{KL} is used in some generative models, as explained below.

Generative models that implement the maximum likelihood principle can be categorised based on the way they approximate this likelihood.^{124,125} The two main categories correspond to the models that define an explicit density function $p_{\text{model}}(x; \theta)$ - *explicit models* -, and models that do not explicitly represent a probability distribution over the data - *implicit models* -.

Explicit Models

In explicit models, the main challenge is to define a function that can capture the complexity of the dataset, while still maintaining computational tractability. In this respect, these models can be sub-classified as tractable and approximate. Among the tractable methods, fully visible belief networks (FVBN) and non-linear independent component analysis (ICA) are some of the most popular.¹²⁶⁻¹²⁸ In (FVBN),

the joint probability distribution of an n -dimensional vector x is decomposed using the chain rule of probability into a product of one-dimensional conditional probabilities as¹²⁹

$$p_{\text{model}}(\mathbf{x}) = \prod_{i=1}^n p_{\text{model}}(x_i | x_1, \dots, x_{i-1}) \quad (2.49)$$

In this model, the distribution of each x_i is computed using a neural network, which makes the model very computationally expensive.¹²⁹

Non-linear ICA perform continuous, non-linear transformations between two different spaces: a latent space Z , and the data space X . It is based in the assumption that a continuous, differentiable, invertible transformation g exists which, when applied over a vector in the latent space Z , it can yield a sample from the model in X space.¹²⁵ This process is defined as

$$p_x(\mathbf{x}) = p_z(g^{-1}(\mathbf{x})) \left| \det \left(\frac{\partial g^{-1}(\mathbf{x})}{\partial \mathbf{x}} \right) \right| \quad (2.50)$$

One of the main drawbacks of ICA is the restrictions imposed in the choice of function g which has to be tractable and invertible.^{124,125} Although defining a tractable function is useful for optimisation purposes, the limitations of the available functions impose restrictions to the models. For this reason, explicit models that approximate the probability density function are used.

The most common approaches for explicit intractable models are variational approximations. In these models, the learning algorithm maximises a lower bound \mathcal{L} to guarantee that the log-likelihood of the p_{model} is at least as high as \mathcal{L} :¹²⁴

$$\mathcal{L}(x; \theta) \leq \log p_{\text{model}}(x; \theta) \quad (2.51)$$

In this category, Kingma and Welling¹³⁰ developed the *Variational Autoencoders* (VAE), to perform inference for intractable deep latent variables. Based on a training set of data or images \mathbf{x} , an approximate inference network called *encoder* is used to obtain the latent space \mathbf{z} which follows a simple multi-Gaussian prior distribution $p_{\theta}(\mathbf{z})$. The encoder, defined as $q_{\phi}(\mathbf{z}|\mathbf{x})$, is represented by a neural net-

work, parametrised parameters ϕ . A *decoder* is then used to represent the conditional distribution of the data \mathbf{x} given the latent variables \mathbf{z} . The decoder, defined as $p_{\theta}(\mathbf{x}|\mathbf{z})$, is also represented by a neural network and parameterised by θ . VAEs are trained by maximizing the variational lower bound $\mathcal{L}(q)$ associated with data point \mathbf{x}

$$\begin{aligned}\mathcal{L}(q) &= \mathbb{E}_{\mathbf{z} \sim q(\mathbf{z}|\mathbf{x})} \log p_{\text{model}}(\mathbf{x}|\mathbf{z}) - D_{KL}(q(\mathbf{z}|\mathbf{x}) || p_{\text{model}}(\mathbf{z})) \\ &\leq \log p_{\text{model}}(\mathbf{x})\end{aligned}\tag{2.52}$$

the first term on the right hand side corresponds to the reconstruction log-likelihood. The second term tries to estimate the divergence between the approximate posterior distribution $q(\mathbf{z}|\mathbf{x})$ and the model prior $p_{\text{model}}(\mathbf{z})$.^{125,130}

Implicit models - Generative Adversarial Networks

Implicit density methods are trained without needing to explicitly define a probability distribution function. Instead, the model is trained to implicitly learn the distribution function based on a set of training samples.¹²⁴ Within this category, the most recent and most widely used method is called Generative Adversarial Networks (GANs).

GANs are defined as deep latent variable models that learn to implicitly represent the density function of a given training set (*i.e.* p_{data}).¹²⁴ As is the case for implicit models, since p_{data} is unknown, the result of the learning process is an estimate of this function defined as p_{model} from which a set of samples can be generated. The idea of GANs originated from game theory, as a two-player game between two parametric functions: the generator $G(\mathbf{z})$ and the discriminator $D(\mathbf{x})$. The generator, $G(\mathbf{z})$, takes as input a latent vector \mathbf{z} and generates synthetic samples (\mathbf{x}_G) that are intended to approximate the real data (\mathbf{x}_{data}). The discriminator, $D(\mathbf{x})$, tries to distinguish between the generated samples and the real ones. This concept was introduced by Goodfellow *et al.*¹³¹ as a counterfeiter-detective game, where the generator is a counterfeiter producing fake currency, while the discriminator is a police detective who aims to distinguish the fake currency from the real. During training, these two players continuously improve by pushing the skills of the other.^{7,131}

The generator and the discriminator are differentiable functions with respect to their inputs and parameters. The generator, defined as $G(\mathbf{z})$ maps a d -dimensional latent vector $\mathbf{z} \sim p_{\mathbf{z}}(\mathbf{z}) \in \mathbb{R}^d$ to a point in the space of real data as $G(\mathbf{z}; \theta^{(G)})$, and uses $\theta^{(G)}$ as parameters. The latent space \mathbf{z} is defined by a prior distribution $p_{\mathbf{z}} \sim \mathcal{N}(0, 1)$; \mathbf{z} is a tensor of dimensionality d , composed of independent, normally distributed, real variables:

$$\mathbf{z} \sim \mathcal{N}(0, 1)^{d \times 1 \times 1 \times 1}$$

$$G_{\theta^{(G)}} : \mathbf{z} \rightarrow \mathbb{R}^{3 \times 64 \times 64 \times 64}$$

The discriminator, $D(\mathbf{x})$ represents the probability that \mathbf{x} comes from p_{data} .¹³¹ $D(\mathbf{x})$, defined by $\theta^{(D)}$ receives samples from the real data \mathbf{x}_{data} and from the synthetic data generated by the generator $G(\mathbf{z})$:

$$\mathbf{x} \sim \mathbb{R}^{3 \times 64 \times 64 \times 64}$$

$$D_{\theta^{(D)}} : \mathbf{x} \rightarrow [0, 1]$$

The aim of the training is to make the implicit density learned by $G(\mathbf{z})$ (*i.e.* p_{model}) to be close to the distribution of real data (*i.e.* p_{data}). Opposed to VAEs that minimise the KL divergence between p_{model} and p_{data} , GANs objective is to minimise the Jensen Shanon divergence $D_{\text{JS}}(p_{\text{model}} || p_{\text{data}})$.¹²⁴ The training consists of an adversarial game in which the two players are in constant competition: the discriminator's task is to label the real and fake data correctly (*i.e.* $D(\mathbf{x}_{\text{data}}) = 1$ and $D(G(\mathbf{z})) = 0$), while the generator attempts to fool the discriminator into misclassifying synthetic data as real (*i.e.* $D(G(\mathbf{z})) = 1$). This training process is formally defined as a minimax game between the generator and discriminator by the following objective function¹³¹:

$$\min_G \left(\max_D (V(G, D)) \right) = \mathbb{E}_{\mathbf{x} \sim p_{\text{data}}(\mathbf{x})} [\log D(\mathbf{x})] + \mathbb{E}_{\mathbf{z} \sim p_{\mathbf{z}}(\mathbf{z})} [\log (1 - D(G(\mathbf{z})))] \quad (2.53)$$

In order to solve equation 2.53, each of the two players, the generator $G_{\theta^{(G)}}(\mathbf{z})$

and the discriminator $D_{\theta^{(D)}}(\mathbf{x})$, has a cost function to be optimised through SGD in a two-step process. First, the discriminator is trained to maximise its loss function $J^{(D)}$:

$$J^{(D)} = \mathbb{E}_{\mathbf{x} \sim p_{\text{data}}(\mathbf{x})} [\log (D(\mathbf{x}))] + \mathbb{E}_{\mathbf{z} \sim p_{\mathbf{z}}(\mathbf{z})} [\log (1 - D(G(\mathbf{z})))] \quad (2.54)$$

This becomes a binary classification problem between the discriminator's prediction and the real label, and is trained as a standard binary cross-entropy loss function. Subsequently, the generator is trained to minimise its loss function corresponding to minimising the log-probability of the discriminator being correct:

$$J^{(G)} = \mathbb{E}_{\mathbf{z} \sim p_{\mathbf{z}}(\mathbf{z})} [\log (1 - D(G(\mathbf{z})))] \quad (2.55)$$

During the early steps of training, the discriminator tends to outperform the generator since it successfully rejects the generated samples with high confidence, leading to a vanishing gradient in the generator. To solve this problem, a heuristic non-saturating game is introduced in the generator's loss function. Instead of minimising $\log (1 - D(G(\mathbf{z})))$, it is convenient to maximise the log-probability of the discriminator being mistaken, defined as $\log (D(G(\mathbf{z})))$ ¹²⁴. The solution to this optimisation problem is a Nash equilibrium¹²⁴ where each of the players achieves a local minimum. At the Nash equilibrium, the generated synthetic samples of $\mathbf{x} = G(\mathbf{z}) \sim p_{\text{model}}(\mathbf{z})$ are indistinguishable from the real samples $\mathbf{x} \sim p_{\text{data}}(\mathbf{x})$, thus $p_{\text{model}}(\mathbf{z}) = p_{\text{data}}(\mathbf{x})$ and $D(\mathbf{x}) = \frac{1}{2}$ for all \mathbf{x} since the discriminator can no longer distinguish between real and synthetic data.¹²⁴

After the introduction of GANs, a large amount of literature has been presented with improvements and new configurations of GANs. One of these improved architectures and perhaps the most widely used was introduced by Radford *et al.*¹³² called Deep Convolutional Neural Networks (DCGANs). The network architecture is based on the all-convolutional net presented by Springenberg *et al.*¹³³ with no pooling layers. It also implements a batch normalisation in almost all layers, except the last layer of the generator and the first layer of the discriminator. For the training process, an ADAM optimiser is used as an alternative of the SGD method, which adds a momentum term.¹³⁴

The GAN architecture implemented in this work is based on the DCGAN architecture, so both the generator $G_{\theta(G)}(\mathbf{z})$ and the discriminator $D_{\theta(D)}(\mathbf{x})$ consist of deep convolutional neural networks. The training data for generative models can be of various types, however in this work the training set consists of three-dimensional images of two types of electrode microstructures: a SOFC anode and a Li-ion cathode.

References

- [1] M. Weyland, P. A. Midgley, and J. M. Thomas, “Electron tomography of nanoparticle catalysts on porous supports: A new technique based on Rutherford scattering,” *Journal of Physical Chemistry B*, vol. 105, no. 33, pp. 7882–7886, 2001.
- [2] J. Méndez-Venegas and M. A. Díaz-Viera, “Geostatistical modeling of clay spatial distribution in siliciclastic rock samples using the plurigaussian simulation method,” *Geofísica Internacional*, vol. 52, no. 3, pp. 229–247, 2013.
- [3] P. Fantazzini, R. J. S. Brown, and G. C. Borgia, “Bone tissue and porous media: Common features and differences studied by NMR relaxation,” *Magnetic Resonance Imaging*, vol. 21, no. 3-4, pp. 227–234, 2003.
- [4] Q. Xiong, T. G. Baychev, and A. P. Jivkov, “Review of pore network modelling of porous media: Experimental characterisations, network constructions and applications to reactive transport,” *Journal of Contaminant Hydrology*, vol. 192, pp. 101–117, 2016.
- [5] H. Moussaoui, R. K. Sharma, J. Debayle, Y. Gavet, G. Delette, and J. Laurencin, “Microstructural correlations for specific surface area and triple phase boundary length for composite electrodes of solid oxide cells,” *Journal of Power Sources*, vol. 412, no. November 2018, pp. 736–748, 2019.
- [6] S. J. Cooper, A. Bertei, D. P. Finegan, and N. P. Brandon, “Simulated impedance of diffusion in porous media,” *Electrochimica Acta*, vol. 251, pp. 681–689, 2017.
- [7] A. Gayon-Lombardo, L. Mosser, N. P. Brandon, and S. J. Cooper, “Pores for thought: generative adversarial networks for stochastic reconstruction of 3D multi-phase electrode microstructures with periodic boundaries,” *npj Computational Materials*, vol. 6, no. 1, pp. 1–11, 2020.
- [8] G. Wei, C. Jia, J. Liu, and C. Yan, “Carbon felt supported carbon nanotubes catalysts composite electrode for vanadium redox flow battery application,” *Journal of Power Sources*, vol. 220, pp. 185–192, dec 2012.
- [9] A. Q. Su, N. F. Wang, S. Q. Liu, T. Wu, and S. Peng, “Modification of Car-

- bon Paper Electrode via Hydrothermal Oxidation Applied in the Vanadium Redox Battery,” *Acta Phys. - Chim. Sin.*, vol. 28, no. 6, pp. 1387–1392, 2012.
- [10] B. Sun and M. Skyllas-Kazacos, “Modification of graphite electrode materials for vanadium redox flow battery application-I. Thermal treatment,” *Electrochimica Acta*, vol. 37, no. 7, pp. 1253–1260, 1992.
- [11] B. Chakrabarti, D. Nir, V. Yufit, F. Tariq, J. Rubio-Garcia, R. Maher, A. Kucernak, P. V. Aravind, and N. P. Brandon, “Performance Enhancement of Reduced Graphene Oxide-Modified Carbon Electrodes for Vanadium Redox-Flow Systems,” *ChemElectroChem*, vol. 4, pp. 194–200, jan 2017.
- [12] Z. He, Z. Chen, W. Meng, Y. Jiang, G. Cheng, L. Dai, and L. Wang, “Modified carbon cloth as positive electrode with high electrochemical performance for vanadium redox flow batteries,” *Journal of Energy Chemistry*, vol. 25, pp. 720–725, 2016.
- [13] X. L. Zhou, Y. K. Zeng, X. B. Zhu, L. Wei, and T. S. Zhao, “A high-performance dual-scale porous electrode for vanadium redox flow batteries,” *Journal of Power Sources*, vol. 325, pp. 329–336, 2016.
- [14] X. L. Zhou, T. S. Zhao, Y. K. Zeng, L. An, and L. Wei, “A highly permeable and enhanced surface area carbon-cloth electrode for vanadium redox flow batteries,” *Journal of Power Sources*, vol. 329, pp. 247–254, 2016.
- [15] A. Gayon Lombardo, B. A. Simon, O. Taiwo, S. J. Neethling, and N. P. Brandon, “A pore network model of porous electrodes in electrochemical devices,” *Journal of Energy Storage*, vol. 24, p. 100736, 2019.
- [16] M. Rebai and M. Prat, “Scale effect and two-phase flow in a thin hydrophobic porous layer. Application to water transport in gas diffusion layers of proton exchange membrane fuel cells,” *Journal of Power Sources*, vol. 192, no. 2, pp. 534–543, 2009.
- [17] X. Ke, J. I. D. Alexander, J. M. Prah, and R. F. Savinell, “Flow distribution and maximum current density studies in redox flow batteries with a single passage of the serpentine flow channel,” *Journal of Power Sources*, vol. 270, pp. 646–657, 2014.
- [18] X. Ke, J. I. D. Alexander, J. M. Prah, and R. F. Savinell, “A simple analytical

- model of coupled single flow channel over porous electrode in vanadium redox flow battery with serpentine flow channel,” *Journal of Power Sources*, vol. 288, pp. 308–313, 2015.
- [19] Q. Zheng, X. Li, Y. Cheng, G. Ning, F. Xing, and H. Zhang, “Development and perspective in vanadium flow battery modeling,” *Applied Energy*, vol. 132, pp. 254–266, 2014.
- [20] N. Pinjari, B. Kumar, A. Bhargav, and P. Ruch, “Effect of Electrode Properties on Performance of Miniaturized Vanadium Redox Flow Battery,” *IEEE*, vol. 3, p. 1040, 2017.
- [21] X. Li, “Modeling and simulation study of a metal free organic-inorganic aqueous flow battery with flow through electrode,” *Electrochimica Acta*, vol. 170, pp. 98–109, 2015.
- [22] A. A. Shah, M. J. Watt-Smith, and F. C. Walsh, “A dynamic performance model for redox-flow batteries involving soluble species,” *Electrochimica Acta*, vol. 53, no. 27, pp. 8087–8100, 2008.
- [23] X. Ma, H. Zhang, and F. Xing, “A three-dimensional model for negative half cell of the vanadium redox flow battery,” *Electrochimica Acta*, vol. 58, no. 1, pp. 238–246, 2011.
- [24] M. D. R. Kok, A. Khalifa, and J. T. Gostick, “Multiphysics Simulation of the Flow Battery Cathode: Cell Architecture and Electrode Optimization,” *Journal of The Electrochemical Society*, vol. 163, no. 7, pp. A1408–A1419, 2016.
- [25] Q. Xu, T. S. Zhao, and P. K. Leung, “Numerical investigations of flow field designs for vanadium redox flow batteries,” *Applied Energy*, vol. 105, pp. 47–56, 2013.
- [26] A. Tang, J. Bao, and M. Skyllas-Kazacos, “Studies on pressure losses and flow rate optimization in vanadium redox flow battery,” *Journal of Power Sources*, vol. 248, pp. 154–162, 2014.
- [27] I. M. Bayanov and R. Vanhaelst, “The numerical simulation of vanadium RedOx flow batteries,” *Journal of Mathematical Chemistry*, vol. 49, no. 9, pp. 2013–2031, 2011.

- [28] Q. Xu and T. S. Zhao, "Fundamental models for flow batteries," *Progress in Energy and Combustion Science*, vol. 49, pp. 40–58, 2015.
- [29] K. Bromberger, J. Kaunert, and T. Smolinka, "A Model for All-Vanadium Redox Flow Batteries: Introducing Electrode-Compression Effects on Voltage Losses and Hydraulics," *Energy Technology*, vol. 2, no. 1, pp. 64–76, 2014.
- [30] C. L. Chen, H. K. Yeoh, and M. H. Chakrabarti, "An enhancement to Vynnycky's model for the all-vanadium redox flow battery," *Electrochimica Acta*, vol. 120, pp. 167–179, 2014.
- [31] J. Houser, J. Clement, A. Pezeshki, and M. M. Mench, "Influence of architecture and material properties on vanadium redox flow battery performance," *Journal of Power Sources*, vol. 302, pp. 369–377, 2016.
- [32] G. Qiu, A. S. Joshi, C. R. Dennison, K. W. Knehr, E. C. Kumbur, and Y. Sun, "3-D pore-scale resolved model for coupled species/charge/fluid transport in a vanadium redox flow battery," *Electrochimica Acta*, vol. 64, pp. 46–64, mar 2012.
- [33] G. Qiu, C. R. Dennison, K. W. Knehr, E. C. Kumbur, and Y. Sun, "Pore-scale analysis of effects of electrode morphology and electrolyte flow conditions on performance of vanadium redox flow batteries," *Journal of Power Sources*, vol. 219, pp. 223–234, 2012.
- [34] M. Vynnycky, "Analysis of a model for the operation of a vanadium redox battery," *Energy*, vol. 36, no. 4, pp. 2242–2256, 2011.
- [35] X. Yang, Y. Mehmani, W. A. Perkins, A. Pasquali, M. Schönherr, K. Kim, M. Perego, M. L. Parks, N. Trask, M. T. Balhoff, M. C. Richmond, M. Geier, M. Krafczyk, L. S. Luo, A. M. Tartakovsky, and T. D. Scheibe, "Intercomparison of 3D pore-scale flow and solute transport simulation methods," *Advances in Water Resources*, vol. 95, pp. 176–189, 2016.
- [36] Z. Shi and X. Wang, "Comparison of Darcy's Law, the Brinkman Equation, the Modified N-S Equation and the Pure Diffusion Equation in PEM Fuel Cell Modeling," *Proceeding of the COMSOL Conference*, 2007.
- [37] F. A. Howes and S. Whitaker, "The spatial averaging theorem revisited," *Chemical Engineering Science*, vol. 40, no. 8, pp. 1387–1392, 1985.

- [38] X. Ke, J. M. Prahl, J. I. D. Alexander, and R. F. Savinell, "Redox flow batteries with serpentine flow fields: Distributions of electrolyte flow reactant penetration into the porous carbon electrodes and effects on performance," *Journal of Power Sources*, vol. 384, no. February, pp. 295–302, 2018.
- [39] Q. Xu, T. S. Zhao, and C. Zhang, "Performance of a vanadium redox flow battery with and without flow fields," *Electrochimica Acta*, vol. 142, pp. 61–67, 2014.
- [40] M. Parvazinia, V. Nassehi, R. J. Wakeman, and M. H. R. Ghoreishy, "Finite element modelling of flow through a porous medium between two parallel plates using the Brinkman equation," *Transport in Porous Media*, vol. 63, no. 1, pp. 71–90, 2006.
- [41] P. C. Lichtner, "Continuum model for simultaneous chemical reactions and mass transport in hydrothermal systems," *Geochimica et Cosmochimica Acta*, vol. 49, no. 3, pp. 779–800, 1985.
- [42] S. J. Cooper, A. Bertei, P. R. Shearing, J. A. Kilner, and N. P. Brandon, "TauFactor: An open-source application for calculating tortuosity factors from tomographic data," *SoftwareX*, vol. 5, pp. 203–210, 2016.
- [43] D. F. Yule and W. R. Gardner, "Longitudinal and Transverse Dispersion Coefficients in Unsaturated Plainfield Sand," *Water Resources Research*, vol. 14, no. 4, pp. 582–588, 1978.
- [44] S. Patankar, *Numerical Heat Transfer and Fluid Flow*. London: CRC Press Taylor & Francis Group, 2 ed., 1980.
- [45] M. A. Spaid and F. R. Phelan, "Lattice Boltzmann methods for modeling microscale flow in fibrous porous media," *Physics of Fluids*, vol. 9, no. 9, pp. 2468–2474, 1997.
- [46] J. Monaghan, "Smoothed particle hydrodynamics," *Annu. Rev. Astron. Astrophys*, vol. 30, pp. 543–574, 1992.
- [47] X. Lu, A. Bertei, D. P. Finegan, C. Tan, S. R. Daemi, J. S. Weaving, K. B. O'Regan, T. M. Heenan, G. Hinds, E. Kendrick, D. J. Brett, and P. R. Shearing, "3D microstructure design of lithium-ion battery electrodes assisted

- by X-ray nano-computed tomography and modelling,” *Nature Communications*, vol. 11, no. 1, pp. 1–13, 2020.
- [48] M. Ji and Z. Wei, “A review of water management in polymer electrolyte membrane fuel cells,” *Energies*, vol. 2, no. 4, pp. 1057–1106, 2009.
- [49] J. T. Gostick, M. A. Ioannidis, M. W. Fowler, and M. D. Pritzker, “Pore network modeling of fibrous gas diffusion layers for polymer electrolyte membrane fuel cells,” *Journal of Power Sources*, vol. 173, pp. 277–290, nov 2007.
- [50] M. El Hannach, J. Pauchet, and M. Prat, “Pore network modeling: Application to multiphase transport inside the cathode catalyst layer of proton exchange membrane fuel cell,” *Electrochimica Acta*, vol. 56, no. 28, pp. 10796–10808, 2011.
- [51] M. El Hannach, M. Prat, and J. Pauchet, “Pore network model of the cathode catalyst layer of proton exchange membrane fuel cells: Analysis of water management and electrical performance,” *International Journal of Hydrogen Energy*, vol. 37, no. 24, pp. 18996–19006, 2012.
- [52] R. Wu, Q. Liao, X. Zhu, and H. Wang, “Pore network modeling of cathode catalyst layer of proton exchange membrane fuel cell,” *International Journal of Hydrogen Energy*, vol. 37, no. 15, pp. 11255–11267, 2012.
- [53] J. Park, M. Matsubara, and X. Li, “Application of lattice Boltzmann method to a micro-scale flow simulation in the porous electrode of a PEM fuel cell,” *Journal of Power Sources*, vol. 173, no. 1, pp. 404–414, 2007.
- [54] Y. Hu, D. Li, S. Shu, and X. Niu, “Full Eulerian lattice Boltzmann model for conjugate heat transfer,” *Physical Review E - Statistical, Nonlinear, and Soft Matter Physics*, vol. 92, no. 6, 2015.
- [55] D. V. Patil, “Chapman-Enskog analysis for finite-volume formulation of lattice Boltzmann equation,” *Physica A: Statistical Mechanics and its Applications*, vol. 392, no. 12, pp. 2701–2712, 2013.
- [56] Y. Mehmani, M. Oostrom, and M. T. Balhoff, “A streamline splitting pore-network approach for computationally inexpensive and accurate simulation of transport in porous media,” *Water Resources Research*, vol. 50, pp. 2488–2517, 2014.

- [57] R. C. Acharya, S. E. A. T. M. Van der Zee, and A. Leijnse, "Transport modeling of nonlinearly adsorbing solutes in physically heterogeneous pore networks," *Water Resources Research*, vol. 41, p. W02020, feb 2005.
- [58] Y. Mehmani, T. Sun, M. T. Balhoff, P. Eichhubl, and S. Bryant, "Multiblock Pore-Scale Modeling and Upscaling of Reactive Transport: Application to Carbon Sequestration," *Transport in Porous Media*, vol. 95, no. 2, pp. 305–326, 2012.
- [59] J. Tansey and M. T. Balhoff, "Pore Network Modeling of Reactive Transport and Dissolution in Porous Media," *Transport in Porous Media*, vol. 113, pp. 303–327, jun 2016.
- [60] M. J. Blunt, *Multiphase Flow in Permeable Media: A Pore-Scale Perspective*. Cambridge: Cambridge University Press, 1 ed., 2017.
- [61] M. Aghighi, M. A. Hoeh, W. Lehnert, G. Merle, and J. Gostick, "Simulation of a Full Fuel Cell Membrane Electrode Assembly Using Pore Network Modeling," *Journal of The Electrochemical Society*, vol. 163, no. 5, pp. F384–F392, 2016.
- [62] L. Li, C. A. Peters, and M. A. Celia, "Upscaling geochemical reaction rates using pore-scale network modeling," *Advances in Water Resources*, vol. 29, pp. 1351–1370, sep 2006.
- [63] R. C. Acharya, M. I. van Dijke, K. S. Sorbie, S. E. Van der Zee, and A. Leijnse, "Quantification of longitudinal dispersion by upscaling Brownian motion of tracer displacement in a 3D pore-scale network model," *Advances in Water Resources*, vol. 30, no. 2, pp. 199–213, 2007.
- [64] D. Kim, C. A. Peters, and W. B. Lindquist, "Upscaling geochemical reaction rates accompanying acidic CO₂-saturated brine flow in sandstone aquifers," *Water Resources Research*, vol. 47, no. 1, pp. 1–16, 2011.
- [65] A. Raof, H. M. Nick, S. M. Hassanizadeh, and C. J. Spiers, "PoreFlow: A complex pore-network model for simulation of reactive transport in variably saturated porous media," *Computers and Geosciences*, vol. 61, pp. 160–174, 2013.
- [66] A. Raof, H. M. Nick, T. K. Wolterbeek, and C. J. Spiers, "Pore-scale mod-

- eling of reactive transport in wellbore cement under CO₂ storage conditions,” *International Journal of Greenhouse Gas Control*, vol. 11, no. SUPPL, pp. S67–S77, 2012.
- [67] L. Holzer, B. Iwanschitz, T. Hocker, B. Münch, M. Prestat, D. Wiedenmann, U. Vogt, P. Holtappels, J. Sfeir, A. Mai, and T. Graule, “Microstructure degradation of cermet anodes for solid oxide fuel cells: Quantification of nickel grain growth in dry and in humid atmospheres,” *Journal of Power Sources*, vol. 196, no. 3, pp. 1279–1294, 2011.
- [68] D. S. Eastwood, R. S. Bradley, F. Tariq, S. J. Cooper, O. O. Taiwo, J. Gelb, A. Merkle, D. J. Brett, N. P. Brandon, P. J. Withers, P. D. Lee, and P. R. Shearing, “The application of phase contrast X-ray techniques for imaging Li-ion battery electrodes,” *Nuclear Instruments and Methods in Physics Research, Section B: Beam Interactions with Materials and Atoms*, vol. 324, pp. 118–123, 2014.
- [69] N. Ni, S. J. Cooper, R. Williams, N. Kemen, D. W. McComb, and S. J. Skinner, “Degradation of (La_{0.6}Sr_{0.4})_{0.95}(Co_{0.2}Fe_{0.8})O_{3-δ} Solid Oxide Fuel Cell Cathodes at the Nanometer Scale and below,” *ACS Applied Materials and Interfaces*, vol. 8, no. 27, pp. 17360–17370, 2016.
- [70] P. Pietsch and V. Wood, “X-Ray Tomography for Lithium Ion Battery Research: A Practical Guide,” *Annual Review of Materials Research*, vol. 47, no. 1, pp. 451–479, 2017.
- [71] A. N. Diógenes, L. O. E. Dos Santos, C. P. Fernandes, A. C. Moreira, and C. R. Apolloni, “Porous Media Microstructure Reconstruction Using Pixel-Based and Object-Based Simulated Annealing – Comparison With Other Reconstruction Methods,” *Revista de Engenharia Térmica*, vol. 8, no. 2, p. 35, 2009.
- [72] P. M. Adler, C. G. Jacquin, and J. A. Quiblier, “Flow in simulated porous media,” *International Journal of Multiphase Flow*, vol. 16, no. 4, pp. 691–712, 1990.
- [73] Z. R. Liang, C. P. Fernandes, F. S. Magnani, and P. C. Philippi, “A reconstruction technique for three-dimensional porous media using image anal-

- ysis and Fourier transforms,” *Journal of Petroleum Science and Engineering*, vol. 21, no. 3-4, pp. 273–283, 1998.
- [74] H. Moussaoui, J. Laurencin, Y. Gavet, G. Delette, M. Hubert, P. Cloetens, T. Le Bihan, and J. Debayle, “Stochastic geometrical modeling of solid oxide cells electrodes validated on 3D reconstructions,” *Computational Materials Science*, vol. 143, pp. 262–276, 2018.
- [75] J. A. Quiblier, “A new three-dimensional modeling technique for studying porous media,” *Journal of Colloid And Interface Science*, vol. 98, no. 1, pp. 84–102, 1984.
- [76] M. Y. Joshi, *A class of stochastic models for porous media*. PhD thesis, University of Kansas, 1974.
- [77] P. Levitz, “Off-lattice reconstruction of porous media: Critical evaluation, geometrical confinement and molecular transport,” *Advances in Colloid and Interface Science*, vol. 76-77, pp. 71–106, 1998.
- [78] R. Hilfer, “Local Porosity Theory and Stochastic Reconstruction for Porous Media,” *Statistical Physics and Spatial Statistics*, pp. 203–241, 2000.
- [79] M. E. Kainourgiakis, E. S. Kikkinides, T. A. Steriotis, A. K. Stubos, K. P. Tzevelekos, and N. K. Kanellopoulos, “Structural and transport properties of alumina porous membranes from process-based and statistical reconstruction techniques,” *Journal of Colloid and Interface Science*, vol. 231, no. 1, pp. 158–167, 2000.
- [80] G. Matheron, *Random sets and integral geometry*. Wiley New York, 1975.
- [81] J. Serra, “The Boolean model and random sets,” *Computer Graphics and Image Processing*, vol. 12, no. 2, pp. 99–126, 1980.
- [82] D. Jeulin, “Random texture models for material structures,” *Statistics and Computing*, vol. 10, no. 1, pp. 121–132, 2000.
- [83] C. L. Yeong and S. Torquato, “Reconstructing random media,” *Physical Review E - Statistical Physics, Plasmas, Fluids, and Related Interdisciplinary Topics*, vol. 57, no. 1, pp. 495–506, 1998.

- [84] S. Torquato, *Random heterogeneous materials: microstructure and macroscopic properties*. Springer Science & Business Media, 1 ed., 2013.
- [85] P. A. Rikvold and G. Stell, “Porosity and specific surface for interpenetrable-sphere models of two-phase random media,” *The Journal of Chemical Physics*, vol. 82, no. 2, pp. 1014–1020, 1985.
- [86] B. Lu and S. Torquato, “N-Point Probability Functions for a Lattice Model of Heterogeneous Media,” *Physical Review B*, vol. 42, no. 7, pp. 4453–4459, 1990.
- [87] C. L. Yeong and S. Torquato, “Reconstructing random media. II. Three-dimensional media from two-dimensional cuts,” *Physical Review E - Statistical Physics, Plasmas, Fluids, and Related Interdisciplinary Topics*, vol. 58, no. 1, pp. 224–233, 1998.
- [88] C. Manwart, S. Torquato, and R. Hilfer, “Stochastic reconstruction of sandstones,” *Physical Review E - Statistical Physics, Plasmas, Fluids, and Related Interdisciplinary Topics*, vol. 62, no. 1 B, pp. 893–899, 2000.
- [89] N. Sheehan and S. Torquato, “Generating microstructures with specified correlation functions,” *Journal of Applied Physics*, vol. 89, no. 1, pp. 53–60, 2001.
- [90] Y. Jiao, F. H. Stillinger, and S. Torquato, “Modeling heterogeneous materials via two-point correlation functions: Basic principles,” *Physical Review E - Statistical, Nonlinear, and Soft Matter Physics*, vol. 76, no. 3, pp. 1–37, 2007.
- [91] Y. Jiao, F. H. Stillinger, and S. Torquato, “Modeling heterogeneous materials via two-point correlation functions. II. Algorithmic details and applications,” *Physical Review E - Statistical, Nonlinear, and Soft Matter Physics*, vol. 77, no. 3, pp. 1–35, 2008.
- [92] V. Sundararaghavan, “Reconstruction of three-dimensional anisotropic microstructures from two-dimensional micrographs imaged on orthogonal planes,” *Integrating Materials and Manufacturing Innovation*, vol. 3, no. 1, pp. 1–11, 2014.
- [93] Y. Suzue, N. Shikazono, and N. Kasagi, “Micro modeling of solid oxide fuel

- cell anode based on stochastic reconstruction,” *Journal of Power Sources*, vol. 184, no. 1, pp. 52–59, 2008.
- [94] A. Hasanabadi, M. Baniassadi, K. Abrinia, M. Safdari, and H. Garmestani, “3D microstructural reconstruction of heterogeneous materials from 2D cross sections: A modified phase-recovery algorithm,” *Computational Materials Science*, vol. 111, pp. 107–115, 2016.
- [95] A. Hasanabadi, M. Baniassadi, K. Abrinia, M. Safdari, and H. Garmestani, “Optimization of solid oxide fuel cell cathodes using two-point correlation functions,” *Computational Materials Science*, vol. 123, pp. 268–276, 2016.
- [96] H. Izadi, M. Baniassadi, A. Hasanabadi, B. Mehrgini, H. Memarian, H. Soltanian-Zadeh, and K. Abrinia, “Application of full set of two point correlation functions from a pair of 2D cut sections for 3D porous media reconstruction,” *Journal of Petroleum Science and Engineering*, vol. 149, no. October 2016, pp. 789–800, 2017.
- [97] A. Hasanabadi, M. Baniassadi, K. Abrinia, M. Safdari, and H. Garmestani, “Optimal combining of microstructures using statistical correlation functions,” *International Journal of Solids and Structures*, vol. 160, pp. 177–186, 2019.
- [98] M. Baniassadi, H. Garmestani, D. S. Li, S. Ahzi, M. Khaleel, and X. Sun, “Three-phase solid oxide fuel cell anode microstructure realization using two-point correlation functions,” *Acta Materialia*, vol. 59, no. 1, pp. 30–43, 2011.
- [99] M. Armstrong, A. Galli, H. Beucher, G. Le Loc’h, D. Renard, B. Doligez, R. Eschard, and G. F., *Plurigaussian simulations in geosciences*. Springer Science & Business Media, 1 ed., 2011.
- [100] L. Mosser, O. Dubrulle, and M. J. Blunt, “Reconstruction of three-dimensional porous media using generative adversarial neural networks,” *Physical Review E*, vol. 96, no. 4, 2017.
- [101] G. Le Loc’h and A. Galli, “A. Truncated Plurigaussian method: theoretical and practical points of view,” *Proc. Geostatistics Int. Conf., Wollongong 96*, no. 1, pp. 211–222, 1997.

- [102] M. Neumann, M. Osenberg, A. Hilger, D. Franzen, T. Turek, I. Manke, and V. Schmidt, “On a pluri-Gaussian model for three-phase microstructures, with applications to 3D image data of gas-diffusion electrodes,” *Computational Materials Science*, vol. 156, no. October 2018, pp. 325–331, 2019.
- [103] N. A. Siddique and F. Liu, “Process based reconstruction and simulation of a three-dimensional fuel cell catalyst layer,” *Electrochimica Acta*, vol. 55, no. 19, pp. 5357–5366, 2010.
- [104] A. Ali, X. Wen, K. Nandakumar, J. Luo, and K. T. Chuang, “Geometrical modeling of microstructure of solid oxide fuel cell composite electrodes,” *Journal of Power Sources*, vol. 185, no. 2, pp. 961–966, 2008.
- [105] B. Kenney, M. Valdmanis, C. Baker, J. G. Pharoah, and K. Karan, “Computation of TPB length, surface area and pore size from numerical reconstruction of composite solid oxide fuel cell electrodes,” *Journal of Power Sources*, vol. 189, no. 2, pp. 1051–1059, 2009.
- [106] Q. Cai, C. S. Adjiman, and N. P. Brandon, “Modelling the 3D microstructure and performance of solid oxide fuel cell electrodes: Computational parameters,” *Electrochimica Acta*, vol. 56, no. 16, pp. 5804–5814, 2011.
- [107] A. Bertei, H. W. Choi, J. G. Pharoah, and C. Nicolella, “Percolating behavior of sintered random packings of spheres,” *Powder Technology*, vol. 231, pp. 44–53, 2012.
- [108] F. L. E. Usseglio-Viretta, A. Colclasure, A. N. Mistry, K. P. Y. Claver, F. Pouraghajan, D. P. Finegan, T. M. M. Heenan, D. Abraham, P. P. Mukherjee, D. Wheeler, P. Shearing, S. J. Cooper, and K. Smith, “Resolving the Discrepancy in Tortuosity Factor Estimation for Li-Ion Battery Electrodes through Micro-Macro Modeling and Experiment,” *Journal of The Electrochemical Society*, vol. 165, no. 14, pp. A3403–A3426, 2018.
- [109] B. L. Trembacki, A. N. Mistry, D. R. Noble, M. E. Ferraro, P. P. Mukherjee, and S. A. Roberts, “Editors’ Choice—Mesoscale Analysis of Conductive Binder Domain Morphology in Lithium-Ion Battery Electrodes,” *Journal of The Electrochemical Society*, vol. 165, no. 13, pp. E725–E736, 2018.
- [110] N. Siddique, A. Salehi, and F. Liu, “Stochastic reconstruction and electrical

- transport studies of porous cathode of Li-ion batteries,” *Journal of Power Sources*, vol. 217, pp. 437–443, 2012.
- [111] M. M. Forouzan, C. W. Chao, D. Bustamante, B. A. Mazzeo, and D. R. Wheeler, “Experiment and simulation of the fabrication process of lithium-ion battery cathodes for determining microstructure and mechanical properties,” *Journal of Power Sources*, vol. 312, pp. 172–183, 2016.
- [112] I. Srivastava, D. S. Bolintineanu, J. B. Lechman, and S. A. Roberts, “Controlling binder adhesion to impact electrode mesostructures and transport,” *ACS Applied Materials and Interfaces*, vol. 12, no. 31, pp. 34919–34930, 2020.
- [113] L. Mosser, O. Dubrulle, and M. J. Blunt, “Stochastic Reconstruction of an Oolitic Limestone by Generative Adversarial Networks,” *Transport in Porous Media*, vol. 125, no. 1, pp. 81–103, 2018.
- [114] T. Mitchell, *Machine learning*. Burr Ridge, IL: McGraw Hill, 1997.
- [115] A. Geron, *Hands-on machine learning with Scikit-Learn and TensorFlow: concepts, tools, and techniques to build intelligent systems*. Sebastopol, CA: O’Reilly Media, 2017.
- [116] F. Rosenblatt, “The Perceptron, a perceiving and recognizing automaton,” tech. rep., Cornell Aeronautical Laboratory, Inc, 1957.
- [117] K. Hornik, “Multilayer Feedforward Networks,” *Neural Networks*, vol. 2, pp. 359–366, 1989.
- [118] Y. Lecun, Y. Bengio, and G. Hinton, “Deep learning,” *Nature*, vol. 521, no. 7553, pp. 436–444, 2015.
- [119] D. E. Rumelhart, G. E. Hinton, and R. J. Williams, “Learning Representations by Back-Propagating Errors,” *Letters to Nature*, vol. 323, pp. 533–536, 1986.
- [120] Y. Lecun, “A Theoretical Framework for Back-Propagation,” *Proceedings of the 1988 Connectionist Models Summer School*, pp. 21–28, 1988.
- [121] Y. Lecun, L. Bottou, G. B. Orr, and K.-R. Muller, “Efficient BackProp,” in *Neu-*

- ral Networks: Tricks of the Trade. Lecture Notes in Computer Science* (M. G., G. Orr, and K. Müller, eds.), vol. 7700, Berlin, Heidelberg: Springer, 2012.
- [122] L. Bottou, “Large-Scale Machine Learning with Stochastic Gradient Descent,” *Proceedings of COMPSTAT’2010*, pp. 177–186, 2010.
- [123] B. A. Krizhevsky, I. Sutskever, and G. E. Hinton, “ImageNet Classification with Deep Convolutional Neural Networks,” *Communications of the ACM*, vol. 60, no. 6, pp. 84–90, 2017.
- [124] I. Goodfellow, “NIPS 2016 tutorial: Generative adversarial networks,” *pre-print*, 2016. arXiv:1701.00160 [stat.ML].
- [125] I. Goodfellow, Y. Bengio, and A. Courville, *Deep Learning*. Cambridge, MA, USA: MIT Press, 2016.
- [126] B. Frey, *Graphical models for machine learning and digital communication*. Cambridge, MA, USA: MIT Press, 1998.
- [127] G. Deco and W. Brauer, “Higher Order Statistical Decorrelation without Information Loss,” *Advances in Neural Information Processing Systems 7*, vol. c, pp. 247–254, 1995.
- [128] L. Dinh, J. Sohl-Dickstein, and S. Bengio, “Density estimation using real NVP,” *5th International Conference on Learning Representations, ICLR 2017 - Conference Track Proceedings*, 2017.
- [129] A. van den Oord, S. Dieleman, H. Zen, K. Simonyan, O. Vinyals, A. Graves, N. Kalchbrenner, A. Senior, and K. Kavukcuoglu, “WaveNet: A Generative Model for Raw Audio,” pp. 1–15, 2016.
- [130] D. P. Kingma and M. Welling, “Auto-encoding variational bayes,” *2nd International Conference on Learning Representations, ICLR 2014 - Conference Track Proceedings*, no. ML, pp. 1–14, 2014.
- [131] I. Goodfellow, J. Pouget-Abadie, M. Mirza, B. Xu, D. Warde-Farley, S. Ozair, A. Courville, and Y. Bengio, “Generative Adversarial Networks,” *pre-print*, pp. 1–9. arXiv:1406.2661 [stat.ML].
- [132] A. Radford, L. Metz, and S. Chintala, “Unsupervised representation learning with deep convolutional generative adversarial networks,” *4th Interna-*

- tional Conference on Learning Representations, ICLR 2016 - Conference Track Proceedings*, pp. 1–16, 2016.
- [133] J. T. Springenberg, A. Dosovitskiy, T. Brox, and M. Riedmiller, “Striving for simplicity: The all convolutional net,” *3rd International Conference on Learning Representations, ICLR 2015 - Workshop Track Proceedings*, pp. 1–14, 2015.
- [134] D. P. Kingma and J. L. Ba, “Adam: A method for stochastic optimization,” *3rd International Conference on Learning Representations, ICLR 2015 - Conference Track Proceedings*, pp. 1–15, 2015.

Chapter 3

A Pore Network Model for electrochemical energy storage devices

3.1 Abstract

A computationally efficient pore network model has been developed to incorporate the transport and electrochemical phenomena occurring within porous electrodes. The Mixed-Cell method commonly implemented in Pore Network Models (PNMs) was extended to include a reactive and electrophoretic term at each pore. A fully explicit Euler scheme was implemented in the time-dependent iterative algorithm to estimate the concentration and potential profile within the electrode at different times. This PNM is evaluated on a synthetic cubic structure developed with the open-source software OpenPNM to represent a carbon paper commonly used in electrochemical devices. The proposed model was implemented over the hypothetical cubic structure to simulate the negative half-cell of a Vanadium Redox Flow Battery (VRFB). The estimated electrode potential for the negative electrode at 400 A m^{-2} and average overpotentials at galvanostatic discharge at discharge at 400 A m^{-2} were compared with a 2D continuum model presented by You *et al.*¹ previously validated with experimental data under the same conditions. This comparison showed that the present PNM model returns an absolute average error of 3% for the half-cell potentials and of 4% for the overpotentials, which proves the validity of the model.

3.2 Background

3.2.1 Transport modelling through porous media

The development of improved electrodes for electrochemical energy storage and energy conversion technologies is essential for the design of next generation battery technologies. Due to their importance in energy storage systems, understanding the multi-transport processes that occur within electrodes is crucial in order to improve their durability and aid in the design of more optimum systems.²⁻⁴ It has been experimentally proved that an improvement in the electrode structures would lead to an increase in the cell performance. However, experimentation can be time consuming, expensive, and hard to optimise. For this reason, it has become of high interest to develop mathematical models that can represent the multi-transport processes within electrodes.

Whether considering batteries or fuel cells, electrodes are constituted by porous materials, therefore modeling the reactive and transport processes within them is considered a non-trivial problem. Over the years, various mathematical techniques have been proposed to simulate the flow and transport phenomena through porous media. The three most commonly used approaches that have been proposed are: continuum models, direct numerical simulations (DNSs), and pore network models (PNMs).⁵ In continuum models, microstructural properties are averaged over a sample volume assumed to be representative. Based on this, velocity and pressure profiles are then defined by phenomenological relationships, and finally transport equations are solved with numerical discretisation methods.^{5,6} DNS approaches perform simulations over the complex pore geometry obtained directly from X-ray computed tomography (X-CT) images. The porous microstructure is represented as a mesh over which discretisation methods (finite volumes or finite elements) or particle-based methods (SPH or LBM) can be implemented to solve the governing equations.^{7,8} In the case of PNMs the porous medium is represented as a simplified network of interconnected pores and throats.^{9,10} In these models, the details of individual pores are ignored, but the complete topology of the pore space is represented.⁶

Comparison of the three computational methods for transport modeling through porous media

Previous authors have performed comparisons between the three types of modeling techniques to simulate the same porous system. Rebai and Prat compared a continuum model with a PNM to describe the two-phase flow in a gas diffusion layer. They outlined the shortcomings associated with continuum models which lead to a poor approximation of water distribution.⁵ These problems are due to the lack of length scale separation and are rooted in the assumption of the existence of a Representative Elementary Volume (REV) much smaller than the porous domain. In this context, García-Salaberry *et al.* used the LBM to compute the effective mass transport properties in different carbon fibre papers (CFPs) and concluded that the macro-homogeneous models of CFPs can lead to non-negligible errors in their predictions.¹¹ One major conclusion of this work is that a CFP medium is too heterogeneous to be treated as a continuum, mainly attributed to their very small thickness. Additionally, they conclude that a REV cannot be defined in CFPs due to the lack of a well-defined separation between pore and volume-averaged scales. These conclusions are in agreement with the findings of Rebai and Prat.⁵

To compare pore-scale models, Yang *et al.* used a ‘benchmark’ 3D problem to perform comparative flow and solute transport simulations of four different modelling approaches: FVM (grid-based), LBM, SPH (particle-based) and PNM.⁶ Quantitative comparisons between the models yielded similar pore-scale velocities and macroscopic properties (*i.e.* permeability, breakthrough curves, effective dispersivity). Among the conclusions reached in all the studies mentioned here, is that PNM demonstrate a far superior computational efficiency relative to DNSs due to their ability to simplify microstructure and electrode topography (in the comparison made by Yang *et al.* the benchmark problem was solved in 61.07 h using an LBM approach on two TESLA® K40c GPU supercomputers while solving a PNM on a standard Intel® Core i7-4790 CPU only took 45 s).^{6,9} These methods are implemented to solve the flow and transport processes through porous media. However, they have recently been extended to analyse components of electrochemical systems, such as battery electrodes and gas diffusion layers in fuel cells.

The following section shows an application of these methods in an electrochemical context.

Examples of application of transport modelling to electrochemical systems

A first approach for analysing multiphase flow in electrochemical systems at a pore-scale was presented by Park *et al.*¹², who proposed a microscopic model based on the LBM to analyse the two-phase flow distribution in the GDL of a PEM fuel cell.¹² The authors implemented a LBM to investigate the effect of the tow orientation carbon fibres and the effective permeability in a carbon-based GDL. Gostick *et al.* presented a less computationally expensive model consisting of a PNM for analysing water formation in the GDL of a PEM fuel cell.¹³ The authors outline a methodology for representing the microstructural properties of SGL 10BA and Toray 090, commonly used as materials for SGL, through a cubic PNM framework. This approach is able to represent the experimental data of permeability and diffusivity with accuracy; nonetheless, it does not represent the actual topology of the porous materials. The advantage of this method lies in the ease with which it can be combined with a macroscopic model of a complete fuel cell. As an extension of this work, Aghighi *et al.* implemented a microscopic model coupled with a macroscopic one to model a complete PEM fuel cell.¹⁴ In their work, the multiphase transport of species in the GDL is modeled as a PNM and a continuous model is applied for representing the membrane and electrode catalyst layer.

In recent years, interest has surged to investigate the transport processes in carbon based electrodes for VRFBs at a pore-scale level. Banerjee *et al.* implemented a PNM to model the multiphase flow of electrolyte in carbon fibre electrodes. This work analyses the transient permeation of electrolyte in different types of commercially available CFPs.¹⁵ Qiu *et al.* extended the applicability of microscale models to analyse the effect of real microstructure in the mass and reactive transport processes within porous electrodes.^{16,17} In their work, the LBM is used to solve the flow equations and with the resulting flow, alongside the FVM, the mass transport processes are simulated over a real X-CT image.

3.3 Model development

The present work outlines, a novel method for implementing a PNM approach to study the multiphysics involved in porous electrodes. In addition to accounting for flow characteristics and reactive transport processes, this model examines pore current and electrolyte concentration at different overpotentials.

The PNM approach introduced in this work comprises three main steps:

1. The pore network structure is generated as a cubic synthetic representation provided by OpenPNM¹⁸ to obtain the pore-scale topology of the network.
2. The pressure and velocity profiles are calculated by solving the Stokes flow equation in each pore
3. The velocity field is integrated with the mass and charge transport equations to obtain the concentration and potential field across the network.

An iterative algorithm is proposed in order to simultaneously solve the coupled potential and species concentration at each pore with the concentration and potential being simultaneously updated until a convergence limit is achieved. As these are dynamic simulations, this procedure is repeated at each time-step.

In the following sections, and indeed throughout the rest of the chapter, terms contained within figure 3.1 will be referred to in the derivations and discussions.

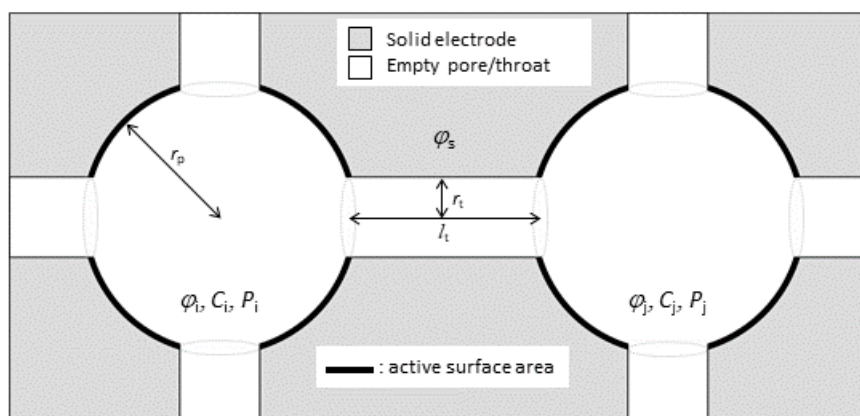


Figure 3.1: Electrochemical and geometric properties of the pore network model.

3.3.1 Fluid transport

In a PNM configuration, the flow field is solved by estimating the flow at each of the throats in the network. As previously described^{19,20}, the flow through each throat is analogous to the analytical solution of the steady-state Navier–Stokes equation for the flow through a pipe given that the flow is considered to be at low Reynolds number (*i.e.* $Re \ll 1$). The pressure and velocity fields are obtained by assuming a single pressure P_i at each pore i , and enforcing a volume balance over each pore, as describe by equation 3.1

$$\sum_{j=1}^{Nth} q_{ij} = \sum_{j=1}^{Nth} g_{h,ij} (P_i - P_j) = 0 \quad (3.1)$$

where q_{ij} is the flow between pores i and j , $g_{h,ij}$ is the hydraulic conductivity of the throat connecting pores i and j , and Nth is the total number of throats connected to pore i .

The hydraulic conductivity ($g_{h,ij}$) represents the resistance towards the electrolyte flowing from one pore to another imposed by the geometry of the throat. It is dependent on the size and length of the throat and will vary depending on the shape of the throat's cross-sectional area. In this work, the throat geometry is assumed to be cylindrical, and thus the hydraulic conductivity is defined as:

$$g_{h,ij} = \frac{\phi r_t^4}{8\mu L} \quad (3.2)$$

where r_t corresponds to the cross-sectional radius, L is the length of the throat, and μ the viscosity of the electrolyte. Equation 3.2 is true for a system in which throats are cylindrical, however these parameters can be changed to have throats of different shapes.

The development of the flow equations are based on the following assumptions:

- The electrolyte consists of a single-phase, Newtonian, incompressible fluid;
- The fluid in the bulk is under creeping flow conditions (*i.e.* $Re \ll 1$);

- The electrolyte viscosity is constant throughout the electrode and indeed throughout the dynamic simulation;
- The pores are considered to be spheres and the throats are cylindrical.

3.3.2 Mass transport

A mixed-cell-method has been previously introduced for solving the convective-diffusive-reactive transport of species in a pore network model.^{19–24} This method is based on the assumption that the concentration of species at the bulk of the pore is the same throughout the extent of the pore. Based on the same principle that derived the MCM for reactive transport, this work derives a method for obtaining the transient distribution of species within the electrode. The transport of species is determined by diffusion, convection and two additional terms are introduced: one due to electrophoretic transport called migration, and a source term due to electrochemical reaction. This model is based on the following assumptions:

- The dilute solution approximation is considered in the transport of species through the porous phase. This assumption implies that the concentrations of species are low enough that their fluxes do not have an impact on the flow of the solvent;
- Given that this model is a pore-scale model, the concentration of species l at the bulk of each pore (c_b^l) is considered to be the same as the concentration at the boundary of the active surface area (c_s^l).

The second assumption can be changed through the implementation of a mass transport coefficient that relates the bulk concentration with the concentration at the surface.

The transport of species due to convection, diffusion, migration and electrochemical reaction at each pore is obtained by performing a volumetric integral of the mass balance over each pore i . The resulting equation is a modification of the MCM, defined as:

$$V_{p_i} \frac{dc_i^l}{dt} = \sum_{j=1}^{N_{th,q<0}} c_i^l q_{ij} + \sum_{j=1}^{N_{th,q>0}} c_j^l q_{ij} + \sum_{j=1}^{N_{th}} D_e A_{ij} \frac{c_j^l - c_i^l}{L_{ij}} + \sum_{j=1}^{N_{th}} z_l D_e c_i A_{ij} \frac{F}{RT} \frac{\phi_j - \phi_i}{L_{ij}} + S(c_i) \quad (3.3)$$

where V_{p_i} is the volume of pore i ; c_i^l the concentration of species l in pore i ; q_{ij} , L_{ij} and A_{ij} the flow rate, length and cross-sectional area of the throats connecting pores i and j , respectively, and D_e corresponds to the effective diffusivity of the porous media. Given that the model is a pore-scale model, the tortuosity and porosity are considered directly in the topology of the network. Therefore, D_e reduces to the diffusion coefficient D_l for each component in the electrolyte.

The first two terms on the RHS of equation 3.3, represent the convective transport into and out of each pore; the third term on the RHS shows the transport due to diffusion, the fourth term represents the migration due to electrophoretic transport of species; and S represents the source/sink term in concentration due to the electrochemical reaction. For the reduced active species, the source term is defined as i_{BV}/F and for the oxidised active species the source term is defined as $-i_{BV}/F$. In both cases i_{BV}/F is the transfer current obtained from the Butler–Volmer equation, as explained in the following subsection.

Electrochemical reaction

In equation 3.3, the last term of the RHS corresponds to the source/sink term, which represents the flux of species l over the active surface area of the pore. The formation/consumption of species at the active area (pore wall) is determined by the current (i_{BV}/F) transferred at each pore, given by the Butler-Volmer equation:

For the anode:

$$i_{BV,a} = i_{0,a} \left[\exp \left(\frac{(1 - \alpha_a) z F \eta}{RT} \right) - \exp \left(\frac{-\alpha_a z F \eta}{RT} \right) \right] \quad (3.4)$$

For the cathode:

$$i_{BV,c} = i_{0,c} \left[\exp \left(\frac{(1 - \alpha_c) z F \eta}{RT} \right) - \exp \left(\frac{-\alpha_c z F \eta}{RT} \right) \right] \quad (3.5)$$

where α_a and α_c are the anodic and cathodic charge transfer coefficients for the electrochemical reaction taking place, z is the number of electrons involved in the reaction, i_0 is the exchange current at each pore in the anode, defined as:

For the anode:

$$i_{0,a} = S_A F k_a (c_R)^{(1-\alpha_a)} (c_{Ox})^{\alpha_a} \quad (3.6)$$

For the cathode:

$$i_{0,c} = S_A F k_c (c_R)^{(1-\alpha_c)} (c_{Ox})^{\alpha_c} \quad (3.7)$$

where k_a and k_c are the reaction rate constants for the electrochemical heterogeneous reaction, c_R and c_{Ox} are the concentration of species in their reduced and oxidised form respectively, and S_A is the active specific surface area of each pore. It must be pointed out that, unless the system is a symmetric cell, species c_R and c_{Ox} are not the same in the anode and in the cathode, and they will depend on the system. The activation overpotential due to the electrochemical reaction is defined as:

$$\eta = \phi_s - \phi_e - E \quad (3.8)$$

where $\phi_s - \phi_e$ represents the potential difference between the solid phase and the electrolyte; E represents the equilibrium potentials calculated with the Nernst equation:

$$E = E^0 + \frac{RT}{F} \ln \left(\frac{c_{Ox}}{c_R} \right) \quad (3.9)$$

where E^0 denotes the standard equilibrium potential of the redox couple involved in the reaction.

The concentration applied in the Butler-Volmer equation²⁵ (equations 3.4 and 3.5) corresponds to the concentration of electrolyte at the active solid interface. Since the surface concentration (c'_s) differs from the bulk concentration (c'_b), a mathematical expression must exist which relates both values. Shah *et al.*²⁵ introduce a modified Butler-Volmer equation that represents a linear dependence for the bulk concentration on the surface concentrations.²⁵ This concentration

gradient between the surface and the bulk can also be accounted for by solving the steady-state mass transport and stokes equation inside each pore. The finite volume method is applied, imposing a boundary condition of concentration at the walls, similar to the procedure defined by Tansey *et al.*²⁰

As stated in the model assumptions, the distribution of species defined in this model are based on the MCM since it is a pore-scale model, therefore the concentration of species at the bulk of each pore is considered to be the same as the concentration at the boundary of the active surface area ($c_b^l = c_s^l$).

3.3.3 Charge transport

Analogous to the methodology followed to obtain the mass transport of species at each pore, a model is proposed to obtain the transport of charge through the network. In a two-phase porous electrode, such as carbon-based electrodes for RFBs, the current is produced within the two phases, namely the electrolyte (ionic current) occupying the porous phase and the solid matrix (electronic current). The method presented in this work for obtaining the transport of charge across the network is based on the following assumptions:

- The solution is electrically neutral;
- The dilute solution approximation is applicable for ionic species within the porous media;²⁶
- The solid matrix is highly conductive, compared to the electrolyte flowing through the porous phase. The potential difference across the solid matrix is therefore negligible ($\nabla\phi_s = 0$).

According to Newman *et al.*²⁷, in a diluted electrolytic solution, the current produced due to the motion of charged particles is obtained by adding the mass fluxes of each of the electroactive species, multiplied by the Faraday constant:

$$\mathbf{i} = F \sum_l^{nc} z_l N_l \quad (3.10)$$

where \mathbf{i} is the current density, $z_l F$ is the charge per mole, nc is the number of electroactive species in solution, and N_l represents the flux of species l in and out

of the system, determined by the Nernst-Plank equation (2.13).

In a similar way, the charge conservation equation is obtained by multiplying Fz_l to each term in the mass conservation equation, and adding the contributions from each of the charged species in solution:

$$\frac{\partial}{\partial t} F \sum_l^{nc} z_l c_l = -\nabla \cdot F \sum_l^{nc} z_l N_l + F \sum_l^{nc} z_l S_l \quad (3.11)$$

The solution is considered to be electrochemically neutral, (*i.e.* $\sum_l z_l N_l = 0$); thus, the term on the L.H.S of equation (3.11) is null, and the convective flux in the Nernst-Plank equation substituted in equations (3.10) and (3.11) is also null. These simplifications lead to an expression of charge conservation in which no accumulation term exists, *i.e.* , the sum of charge transported by migration due to a potential difference into/out of one pore (corresponding to the first term on the RHS of equation 3.11) must be equal to the charge transferred outside the pore into the solid matrix due to the electrochemical reaction (corresponding to second term on the RHS of equation 3.11).

$$\nabla \cdot F \sum_l^{nc} z_l N_l = F \sum_l^{nc} z_l S_l \quad (3.12)$$

The L.H.S term corresponds to the current transfer per unit volume due to the potential (migration) and concentration gradients (diffusion) between pores, defined as:

$$i_t = -\nabla \cdot \left[F^2 \nabla \phi \sum_l^{nc} z_l^2 \frac{D_l c_l}{RT} + F \sum_l^{nc} D_l \nabla c_l \right] \quad (3.13)$$

The R.H.S. term in equation (3.12) accounts for the current transport due to the faradaic transfer of charge from the electrolytic solution into the electrode matrix. This source term is determined by the B-V equation, as defined in eq. 3.4 and 3.5, and thus is dependent on the overpotential at each pore.

To obtain an expression analogous to the MCM for the charge transport at each pore, a volumetric integral of equation (3.13) is performed. The resulting expression represents the charge transfer into/out of each pore due to a potential

difference between pores:

$$i_t = -F \sum_l^{nc} z_l \left[z_l D_l c_i^l \frac{F}{RT} \left[\sum_j^{N_{th}} A_{ij} \frac{\phi_j - \phi_i}{L_{ij}} \right] + D_l \left[a_{ij} \frac{c_j^l - c_i^l}{L_{ij}} \right] \right] \quad (3.14)$$

where c_i^l is the concentration of species l in pore i , ϕ_i is the potential of the electrolyte in pore i ; L_{ij} and A_{ij} are the length and cross-sectional area of the throats connecting pores i and j respectively.

3.4 Boundary conditions

This section presents the available boundary conditions that can be implemented in the present model to solve the equations of flow, mass and current transport defined in the previous section. The implementation of each boundary condition is determined by the specifications of the system studied.

3.4.1 Boundary conditions for flow transport

The flow of electrolyte is driven by a pressure gradient across the electrolyte. To determine the electrolyte flow profiles across the network, two possible boundary conditions can be established:

- Case I: The flow of electrolyte is driven by a pressure gradient between the inlet and outlet pressures. Thus, constant pressures are specified at the inlet (P_{in}) and outlet (P_{out}) pores as Dirichlet boundary conditions.
- Case II: A fixed flux is established at the inlet or outlet, and a Dirichlet boundary of pressure on the opposite side.

The first case is more convenient since the inlet and outlet pressures are usually known variables.

3.4.2 Boundary conditions for species transport

In all cases, an assumption of constant concentration at the inlet pores is established. For the outlet pores, the following conditions can be implemented to obtain

the concentration profiles across the network:

- Case I: The concentrations at the inlet and outlet pores boundaries are fixed as Dirichlet boundaries and unchanged throughout the simulation. This assumption is valid for the cases in which the conversion of species is known and therefore the concentration of species at the inlet and outlet pores are set constant.
- Case II: A Dirichlet boundary is established at the inlet pores and a Newman boundary condition of zero diffusive flux out of the system is established at the outlet throats. This condition must be implemented for the cases in which there is no information available regarding the conversion of species.

3.4.3 Boundary conditions for charge transport

The cell can be considered to be operated at either potentiostatic or galvanostatic conditions. For the case of a potentiostatic operation, electrolyte potentials are fixed at the inlet and outlet pores as Dirichlet boundaries, and the electrolyte potential in each pore across the network is recalculated at every time-step in the transient concentration. For the case in which the cell is assumed to be operating under galvanostatic conditions, the potentials at one of the walls are fixed as a Dirichlet boundary and the potentials at the other wall are recalculated iteratively to fit the external current density applied to the electrode (*i.e.* $\phi_s = 0$). A constant distribution of potential along the solid matrix is considered, since the fibre is assumed to be significantly more conductive than the electrolyte. This assumption is based on the experimental data presented by Gandomi *et al.* .²⁶

3.5 Iterative algorithm

This section presents the main steps involved in the algorithm for implementing the PNM framework proposed in this work to solve the coupled mass and charge transport equations that occur at the pore phase within the electrode. This process consists of three main steps:

First step

The steady-state Stokes flow equation is implemented to obtain the pressure and flow field across the network. For this, a successive over-relaxation (SOR) method is used to solve the system of linear equations, given by equation 3.1. Since the velocity field only depends on the geometrical topology of the microstructure, a steady-state pressure drop is assumed throughout the transient concentration simulation. The pressure difference between the inlet and outlet is specified such that the $Re \ll 1$ and the resulting average velocity was comparable to the values used in continuum models.

Second step

Once the flow field along all throats is estimated, and iterative algorithm is implemented to compute the transient distribution of concentrations throughout the network. This algorithm is iterative for calculating the potentials at each pore and explicit for calculating the concentration at each time-step. For this, an explicit Euler scheme was implemented for discretising equation 3.3 as follows:

$$\begin{aligned}
 c_{i,l}^{n+1} = & c_{i,l}^n + \frac{\Delta t}{V} \left[\sum_{j=1}^{N_{th,q<0}} c_{i,l}^n q_{ij} + \sum_{j=1}^{N_{th,q>0}} c_{j,l}^n q_{ij} \right] + \frac{\Delta t}{V} \left[\sum_{j=1}^{N_{th}} D_l A_{ij} \frac{c_{j,l}^n - c_{i,l}^n}{L_{ij}} \right] \\
 & + \frac{\Delta t}{V} \left[\sum_{j=1}^{N_{th}} z_l D_l c_i^l A_{ij} \frac{F}{RT} \frac{\phi_j^n - \phi_i^n}{L_{ij}} \right] + \frac{\Delta t}{V} \left[\frac{i_{BV}^n}{F} \right]
 \end{aligned} \tag{3.15}$$

From equation 3.15 it is seen that the transport of species between pores is influenced by the migration and source terms, corresponding to the last two terms on the RHS of the equation respectively. This implies that the movement of active species is affected by the electrolyte potential at each pore (*i.e.* in the source term), as well as the electrolyte potential of the neighbouring pores (*i.e.* in the migration term). In order to obtain the distribution of potentials and concentrations across the network, the species and charge transport equations (*i.e.* equations 3.15 and 3.14 respectively) are solved simultaneously for every pore at each time-step. Thus, each time-step will correspond to a specific concentration and potential distribution. For every time-step, the potential distribution is obtained iteratively

with a SOR method, where the error function is defined as the absolute average deviation (AAD) between it and i_{BV} at each pore:

$$AAD = \frac{1}{np} \sum_{i=1}^{np} i_{t,i}^n - i_{BV}^n \quad (3.16)$$

Third step

With the electrolyte potential distribution at each pore, the migration and source terms can be estimated. As a final step, the concentrations at each pore are calculated, providing the concentrations at the next time-step (*i.e.* c_i^{n+1}). With the new concentration profiles, the same iterative process of solving the potentials and updating the concentrations is repeated for the next time-step, until a time limit is achieved. A schematic of the solution algorithm introduced in this work is shown in APPENDIX A.

The convergence criteria for calculating the pressure field is defined as the average residual of the sum of all flows, non-dimensionalised against the total sum of the absolute flows in all throats. This convergence criteria for stopping the simulation is established when the average residual is less than or equal to 1×10^{-12} . The convergence criteria for the potential fields is obtained with the AAD, where the simulation converges when the AAD is less than or equal to 1×10^{-8} A. The implementation of the numerical algorithm requires the following inputs: physical parameters of the electrolyte (e.g. diffusivity, Table 3.1), initial SOC, inlet velocity, outlet pressure, external current density or boundary potentials, input file of the reconstructed pore network with data including pore volume/position and throats radius/length and connecting pores indexes/identities. The program developed in this work is written in C++ and implemented on an HP workstation with the following specifications: Intel® Xeon® CPU E5-166-v3.

3.6 Results and discussion

3.6.1 Verification of the Explicit Euler Scheme

The implementation of a fully explicit Euler scheme for the MCM equation for convective, diffusive, reactive and electrophoretic transport is verified with its corresponding analytical solution. Since the volumetric integral of the transport equation solved at each pore to obtain the MCM equation is analogous to a system of continuous stirred-tank reactors (CSTR), a hypothetical system of 8 pores connected in series by 7 throats is implemented under the following assumptions:

- All pores have the same volume: $V_1 = V_2 = V$.
- All connecting throats have the same cross-section area ($A_{ij} = A$) and length ($L_{ij} = L$), thus the volumetric flow rate between pores is the same for all throats: *i.e.* $Q_{12} = Q_{23} = Q$.
- The potential gradient between pores is equal for all connections: $\Delta\phi_{12} = \Delta\phi_{23} = \Delta\phi$.
- The system is operating under limiting current conditions.
- No diffusive flux out of the pores is considered.
- Dirichlet boundary conditions are assumed at the inlet and outlet pores. The concentration at the inlet pore is set to $C_{in} = 10 \text{ mol} \cdot \text{m}^{-3}$, and the concentration at the outlet pore is $C_{out} = 0 \text{ mol} \cdot \text{m}^{-3}$.

For simplicity, the concentrations c_i^l will be written as c_i . The MCM equation (eq.3.3) for a hypothetical system of pores connected in series is written as:

$$V_i \frac{dc_i}{dt} = c_{i-1}Q_{i,i-1} - c_iQ_{i,i+1} + D_l A \frac{(c_{i-1} - c_i)}{L} + z_l D_l c_i \frac{F}{RT} A \frac{2\Delta\phi}{L} + S(c_i) \quad (3.17)$$

Based on the assumptions stated for this model, equation (3.17) can be rewritten in terms of the characteristic time $\tau = V/Q$ as:

$$\frac{dc_i}{dt} = \frac{1}{\tau} (c_{i-1} - c_i) + D_l A \frac{(c_{i-1} - c_i)}{LV} + z_l D_l c_i \frac{F}{RT} A \frac{2\Delta\phi}{LV} + \frac{S(c_i)}{V} \quad (3.18)$$

since the system is working under limiting current conditions, the source term of equation (3.18) is defined as:

$$S(c_i) = \frac{-i_l \cdot S_A}{F} \quad (3.19)$$

where S_A is the active surface area of each pore, F is the Faraday constant, and i_{lim} is the limiting current:

$$i_{lim} = z_l F k_m c_i \quad (3.20)$$

All constants in equations (3.19) and (3.20) are rearranged and renamed as the following parameters:

$$\alpha = \frac{1}{\tau} + \frac{D_l A}{LV} \quad (3.21)$$

$$\beta = \frac{2z_l D_l F A}{RTL V} \cdot \Delta\phi \quad (3.22)$$

$$\gamma = \frac{z_l k_m S_A}{V} \quad (3.23)$$

$$\lambda = \beta + \alpha + \gamma \quad (3.24)$$

Equation (3.18) is solved analytically as an infinite series, given the following boundary conditions: at $t \geq 0$, $c_0 = 10$. The analytical solution for the concentration of species as a function of the time for the N^{th} pore is:

$$\frac{c_N}{c_0} = \frac{\alpha^N}{\lambda^N} \left(1 - e^{-\lambda t} \sum_{n=1}^N \frac{\lambda^{n-1} t^{n-1}}{(n-1)!} \right) \quad (3.25)$$

Comparison of the analytical solution with the explicit Euler scheme is graphically represented on Figure 3.2

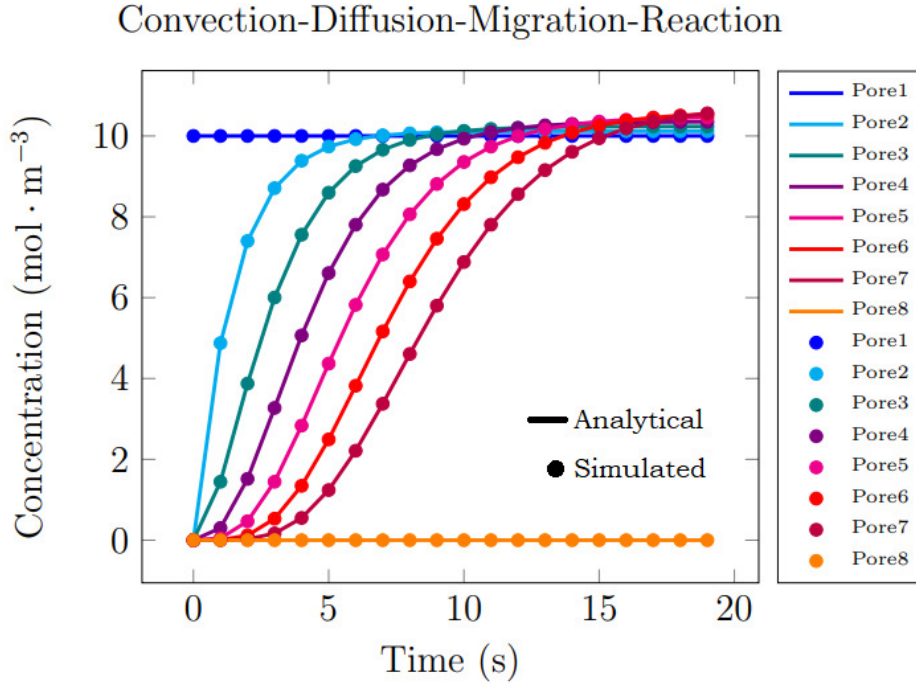


Figure 3.2: Comparison of simulated explicit Euler scheme (dots) and analytical solution (solid line) for convective-diffusive-migration-reactive flow in MCM transport for 8 pores connected in series.

3.6.2 Implementation of the proposed framework in a VRFB

Vanadium chemistries are the most widely studied RFB systems and also most commercially mature.^{28,29} Thus, significant progress in VRFBs cell power density has been made over the last 30 years.³⁰⁻³² In order to prove the PNM framework developed in this work, the anode couple of a VRFB was used.

VRFB electrolyte chemistries utilise all four stable oxidation states available to vanadium. They are V^{2+}/V^{3+} at the negative electrode (anode) and VO^{2+}/VO_2^+ (V^{4+}/V^{5+}) at the positive electrode (cathode). Complicated kinetic and mechanistic equations are omitted in the following simplified electrochemical couples.²⁶

Anode:



Cathode:

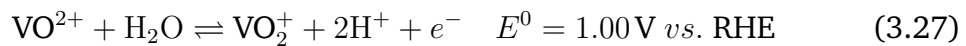


Table 3.1: Physical parameters for the mass transport equation (eq. 3.3) from literature

Parameter	Symbol	Value	Units
Anodic transfer coefficient	α_-	0.5	-
Cathodic transfer coefficient	α_+	0.5	-
Standard reaction rate constant: anode	k_a	1.7×10^7	$\text{m} \cdot \text{s}^{-1}$
Equilibrium potential: anode	$E_{0,a}$	-0.255	V
Temperature	T	298	K
Diffusivity of V(II)	$D_{\text{V(II)}}$	2.4×10^{-10}	$\text{m}^2 \cdot \text{s}^{-1}$
Diffusivity of V(III)	$D_{\text{V(III)}}$	2.4×10^{-10}	$\text{m}^2 \cdot \text{s}^{-1}$

Table 3.1 presents the physical parameters corresponding to the electrochemical reaction undertaken by the redox couple $\text{V}^{2+}/\text{V}^{3+}$ at the anode. These parameters were implemented in the species transport equations defined previously.

To validate the implementation of a PNM approach, a hypothetical network was built using the open-source software OpenPNM¹⁸ to represent the carbon paper electrode, in particular Toray090. The module for building a Toray090 architecture from OpenPNM was previously verified in terms of permeability and diffusivity elsewhere.¹³ The proposed framework was implemented over the hypothetical network to simulate the negative half-cell of a VRFB. The results were compared with the 2D continuum simulation by You *et al.*¹ of the same system under the same conditions. The hypothetical system consisted of 2336 pores and 4048 throats, with an architecture specially designed to preserve the geometric parameters and specific surface area used by You *et al.*^{1,18}. The parameters that define the PNM are given in Table 3.2.

For the purpose of validating the model, a steady-state approach, analogous to the simplified structure presented by Qiu *et al.*¹⁷ is implemented. This methodology is based on the charge conservation between the applied current density (*i.e.* J_{ext}) and the current balance in the network. For the model validation, the following assumptions were made:

- The conductivity of the solid phase is significantly larger than the electrolyte conductivity, and so the loss of current in the solid matrix is ignored (*i.e.* $\nabla \phi_s = 0$);
- The distribution of concentrations across the network is uniform and remains

Table 3.2: Parameters of pore-network model for OpenPNM system

Description	Symbol	Value	Units
Specific surface area	A_e	16,200	m^{-1}
Half-cell width	L	0.003	m
Flow velocity	u_{av}	0.00219	$\text{m} \cdot \text{s}^{-1}$
Average pore size	-	3.90×10^{-15}	m^3
Number of pores	N_p	2336	-
Number of throats	N_t	4048	-
Total vanadium concentration	C_{tot}^0	1500	$\text{m}^3 \cdot \text{s}^{-1}$
External current density	$-J_{ext}$	-400	A
Equilibrium potential	E^0	-0.255	V

constant at each SOC analysed;

- The VRFB is under steady-state conditions;
- The effect of side reactions are negligible;
- Only the half reaction of the negative electrode is considered.

Boundary conditions for flow transport

Dirichlet boundary conditions of pressure were implemented at the inlet and outlet pores to obtain an average velocity of $0.00219 \text{ m} \cdot \text{s}^{-1}$, equivalent to experimental data and the continuum model presented by You *et al.*¹. Both models are hypothetical since the actual morphology is not accounted for, however the continuum model consists of a 2D grid where microstructural parameters are homogenised into effective properties. In the case of the hypothetical PNM, the dimensions of the microstructure (*i.e.* pore and throat diameter) are modified to fit experimental microstructural properties such as permeability and specific surface area.

Boundary conditions for species transport

The concentration of species within each pore was determined by the solution SOC within the electrode, defined as:

$$SOC = \frac{C_{II}}{C^{0-}} \quad (3.28)$$

where C_{II} corresponds to the concentration of V(II), C^{0-} is the total concentration of vanadium species in the electrolyte. Since the system is considered to be

operating under steady-state at each SOC analysed, Dirichlet boundary conditions of concentration were implemented at the inlet and outlet pores.

Boundary conditions for current transport

Given the conditions of a perfect mix due to the mixed-cell method, the potentials in the electrolyte (ϕ_e) represent the potential at the electrode-electrolyte interface. Therefore, a distribution of potentials exists at each state of charge during operation. In order to implement a simulation under galvanostatic conditions to compare against the data gathered by You *et al.*¹, the potential at one boundary of the PNM was set constant, while the potential at the other boundary was calculated iteratively until the calculated external current density ($J_{\text{ext,calc}}$) matched the desired external current density (J_{ext}). The calculated external current density is derived from charge conservation in the network as:

$$J_{\text{ext,calc}} = \frac{\sum_{i=1}^{N_p} i_{\text{BV},i}}{\sum_{i=1}^{N_p} S_{A,i}} \cdot A_e L \quad (3.29)$$

where $S_{A,i}$ is the surface area of pore i , $j_{\text{BV},i}$ is the current at pore i , A_e is the specific surface area of the PNM and L is the electrode thickness or half-cell width. The current at each pore obtained by the Butler-Volmer equation (equation 3.4) *i.e.* i_{BV} must be equal to the current obtained due to transport of charged species (equation 3.14) *i.e.* i_t ; thus, the calculation of the external current density represents a secondary iteration that encompasses the primary iterative algorithm.

The steady-state solution of the pressure and flow fields converged in 4 s, and the coupled charge and species transport distributions converged after 14 min for each time-step in the simulation, using a single core of a HP workstation: Intel® Xeon ® CPU E5-166-v3. The potential difference between the solid phase and the electrolyte (*i.e.* $\phi_s - \phi_e$) represents the potential drop across the electrode active surface. These values are estimated from the numerical algorithm and averaged for all pores to obtain the electrode potential. The overpotential at each pore is calculated with equation 3.8 based on the output data of the potentials and concentration distributions and the equilibrium potentials.

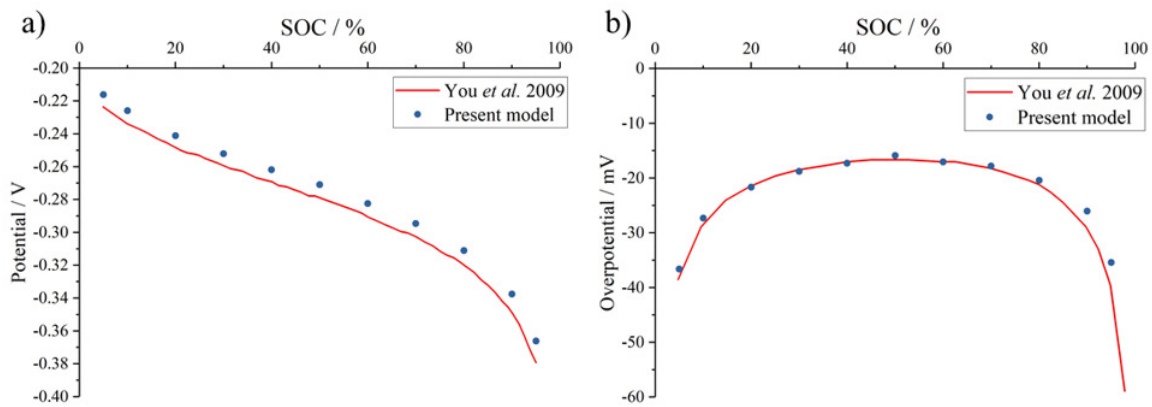


Figure 3.3: Plots showing graphical validation of cell discharge at $400 \text{ A} \cdot \text{m}^2$ compared with literature results [55].

The results of the simulated electrode potentials of the negative half-cell of a VRFB as a function of the SOC for an applied current density of $400 \text{ A} \cdot \text{m}^2$ are shown in Fig. 3.3(a). Fig. 3.3(b) shows the averaged overpotentials of the negative electrode at galvanostatic charge at $400 \text{ A} \cdot \text{m}^2$. The results of the electrode potentials and overpotentials estimated with the PNM approach are compared with the 2D continuum model presented by You *et al.*¹. The results of the 2D continuum model had been previously validated with experimental data with a 1% error, making it reliable for validation purposes. Compared to those results, the present PNM model returns an absolute average error of 3% for the half-cell potentials and of 4% for the overpotentials.

3.7 Conclusions

In this work, a framework based on a pore-network model is introduced to simulate the coupled flow, mass and charge transport that occur within electrodes in electrochemical devices. This work represents a bridge between volume-averaged models that simulate the transport processes in a continuum space, and pore-scale models which perform direct numerical simulations over X-CT reconstructed images.

The main advantage of this model is its ability to visually represent the concentration and current distributions inside the electrode within a low computational time. Although the hypothetical network generated in OpenPNM does

not represent the real topology of the electrode, the pore-size distribution and throat sizes are fitted to the estimated permeability and diffusivity of the real electrode¹³. Therefore this approximation involves more microstructural data than a continuum model where the grid spaces have the same size.

The proposed PNM framework is derived from an MCM approach and uses an explicit Euler scheme for obtaining the transient concentration distributions as a function of convection, diffusion, migration and electrochemical reaction. The methodology was validated with a cubic hypothetical PNM built with OpenPNM representing an anode with a specific surface area of $16,200 \text{ m}^{-1}$. A comparison between the steady-state electrode potential and overpotentials as a function of SOC estimated with the PNM algorithm, and the results presented by You *et al.*¹ show that the values predicted with the present model are consistent with the values reported in the literature for continuum models and experimental results. This proves that the PNM method is a computationally inexpensive pore-scale model that involves microstructural details and is able to reproduce the same results as a continuum model. To the author's knowledge, this work constituted the first one to introduce a PNM to analyse the coupled mass and charge transport equations for a VRFB system.

One drawback of the model is that the idealisation of the microstructure could lead to an over or under estimation of the real surface area. This can be mitigated by fitting the size of the pores to a surface area estimated experimentally. Additionally, in this study, the method has been proved accurate by implementing a hypothetical large cube of pores and throats. However, important conclusions regarding the flow, species and current distribution can be obtained by implementing this method over a PNM extracted from a real microstructure. This will be analysed in the following chapter.

References

- [1] D. You, H. Zhang, and J. Chen, “A simple model for the vanadium redox battery,” *Electrochimica Acta*, vol. 54, no. 27, pp. 6827–6836, 2009.
- [2] M. H. Chakrabarti, N. P. Brandon, S. A. Hajimolana, F. Tariq, V. Yufit, M. A. Hashim, M. A. Hussain, C. T. Low, and P. V. Aravind, “Application of carbon materials in redox flow batteries,” *Journal of Power Sources*, no. 253, pp. 150–166, 2014.
- [3] G. Wei, C. Jia, J. Liu, and C. Yan, “Carbon felt supported carbon nanotubes catalysts composite electrode for vanadium redox flow battery application,” *Journal of Power Sources*, vol. 220, pp. 185–192, dec 2012.
- [4] A. Q. Su, N. F. Wang, S. Q. Liu, T. Wu, and S. Peng, “Modification of Carbon Paper Electrode via Hydrothermal Oxidation Applied in the Vanadium Redox Battery,” *Acta Phys. - Chim. Sin.*, vol. 28, no. 6, pp. 1387–1392, 2012.
- [5] M. Rebai and M. Prat, “Scale effect and two-phase flow in a thin hydrophobic porous layer. Application to water transport in gas diffusion layers of proton exchange membrane fuel cells,” *Journal of Power Sources*, vol. 192, no. 2, pp. 534–543, 2009.
- [6] X. Yang, Y. Mehmani, W. A. Perkins, A. Pasquali, M. Schönherr, K. Kim, M. Perego, M. L. Parks, N. Trask, M. T. Balhoff, M. C. Richmond, M. Geier, M. Krafczyk, L. S. Luo, A. M. Tartakovsky, and T. D. Scheibe, “Intercomparison of 3D pore-scale flow and solute transport simulation methods,” *Advances in Water Resources*, vol. 95, pp. 176–189, 2016.
- [7] M. A. Spaid and F. R. Phelan, “Lattice Boltzmann methods for modeling microscale flow in fibrous porous media,” *Physics of Fluids*, vol. 9, no. 9, pp. 2468–2474, 1997.
- [8] J. Monaghan, “Smoothed particle hydrodynamics,” *Annu. Rev. Astron. Astrophys.*, vol. 30, pp. 543–574, 1992.
- [9] M. J. Blunt, *Multiphase Flow in Permeable Media: A Pore-Scale Perspective*. Cambridge: Cambridge University Press, 1 ed., 2017.
- [10] B. Bijeljic and M. J. Blunt, “Pore-scale modeling of transverse dispersion in porous media,” *Water Resources Research*, vol. 43, no. 12, pp. 1–8, 2007.

- [11] P. A. García-Salaberri, I. V. Zenyuk, A. D. Shum, G. Hwang, M. Vera, A. Z. Weber, and J. T. Gostick, "Analysis of representative elementary volume and through-plane regional characteristics of carbon-fiber papers: diffusivity, permeability and electrical/thermal conductivity," *International Journal of Heat and Mass Transfer*, vol. 127, pp. 687–703, 2018.
- [12] J. Park, M. Matsubara, and X. Li, "Application of lattice Boltzmann method to a micro-scale flow simulation in the porous electrode of a PEM fuel cell," *Journal of Power Sources*, vol. 173, no. 1, pp. 404–414, 2007.
- [13] J. T. Gostick, M. A. Ioannidis, M. W. Fowler, and M. D. Pritzker, "Pore network modeling of fibrous gas diffusion layers for polymer electrolyte membrane fuel cells," *Journal of Power Sources*, vol. 173, pp. 277–290, nov 2007.
- [14] M. Aghighi, M. A. Hoeh, W. Lehnert, G. Merle, and J. Gostick, "Simulation of a Full Fuel Cell Membrane Electrode Assembly Using Pore Network Modeling," *Journal of The Electrochemical Society*, vol. 163, no. 5, pp. F384–F392, 2016.
- [15] R. Banerjee, N. Bevilacqua, L. Eifert, and R. Zeis, "Characterization of carbon felt electrodes for vanadium redox flow batteries – A pore network modeling approach," *Journal of Energy Storage*, vol. 21, no. November 2018, pp. 163–171, 2019.
- [16] G. Qiu, A. S. Joshi, C. R. Dennison, K. W. Knehr, E. C. Kumbur, and Y. Sun, "3-D pore-scale resolved model for coupled species/charge/fluid transport in a vanadium redox flow battery," *Electrochimica Acta*, vol. 64, pp. 46–64, mar 2012.
- [17] G. Qiu, C. R. Dennison, K. W. Knehr, E. C. Kumbur, and Y. Sun, "Pore-scale analysis of effects of electrode morphology and electrolyte flow conditions on performance of vanadium redox flow batteries," *Journal of Power Sources*, vol. 219, pp. 223–234, 2012.
- [18] J. Gostick, M. Aghighi, J. Hinebaugh, T. Tranter, M. A. Hoeh, H. Day, B. Spellacy, M. H. Sharqawy, A. Bazylak, A. Burns, W. Lehnert, and A. Putz, "OpenPNM: A Pore Network Modeling Package," *Computing in Science & Engineering*, vol. 18, pp. 60–74, jul 2016.

- [19] Y. Mehmani, M. Oostrom, and M. T. Balhoff, "A streamline splitting pore-network approach for computationally inexpensive and accurate simulation of transport in porous media," *Water Resources Research*, vol. 50, pp. 2488–2517, 2014.
- [20] J. Tansey and M. T. Balhoff, "Pore Network Modeling of Reactive Transport and Dissolution in Porous Media," *Transport in Porous Media*, vol. 113, pp. 303–327, jun 2016.
- [21] R. C. Acharya, S. E. A. T. M. Van der Zee, and A. Leijnse, "Transport modeling of nonlinearly adsorbing solutes in physically heterogeneous pore networks," *Water Resources Research*, vol. 41, p. W02020, feb 2005.
- [22] L. Li, C. A. Peters, and M. A. Celia, "Upscaling geochemical reaction rates using pore-scale network modeling," *Advances in Water Resources*, vol. 29, pp. 1351–1370, sep 2006.
- [23] D. Kim, C. A. Peters, and W. B. Lindquist, "Upscaling geochemical reaction rates accompanying acidic CO₂-saturated brine flow in sandstone aquifers," *Water Resources Research*, vol. 47, no. 1, pp. 1–16, 2011.
- [24] Y. Mehmani, T. Sun, M. T. Balhoff, P. Eichhubl, and S. Bryant, "Multiblock Pore-Scale Modeling and Upscaling of Reactive Transport: Application to Carbon Sequestration," *Transport in Porous Media*, vol. 95, no. 2, pp. 305–326, 2012.
- [25] A. A. Shah, M. J. Watt-Smith, and F. C. Walsh, "A dynamic performance model for redox-flow batteries involving soluble species," *Electrochimica Acta*, vol. 53, no. 27, pp. 8087–8100, 2008.
- [26] Y. A. Gandomi, D. S. Aaron, T. A. Zawodzinski, and M. M. Mench, "In Situ Potential Distribution Measurement and Validated Model for All-Vanadium Redox Flow Battery," *Journal of The Electrochemical Society*, vol. 163, no. 1, pp. A5188–A5201, 2016.
- [27] J. Newman and K. E. Rhomas-Alyea, *Electrochemical Systems*. Hoboken, New Jersey: John Wiley and Sons, Inc., 3 ed., 2004.
- [28] Z. Yang, J. Zhang, M. C. W. Kintner-Meyer, X. Lu, D. Choi, J. P. Lemmon, and

- J. Liu, "Electrochemical Energy Storage for Green Grid," *Chemical Reviews*, vol. 111, no. 5, pp. 3577–3613, 2011.
- [29] IRENA, "IRENA, Renewable Energy Statistics 2018, Renewable Energy Statistics." <http://www.irena.org/publications/2018/Jul/Renewable-Energy-Statistics-2018>, 2018. [Online; accessed 14-August-2018].
- [30] M. Kazacos and M. Skyllas-Kazacos, "Performance Characteristics of Carbon Plastic Electrodes in the All-Vanadium Redox Cell," *Journal of The Electrochemical Society*, vol. 136, no. 9, pp. 2759–2760, 1989.
- [31] M. L. Perry, R. M. Darling, and R. Zaffou, "High Power Density Redox Flow Battery Cells," *ECS Transactions*, vol. 53, no. 7, pp. 7–16, 2013.
- [32] M. L. Perry and A. Z. Weber, "Advanced Redox-Flow Batteries: A Perspective," *Journal of The Electrochemical Society*, vol. 163, no. 1, pp. A5064–A5067, 2016.

Chapter 4

PNM implementation for carbon-based VRFB electrodes

4.1 Abstract

A PNM was implemented over networks extracted from X-ray computed tomography (X-CT) images of four samples of commercial porous carbon electrodes commonly used in RFBs: Toray 090, SGL29AA, Freudenberg and ELAT-H. The carbon electrodes' physical characteristics (pore-size distribution, permeability, porosity and electroactive surface area) are discussed. The concentration distribution of active species is examined considering solely the transient convective and diffusive transport processes initially, and subsequently is compared to the concentration of active species when migration and reactive transport factors are included. The results show non-uniformity in the concentration and pressure distributions in the electrode when considering the pure convective/diffusive transport processes. The migration and reactive processes are subsequently considered and are shown to be influenced by the rate in which the convective/diffusive flow permeates the electrode. A uniform steady decline in volume-averaged state of charge is shown, followed by a pore-scale non-uniform current density and state of charge distribution upon discharge. These results were obtained on a standard single core workstation highlighting the benefits of using a computationally inexpensive model.

4.2 Background

Redox Flow Batteries (RFBs) are considered one of the most compelling technologies for grid-scale energy storage. The unprecedented large-scale installation of intermittent renewable sources has led to a growing need for high-capacity energy storage systems (ESSs) as balancing mechanisms to stabilise the grid. Compared to their conventional battery counterparts, RFBs offer several advantages. One of their most attractive features is their unique ability to decouple energy and power. The electrolytes containing active redox couples are stored in external tanks and pumped into the cell stack when power is needed through an energy-conversion cell stack.¹

The inherent capabilities of RFBs have been effectively demonstrated, and over the past years significant research has been focused on technological improvements of these systems. Nevertheless, the cost of development of RFBs needs to be decreased in order to meet the aggressive cost targets required for their widespread commercialisation.^{2,3} Two pathways have been proposed for achieving the desired cost reduction. The most obvious one involves implementing lower-cost materials as active redox couple in electrolytes. The second route requires improving the performance at stack level to develop higher power systems and reduce polarisation losses.¹ These improvements in RFB technologies require the design of better architectures and the optimisation of electrode materials.^{4,5} Given that both activation and concentration polarisations occur within the electrode, the design and optimisation of new configurations is imperative.⁴

In this context, carbon-based electrodes represent an ideal material for RFBs due to their wide operating potential, high stability and low cost. Notwithstanding these properties, an enhancement in the electrode structure at a micro or nano scale could lead to an increase in stack power density due to improvements in the effective surface area⁴. Moreover, an alteration in the electrode properties (*e.g.* permeability, pore size, and thickness), has a major influence in the overall power density or efficiency of the RFB. To date, little work has focused on analysing the effect of real electrode morphology in the electrochemical performance of

the cell. Therefore, further research is necessary to understand the effects of micro/nano structure on the RFB performance and degradation mechanisms, in order to design more optimised structures.⁴

An optimisation of the current electrodes for RFBs systems can only be achieved through a deep understanding of the underlying multi-physical processes within the cell. Furthermore, optimisation of current technologies based on experimental trial and error is expensive, time consuming and prone to external errors. For this reason it has become of high interest to employ mathematical modelling and simulation techniques for developing new optimised battery systems.

Most of the numerical models of RFBs reported to date are macroscopic models, in which the porous electrode is treated as a continuum for modelling, and electrode properties such as porosity and tortuosity are volume averaged. Plus, the active surface area for electrochemical reactions is not based on measurements of the actual electrode geometry^{6,7}. As a consequence, most macroscopic models cannot be used to examine the precise roles of the electrode microstructure on the overall performance of RFBs. The main reason for “over-simplifying” the electrode microstructure in current models is because electrodes are composed of porous materials. Therefore, modelling flow and transport processes within these systems is mathematically complex and computationally expensive.

The objective of this section is the implementation of a computationally inexpensive PNM over a set of real carbon electrodes to correlate the electrode morphology with the performance VRFB. This model would be based on the physical and functioning principles that theoretically determine the performance of batteries. This work aims to provide an understanding of the transport processes that limit the cell performance, especially mass transport and electrochemical reaction that occur simultaneously at the electrode.

4.3 Pore Network Model implementation for Toray 090 from XCT

A pore network model for electrochemical systems has been previously developed and validated for a VRFB anode.⁸ This numerical algorithm is implemented over a pore network extracted from a segmented X-CT image of Toray 090 carbon paper sample, typically used as electrode in VRFBs. For this study, the carbon paper was imaged using a laboratory X-ray computed tomography system (Nanotom 180 S, GE Phoenix, USA). The technique applied for segmentation and reconstruction of the image is explained elsewhere⁹, but in short, a 3D median smoothing filter was applied to the reconstructed volume to reduce the image noise. Threshold-based image segmentation of the volume was then performed to isolate the carbon fibres from the pore/electrolyte phase, as shown in Figure 4.1⁹. Characterisation of the electrode in terms of physical size is shown in Table 4.1.

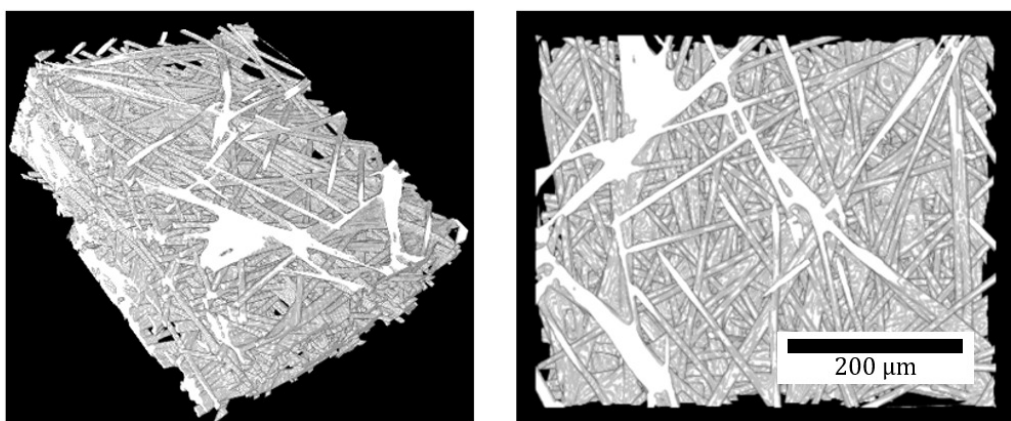


Figure 4.1: Segmented reconstructed image of Toray 090 from XCT data

The pore network of Toray 090 paper was extracted using Avizo software and is based on the “Maximal Ball” algorithm.¹⁰ The pore network is comprised of 2928 pores and 8510 throats, with a pore size distribution shown in Figure 4.2. The process of extracting the pore network from the XCT image is shown in Figure 4.3, where the segmented image is sectioned into porous regions, and from the centre of such regions, the pores are grown.

To initialise the iterative pressure solver, each pore was set to $P_i = 0$. The solution to the system of equations given by Eq. 3.1 provides the flow rate through

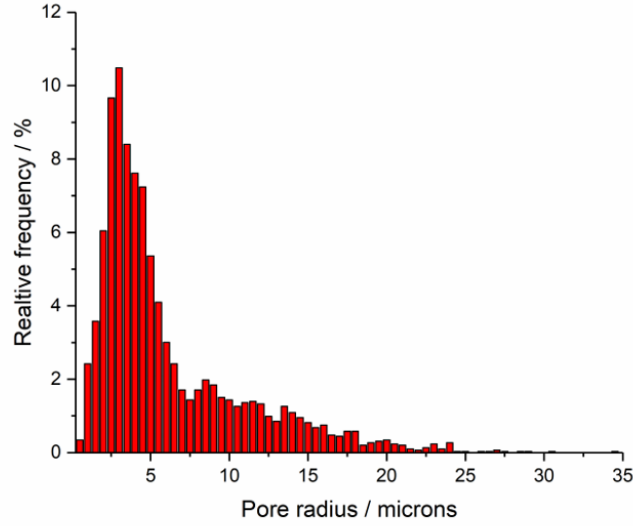


Figure 4.2: Pore size distribution histogram representing the pore network extracted from an X-CT image of a Toray 090 sample with dimensions $441 \times 215 \times 546 \mu\text{m}$.⁸

each throat. The sum of all input flows gives the total macroscopic flow rate of the network (Q_T). From Darcy's law, the bulk permeability can be computed through back-calculation with equation 4.1, in the largest and the smallest faces:

$$Q_T = \frac{KA(P_{in} - P_{out})}{\mu L} \quad (4.1)$$

where K corresponds to the permeability, A is the area normal to the flow direction and L is the length parallel to the flow direction. A and L were calculated from the XCT images.

Table 4.1: Toray 090 sample electrode dimensions.

Resolution $0.65 \mu\text{m}$	Voxels	μm
x	678	441
y	330	215
z	840	546

In all the simulations performed in this work, the smallest and the largest faces of the electrode were set as boundaries and the absolute permeabilities were calculated through both planes. The values of the calculated absolute permeabilities are

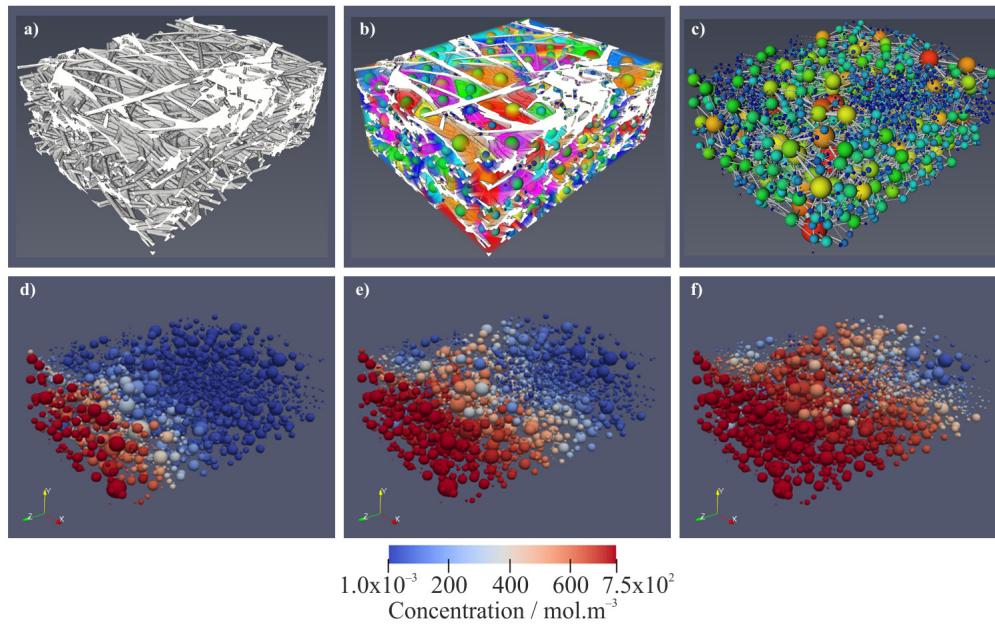


Figure 4.3: Overview of pore network extraction and operation: (a) X-CT segmented image, (b) pore fractions with inserted pore network, (c) standalone pore network, (d–f) 3D example of simulation.⁸

Table 4.2: Permeability data ($\times 10^{12} \text{m}^2$) of a sample of Toray 090 calculated from pore network model using different viscosities^{6,11}, compared with literature¹².

Plane	Model	
	$(\mu = 4.928 \times 10^{-3} \text{ Pa s})^{11}$	$(\mu = 2.5 \times 10^{-3} \text{ Pa s})^6$
Smallest face	16.16	8.20
Largest face	11.44	5.80
Literature values based on Toray 090¹²		
	Experimental	Model
K_x	15	14
K_y	9.0	9.5

reported in Table 4.2 with the two values of viscosity for the vanadium solution reported on the literature.^{6,11} The estimated permeabilities using the pore-network extracted from a XCT scan of Toray 090 were compared to the values reported by Gostick *et al.*¹², both experimental and modelled for a Toray 090 carbon paper. It is shown that the values reported in the literature are similar and within the same order of magnitude as the values calculated in this work. These results show that the electrode topology determined by the pore-network extracted with Avizo represents the Toray 090 paper microstructure in terms of flow. The porosity, given by Avizo was 68% and the specific surface area was calculated as 41062 m^{-1} .

4.3.1 Boundary conditions

The transport of species defined in the previous section by equation 3.3 is determined by the interplay between four main factors: convection, diffusion, migration and electrochemical reaction. Each contribution is determined by thermodynamic and kinetic properties of the electrolyte, as well as by geometric parameters determined by the topology of the electrode. To understand the effect of each contributing factor, they were analysed separately as follows: the effect of the electrolyte permeation due to convection and diffusion were analysed first as if the system was not electrochemically reactive. Following this, the additional transient distribution of species due to migration and electrochemical reaction were included.

An additional algorithm was developed to determine the boundary pores (*i.e.* inlets and outlets) of the pore network extracted from the XCT image. The maximum length of XCT image in each dimension was calculated by measuring the largest perpendicular distance between the two furthest-most pores (in each dimension). Using this, a virtual film spanning each face of the image, with a thickness of 1% of the total thickness of the 3D image, was calculated as a threshold to determine boundary pores from the other pores. If any given pore volume overlapped with this virtual film, it was taken to be a boundary inlet or outlet pore.

Boundary conditions for flow transport

Dirichlet boundary conditions of pressure were set at the inlet and outlet pores to obtain the flow distribution through the throats in the network, as given by equation 3.1. A total pressure drop of 10 Pa was set across the network from the inlet to the outlet pores.

Boundary conditions for mass transport

For the concentration distribution, Dirichlet boundary condition was established at the inlet wall determined by the initial state of charge (SOC) of the inlet solution. The SOC is defined as:

$$SOC = \frac{C_{II}}{C^{0-}} \quad (4.2)$$

$$C_{II}^{in} = C^{0-} \cdot SOC \quad (4.3)$$

$$C_{III}^{in} = C^{0-} \cdot (1 - SOC) \quad (4.4)$$

where C_{II} corresponds to the concentration of V(II), C^{0-} is the total concentration of vanadium species in the electrolyte, C_{II}^{in} and C_{III}^{in} are the concentrations of V(II) and V(III) respectively at the inlet boundary. A Newman condition of zero diffusive flux was established at the outlet wall. To implement an open boundary to the system of irregularly distributed pores, the addition of a layer of *dummy pores* was required. At the connection between the outlet pores and their respective dummy pores, the concentrations were set to be equal in order to achieve a zero diffusive flux.

Boundary conditions for charge transport

Dirichlet boundaries of electrolyte potential at the inlet and outlet pores were implemented. This is in order to set the boundary walls to be operating under potentiostatic conditions. With the solution to the coupled mass and current equations, the potential distribution at each pore were recalculated at every time-step in the transient simulation.

4.3.2 Purely convective-diffusive transport

Figure 4.4 shows the steady-state pressure profile and flow distribution throughout the network. The pressures at each pore from figure 4.4(a) are obtained by imposing Dirichlet boundaries at the inlet and outlet pores, with a pressure difference of 10 Pa (*i.e.* $P_{in} = 10$ Pa and $P_{out} = 0$ Pa). Figure 4.4(b) shows the distribution of flows through each of the throats. The solution of the pressure and flow profiles is achieved in 6 s. By analysing the flow distribution through the throats, it can be seen that the electrolyte flow is not uniformly distributed within the electrode, leading to regions in which the flow rate is close to zero and regions where the flow rate is maximum (*i.e.* $4.0 \times 10^{-13} \text{ m}^3\text{s}^{-1}$).

The irregularity in flow distribution across the electrode draws *flow paths*

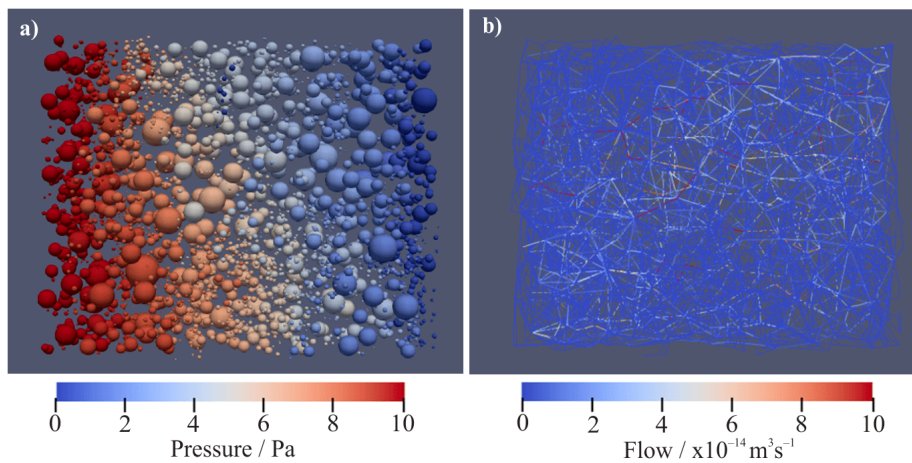


Figure 4.4: Decoupled steady-state (a) pressure, and; (b) flow distributions.⁸

through which the electrolyte will infiltrate the pores more rapidly. Such paths of maximum flow rate (red throats) represent the regions where the convective transport is dominant, rather than diffusion. On the other hand, the regions where the convective flow is minimum (blue throats), the transport of species would be dictated by the diffusive flux between pores. This is demonstrated by the analysis of the permeation of electrolyte as a function of time, as shown in Figure 4.5.

At time $t = 0$ (Fig. 4.5a), the concentration of vanadium species was close to zero (*i.e.* $C_{II}(0) = 0.001 \text{ mol m}^{-3}$) at every pore, except at the inlet pores, where the concentration was set to $C_{II}^{in}(0) = 750 \text{ mol m}^{-3}$ (corresponding to a SOC of 50%). As the simulation proceeds, the electrolyte primarily permeates the pores located along the path of maximum flow. Concentration changes due to diffusive flow could only be noticed until the electrolyte had infiltrated the outlet wall. The concentration in regions which until this point had not been permeated with electrolyte, started to increase. The effect of an initially high convective flow enhanced a subsequent diffusive flux, since a higher concentration gradient between pores was imposed due to the convective flux. Despite the effect of both convection and diffusion, some pores remained largely untouched throughout the simulation. This nonuniform distribution of electrolyte has an impact on the battery performance since it implies a non-uniform utilisation of the electrode. These results are consistent with the work by Banerjee *et al.* which demonstrate that the electrolyte permeates the electrode pores in a nonuniform way, drawing

flow paths that are dependent on the pore's connectivity and therefore the electrode internal structure.¹³

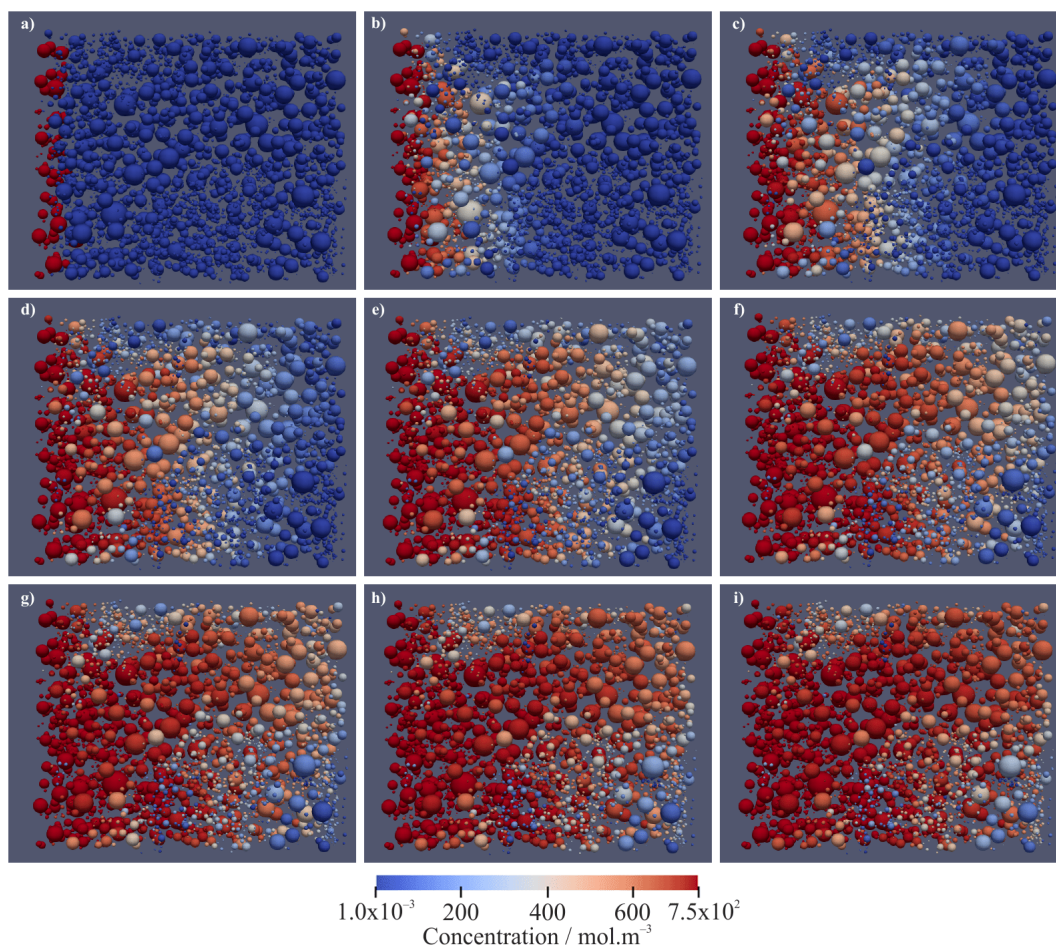


Figure 4.5: Permeation of V(II) through a PNM representing a section of Toray 090. The 3D images proceed in 1 s steps starting from 0 s (a).⁸

4.3.3 Convection, diffusion, migration and electrochemical reaction

This section implements the modified PNM equation to analyse the distribution of concentration and current density due to four contributing factors, namely convection, diffusion, migration and electrochemical reaction. The model is implemented over the pore-network extracted from Toray 090 carbon paper sample. The steady-state simulation of the pressure and flow distributions converged after 9 s, while the coupled charge and species transport distributions converged after 16 min for each time-step in the simulation, using a single core of

a HP workstation: Intel® Xeon® CPU E5-166-v3.

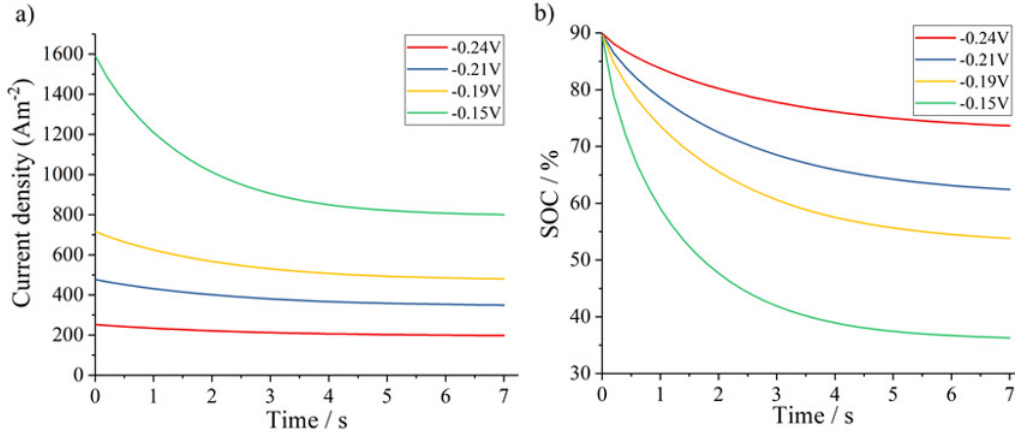


Figure 4.6: (a) Current density; and, (b) state of charge variation with time at various electrode potential drops.⁸

Figure 4.6 shows the volume averaged values of current density in the anode under potentiostatic discharge at different averaged electrode potentials. The averaged electrode potentials are defined according to Qiu *et al.*⁷ as the potential drop across the active surface area ($\phi_s - \phi_e$) at each pore in the simulation, as given by the following equation:

$$\Delta\phi = \frac{1}{np} \sum_i^{np} (\phi_s - \phi_{e,i}) \quad (4.5)$$

The simulations were run at four different values of average electrode potential difference across the solid–electrolyte interface: -0.15 V , -0.19 V , -0.21 V and -0.24 V . These values are independent of concentration and therefore equilibrium potential, E_a .

By analysing figure 4.6 it is concluded that lower current densities were obtained at more negative electrode potentials (e.g. -0.24 V) - which implies lower overpotentials - and higher current densities at more positive electrode potentials (e.g. -0.15 V) - *i.e.* higher overpotentials. At more positive electrode potentials, a more significant drop in current density leads to a faster consumption of species. This is graphically represented in figure 4.6(b) where the SOC is plotted for different electrode potentials. For the most positive electrode potential

(-0.15 V) – highest overpotentials – the electrode is discharged from 50% to 25% in 2.5 s, while at the most negative electrode potential (-0.24 V) - lowest overpotentials - the electrode only discharges 2.5% (to 47.5%) in the same amount of time. This volume-averaged analysis offers insight into the correlated parameters that play a key role on the cell performance (*i.e.* current density, cell potential and average SOC) at a macroscopic level. However, pore-scale results offer much more detail about species and current transport in VRFBs compared to volume-averaged methods.

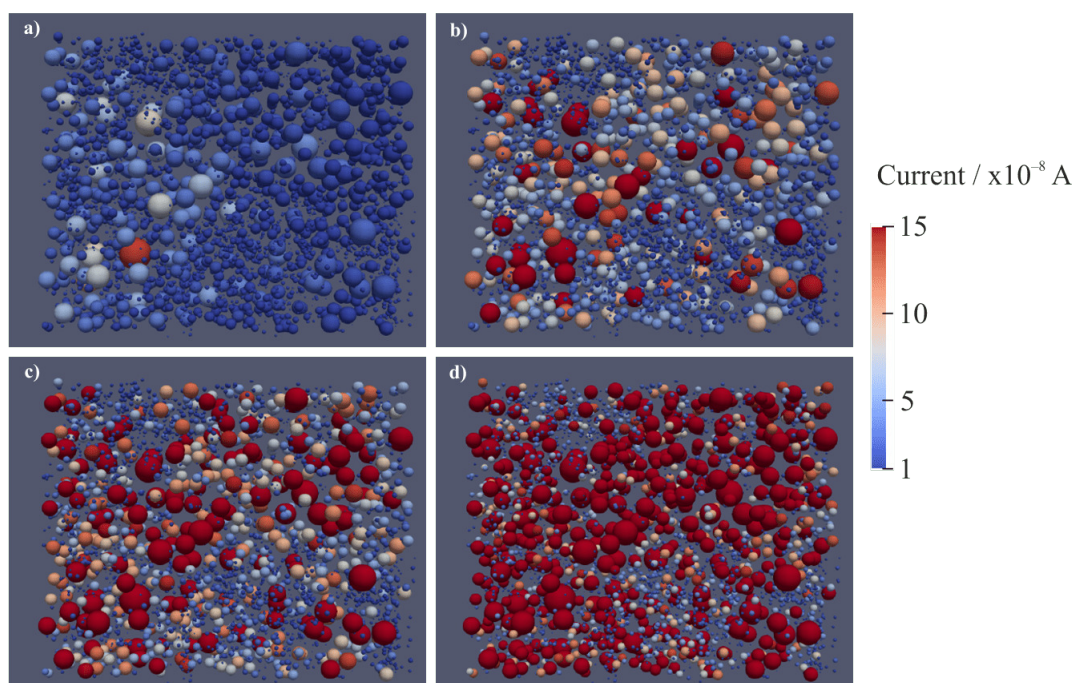


Figure 4.7: Current distribution at various electrode potentials (a) -0.24 V , (b) -0.21 V , (c) -0.19 V and (d) -0.15 V (at 50% state of charge).⁸

An analysis of the current distribution at a pore-scale is presented in figure 4.7. The electrode is at 50% SOC under potentiostatic discharge at different electrode potentials (-0.15 V , -0.19 V , -0.21 V and -0.24 V). In the same way as the volume-averaged results, higher currents are obtained at more positive electrode potentials - higher overpotentials -; however, the pore-scale results obtained with the PNM simulation show a non-uniform distribution of current throughout the electrode, which agrees with the LBM models by Qiu *et al.*⁶. This

leads to the existence of regions within the electrode that are more reactive than others and contribute to electrode performance to a greater extent.

Figure 4.8 shows a comparison between electrolyte concentration (under a purely convective-diffusive regime) and absolute current at each pore. By comparing the location of pores where the absolute current is higher (Fig. 4.8a) with the concentration distribution in a purely convective-diffusive regime (Fig. 4.8b), it is seen that the ‘path’ of large pores (*i.e.* higher absolute current) correlates with the regions that are permeated by electrolyte at a higher rate. This analysis shows the benefits of implementing a pore-scale model such as the PNM approach. A PNM provides insight into the local correlation of transport parameters (*i.e.* pore size, current and concentration distributions) at a pore-scale level, while volume averaged models only consider changes in the current and concentration distributions along the length of the cell. The results presented in this work with a PNM approach reinforce the findings of Qiu *et al.*⁶ which prove that the current density is non-uniformly distributed along the three-dimensional space.

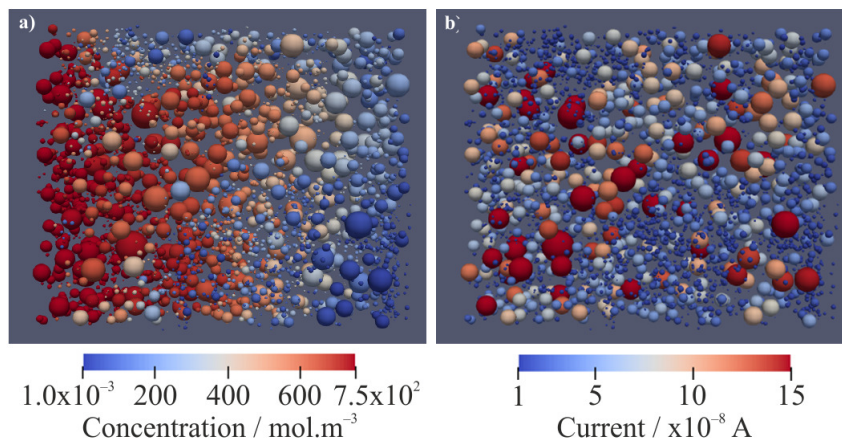


Figure 4.8: (a) Current distribution (at -0.21 V electrode potential and state of charge 50%), and; (b) concentration (purely convective-diffusive regime) distribution after 4 s.⁸

A further analysis on the transient distribution of vanadium species is performed in which the concentration is influenced by convective, diffusive, reactive and migration transport conditions. The concentration transient concentration distribution for a potentiostatic discharge with an electrode potential of -0.21 V and an initial SOC of 90% is shown in figure 4.9. This SOC corresponds to an initial concentration of species in all pores of $C_{II}(0) = 1350 \text{ mol m}^{-3}$.

The inlet concentration is constant throughout the simulation with a value of $C_{II}^{in}(0) = 1350 \text{ mol m}^{-3}$ corresponding to 90% SOC. As expected, it is shown that the concentration profile of V(II) is not uniform within the electrode which leads to a non-uniform depletion of vanadium species across the electrode during discharge. It is therefore evident that a volume averaged value of the electrode SOC only poorly resembles the actual concentration distribution of species within the cell. This can be graphically shown by comparing figure 4.6(b) (volume-averaged results) with 4.9 (pore-scale results). At 4 s, the volume-averaged results give a SOC of 67.52%, while the pore-scale 3D results show areas in which the SOC significantly differs from this value.

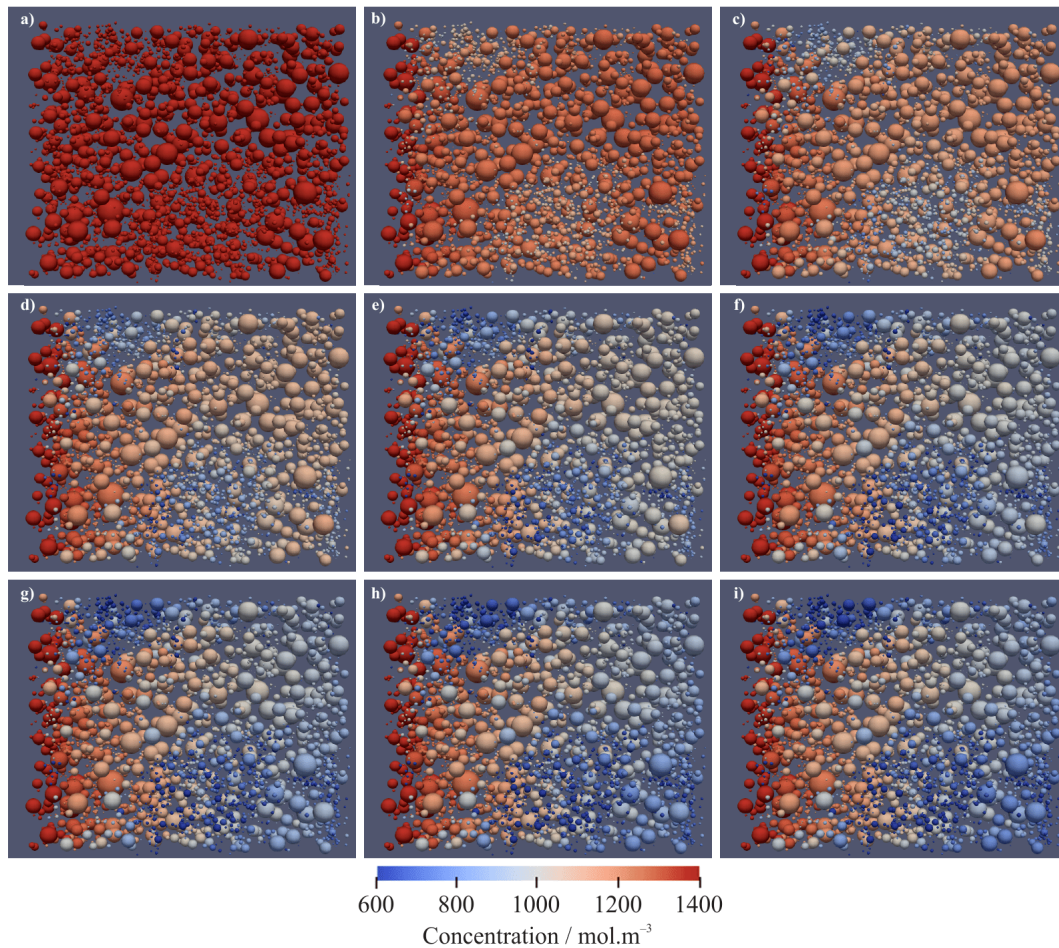


Figure 4.9: Transient concentration distribution with electrochemical reaction at an electrode potential of -0.21 V for Toray 090. The 3D images proceed in 1 s steps starting from 0 s (a) to 8 s (f).⁸

Figure 4.10 represents the transient current density distribution across the electrode for a potentiostatic discharge with electrode potential of -0.21 V and

an initial SOC of 90%. By comparing figure 4.9(a) and figure 4.10(a), it is clearly shown that when the concentration of species is constant in the electrode, the gradient of the current density across the electrode is determined by the potential difference in the electrolyte from the inlet to the outlet. This result is in accordance with the MCM equation for transport of current (*i.e.* equation 3.14), since it implies that the second term on the RHS, corresponding to the current transport due to a concentration gradient, is zero. As the concentration of species changes with time due to convection, migration, reaction and diffusion, the second term of equation 3.14 presents a significant influence on the current density distribution. This shows the interplay between various factors occurring at a pore-scale level which significantly influence the cell performance.

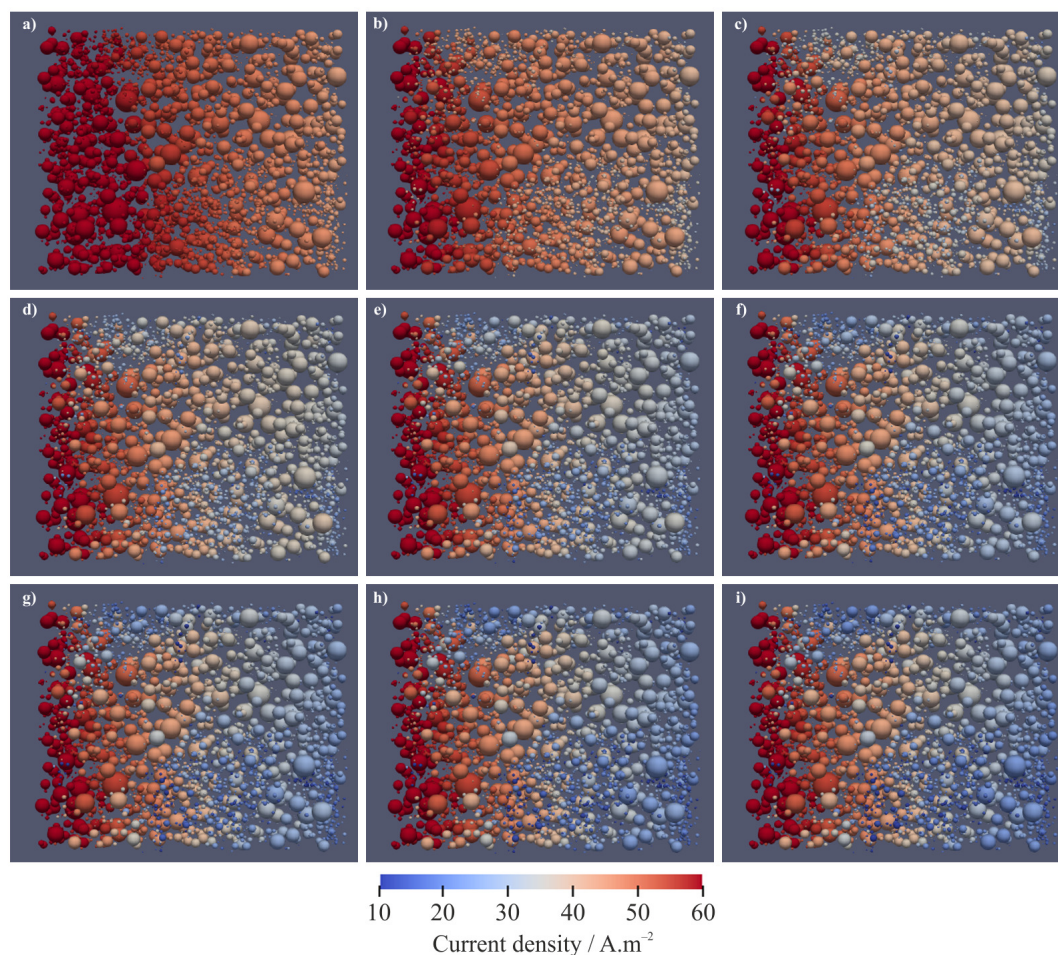


Figure 4.10: Transient current density distribution with electrochemical reaction with electrode potential of -0.21 V. The 3D images proceed in 1 s steps starting from 0 s (a) to 8 s (f).⁸

It is shown from figures 4.9 and 4.10 that the pore size distribution is directly correlated to the starvation of electrolyte in certain pores, leading to a non-even rate of discharge and current density distribution throughout the electrode. This causes the existence of areas within the electrode which are more utilised than others and therefore contribute to a higher extent to the fast discharge of the battery. A more direct comparison can be made by analysing the results of a transient concentration change when the system is under pure convective-diffusive transport and when the system is influenced by electrophoretic and reactive transport, as shown in figure 4.11. It is shown that the regions where convective flow is dominant (*i.e.* rapidly permeated by electrolyte) result in a lower rate of V(II) depletion than the regions where the electrolyte permeation is slower. As previously analysed, these regions also correspond to the sites with higher values of transfer current (figure 4.8). This can be rationalised due to a faster and continuous replenishment of fresh electrolyte into the pores with a higher convective flux. This fast replenishment of species allows a constant consumption of new V(II), thus enhancing the electrochemical reaction.

In an analogous way, the pores that present a limited convective transport (highlighted by the green rings in figure 4.11(a)) are also the ones that present a faster rate of depletion of vanadium species. This implies that the sites where the flow is minimum are discharged at a higher rate than the sites with high convective flow. The existence of these *clusters of pores* where limited convective transport is dominant leads to a faster rate of discharge of the cell as a whole. As the concentration of V(II) in these pores tends to zero, the effect of diffusion becomes dominant: the concentration gradient between two pores of very different concentration increases and therefore becomes more significant than the convective or migration terms. This effect of the non-uniform distribution of species on the depletion of vanadium species could be interpreted as one of the factors that influence a fast discharge in RFB electrodes.

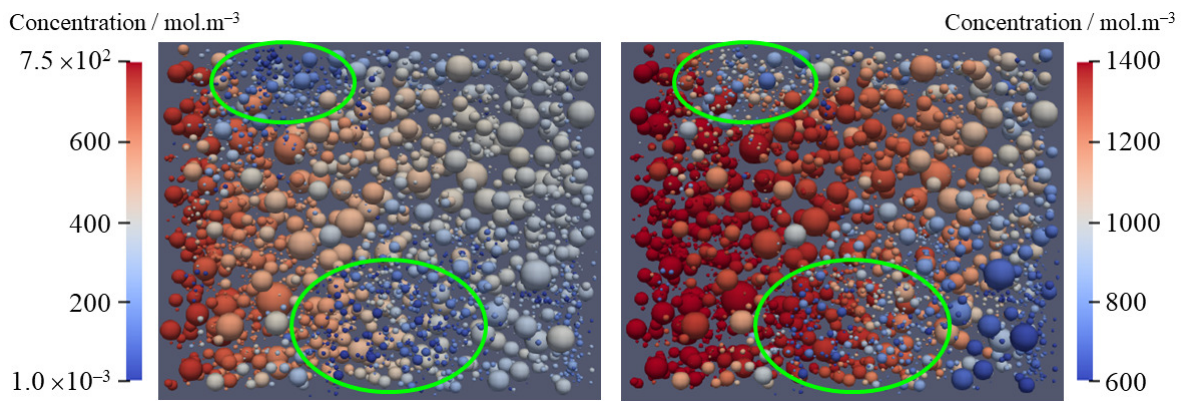


Figure 4.11: Comparison of concentration distribution at 5 s in (a) a purely convective-diffusive transport system and, (b) a convective-diffusive transport system with electrochemical migration. Green rings highlight the regions where convective flow is limited.⁸

4.3.4 Comparison of pore-scale models in terms of computational expense

The objective of this work was to introduce a pore-scale model that can provide insights into the transport processes within the microstructure while being computationally inexpensive. Thus, an interesting comparison can be drawn in terms of computational expense between the model presented in this work and the model introduced by Qiu *et al.*^{6,7}. The first sample analysed by Qiu *et al.*⁶ is a geometric subset from an original master X-CT structure. The subset occupies a volume of dimensions $600 \times 150 \times 600 \mu\text{m}^3$, and a specific surface area of $39,700 \text{ m}^{-1}$. Qiu *et al.*⁶ implement an LBM to solve the flow field within the electrolyte, and a fully implicit 3D FVM to solve the coupled charge and species transport equations in the pore-space domain. The authors implement the LBM and FVM methods in FORTRAN 90 using the Message Passing Interface for parallel processing. The simulation for this subset of the XCT structure is reported to converge in 20 h using a 64-core computer running on the TeraGrid. The second work presented by Qiu *et al.*⁷ analyses three different electrode structures reconstructed from X-CT images. All structures occupy a volume of dimensions $900 \times 135 \times 450 \mu\text{m}^3$, and specific surface areas of $37,500 \text{ m}^{-1}$, $47,700 \text{ m}^{-1}$ and $69,700 \text{ m}^{-1}$. Analogous to the first case⁶, LBM and FVM were implemented to solve the flow field and coupled charge and species transport within the electrolyte respectively. All simulations are reported to converge within 20 h using a 112-core cluster running on the NSF XSEDE system⁷. The PNM approach presented in this work analyses a network extracted

from X-CT images with dimensions reported in Table 3 and specific surface area of $41,062 \text{ m}^{-1}$. The steady-state flow equations were solved with a successive over relaxation method and the transient coupled charge and species transport were solved with an explicit Euler scheme. The flow equations converged in 9 s and the species transport in 16 min for each time-step outputted from the simulation. The system was solved using a single core of a HP workstation: Intel® Xeon® CPU E5-166-v3.

4.4 Case studies: implementation of PNM for SGL 29AA, Freudenberg, ELAT-H

The analysis performed in section 4.3 proved the extension of the pore network modelling framework introduced in chapter 3 for a real microstructure in which the network is extracted from an XCT image. In order to analyse the effect of the electrode microstructure in the electrolyte distribution, this method was implemented in various carbon electrodes commonly used for RFBs. The imaging was performed using an X-ray computed tomography system (Nanotom 180 S, GE Phoenix, USA) with a resolution based on each system, and the segmentation techniques are the same as described in section 4.3⁹, and the pore networks were extracted using the “Maximal Ball” algorithm.¹⁰

4.4.1 SGL29AA

The dimensions and image resolution of the electrode SGL29AA is shown in table 4.3, and a segmented image is shown in figure 4.12. The pore network was extracted from the XCT image obtained using an X-ray computed tomography system (Nanotom 180 S, GE Phoenix, USA) at a resolution of $1.20 \mu\text{m}$ per voxel. The pore network consists of 1577 pores and 4801 throats, and the process of extracting the PNM is shown in figure 4.13.

An initial simulation is performed to obtain the flow distribution throughout the network. A pressure drop of $\Delta P = 10 \text{ Pa}$ was established by imposing Dirichlet boundaries at the inlet and outlet pores (*i.e.* $P_{in} = 10 \text{ Pa}$ and $P_{out} = 0 \text{ Pa}$). The pressure and flow profiles were solved in 5 s . To solve the mass transport

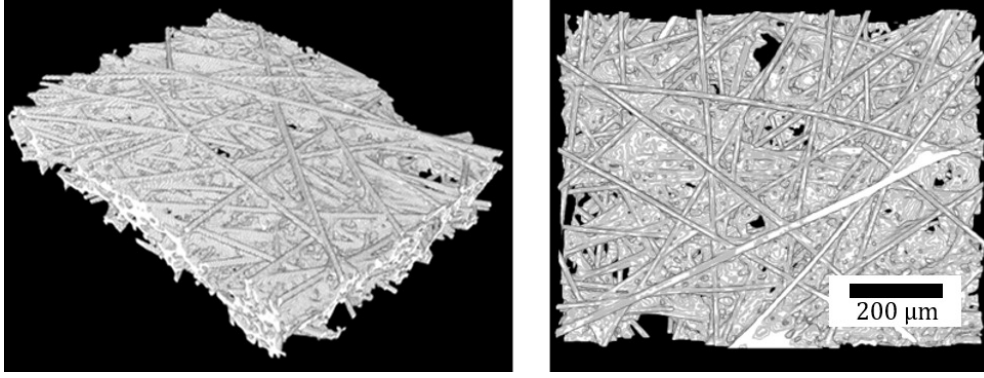


Figure 4.12: Segmented reconstructed image of SGL29AA

Table 4.3: SGL29AA sample electrode dimensions.

Resolution	Voxels	μm
1.20 μm		
x	776	931
y	162	194
z	616	739

balance, a Dirichlet boundary was established at the inlet pores determined by the initial SOC of the inlet solution, as defined by equations 4.2, 4.3 and 4.4. A Newman boundary condition of zero flux was established at the outlet wall, where an additional layer of *dummy pores* were implemented to impose this boundary. In order to obtain the distribution of charge and potentials throughout the network, Dirichlet boundaries of electrolyte potential at the inlet and outlet pores were implemented. This implies that the simulations were performed under potentiostatic conditions, and the potential distribution at each pore is recalculated at every time-step.

Based on the pressure and flow profiles, a purely diffusive-convective transient simulation was performed to analyse the effect of the microstructure in these transport processes. At time $t = 0$, the concentration of vanadium species was close to zero (*i.e.* $C_{II}(0) = 0.001 \text{ mol m}^{-3}$) in all pores except at the inlet pores, where the concentration was set to $C_{II}^{in}(0) = 750 \text{ mol m}^{-3}$ corresponding to a SOC of 50%. The inlet concentration is constant at every time-step to guarantee a constant replenishment of active species (V(II)). Figure 4.14 shows the concentration profiles from $t = 0 \text{ s}$ to $t = 8 \text{ s}$. In a similar way as with Toray, it can be seen that the permeation of electrolyte is non-uniform and so the concentration profiles

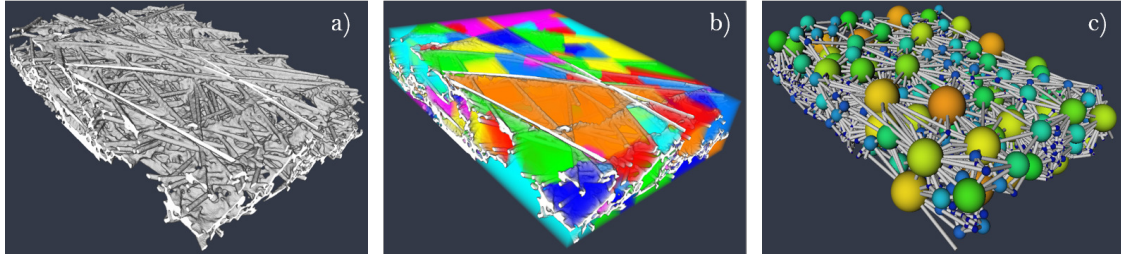


Figure 4.13: Overview of pore network extraction of SGL29AA: (a) X-CT segmented image of SGL, (b) pore fractions in segmented image obtained using Avizo software, (c) standalone pore network extracted using the Maximal Ball algorithm¹⁰.

at different time-steps are diverse. A flow path is drawn where the convective flow is predominant and the permeation of electrolyte is more rapid, as can be seen in figure 4.14 (e), where the lower part of the electrode is fully permeated (red), while the upper part has a low concentration of active species (blue). By analysing the upper left corner of the electrode it is seen that, despite being close to the inlet, the area does not get permeated with electrolyte. This shows the existence of *dead zones* where the electrode is non-utilised since the concentration of active species in the pores remains unchanged throughout the simulation. Based on this result, it can be concluded that the estimated total surface area obtained experimentally or through imaging techniques does not correspond to the actual surface area used during operation.

An additional analysis of the transient distribution of species considering all four transport processes is performed: convection, diffusion, migration and reaction. An initial concentration of species in all pores is established as $C_{II}(0) = 1350 \text{ mol m}^{-3}$ corresponding to an initial SOC of 90%. The inlet concentration is constant throughout the simulation, with a value of $C_{II}^{in}(0) = 1350 \text{ mol m}^{-3}$, and the cell is operated under potentiostatic discharge with an electrode potential of -0.21 V . Figure 4.15 shows the discharge process of the cell during 8 s of operation. As expected, the distribution of species is non-uniform across the electrode. During the first seconds of the discharge process (*i.e.* figure 4.15 (a)-(d)), the transient change of species appears to be uniform, reaching a concentration of 1200 mol m^{-3} in almost all pores. However, as the simulation continues, certain zones, which coincide with the previously

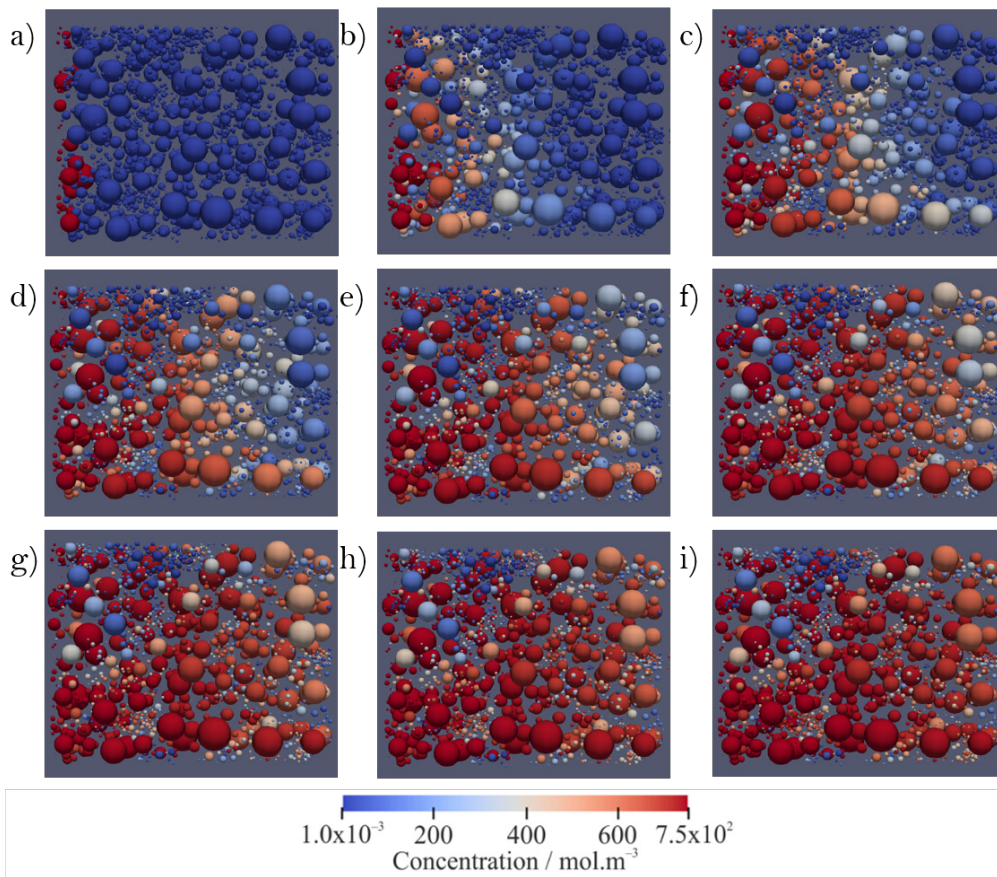


Figure 4.14: Permeation of V(II) through a PNM representing a section of SGL29AA. The 3D images proceed in 1 s steps starting from 0 s (a).

called *dead zones*, appear to discharge at a much faster rate than the rest of the pores. This indicates that the constant replenishment of species does not reach these areas, leading to a fast consumption of V(II) without replacement. It is clear that some areas initially discharge from 90% to 86% and stay constant throughout the rest of the simulation. These areas also correspond to the pores that conform the predominant path of species permeation. If this 86% stays constant, it would be expected that the battery discharge would achieve a balance between consumption/replenishment of species. Nonetheless, the existence of regions that discharge down to 45% in 8 s due to starvation of electrolyte lead to an overall discharge of the whole system. This analysis shows that major transport limitations due to the non-uniform distribution of electrolyte significantly impacts the performance of the overall cell performance. Based on this, it would be reasonable to hypothesise that an improvement in the electrode design can lead to improvements in the cell performance by reducing the mass transport limitations that occur at a pore-scale level.

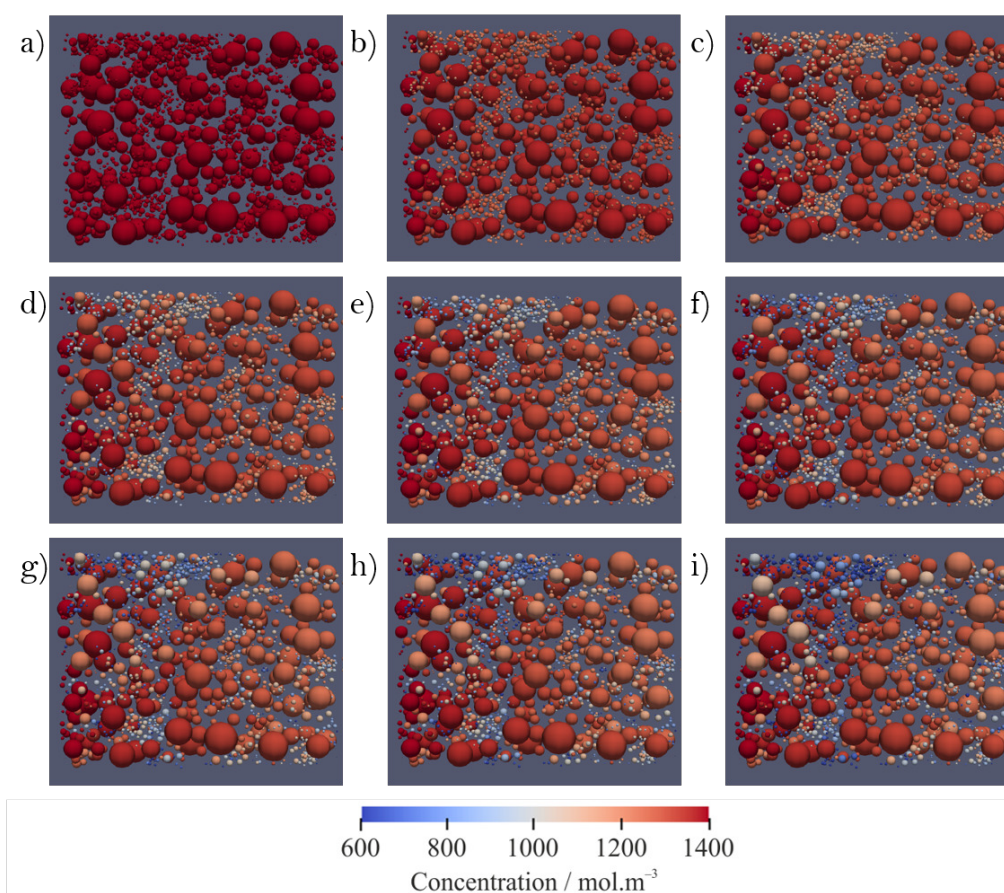


Figure 4.15: Transient concentration distribution with electrochemical reaction at an electrode potential of -0.21 V for SGL29AA. The 3D images proceed in 1 s steps starting from 0 s(a) to 8 s(f)

These results are similar to the ones obtained for Toray, where the presence of non-utilised zones corresponded also to the areas where a fast discharge occurred, leading to an overall reduction in performance. This can be rationalised as an effect of the random distribution of the fibres along all directions. This random distribution could lead to the existence of preferred flow paths where convective transport is predominant, (mostly dominated by connection of large pores) or the presence of pores with low connectivity. In this respect, other carbon-based electrodes have been explored which contain a more uniform distribution of pores sizes, or an alignment in the fibre distribution. Some of these widely used carbon-based electrodes are Freudenberg and carbon cloths, which will be analysed in the next sub-sections.

4.4.2 Freudenberg

The characterisation of the carbon-based electrode Freudenberg (FBH3) is shown in table 4.4, and a segmented image is shown in figure 4.16. The XCT image was obtained using an X-ray computed tomography system (Nanotom 180 S, GE Phoenix, USA) at a resolution of $0.60 \mu\text{m}$ per voxel. The process of extracting the PNM is shown in figure 4.17, as long as the resulting pore network consisting of 2470 pores and 9890 throats.

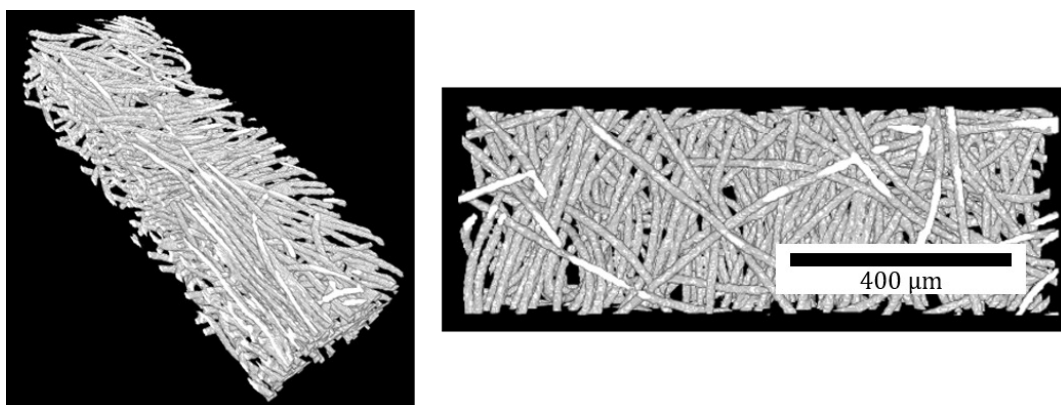


Figure 4.16: Segmented reconstructed image of Freudenberg electrode

An analysis of the transport of species was performed first for a purely convective-diffusive regime and then for an additional electrophoretic and reactive transport. The boundary conditions for flow, mass and charge transport were the same as those implemented for Toray and SGL. To calculate the pressure and flow profiles, a pressure drop of $\Delta P = 10 \text{ Pa}$ was imposed across the electrode, with Dirichlet boundaries of $P_{in} = 10 \text{ Pa}$ and $P_{out} = 0 \text{ Pa}$.

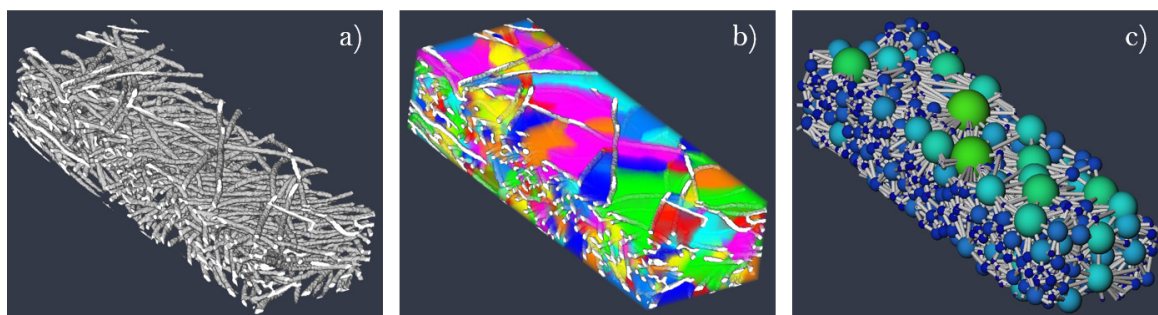


Figure 4.17: Overview of pore network extraction of Freudenberg: (a) X-CT segmented image, (b) pore fractions in segmented image, (c) standalone pore network

Table 4.4: Freudenberg sample electrode dimensions.

Resolution 0.60 μm	Voxels	μm
x	338	203
y	971	583
z	219	131

The results of a purely convective-diffusive transport are shown in figure 4.18. An initial concentration of species of $C_{II}(0) = 0.001 \text{ mol m}^{-3}$ was imposed over all pores except at the inlet, where the concentration was set to $C_{II}^{in}(0) = 750 \text{ mol m}^{-3}$, corresponding to a SOC of 50%, and was kept constant throughout the transient simulation. An analysis of the species transport shows that the electrode is permeated with electrolyte in a uniform way. This result is contrary to the results of the species distribution for Toray 090 and SGL29AA, where the existence of preferred flow paths created areas where the electrode is not permeated. In the case of Freudenberg, the purely convective and diffusive flows allow the full permeation of all pores after 8 s of simulation. It can be rationalised that a more uniform distribution is the result of a higher interconnectivity between pores and a more uniform distribution of the pores sizes. The effect of directionality fibre alignment is believed to also affect the uniformity of the electrolyte distribution; however in the case of Freudenberg the fibres appear to be randomly distributed. A comparison of the transport processes within the electrode between Toray, SGL and Freudenberg prove the importance of the electrode microstructure in the distribution of active species during operation, which can either lead to a uniform distribution of species, or to the existence of starvation zones that significantly reduce the performance. Furthermore, it is seen that in the case of Freudenberg, the utilisation of the electrode is almost complete, which implies that the estimated active surface area through imaging techniques corresponds to the actual surface area used for the charge transfer reaction.

A further analysis is made to incorporate the additional electrophoretic and reactive terms into the transient simulation. An initial concentration of $C_{II}(0) = 1350 \text{ mol m}^{-3}$ is established in all pores, which corresponds to an initial SOC of 90% before discharge. The cell is discharged under potentiostatic

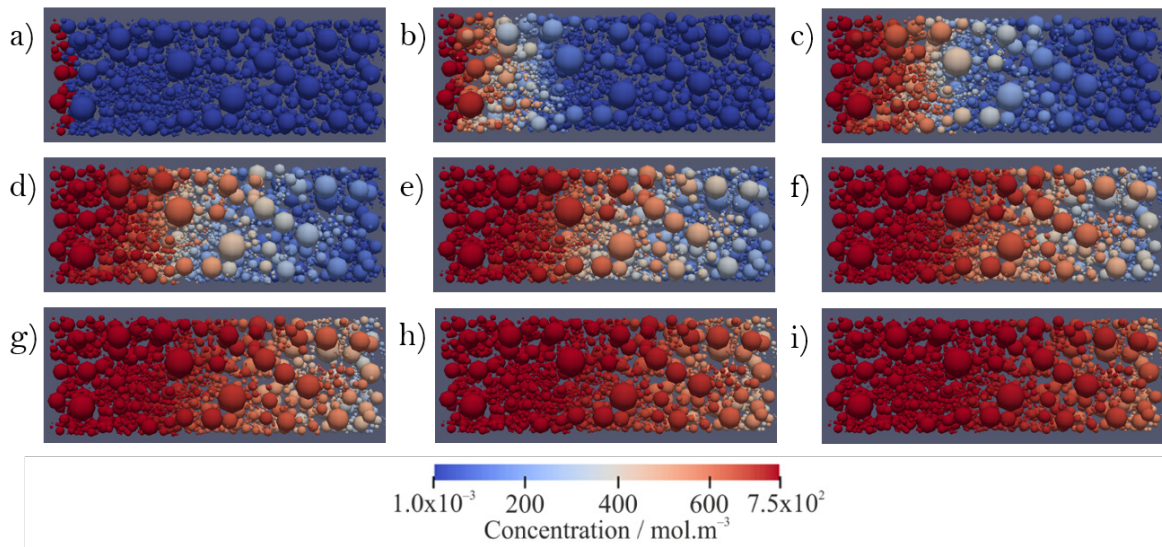


Figure 4.18: Permeation of V(II) through a PNM representing a section of Freudenberg. The 3D images proceed in 1 s steps starting from 0 s (a).

conditions at -0.21 V. The concentration of species at the inlet pores is constant and is set to $C_{II}^{in}(0) = 1350 \text{ mol m}^{-3}$. Figure 4.19 shows the results of the transient distribution of species considering all four transport processes. Analogous to the case of the purely convective-diffusive transport, the consumption of species is uniform throughout the simulation, which indicates that no *dead zones* exist where the electrolyte depletion is caused by starvation. Nonetheless, it can be seen that as time progresses, the right-most section of the electrode (*i.e.* furthest from the inlet) starts to be depleted of electrolyte until 8 s when the SOC reaches 64%. This indicates that the rate of consumption of species is slower than the rate of replenishment of species. In other words, the decrease in the concentration of V(II) is not caused by electrolyte starvation due to lack of pore-to-pore connectivity, but instead is given due to a slow convective-diffusive-electrophoretic transport that is not as fast as the rate of consumption of species at the active surface area. This problem can be solved by increasing the inlet pressure (*i.e.* pumping power) in order to guarantee that the regions far from the inlet are replenished with fresh electrolyte faster or at an equilibrium with the consumption rate.

4.4.3 ELAT-H

In recent years, the use of carbon cloths in RFBs has become of interest to many researchers. It has been shown experimentally that higher performances can be

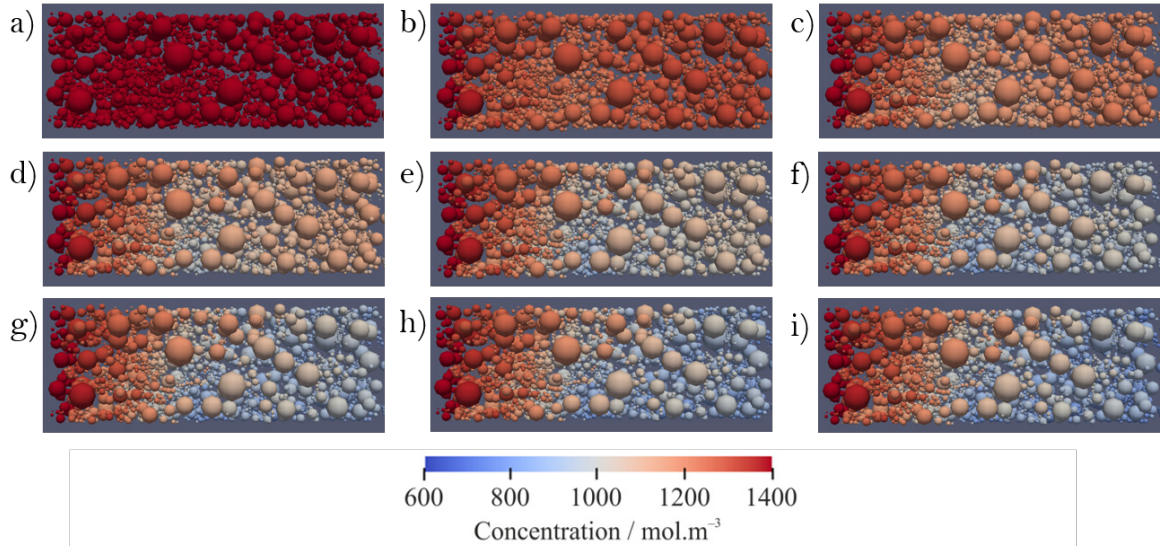


Figure 4.19: Transient concentration distribution with electrochemical reaction at an electrode potential of -0.21 V for Freudenberg. The 3D images proceed in 1 s steps starting from 0 s(a) to 8 s(f)

obtained using carbon cloths due to lower mass transport limitations.¹⁴ This has been attributed to the woven patterns of cloths, which allows a more uniform distribution of species throughout the electrode and thus higher utilisation. With the purpose of analysing the effect of the microstructure in the distribution of species, a PNM is implemented over the extracted pore network from an XCT image of a carbon cloth ELAT-H.

The XCT image was obtained using an X-ray computed tomography system (Nanotom 180 S, GE Phoenix, USA) at a resolution of $1.20 \mu\text{m}$ per voxel. A segmented view of the XCT image of ELAT-H is shown in figure 4.20, and the dimensions and image resolution of the electrode subsample are shown in table 4.5. The pore network extracted from the XCT image consists of 1389 pores and 8382 throats, as can be seen in figure 4.21 that shows the process of extracting a PNM.

Table 4.5: ELAT-H sample electrode dimensions.

Resolution $1.20 \mu\text{m}$	Voxels	μm
x	243	291
y	1391	1669
z	1256	1507

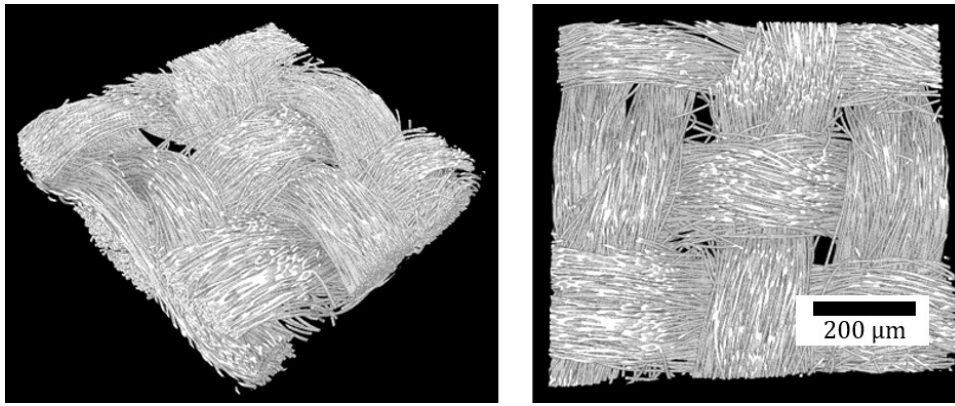


Figure 4.20: Segmented reconstructed image of ELAT-H carbon cloth

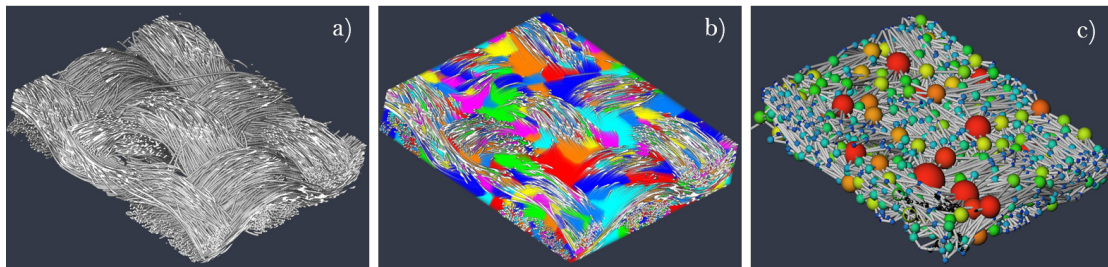


Figure 4.21: Overview of pore network extraction of ELAT-H: (a) X-CT segmented image, (b) pore fractions in segmented image, (c) standalone pore network

The flow and pressure profiles were estimated by imposing Dirichlet boundary conditions of pressure at the inlet and outlet pores of the electrode: $P_{in} = 10$ Pa and $P_{out} = 0$ Pa. For the mass transport simulation, a Dirichlet boundary was established at the inlet pores based on the initial SOC of the inlet solution, as defined by equations 4.2, 4.3 and 4.4. For the outlet pores, a Newman boundary condition of zero flux was established, where the implementation of *dummy pores* was used to impose this boundary. The simulations were performed under potentiostatic conditions with Dirichlet boundaries of electrolyte potential at the inlet and outlet pores.

An initial purely diffusive-convective transient simulation was performed for 8 s, as shown in figure 4.22. At time $t = 0$ the concentration in all pores was set close to zero (*i.e.* $C_{II}(0) = 0.001 \text{ mol m}^{-3}$) except at the inlet pores, where the concentration corresponded to a 50% SOC, equivalent to $C_{II}^{in}(0) = 750 \text{ mol m}^{-3}$. The concentration at the inlet pores was kept constant throughout the simulation to ensure a constant replenishment of species. By analysing figure 4.22, it can be seen that during the first steps of the simulation (b-c) a preferred flow path

is evident, corresponding to a straight path that connects the largest pores. However, as the simulation continues, the permeation of electrolyte becomes consistent throughout the electrode, leading to a complete permeation after 8 s. The presence of straight flow paths is a direct consequence of the alignment of pores due to the directionality of the fibres, which is proper of carbon cloths as opposed to other type of carbon based electrodes where the fibre alignment is random (e.g. Toray and SGL).

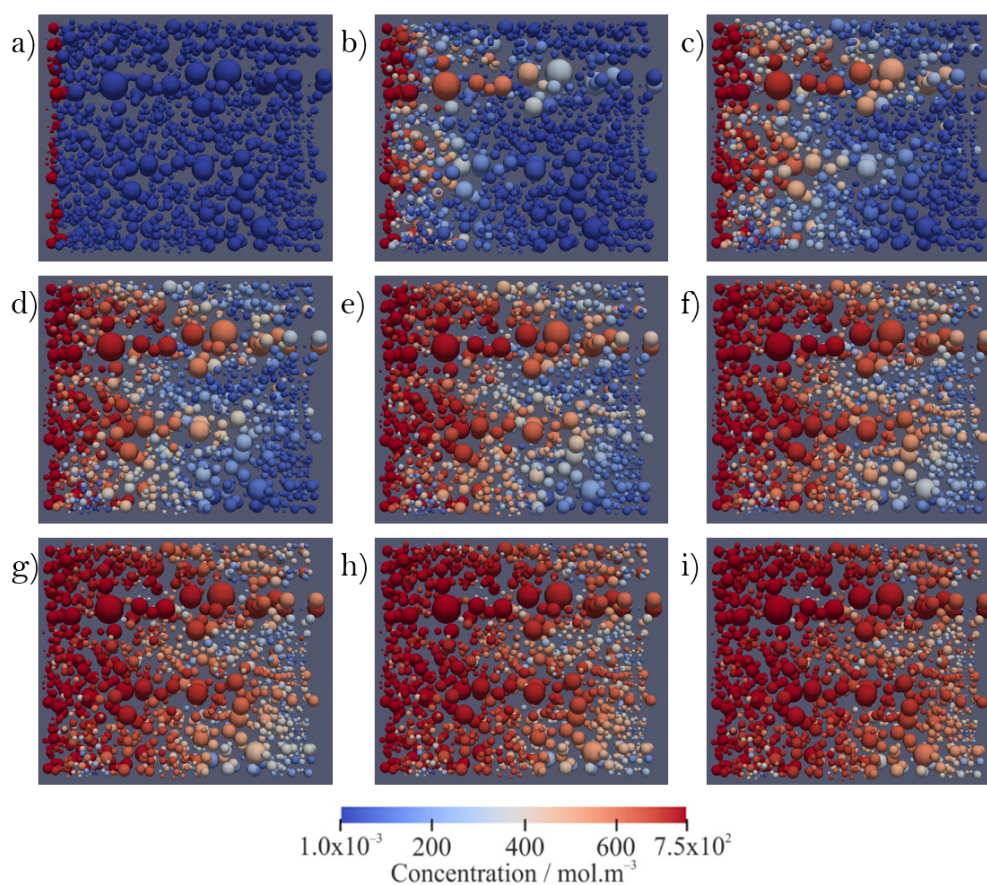


Figure 4.22: Transient concentration distribution with electrochemical reaction at an electrode potential of -0.21 V for ELAT-H. The 3D images proceed in 1 s steps starting from 0 s(a) to 8 s(f)

It has been demonstrated in previous works that the permeability of carbon cloths compared to carbon papers is significantly higher^{14,15}. This can be qualitatively proved by comparing the flow distribution of ELAT-H (figure 4.22) with the flow distribution of SGL (figure 4.14) and Toray 4.5. In ELAT-H, the fast permeation of all pores in the network due to an incoming convective flux implies a high permeability in the microstructure, while in the case of Toray and SGL, the

electrolyte permeates only the preferred flow paths due to a convective flux. The rest of the pores are then slowly replenished through a diffusive flux given by a concentration gradient between pores.

To further comprehend the effect of the microstructure in the transport processes within the electrode, additional terms for migration and reaction were involved in the transient simulation. An initial concentration of $C_{II} = 1350 \text{ mol m}^{-3}$ was established in all pores, corresponding to an initial SOC of 90%. For the inlet pores, the concentration was set to $C_{II}^{in} = 1350 \text{ mol m}^{-3}$ and was kept constant for every time-step in the simulation to ensure a continuous replenishment of species to the pore network. Figure 4.23 shows the results of the transient potentiostatic discharge at an electrode potential of -21 V for 8 s. The results of the simulation show a uniform discharge where most pores are between 85% and 90% SOC after 8 s. The uniformity of the electrolyte distribution in the whole electrode due to a high permeability and a straight pore alignment avoids the existence of agglomerates of pores where the transport limitations are predominant. This implies that no regions are deprived of electrolyte replenishment due to lack of inter-pore connectivity, and therefore the previously seen zones of fast discharge due to electrolyte starvation do not exist in this type of electrode. Additionally it can be seen that the whole active surface area of the electrode is uniformly utilised due to the high permeability of carbon cloths. Based on these results, it is shown that the microstructure of the cloth is beneficial for the cell performance since it enhances a uniform distribution of electrolyte and therefore a constant replenishment of species. A comparison between the carbon cloth and the carbon papers (*i.e.* SGL and Toray) shows that the presence of starvation zones in the carbon papers reduce the overall SOC of the electrodes, which is a main limitation in the cell performance. These findings are relevant for the design of RFBs since it is shown that the choice of electrode significantly impacts the battery performance due to the transport processes that occur within the electrode microstructure.

4.5 Conclusions

This work extended the implementation of a previously introduced framework based on a pore-network model to simulate the coupled flow, species and charge

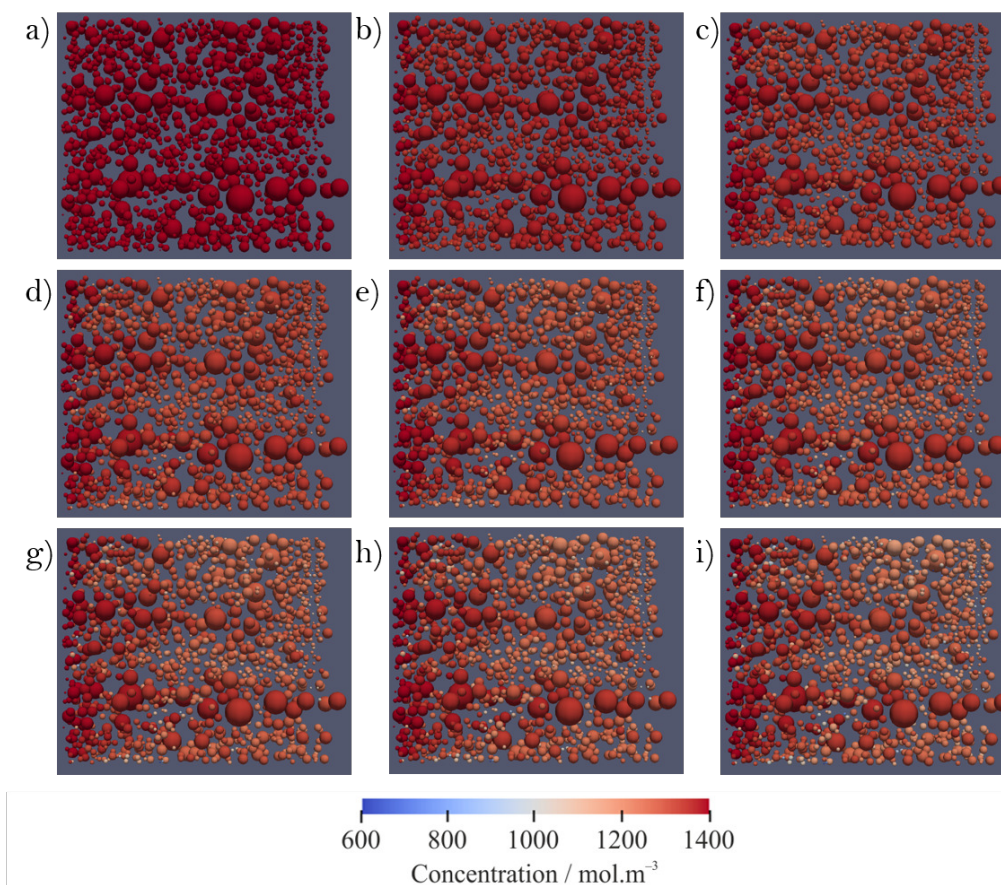


Figure 4.23: Transient concentration distribution with electrochemical reaction at an electrode potential of -0.21 V for ELAT-H. The 3D images proceed in 1 s steps starting from 0 s(a) to 8 s(f)

transport that occur within electrodes in electrochemical devices. The algorithm was implemented to simulate the transport processes in a VRFB anode, and was used over pore-networks extracted from XCT data of three carbon-based electrodes: Toray 090, SGL 29AA, Freudenberg and ELAT-H cloth. The results show that the pore-size distribution representing the electrode void space is directly related to the flow, concentration and current distribution within the network. In cases where the diversity of pore sizes is wider, such as Toray and SGL, it can be seen that the flow draws preferred paths that connect the largest pores across the electrode length. As a counterpart of these paths where convection is predominant, the flow profiles show the existence of routes within the electrode through which the convective flow of electrolyte is minimum. These areas are therefore mass transport limited as the movement of species is almost purely diffusive. Since the pores on these routes are not constantly replenished with fresh electrolyte, they will discharge at a faster rate than the pores on

routes with high convective flow. Contrary to this scenario, Freudenberg and ELAT-H present a uniform convective flow throughout the whole network, which prevents the existence of mass-transport-limited agglomerates of pores. In the case of Freudenberg, this uniformity in the electrolyte distribution is given by the distribution of pores of similar sizes, while in the case of ELAT-H, this is a result of the fibre alignment proper of carbon cloths.^{14,15}

An analysis of the concentration distribution under convection, diffusion, migration and reaction shows that, as expected, for SGL and Toray, the concentration is not uniform throughout the network, leading to areas in which the SOC is almost half of its initial state (*i.e.* 90%) In the case of ELAT-H, it is seen that the electrode discharges at the same rate for all regions, while for Freudenberg, the electrode discharge is affected by the rate of depletion being faster in areas further from the inlet but not isolated due to limitations in inter-pore connectivity. This analysis proves the advantage of using a pore-scale model over a continuous volume-averaged one for representing more accurately the effects of transport processes in electrode utilisation. This leads to two major conclusions: (a) the SOC is not uniform across the electrode and dependent on the topology of the pore distribution in the microstructure, and; (b) the effect of mass-transport limited areas in the electrode leads to a faster discharge. Based on this, it is reasonable to conclude that an analysis of the effect of electrode microstructure in mass transport processes is crucial for the design of RFBs with improved performance. These results represent the first visual showcase of how regions limited by low convective flow affect the rate of discharge in an electrode.

In terms of computational expense, the results show that the framework presented in this work based on a PNM approach is significantly less expensive than the previous works presented by Qiu *et al.* which use a LBM coupled with a FVM^{6,7}. The PNM approach converges within 16 min on a standard single core workstation, while the LBM-FVM simulations converge in 20 h running on a cluster. This represents a significant advantage of the present model over existing models since it has the ability to simulate the coupled flow, species and charge transport distributions at a pore-scale within the electrode without requiring a high processing power.

It must be emphasised that the segmented images of Toray 090, SGL29AA, Freudenberg and ELAT-H used in this work do not represent a REV of the whole electrode. A REV analysis falls beyond the purpose of this work. The purpose of using XCT images is to show the capabilities of the model when implemented in a real system. Future work should analyse the effect of different flow rates (*i.e.* pressure drops) in the electrode potential, current distribution and consumption of species. Additionally, an interesting future step should seek to couple this framework with a continuum model of different flow channel configurations and eventually represent a micro/macro model of the full cell.

References

- [1] M. L. Perry and A. Z. Weber, “Advanced Redox-Flow Batteries: A Perspective,” *Journal of The Electrochemical Society*, vol. 163, no. 1, pp. A5064–A5067, 2016.
- [2] U.S. DOE, “Grid Energy Storage,” 2013.
- [3] EASE, “Joint EASE/EERA recommendations for a European Energy Storage Technology Development Roadmap towards 2030,” 2018.
- [4] M. H. Chakrabarti, N. P. Brandon, S. A. Hajimolana, F. Tariq, V. Yufit, M. A. Hashim, M. A. Hussain, C. T. Low, and P. V. Aravind, “Application of carbon materials in redox flow batteries,” *Journal of Power Sources*, no. 253, pp. 150–166, 2014.
- [5] A. A. Shah, M. J. Watt-Smith, and F. C. Walsh, “A dynamic performance model for redox-flow batteries involving soluble species,” *Electrochimica Acta*, vol. 53, no. 27, pp. 8087–8100, 2008.
- [6] G. Qiu, A. S. Joshi, C. R. Dennison, K. W. Knehr, E. C. Kumbur, and Y. Sun, “3-D pore-scale resolved model for coupled species/charge/fluid transport in a vanadium redox flow battery,” *Electrochimica Acta*, vol. 64, pp. 46–64, mar 2012.
- [7] G. Qiu, C. R. Dennison, K. W. Knehr, E. C. Kumbur, and Y. Sun, “Pore-scale analysis of effects of electrode morphology and electrolyte flow conditions on performance of vanadium redox flow batteries,” *Journal of Power Sources*, vol. 219, pp. 223–234, 2012.
- [8] A. Gayon Lombardo, B. A. Simon, O. Taiwo, S. J. Neethling, and N. P. Brandon, “A pore network model of porous electrodes in electrochemical devices,” *Journal of Energy Storage*, vol. 24, p. 100736, 2019.
- [9] Y. Zhu and C. Huang, “An Improved Median Filtering Algorithm for Image Noise Reduction,” *Physics Procedia*, vol. 25, pp. 609–616, 2012.
- [10] M. J. Blunt, *Multiphase Flow in Permeable Media: A Pore-Scale Perspective*. Cambridge: Cambridge University Press, 1 ed., 2017.

- [11] D. You, H. Zhang, and J. Chen, “A simple model for the vanadium redox battery,” *Electrochimica Acta*, vol. 54, no. 27, pp. 6827–6836, 2009.
- [12] J. T. Gostick, M. A. Ioannidis, M. W. Fowler, and M. D. Pritzker, “Pore network modeling of fibrous gas diffusion layers for polymer electrolyte membrane fuel cells,” *Journal of Power Sources*, vol. 173, pp. 277–290, nov 2007.
- [13] J. T. Gostick, “Versatile and efficient pore network extraction method using marker-based watershed segmentation,” *Physical Review E*, vol. 96, no. 2, pp. 1–15, 2017.
- [14] A. Forner-Cuenca, E. E. Penn, A. M. Oliveira, and F. R. Brushett, “Exploring the Role of Electrode Microstructure on the Performance of Non-Aqueous Redox Flow Batteries,” *Journal of The Electrochemical Society*, vol. 166, no. 10, pp. A2230–A2241, 2019.
- [15] K. M. Tenny, A. Forner-Cuenca, Y.-M. Chiang, and F. R. Brushett, “Comparing Physical and Electrochemical Properties of Different Weave Patterns for Carbon Cloth Electrodes in Redox Flow Batteries,” *Journal of Electrochemical Energy Conversion and Storage*, vol. 17, no. 4, 2020.

Chapter 5

Generative Adversarial Networks for the reconstruction of three-dimensional multi-phase electrode microstructure

5.1 Abstract

The generation of multiphase porous electrode microstructures is a critical step in the optimisation of electrochemical energy storage devices. This work implements a deep convolutional generative adversarial network (DC-GAN) for generating realistic n-phase microstructural data. The same network architecture is successfully applied to two very different three-phase microstructures: A lithium-ion battery cathode and a solid oxide fuel cell anode. A comparison between the real and synthetic data is performed in terms of the morphological properties (volume fraction, specific surface area, triple-phase boundary) and transport properties (relative diffusivity), as well as the two-point correlation function. The results show excellent agreement between datasets and they are also visually indistinguishable. By modifying the input to the generator, we show that it is possible to generate microstructure with periodic boundaries in all three directions. This has the potential to significantly reduce the simulated volume required to be considered “representative” and therefore massively reduce the computational cost of the

electrochemical simulations necessary to predict the performance of a particular microstructure during optimisation.

5.2 Background

Porous multiphase materials are widely studied throughout a variety of engineering disciplines, for instance, the distribution of precious metal catalysts on porous supports; the structure of metallic phases and defects in high-performance alloys; the arrangement of sand, organic matter, and water in soil science; and the distribution of calcium, collagen and blood vessels in bone.¹⁻³ Therefore understanding their microstructural and geometrical properties is of great interest to many researchers. In electrochemistry, electrodes constitute one of the most important components since they are the sites where the main transport and reactive processes occur. Whether considering batteries or fuel cells, these electrodes are porous materials to allow a maximum surface area and contain percolating paths to enhance the transport of both electrons and ions; however, their design also requires a solid matrix strong enough to sustain the mechanical integrity of the material.^{4,5} Due to the complexity of these electrodes, their microstructure significantly impacts their performance and therefore their morphological optimisation is vital for developing the next generation of energy storage technologies.⁶

Recent improvements in 3D imaging techniques such as X-ray computed tomography (XCT) have allowed researchers to view the microstructure of porous materials at sufficient resolution to extract relevant metrics⁷⁻¹⁰. However, a variety of challenges remain, including how to extract the key metrics or “essence” of an observed microstructural dataset such that synthetic volumes with equivalent properties can be generated, and how to modify specific attributes of this microstructural data without compromising its overall resemblance to the real material. A wide variety of methods that consist of generating synthetic microstructure by numerical means have been developed to solve these challenges.⁶ Quiblier *et al.* introduced a statistical method based on simulation annealing to reconstruct synthetic three-dimensional porous media based on a two-point correlation function.¹¹ This statistical method was established as basis for future works: Torquato *et al.* implemented a stochastic approach based on the n-point

correlation functions for generating reconstructions of heterogeneous materials;^{12–16} Jiao *et al.*^{17,18} presented an isotropy-preserving algorithm to generate realisations of materials from their two-point correlation functions (TPCF). Based on these previous works, the most widely used approach for reconstruction of microstructure implements simulated annealing methods through the calculation of the TPCF.^{2,19–24}

In the area of energy materials, interest has recently surged for generating synthetic microstructure in order to aid the design of optimised electrodes. The three-phase nature of most electrochemical materials adds an extra level of complexity to their generation compared to two-phase materials. A first approach was introduced by Suzue *et al.*²⁰, following the work of Quiblier *et al.*,²¹ and implemented a TPCF from a two-dimensional phase map to reconstruct a three-dimensional microstructure of a porous composite anode. Baniassadi *et al.*²⁵ extended this method by adding a combined Monte Carlo simulation with a kinetic growth model to generate three-phase realisations of a SOFC electrode. Parallel to these statistical methods, other authors have introduced algorithms for the synthetic generation of porous electrodes based on mimicking the experimental fabrication process. A stochastic algorithm based on the process of nucleation and grain growth was developed by Siddique *et al.*²⁶ for reconstructing a three-dimensional fuel cell catalyst layer. Siddique *et al.* extended their work and implemented it for the reconstruction of a three-dimensional LiFePO_4 cathode.²⁷ A commonly used object-based model for representing the microstructure of SOFC electrodes consist on random packing of initial “seeds”, usually spheres, followed by their growth and expansion of to simulate the sintering process.^{28–31} Moussaoui *et al.*⁶ implement a combined model based on sphere packing and truncated Gaussian random field to generate synthetic SOFC electrodes. Additional authors have implemented plurigaussian random fields to model the three-phase microstructure of SOFC electrodes and establish correlations between the microstructure and model parameters^{4,32,33}.

In the area of Li-ion batteries, many authors have focused on developing models that can represent the carbon-binder domain (CBD) which is usually hard to image with XCT techniques. Usseglio-Viretta *et al.* implemented a computational

method to adhere a synthetic CBD over XCT three-dimensional images of the NMC/pore phases^{34,35}. Forouzan *et al.*³⁶ introduced a particle-based simulation coupled with a physics-based simulation that defines the fabrication process of Li-ion electrodes, to superimpose CBD particles to the electrode microstructure. Srivastava *et al.*³⁷ also presented a physics-based dynamic model that simulated the fabrication process of Li-ion electrodes. The growth of phases is determined by controlling the adhesion of active material and CBD phases. The results of this work proved to accurately predict the effect of the microstructure in transport properties.

Recent work by Mosser *et al.*^{38,39} introduces a deep learning approach for the stochastic generation of three-dimensional two-phase porous media. The authors implement a Generative Adversarial Network (GANs)⁴⁰ for the stochastic reconstruction of three-dimensional microstructure of synthetic and natural granular porous media. Li *et al.*⁴¹ extended this work and implemented GANs for the generation of optimised sandstones. The advantage of GANs over other common microstructure generation techniques is that GANs are able to provide fast sampling of high-dimensional and intractable density functions without the need for an a priori model of the probability distribution function to be specified³⁹. The present chapter presents an expansion of the research of Mosser *et al.*^{38,39} to implement GANs for generating three-dimensional, three-phase microstructure for two types of electrode commonly used in electrochemical devices: a Li-ion battery cathode and an SOFC anode. A comparison between the statistical, morphological and transport properties of the generated images and the real tomographic data is performed. The two-point correlation function is further calculated for each of the three phases in the training and generated sets to investigate the long-range properties. Due to the fully convolutional nature of the GANs used, it is possible to generate arbitrarily large volumes of the electrodes based on the trained model. Lastly, by modifying the input of the generator, structures with periodic boundaries were generated.

Performing multiphysics simulations on representative 3D volumes is necessary for microstructural optimisation, but it is typically very computationally expensive. This is compounded by the fact that the regions near the boundaries

can show unrealistic behaviour due to the arbitrary choice of boundary condition. However, synthetic periodic microstructures (with all the correct morphological properties) enable the use of periodic boundary conditions in the simulation, which will significantly reduce the simulated volume necessary to be considered representative. This has the potential to greatly accelerate these simulations and therefore the optimisation process as a whole.

5.3 Generative Adversarial Networks

Generative Adversarial Networks (GANs) were introduced by Goodfellow *et al.* as a type of implicit generative model that learns to represent the probability distribution function (pdf) of a given dataset (*i.e.* p_{data}).⁴² Since p_{data} is unknown, the result of the learning process is an estimate of the pdf called p_{model} from which a set of samples can be generated. Although GANs by design do not admit an explicit probability density, they learn a function that can sample from p_{model} , which reasonably approximate those from the real dataset (p_{data}).

The training process consists of a minimax game between two functions, the generator $G(\mathbf{z})$ and the discriminator $D(\mathbf{x})$. $G(\mathbf{z})$ maps an d -dimensional latent vector $\mathbf{z} \sim p_z(\mathbf{z}) \in \mathbb{R}^d$ to a point in the space of real data as $G(\mathbf{z}; \theta^{(G)})$, while $D(\mathbf{x})$ represents the probability that \mathbf{x} comes from p_{data} .⁴⁰ The objective of the training process is to implicitly learn the distribution of the real data (*i.e.* p_{data} through a process of constant sampling, until the density function learned by $G(\mathbf{z})$ (*i.e.* p_{model}) is as close as possible to the real distribution.

In this work, both the generator $G_{\theta^{(G)}}(\mathbf{z})$ and the discriminator $D_{\theta^{(D)}}(\mathbf{x})$ consist of deep convolutional neural networks.⁴³ Each of these has a cost function to be optimised through stochastic gradient descent in a two-step training process. First, the discriminator is trained to maximise its loss function $J^{(D)}$:

$$J^{(D)} = \mathbb{E}_{\mathbf{x} \sim p_{\text{data}}(\mathbf{x})} [\log(D(\mathbf{x}))] + \mathbb{E}_{\mathbf{z} \sim p_z(\mathbf{z})} [\log(1 - D(G(\mathbf{z})))] \quad (5.1)$$

This is trained as a standard binary cross-entropy cost in a classifier between the discriminator's prediction and the real label. Subsequently, the gen-

erator is trained to minimise its loss function corresponding to minimising the log-probability of the discriminator being correct:

$$J^{(G)} = \mathbb{E}_{\mathbf{z} \sim p_{\mathbf{z}}(\mathbf{z})} [\log (1 - D (G(\mathbf{z})))] \quad (5.2)$$

These concepts are summarised in Figure 5.1.

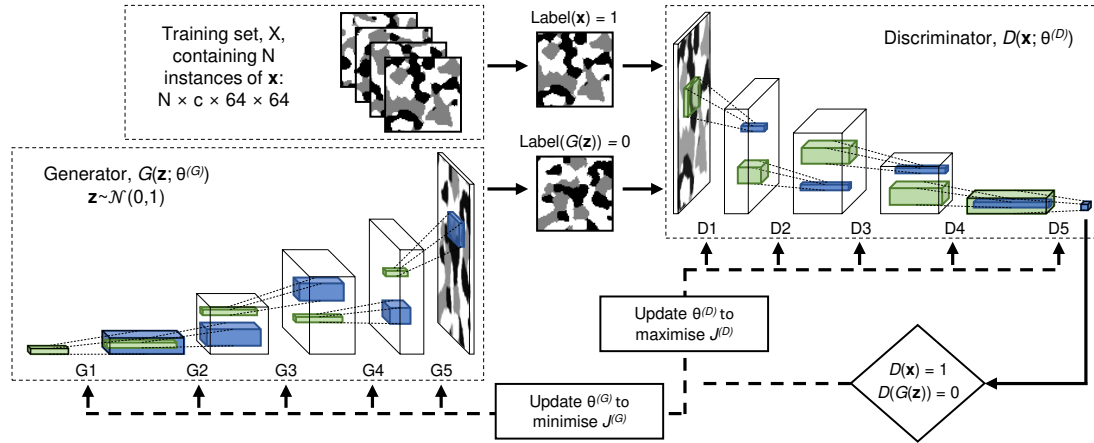


Figure 5.1: GAN architecture: Schematic showing the architecture of the DC-GAN for 2D microstructural data. Generalisation to 3D samples is conceptually straightforward, but difficult to show as it requires the illustration of 4D tensors. In each layer, the green sub-volume shows a convolutional kernel at an arbitrary location in the volume and the blue sub-volume is the result of that convolution. In each case, the kernel is the same depth as the one non-spatial dimension, c , but must scan through the two spatial dimensions in order to build up the image in the following layer.

The solution to this minimax game is a Nash equilibrium.⁴² where the samples of $\mathbf{x} = G(\mathbf{z}) \sim p_{\text{model}}(\mathbf{z})$ are indistinguishable from the real samples $\mathbf{x} \sim p_{\text{data}}(\mathbf{x})$.⁴² thus $p_{\text{model}}(\mathbf{z}) = p_{\text{data}}(\mathbf{x})$ and $D(\mathbf{x}) = \frac{1}{2}$ for all \mathbf{x} since the discriminator can no longer distinguish between real and synthetic data.

5.4 Microstructural data

This work considers two electrode microstructures as training sets corresponding to two different types of battery materials: a SOFC anode and a Li-ion cathode.

The sample details are described below.

5.4.1 Sample details

Li-ion cathode

This material was generated at the Cell Analysis, Modelling and Prototyping (CAMP) facility at the Argonne National Laboratory. The electrode is composed of three phases: the active material corresponding to $\text{Li}(\text{Ni}_{0.5}\text{Mn}_{0.3}\text{Co}_{0.2})\text{O}_2$ (NMC532, TODA America Inc.), the carbon/binder domain composed of C45 carbon (Timcal) and polyvinylidene fluoride (PVDF) (Solvay, Solef 5130), and the porous phase. Since the carbon/binder domain is not visible directly at the XCT images, the authors generated this phase over the three-dimensional geometry of the scanned images.³⁴

SOFC anode

This material consists of a commercial anode-supported button MSRI (Materials and Systems Research, Inc.) cell composed of three phases: Yttria-stabilised zirconia (YSZ), nickel (Ni) and the porous phase.⁴⁴ This voxelised image is cropped into a total of 45,492 overlapping sub-volumes of 643 voxels each, at a spacing of 16 to be used as training database for reconstruction. This image size is sufficient enough to represent the TPCF of the whole electrode sample.

5.4.2 Image data

The two electrode materials used in this work were obtained from open-source nano-tomography data.^{34,44} The data available had already been segmented into their respective three phases, as seen in Figure 5.2. The first dataset is from a Li-ion battery cathode, comprising particles of a ceramic active material (nickel manganese cobalt oxide – NMC 532), a conductive organic binder (polymer with carbon black) and pores. The fabrication process of this material consists on mixing the components in a solvent, thinly spreading this ink onto an aluminium foil and then drying. The second dataset is from an SOFC anode, composed of a porous nickel/yttria stabilised zirconia (Ni-YSZ) cermet. This material is also made by mixing an ink, but this time it is deposited onto a ceramic substrate and

then sintered at high temperature to bind the components together. Details of the sample preparation, imaging, reconstruction and segmentation approaches used can be found in³⁴ for the cathode and⁴⁴ for the anode. The specifications of both datasets in terms of sizes and resolutions are shown in Table 5.1.

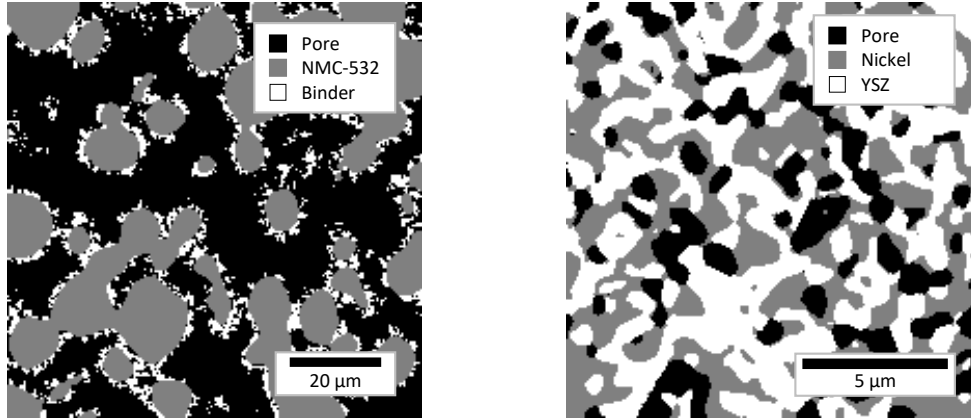


Figure 5.2: Original microstructures: 2D images of the 3D microstructures used as training sets in this work (L) Li-ion cathode, where the black phase represents pore, grey is NMC active material, and white is the organic binder; (R) SOFC anode, where the black phase corresponds to the pore, grey is Nickel and white is YSZ.

Table 5.1: Key details about the two open-source, segmented, nano-tomography datasets

Name	Li-ion cathode	SOFC anode
Materials	NMC-532/Binder/Pore	YSZ/Ni/Pore
Total volume of data / μm^{-3}	$100.7 \times 100.3 \times 100.3$	$124 \times 110 \times 8$
Number of voxels / voxels	$253 \times 252 \times 252$	$1900 \times 1697 \times 124$
Cubic voxel size / nm^3	398^3	65^3
Number of training sub-volumes	13,824	45,492
Reference	34	44

For the Li-ion cathode, approximately 14,000 sub-volumes were extracted from the original image using a rolling function with a stride of 8 voxels. In the case of the SOFC anode, the same process was implemented to extract approximately 45,000 overlapping samples, as shown in in table 5.1. The spatial dimensions of the cropped volumes were selected based on the average size of the largest structuring element. The sub-volume size was selected to guarantee that at least two structuring elements (*i.e.* particular geometric shape that we attempt to extract from the XCT image) could fit in one sub-volume⁴⁵. In the case of the

Li-ion cathode, this structuring element corresponds to the particle size. In the case of the SOFC anode, “particle size” is not easy to define once the sample is sintered, so the sub-volume was selected based on the stabilisation of the two-point correlation function (TPCF).

5.5 Method

This section outlines the architecture of the two neural networks (*i.e.* the Generator and the Discriminator) that constitute the GAN, as well as the methodology implemented for training. A set of microstructural properties are also defined, which are later used to analyse the quality of the microstructural reconstruction when compared to the real datasets.

5.5.1 Pre-treatment of the training set

The image data used in this study is initially stored as 8-bit greyscale elements, where the value of each voxel (3D pixel) is used as a label to denote the material it contains. For example, as in the case of the anode in this study, black (0), grey (127), and white (255), encode pore, metal, and ceramic respectively.

In several previous studies where GANs were used to analyse materials, the samples in question had only two phases and as such, the materials information could be expressed by a single number representing the confidence it belongs to one particular phase. In these cases, any value between 0 and 255 corresponds to a level of uncertainty in the phase prediction, and is commonly shown at the interface between the two phases. However, in cases where the material contains three or more phases, the use of images stored grayscale images can be problematic. The reason for this is that any voxel with a value close to grey (close to 127) could have a double meaning: it could be interpreted as uncertainty in the generator’s prediction between black and white, or it could be interpreted as the grey phase of the material.

The solution to this is the implementation of a data pre-treatment of the materials information referred to as “one-hot” encoding. This means that an

additional dimension is added to the dataset (*i.e.* three spatial dimensions, plus one materials dimension), so an initially 3D cubic volume of $n \times n \times n$, is encoded to a 4D $c \times n \times n \times n$ volume, where c is the number of material phases present. This materials dimension contains a ‘1’ in the element corresponding to the particular material at that location and a ‘0’ in all other elements (hence, “one-hot”). So, what was previous black, white, and grey, would now be encoded as [1,0,0], [0,1,0], and [0,0,1] respectively. This concept is illustrated in figure 5.3 for a three-material sample. It is also easy to decode these 4D volumes back to 3D greyscale, even when there is uncertainty in the labelling, as the maximum value can simply be taken as the label. The advantage of using this technique is the ability to extend the implementation of GANs for the generation of materials with multiple phases. Thus the method introduced in this work is not only restricted for three-phase data, but can be implemented to n -phase materials materials.

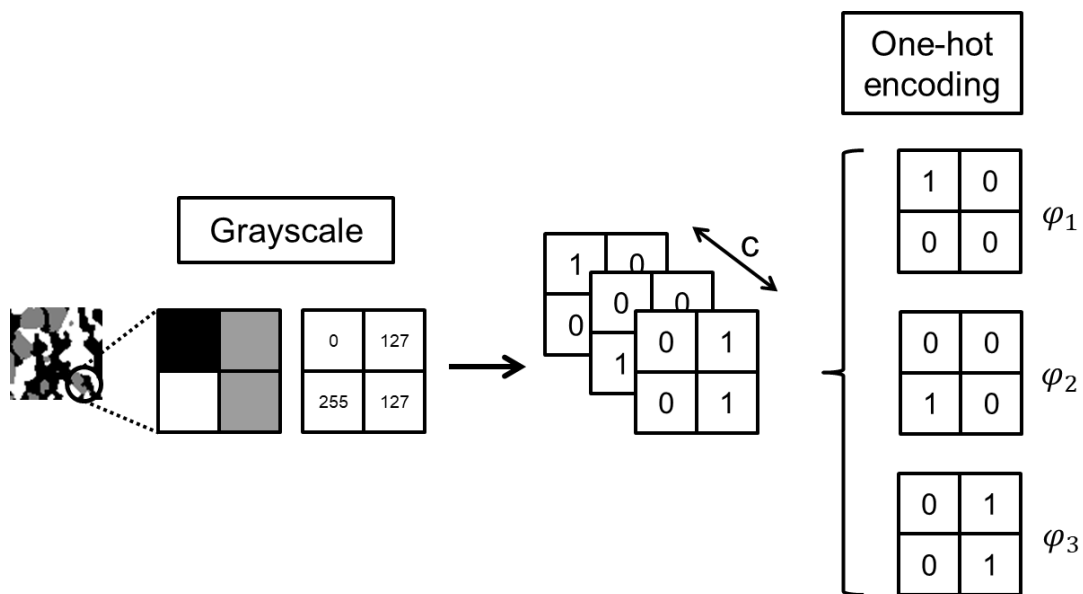


Figure 5.3: One-hot encoding: Schematic showing the implementation of a one-hot encoding techniques for a simple sample of four voxels with three phases: white, grey and black. The 2D image is divided into three channels (corresponding to the three phases), each with two-dimensional matrices of zeros and ones that indicate the phase each voxel corresponds to.

5.5.2 GAN Architecture and Training

The GAN architecture implemented in this work is a volumetric version based on the deep convolutional GAN (DC-GAN) model proposed by Radford et al.⁴⁶. Both generator and discriminator are represented by fully convolutional neural networks. In particular, the convolutional nature of the generator allows it to be scalable, thus it can generate instances from the p_{model} larger than the instances in the original training set, which is useful.

The discriminator is composed of five layers of convolutions, each followed by a batch normalisation. In all cases, the convolutions cover the full length of the materials dimension, c but the kernels within each layer are of smaller spatial dimension than the respective inputs to these layers. The first four layers apply a “leaky” rectified linear unit (leaky ReLU) activation function and the last layer contains a sigmoid activation function that outputs a single scalar constrained between 0 and 1, as it is a binary classifier. This value represents an estimated probability of an input image to belong to the real dataset (output = 1) or to the generated sample (output = 0).

The generator is an approximate mirror of the discriminator, also composed of five layers, but this time transposed convolutions⁴⁷ are used to expand the spatial dimensions in each step. Once again, each layer is followed by a batch normalization and all layers use ReLU as their activation function, except for the last layer which uses a Softmax function, given by equation (5.3)

$$\sigma(\mathbf{x})_i = \frac{e^{x_i}}{\sum_{j=1}^K e^{x_j}} \text{ for } i = 1, \dots, K \text{ and } \mathbf{x} = (x_1, \dots, x_K) \in \mathbb{R}^K \quad (5.3)$$

where x_j represents the j^{th} element of the one-hot encoded vector \mathbf{x} at the last convolutional layer.

It is well known that the hyperparameters that define the architecture of the neural networks have significant impact on the quality of the results and the speed of training. In this work, although a formal hyperparameter optimisation

was not performed due to computational expense, a total of 16 combinations between four hyperparameters was performed. A statistical analysis between the real and generated microstructures was performed (as described in section 5.6), and the optimum architecture was chosen based on these results.

The generator requires a latent vector \mathbf{z} as its input in order to produce variety in its outputs. In this study, the input latent vector \mathbf{z} is of length 100. Table 5.2 summarises all of the GAN’s layers configuration described above, as well as the size, stride and number of kernels applied between each layer, and the padding applied around the volume when calculating the convolutions. As will be discussed later in this paper, although zeros were initially used for padding, the study also explores the use of circular padding, which forces the microstructure to become periodic.

Table 5.2: Dimensionality of each layer in the GAN architecture for each porous material (layers, dimensions, optimiser, input image size, number of training samples) See Figure 5.1

Layer	Function	Input channels	Output channels	Spatial Kernel	Stride	Padding	Batch normalisation	Activation function
Discriminator								
D1	Conv3d	3	16	$4 \times 4 \times 4$	2	1	Yes	LeakyReLU
D2	Conv3d	16	32	$4 \times 4 \times 4$	2	1	Yes	LeakyReLU
D3	Conv3d	32	64	$4 \times 4 \times 4$	2	1	Yes	LeakyReLU
D4	Conv3d	64	128	$4 \times 4 \times 4$	2	1	Yes	LeakyReLU
D5	Conv3d	128	1	$4 \times 4 \times 4$	1	0	No	Sigmoid
Generator								
G1	ConvTransposed3d	100	512	$4 \times 4 \times 4$	1	0	Yes	ReLU
G2	ConvTransposed3d	512	256	$4 \times 4 \times 4$	2	1	Yes	ReLU
G3	ConvTransposed3d	256	128	$4 \times 4 \times 4$	2	1	Yes	ReLU
G4	ConvTransposed3d	128	64	$4 \times 4 \times 4$	2	1	Yes	ReLU
G5	ConvTransposed3d	64	3	$4 \times 4 \times 4$	2	1	No	Softmax

In theory, a Nash equilibrium is achieved after sufficient training; however, in practice this is not always the case. GANs have shown to present instability during training that can lead to mode collapse⁴². Mescheder et al.⁴⁸ present an analysis of the stability of GAN training, concluding that instance noise and zero-centred gradient penalties lead to local convergence. Another proposed stabilisation mechanism, which was implemented effectively in this work, is called one-sided label smoothing⁴². Through this measure, the label 1 corresponding to real images is reduced by a constant ε , such that the new label has the value of $1-\varepsilon$. For all cases in this work, ε has a value of 0.1.

An additional source of instability during training is attributed to the fact that the discriminator learns faster than the generator, particularly at the early stages of training. To stabilise the alternating learning process, it is convenient to set a ratio of network optimisation for the generator and discriminator to $k : 1$. In other words, the generator is updated k times while the discriminator is updated once. In this work k has a value of 2. In both cases (*i.e.* cathode and anode data) stochastic gradient descent is implemented for learning using the ADAM optimiser⁴⁹. The momentum constants are $\beta_1 = 0.5$, $\beta_2 = 0.999$ and the learning rate is 2×10^{-5} . All simulations are performed on a GPU (Nvidia TITAN Xp) and the training process is limited to 72 epochs (c. 48 h).

5.5.3 Microstructural characterisation parameters

As expressed in the introduction, GANs are implicit deep generative models and therefore the learned pdf corresponding to p_{model} is not explicitly provided after training. In order to estimate the accuracy with which p_{model} approximates the real pdf p_{data} , other statistical methods are required as a measure of the error between functions. In this work, the ability of the trained model to accurately capture the pdf of the dataset is estimated by comparing a set of parameters calculated for 100 instances of GAN generated data and 100 randomly chosen real data. These parameters consist on microstructural parameters commonly used to characterise the electrode from 3D volumes, and include morphological properties, transport properties, and statistical correlation functions.

Morphological properties

Three morphological properties are considered in this work, each computed using the open-source software TauFactor⁵⁰. These consist of the volume fractions and specific surface areas, as well as the triple-phase boundary (TPB) densities.

The phase volume fraction ϕ_i is defined as:

$$\phi_i = \frac{V_i}{V} \quad (5.4)$$

where V_i refers to the volume of phase i , calculated as the percentage of voxels

corresponding to this phase, and V to the total volume of the microstructure domain.

The volume specific surface area S_{Ai} is defined as:

$$S_{Ai} = \frac{A_i}{V} = \frac{1}{V} \int dA_i \quad (5.5)$$

where A_i refers to the total surface area of the interface between phase i and the rest of the phases

The TPB density is defined as the length of the intersection among three phases i , j , and k , normalised by the total volume of the microstructure domain. For a cuboid lattice a TPB is defined as the length of the edges where three of the four connecting voxels contain different phases.⁵

Tortuosity and relative diffusivity

The tortuosity factor τ is defined by Cooper *et al.*⁵ as the resistance offered by the morphology of the porous medium towards diffusive transport. Other authors define the tortuosity factor or geometric tortuosity (τ^{geo}) as the ratio of the effective pathway length l^{eff} over the length of the sample l . In both definitions this parameter measures the geometric deviation of the conductive phase from the straight path. Two properties of the tortuosity factor are presented by Cooper *et al.*⁵: firstly, when $\tau = 1$, the flow must be direct, and secondly for all systems $\tau \geq 1$. The tortuosity factor is estimated as the ratio between the steady-state diffusive flow through a conductive phase, F_p , and a fully dense volume of the same size, F_{CV} as:

$$F_p = -A_{CV} D \frac{\phi_i}{\tau} \frac{\Delta c}{L_{CV}} \quad (5.6)$$

$$F_{CV} = -A_{CV} D \frac{\Delta c}{L_{CV}} \quad (5.7)$$

where D is the diffusivity of the conductive phase, c is the local concentration of diffusing species, A_{CV} is the cross-sectional area of the control volume and L_{CV}

is the length of the control volume.⁵

The relative diffusivity, D^{rel} , is a dimensionless measure of the ease with which diffusive transport occurs through a system held between Dirichlet boundaries applied to two parallel faces. The relative diffusivity is inversely correlated to the tortuosity factor of phase i as can be seen from the following equation,

$$D_i^{\text{rel}} = \frac{D_i^{\text{eff}}}{D_i^0} = \frac{\phi_i}{\tau_i} \quad (5.8)$$

where ϕ_i is the volume fraction of phase i , D_i^0 is the intrinsic diffusivity of the bulk material (arbitrarily set to unity), and D_i^{eff} is the calculated effective diffusivity given the morphology of the system. In this study, it is calculated for each of the three material phases separately, as well as in each of the three principal directions in a cubic volume. The tortuosity factors were obtained with the open-source software *TauFactor*⁵⁰, which models the steady-state diffusion problem using the finite difference method and an iterative solver.

Two-point correlation function

Pixel-based reconstruction methods implement statistical correlations to fully characterise a microstructure. According to Lu *et al.*¹² the morphology of heterogeneous media can be fully characterised by specifying the n -point probability function ($S_n(\mathbf{x}^n)$). $S_n(\mathbf{x}^n)$ is defined as the probability of finding n points with positions \mathbf{x}_n in the same phase¹²⁻¹⁴. Based on this, the so-called two-point correlation function (TPCF), $S_2(r)$, allows the first and second-order moments of a microstructure to be characterised^{14,39}. This function has been widely implemented for the stochastic reconstruction of porous media. In this work, this function is used as a metric to compare the generated microstructures and the real ones. It is known that each microstructure has a unique TPCF determined by its exponential decay and stabilisation value. Therefore if the generated microstructures represent the same density function as the real data, it is logical to assert that on average both microstructures will present the same TPCF.

Assuming stationarity (*i.e.* the mean and variance have stabilised), the TPCF is

defined as the non-centred covariance, which is the probability P that two points $x_1 = x$ and $x_2 = x + r$ separated by a distance r belong to the same phase p_i ,

$$S_2(r) = P(x \in p_i, x + r \in p_i) \text{ for } x, r \in \mathbb{R}^d \quad (5.9)$$

At the origin, $S_2(0)$ is equal to the phase volume fraction ϕ_i . The function $S_2(r)$ stabilised at the value of ϕ_i^2 as the distance, r , tends to infinity. This function is not only valuable for analysing the anisotropy of the microstructure, but also to account for the representativeness in terms of volume fraction of sub-volumes taken from the same microstructure sample. In this work, the TPCF of the three phases is calculated along the three Cartesian axes.

5.6 Results

The two GANs implemented in this work, one for each microstructure, used the same architecture defined by table 5.2 and were trained for a maximum of 72 epochs (*i.e.* 72 complete iterations of the training set). The stopping criteria was established through the manual inspection of the microstructural and transport properties every two epochs. Figures 5.4 and 5.5 show the visual reconstruction of both microstructures, beginning with Gaussian noise at epoch 0, and ending with a visually equivalent microstructure at epoch 50. It can be seen that the quality of the generated images improves with an increasing number of iterations; however, as pointed out by Mosser et al.³⁸, this improvement cannot be observed directly from the loss function of the generator. For this reason, a metric for comparing the quality of the generated structures consisted on the morphological parameters and the TPCF. The middle column of figures 5.4 and 5.5 represents a metric of the uncertainty in the generator at each voxel. This uncertainty is estimated in the 2D slices of the generated volumes as the max value in the phase dimension (rather than the label), which indicates the confidence with which it was labelled. A lower uncertainty in the label assigned is shown as a white pixel, while a higher uncertainty is shown as a grey colour. It can be seen that at the beginning of the simulation, the uncertainty was high everywhere, and as the training process proceeds, the uncertainty reduces, mainly at the “bulk” of the phases. The highest uncertainty as expected is presented at the interface, but its significantly reduce

as the epochs increase (as can be seen by comparing epoch 10 with epoch 50).

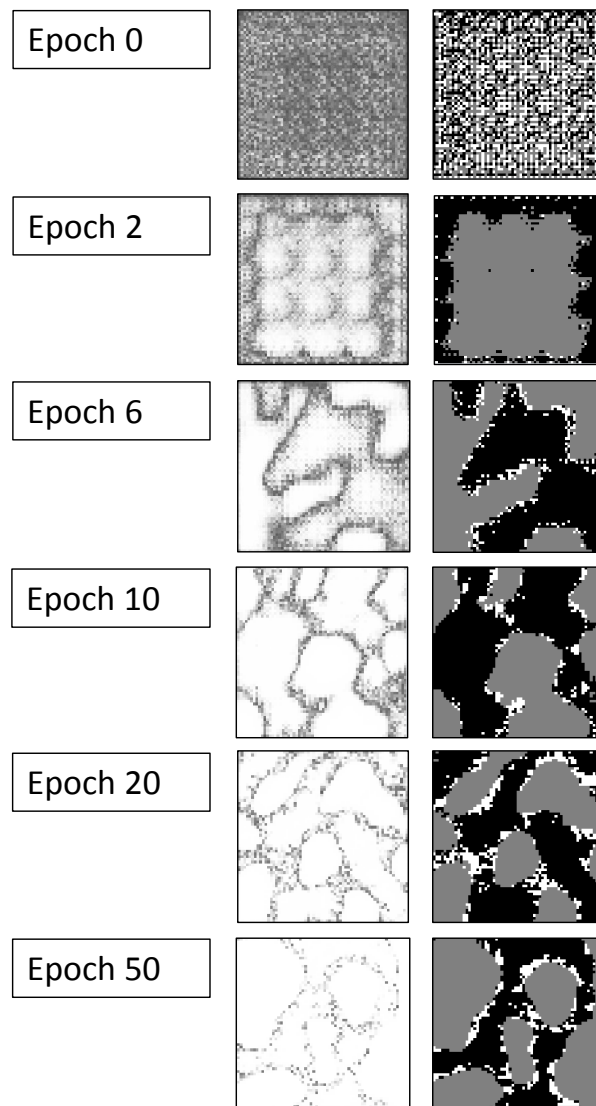


Figure 5.4: Uncertainty maps along the training process for Li-ion cathode. The first column indicates the number of epochs, the middle column shows the uncertainty of the generator for assigning labels to the phases. The final column shows a 2D slice of the generated microstructure as a function of the training epochs.

An initial qualitative comparison of the real and synthetic microstructures is performed. A visual comparison that shows an excellent qualitative agreement between the real and generated data can be seen in figure 5.6, which shows six instances of both real and synthetic data from both the anode and cathode samples. Each slice consists of 64^2 voxels and is obtained from a 64^3 generated

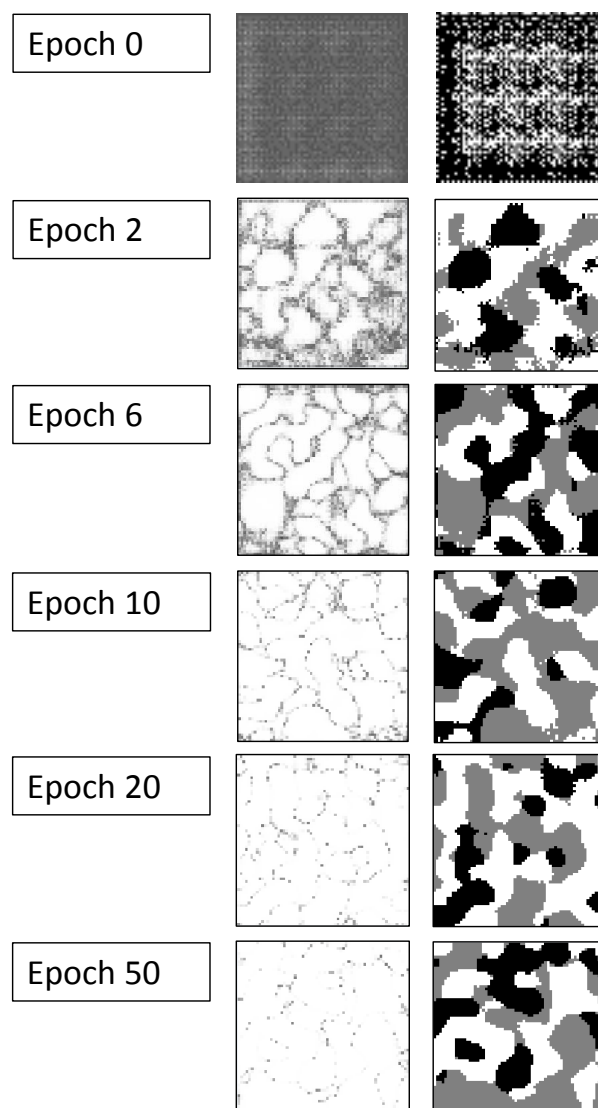


Figure 5.5: Uncertainty maps along the training process for SOFC anode as a function of the training epochs. The first column indicates the number of epochs, the middle column shows the uncertainty of the generator for assigning labels to the phases. The final column shows a 2D slice of the generated microstructure as a function of the training epochs.

volumetric image. This qualitative analysis consisted of visually comparing some key features of the data. In the case of the Li-ion cathode, the structuring element in the microstructure (*i.e.* the NMC particles – grey phase) shows round borders surrounded by a thin layer of binder (white phase), and the phases seem distributed in the same proportion in the real and generated images. In the case of the SOFC, no structuring element is clearly defined; however, the shapes of the white and grey phases of the generated set show the typical shape of the real

data which is particular for the sintering process in the experimental generation of these materials⁴⁴.

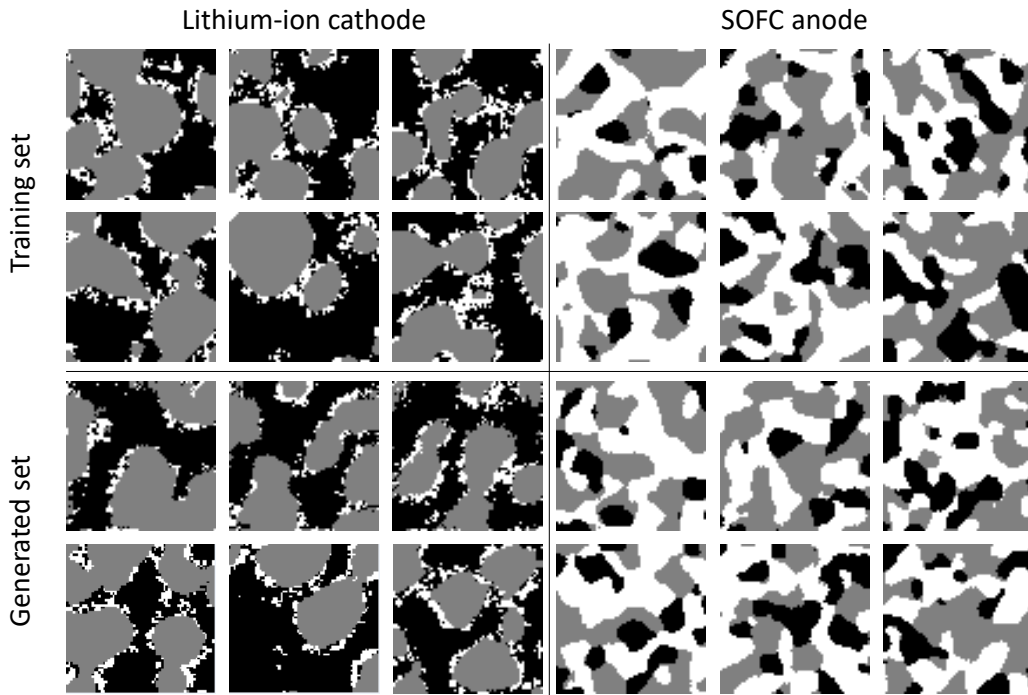


Figure 5.6: Generated vs real: Images from both the cathode and anode samples, illustrating the excellent qualitative correspondence between the real and generated microstructures.

An additional quantitative comparison was performed between the training set and the generated images. For this, 100 microstructures were generated, and 100 were randomly selected from the training set ($64 \times 64 \times 64$ voxels). The comparison results are presented in the following sections.

5.6.1 Lithium-ion cathode results

The results of the calculation of the microstructural characterisation parameters (*i.e.* phase volume fraction, specific surface area and TPB) for the three phases are presented in Figure 5.7. For ease of comparison in a single figure, the results of the specific surface area analysis are presented in terms of the percentage deviation from the maximum mean area value among the three phases, $\Delta(SSA)$. In the case of the cathode, the maximum mean area, $A_{\max, \text{mean}}$, corresponds to the mean area of the white phase (binder) of the training set ($A_{\max, \text{mean}} = 0.72 \mu\text{m}^{-1}$) and all other areas, A_i , are normalised against this.

$$\Delta(SSA) = \frac{A_i - A_{\max, \text{mean}}}{A_{\max, \text{mean}}} \quad (5.10)$$

The phase volume fraction, specific surface area and relative diffusivity show good agreement between the real and the synthetic data, particularly in the mean values of both distributions. These mean values and standard deviations are reported in Table 5.3. The distribution of relative diffusivity in the white phase is very close to zero due to the low volume fraction and resulting low percolation of this phase. For the TPB density, the mean of the generated set is nearly 10% greater than that of the training data; however, nearly all of the values for the synthetic data do still fall within the same range as the training set.

Table 5.3: Results of volume fractions, specific surface areas, triple-phase boundary densities and relative diffusivities calculated from the real and generate datasets. The black phase corresponds to the pores, white phase corresponds to the binder and grey phase corresponds to the NMC-532.

Dataset	Phase	Volume fraction	Specific surface area / μm^{-1}	TPB density / μm^{-2}	D^{rel}
Real	Black	0.50 ± 0.06	0.71 ± 0.06	0.43 ± 0.04	0.26 ± 0.07
	Grey	0.39 ± 0.06	0.34 ± 0.03		0.08 ± 0.04
	White	0.11 ± 0.01	0.72 ± 0.06		0.003 ± 0.001
Generated	Black	0.49 ± 0.01	0.72 ± 0.02	0.48 ± 0.02	0.26 ± 0.02
	Grey	0.41 ± 0.01	0.36 ± 0.02		0.07 ± 0.02
	White	0.102 ± 0.003	0.72 ± 0.02		0.003 ± 0.001

From Figure 5.7 it is clear that the synthetic realisations show a smaller variance in all of the calculated microstructural properties compared to the real datasets.

The averaged $S_2(\mathbf{r})/S_2(0)$ along three directions is shown in Figure 5.8 for each of the three phases present in a Li-ion cathode. Since $S_2(0)$ represents the volume fraction ϕ_i of each phase, $S_2(\mathbf{r})/S_2(0)$ is a normalisation of the TPCF that ranges between 0 and 1. In this expression, $S_2(\mathbf{r})/S_2(0)$ stabilised at the value of ϕ_i . In all cases, the average values of $S_2(\mathbf{r})/S_2(0)$ of the synthetic realisations follow the same trend as the training data. The black phase shows a near exponential decay, the grey phase presents a small hole effect and the white phase shows an exponential decay. A hole effect is present in a two-point correlation function when the decay is non-monotonic and presents peaks and

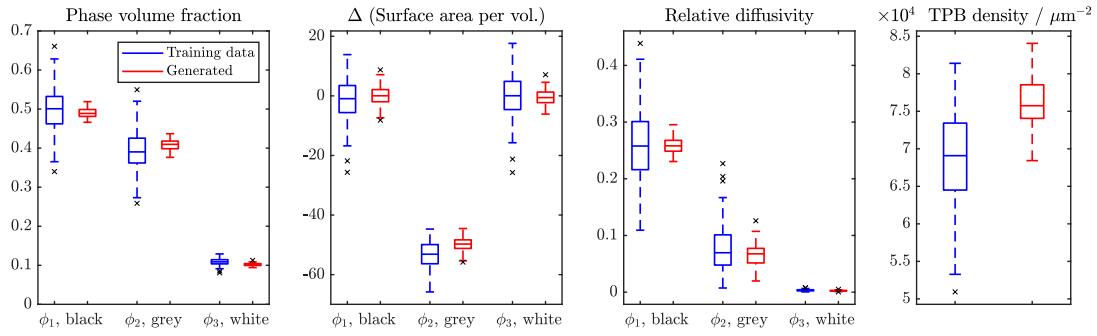


Figure 5.7: Characterisation properties Li-ion: Microstructural characterisation properties for 100 training samples (blue) and 100 generated realisations (red) for the Li-ion cathode. In all cases, greater diversity is observed in the training set than the generated samples. Boxes show 25th to 75th percentiles and the median. Black crosses show outliers.

valleys. This property indicates a form of pseudo-periodicity and in most cases is linked to anisotropy^{51,52}. For the black and grey phases, the $S_2(\mathbf{r})/S_2(0)$ values of the generated images show a slight deviation from the training set, however this value falls within the standard deviation of the real data.

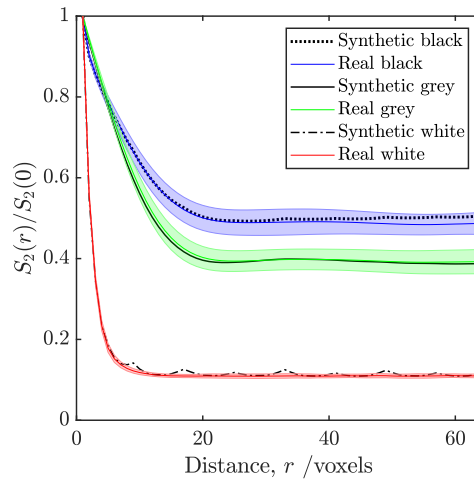


Figure 5.8: TPCF Li-ion cathode Averaged TPCF for the three phases present in the Li-ion cathode. The averaged values are obtained from 100 training samples and 100 synthetic realisations generated with the GAN model. The coloured band represents the standard deviation of the metric from the real data at each value of r .

Figure 5.9 shows the results of the normalised TPCF (*i.e.* $S_2(\mathbf{r})/S_2(0)$) of the three phases (pores, NMC-532 and binder) along the three directions. For all cases, the synthetic data follows the same trend as the real dataset, and is

able to represent the anisotropy of some phases in the material. Table 5.4 shows the results of a detailed description of the decay along the three axis and the stabilisation of $S_2(\mathbf{r})/S_2(0)$ for each phase.

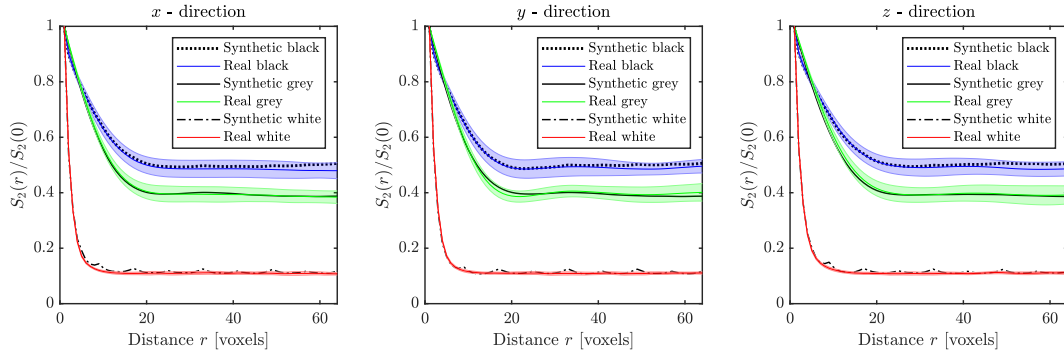


Figure 5.9: $S_2(\mathbf{r})/S_2(0)$ of the black phase corresponding to the pores (blue line), grey phase corresponding to the NMC particles (green line) and white phase corresponding to the binder (red line) in a Li-ion cathode.

Table 5.4: Detailed description of the normalised TPCF for the Li-ion cathode along the three directions for each of the three phases (pores, NMC and binder)

Phase	x	y	z	Stabilisation
Black (pores)	near exponential decay	near exponential decay	near exponential decay	0.5
Grey (NMC)	near exponential decay	small hole effect	near exponential decay	0.39
White (binder)	exponential decay	exponential decay	exponential decay	0.11

5.6.2 SOFC anode results

Figure 5.10 presents the results of the SOFC anode microstructural characterisation parameters calculated for the training data and for the synthetic realisations generated with the GAN model. The $\Delta(SSA)$ was calculated using the same approach as described in the previous section, but in the case of the anode, the maximum mean area was the mean area of the white phase (YSZ) of the training set ($A_{\max, \text{mean}} = 3.98 \mu\text{m}^{-1}$)

The results in Figure 5.10 show a comparable mean and distributions for the morphological properties calculated, as well as for the effective diffusivity of the training images and the synthetic realisations. Once again, the synthetic images

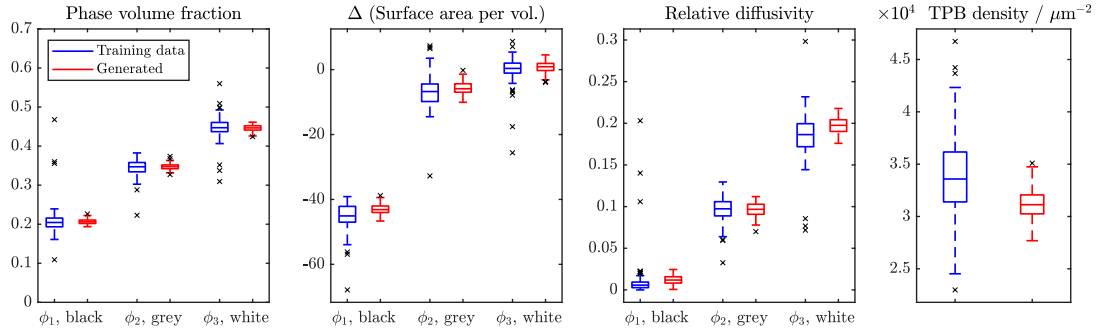


Figure 5.10: Characterisation properties SOFC: Microstructural characterisation properties for 100 training samples and 100 generated realisations for the SOFC anode. Boxes show 25th to 75th percentiles and the median. Black crosses show outliers.

show lower variance in the calculated properties than the training set. These mean values and standard deviations are reported in Table 5.5.

Table 5.5: Results of volume fractions, specific surface areas, triple-phase boundary densities and relative diffusivities calculated from the real and generate datasets. The black phase corresponds to the pores, white phase corresponds to the ceramic (*i.e.* YSZ) and grey phase corresponds to the metal (*i.e.* Ni).

Dataset	Phase	Volume fraction	Specific surface area / μm^{-1}	TPB density / μm^{-2}	D^{rel}
Real	Black	0.21 ± 0.04	2.15 ± 0.17	8.10 ± 0.97	0.01 ± 0.03
	Grey	0.34 ± 0.02	3.66 ± 0.21		0.10 ± 0.02
	White	0.45 ± 0.03	3.93 ± 0.16		0.19 ± 0.03
Generated	Black	0.21 ± 0.01	2.24 ± 0.06	7.37 ± 0.32	0.01 ± 0.01
	Grey	0.35 ± 0.01	3.71 ± 0.08		0.10 ± 0.01
	White	0.45 ± 0.01	3.96 ± 0.06		0.20 ± 0.01

Once again, the difference in the diversity of synthetic images with respect to the training set can be clearly seen in supplementary Figure S3 where the effective diffusivity averaged over the three directions for each phase is plotted against its respective volume fraction.

The TPCF was calculated for the three phases along the three Cartesian directions. Figure 5.11 shows the value of $S_2(\mathbf{r})/S_2(0)$ for the three phases present in the SOFC anode. The averaged results show an exponential decay in the black phase, a small hole effect⁵² in the grey phase and a pronounced hole effect in the white phase.

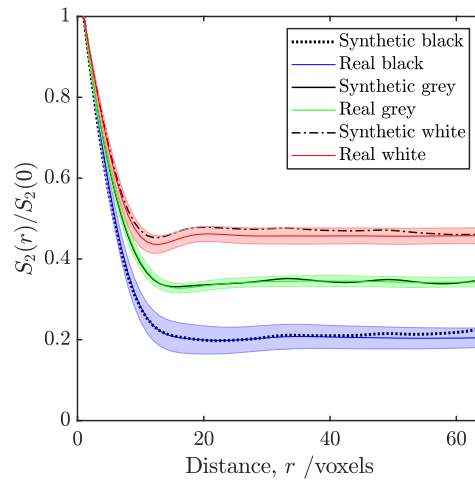


Figure 5.11: TPCF SOFC anode: Averaged TPCF for the three phases present the SOFC anode. The averaged values are obtained from 100 training samples and 100 synthetic realisations generated with the GAN model

Figure 5.12 shows the results of the normalised TPCF (*i.e.* $S_2(\mathbf{r})/S_2(0)$) of the three phases (pores, Ni and YSZ) along the three directions. For all cases, the synthetic data follows the same trend as the real dataset, and is able to represent the anisotropy of some phases in the material. Table 5.6 shows the results of a detailed description of the decay along the three axis and the stabilisation of $S_2(\mathbf{r})/S_2(0)$ for each phase.

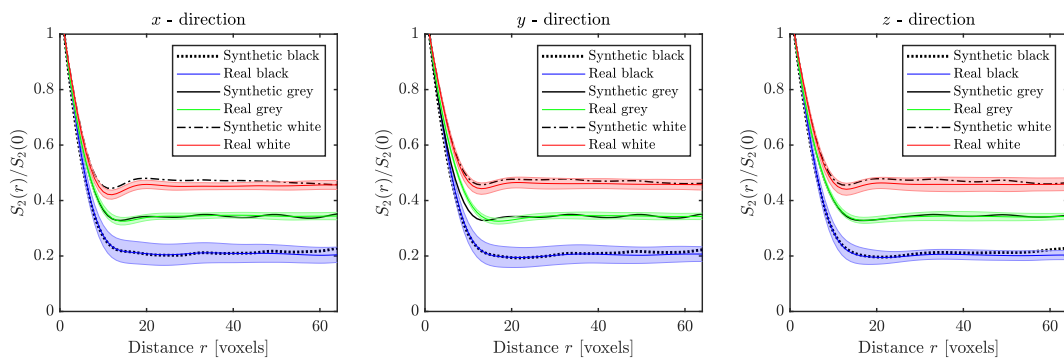


Figure 5.12: $S_2(\mathbf{r})/S_2(0)$ of the black phase corresponding to the pores (blue line), grey phase corresponding to the Nickel (green line) and white phase corresponding to the YSZ (red line) in a LI-ion cathode.

Table 5.6: Detailed description of the normalised TPCF for the SOFC anode along the three directions for each of the three phases (pores, Ni and YSZ)

Phase	x	y	z	Stabilisation
Black (pores)	near exponential decay	near exponential decay	near exponential decay	0.2
Grey (Ni)	small hole effect	small hole effect	near exponential decay	0.35
White (YSZ)	pronounced hole effect	pronounced hole effect	pronounced hole effect	0.45

5.6.3 Representativity

This method uses a set of sub-volumes obtained from X-ray tomographic images for the Li-ion cathode and PFIB-SEM for the SOFC anode, as training sets for the GANs. In this work, the methodology was applied for the reconstruction of two different microstructures commonly used for energy storage technologies: a Li-ion cathode and an SOFC anode. The size of the training images was selected according to the size of the structuring element of the microstructure. For the Li-ion cathode, there is a clear characteristic feature consisting on the NMC particle size (*i.e.* grey phase). The average particle diameter is 35 voxels, so a 64^3 voxels sub-volume can capture the volume of an entire particle and most of the volume of neighbouring particles. In the case of the SOFC anode, all three phases form continuous networks so no structuring element (such as grain size)³⁸ is observed. Therefore, a standard training size of 64^3 voxels⁴⁶ was implemented based on a level of representativity in the measured volume fraction.

The image training size is a topic of interest as it is closely related to the representativeness of the training set. As previously shown, in the case of structures with a characteristic feature such as grain size or particle size, it is possible to use this as a criteria for selecting a training image size; however for the cases where the structure is irregular (as is the case of the SOFC anode), highly porous or a continuously fibrous media, choosing the ideal training size becomes a challenging task.

It is well established among authors¹²⁻¹⁶ that a two-point statistics function provides an accurate description of the long-range properties and therefore could provide an insight into the size of a representative elementary volume (REV). In some cases, the size of a representative volume can be estimated based on the stabilisation value of the two-point statistic function $S_2(\mathbf{r})$ ³⁹. This would

require an evaluation of $S_2(\mathbf{r})$ along the three directions and in all phases present in the microstructure. In the two materials analysed in this work, stabilisation was achieved at an average of 40 voxels along the three directions in the three phases. This shows that a selection of 64^3 sub-volume as training set provides a fair representation of the microstructure, at least in terms of volume fraction.

Although the $S_2(\mathbf{r})$ provides essential information about the constitution and long-range properties of microstructures, for more complex samples where the $S_2(\mathbf{r})$ does not achieve stabilisation, a better understanding of the REV in terms of the microstructural characterisation parameters is required³⁹. As mentioned by Mosser et al.³⁸, an estimation of the REV of the specific surface area is more representative of the morphology of a porous medium. In the case of three-phase data, an analysis of a REV of the TPB could provide an even deeper insight of the representativeness of the sub-volume since this particular parameter accounts for the interaction of the three phases. To the authors' knowledge no conclusive research has been reported in the literature which provides a full analysis on the representativeness of properties like specific surface area and TPB. An initial approximation would involve a statistical analysis of such properties obtained experimentally from sub-volumes of tomographic data at different sections of a larger volume. This approach however is exhaustive in terms of experimentation, and unique for each microstructure, therefore it cannot be generalised for a wide range of porous materials. Based on this, a thorough research on the implementation of long range functions, such as the two-point statistics function, that can provide information on the REV of additional properties is recommended as future work.

5.6.4 Generating larger volumes

The minimum generated samples are the same size as the training data sub-volumes (i.e. 64^3 for both cases analysed in this work), but can be increased to any arbitrarily large size by increasing the size of the input z .

In this work samples as large as 3203 voxels were generated. The generated images are shown in figure 5.13

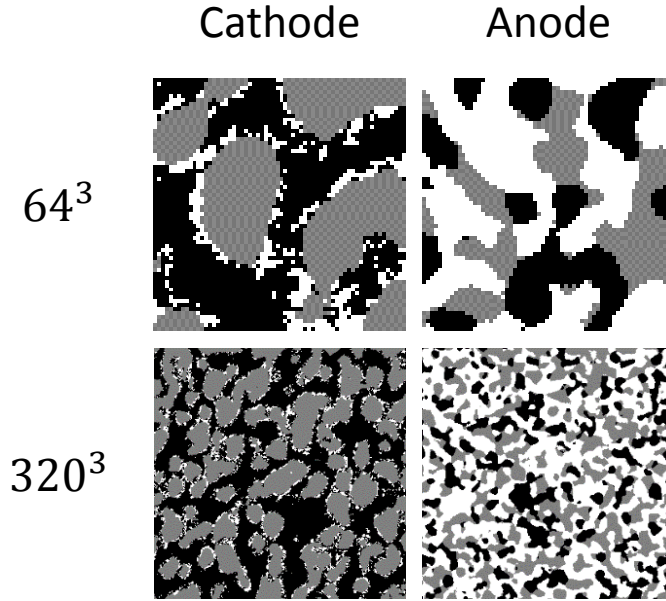


Figure 5.13: Large generated images of SOFC anode and Li-ion cathode based on previously trained generator with training data of 64^3 voxels.

5.6.5 Computational expense

GANs present the capability of generating larger images with the same probability distribution function of the real dataset by increasing the size of the \mathbf{z} space and using this larger latent space as input of the trained generator. The size of the larger images is given by the following equation:

$$\mathbf{z} \sim \mathcal{N}(0, 1)^{100 \times 1 * \alpha \times 1 * \alpha \times 1 * \alpha} \quad (5.11)$$

$$G_{\theta}(\mathbf{z}) \rightarrow \mathbb{R}^{3 \times \lambda \times \lambda \times \lambda} \quad (5.12)$$

$$\lambda = 64 + (\alpha - 1) \times 16 \quad (5.13)$$

where α corresponds to the incremental factor. Since the generation of larger images does not require further training, the generation is comparatively faster than the training process. The increase in computational time with respect to an increase in the size of the generated images is linear, as shown in figure 5.14. This linear trend is in agreement with the results presented by Mosser et al.^{38,39}.

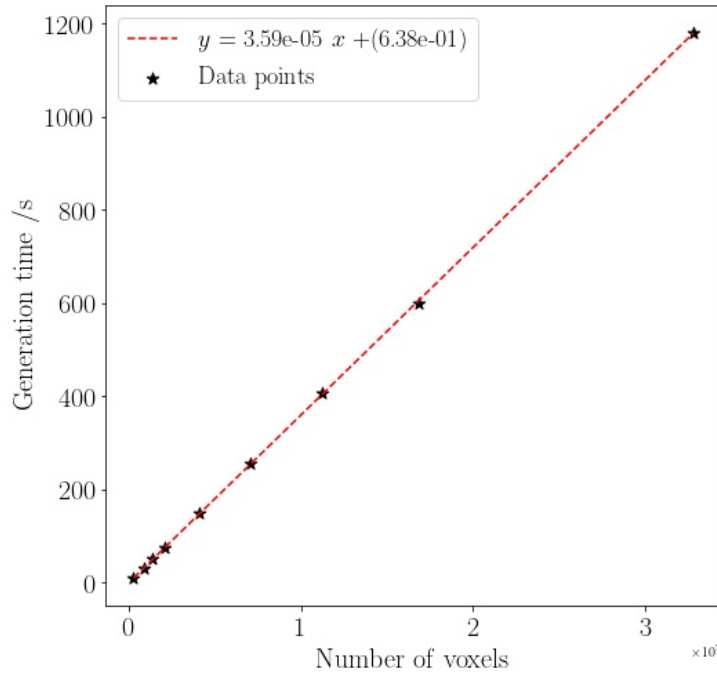


Figure 5.14: Generation time of 3D microstructures of various sizes using one single trained generator as a function of the number of voxels

5.6.6 Mode collapse

In the presence of mode collapse, the generator does not have an incentive to move to a different area within the optimisation space since it has found a local minimum. There are different levels of mode collapse, the perfect case being when the generator memorises the training set, thus producing the same image every time. A thorough characterisation of the microstructure according to their morphological features can determine the accuracy of the generator in representing the real data; however, it does not account for the existence or level of mode collapse. An approach suggested by Radford et al.⁴⁶ is implemented in this work to visually analyse the existence of memorisation of the dataset. This approach consists on performing an interpolation between two points in the latent space \mathbf{z} , given by equations 5.14 and 5.15:

$$\mathbf{z}_{\text{start}}, \mathbf{z}_{\text{end}} \sim \mathcal{N}(0, 1)^{100 \times 1 \times 1 \times 1}, \beta \in [0, 1] \quad (5.14)$$

$$\mathbf{z}_{\text{int}} = \beta * \mathbf{z}_{\text{start}} + (1 - \beta) * \mathbf{z}_{\text{end}} \quad (5.15)$$

Where β is a set of integers between 0 and 1. The smooth transition in the images generated between the two points $G(\mathbf{z}_{\text{start}})$ and $G(\mathbf{z}_{\text{end}})$ indicates that the generator has not memorised the training set but has accurately learned a lower-dimensional representation of \mathbf{z} .³⁹ The interpolation between two points in the \mathbf{z} space is shown in figure 5.15.

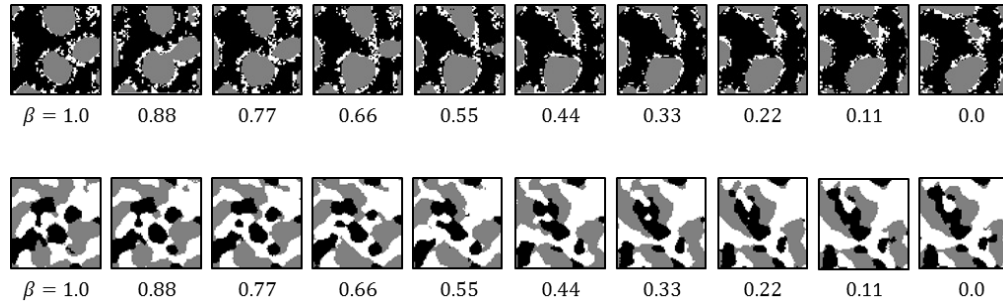


Figure 5.15: Interpolation in the latent space \mathbf{z} from $\mathbf{z}_{\text{start}}$ to \mathbf{z}_{end} . The smooth transition between both points in both microstructures shows the inexistence of a total mode collapse.

5.6.7 Periodic boundaries

Once the generator parameters have been trained, the generator can be used to create periodic microstructures of arbitrary size. This is simply achieved by applying circular spatial padding to the first transposed convolutional layer of the generator (although other approaches are possible). Figure 5.16 shows generated periodic microstructures for both the cathode and anode, arranged in an array to make their periodic nature easier to see. Additionally, local scalar flux maps resulting from steady-state diffusion simulations in *TauFactor*⁵⁰ are shown for each microstructure. In both cases, the upper flux map shows the results of the simulation with mirror (*i.e.* zero flux) boundaries on the vertical edges, and the lower one shows the results of the simulation with periodic boundaries on the vertical edges. Comparing the results from the two boundary conditions, it is clear that using periodic boundaries opens up more paths that enable a larger flux due to the continuity of transport at the edges. Furthermore, this means that the flow effectively does not experience any edges in the horizontal direction, which means that, unlike the mirror boundary case, there are no unrealistic regions of the volume due to edge effects.

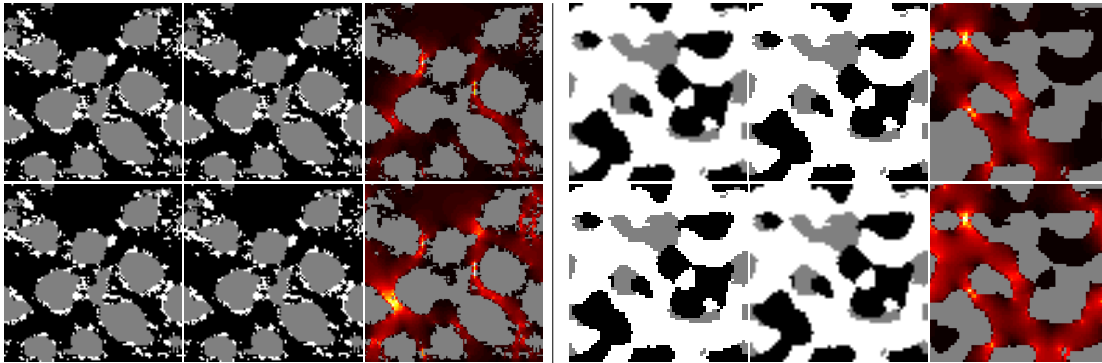


Figure 5.16: Periodic boundaries: For both the Li-ion cathode (L) and the SOFC anode (R), periodic microstructures were generated by slightly changing the input to the generator. For each electrode, four instances are shown making the periodicity easier to observe. Also shown are local scalar flux maps generated from steady-state diffusion simulations in TauFactor with either mirror (top) or periodic (bottom) boundary conditions implemented on the vertical edges.

5.7 Discussion

This work presents a technique for generating synthetic three-phase, three-dimensional microstructure images through the use of deep convolutional generative adversarial networks. The main contributions of this methodology are mentioned as follows: The results from comparing the morphological metrics, relative diffusivities and two-point correlation functions all show excellent agreement between the real and generated microstructure. One of the properties that is different from the averaged value in both cases is the TPB density. Nevertheless, its value falls within the confidence interval of the real dataset. This comparison demonstrates that the stochastic reconstruction developed in this work is as accurate as the state-of-the-art reconstruction methods reported in the introduction of this article, since the results of the TPCF and microstructural data fall in line with the ones reported in the literature. One variation from previous methodologies is that GANs do not require additional physical information from the microstructure as input data. The methodology was developed to approximate the probability distribution function of a real dataset, so it learns to approximate the voxel-wise distribution of phases, instead of directly inputting physical parameters, which is significant; although inputting physical parameters in addition may be

beneficial⁵³.

Despite the accurate results obtained in terms of microstructural properties, a number of questions still need to be addressed. One of which involves the diversity in terms of properties of the generated data. Particularly in the case of the Li-ion cathode microstructure, the generated samples present less variation than the training set. This issue was already encountered by Mosser et al.³⁹ and low variation in the generated samples is a much discussed issue in the GAN literature. The typical explanation for this is based on the original formulation of the GAN objective function, which is set to represent unimodal distributions, even when the training set is multimodal^{39,40,42}. This behaviour is known as “mode collapse” and is observed as a low variability in the generated images. A visual inspection of the generated images as well as the accuracy in the calculated microstructural properties do not provide a sufficient metric to guarantee the inexistence of mode collapse or memorisation of the training set.

Figures 5.7 and 5.10 show some degree of mode collapse given by the small variance in the calculated properties of the generated data. Nevertheless, further analysis of the diversity of the generated samples is required to evaluate the existence of mode collapse based on the number of unique samples that can be generated^{54,55}. Following the work of Radford et al.⁴⁶, an interpolation between two points in the latent space is performed to test the absence of memorisation in the generator. The results shown in Figure S8 present a smooth transformation of the generated data as the latent vectors is progressed along a straight path. This indicates that the generator is not memorising the training data but has learned the meaningful features of the microstructure.

The presence of mode collapse and vanishing gradient remain the two main issues with the implementation of GANs. As pointed out by⁵⁶, these problems are not necessarily related to the architecture of GANs, but potentially to the original configuration of the loss function. This work implements a DC-GAN architecture with the standard loss function; however, recent improvements of GANs have focused on reconfiguring the loss function to enable a more stable

training and more variability in the output. Some of these include WGAN (and WGAN-GP) based on the Wasserstein or Earthmover distance^{57,58}, LSGAN which uses least squares and the Pearson divergence⁵⁹, SN-GAN that implement a spectral normalisation⁶⁰, among others⁵⁶. Therefore, an improvement of the GAN loss function is suggested as future work in order to solve the problems related to low variability (i.e. slight mode collapse) and training stability.

The applicability of GANs can be extended to transfer the learned weights of the generator (i.e. $G_\theta(\mathbf{z})$) into a) generating larger samples of the same microstructure, b) generating microstructure with periodic boundaries, c) performing an optimisation of the microstructure according to a certain macroscopic property based on the latent space \mathbf{z} . As such, G_θ can be thought of as a powerful “virtual representation” of the real microstructure and it interested to note that the total size of the trained parameters, $\theta^{(G)}$ is just 55 MB.

The minimum generated samples are the same size as the training data sub-volumes (i.e. 64^3 for both cases analysed in this work), but can be increased to any arbitrarily large size by increasing the size of the input \mathbf{z} . Although the training process of the DC-GAN is computationally expensive, once a trained generator is obtained, it can produce image data inexpensively. The relation between computation time and generated image size is shown in Figure S7.

The ability of the DC-GAN to generate periodic structures has potentially profound consequences for the simulation of electrochemical processes at the microstructural scale. Highly coupled, multiphysics simulations are inherently computational expensive^{61,62}, which is exacerbated by the need to perform them on volumes large enough to be considered representative. To make matters worse, the inherent non-periodic nature of real tomographic data, combined with the typical use of “mirror” boundary conditions means that regions near the edges of the simulated control volume will behave differently from those in the bulk. This leads to a further increase in the size of the simulated volume required, as the impact of the “near edge” regions need to be eclipsed by the bulk response. Already common practice in the study of turbulent flow^{63,64}, the

use of periodic boundaries enables much smaller volumes to be used, which can radically accelerate simulations. The flux maps shown in Figure 5.16 highlight the potential impact even for a simple diffusion simulation and the calculated transport parameters of these small volumes are much closer to the bulk response when periodic boundaries are implemented.

Examples of generated periodic (and similar non-periodic) volumes for both the Li-ion cathode and SOFC anode can be found in the supplementary materials accompanying this paper and the authors encourage the community to investigate their utility. A detailed exploration of the various methods for reconfiguring the generator's architecture for the generation of periodic boundaries, as well as an analysis of the morphological and transport properties of the generated microstructures compared to the real ones are ongoing and will be presented in future work.

An additional benefit of the use of GANs in microstructural generation lies in the ability to interpolate in the continuous latent space to generate more samples of the same microstructure. The differentiable nature of GANs enables the latent space that parametrises the generator to be optimised. Li et al.⁴¹ have implemented a Gaussian process to optimise the latent space in order to generate an optimum 2D two-phase microstructure. Other authors⁶⁵ have used an in-painting technique to imprint over the three-dimensional image some microstructural details that are only available in two-dimensional conditioning data. This process is performed by optimising the latent vector with respect to the mismatch between the observed data and the output of the generator^{39,65}. A potential implementation of the in-painting technique could involve adding information from electron backscatter diffraction (EBSD), such as crystallographic structure and orientation, into the already generated 3D structures, which would be of great interest to the electrochemical modelling community.

Future work will aim to extend the study by Li et al.⁴¹ to perform an optimisation of the 3D three-phase microstructure based on desired morphological properties by optimising the latent space. One proposed pathway to improve these

optimisation process would involve providing physical parameters to the GAN architecture. This could be achieved by adding a physics-specific loss component to penalise any deviation from a desired physical property⁵³. It could also involve giving a physical meaning to the \mathbf{z} space through the implementation of a Conditional GAN algorithm⁶⁶. With this, apart from the latent vector, the Generator has a second input \mathbf{y} related to a physical property. Thus, the Generator becomes $G(\mathbf{z}, \mathbf{y})$ and produces a realistic image with its corresponding physical property

5.8 Conclusions

This work presents a method for generating synthetic three-dimensional microstructures composed of any number of distinct material phases, through the implementation of DC-GANs. This method allows the model to represent the statistical and morphological properties of the real microstructure, which are captured in the weights of the trained discriminator and generator networks.

A pair of open-source, tomographically derived, three-phase microstructural datasets were investigated: a lithium-ion battery cathode and a solid oxide fuel cell anode. Various microstructural properties were calculated for 100 sub-volumes of the real data and these were compared to 100 instances of volumes created by the trained generator. The results showed excellent agreement across all metrics, although the synthetic structures showed a smaller variance compared to the training data, which is a commonly reported problem for DC-GANs and mitigation strategy will be reported in future work.

Two issues encountered when training the DC-GANs in this study were instability (likely due to a vanishing gradient) and moderate mode collapse. Both issues can be attributed to the GANs loss function and solutions have been suggested in the literature, the implementation of which will be explored in future work.

Two particular highlights of this work include the ability to generate arbitrarily large synthetic microstructural volumes and the generation of periodic

boundaries, both of which are of high interest to the electrochemical modelling community. A detailed study of the impact of periodic boundaries on the reduction of simulation times is already underway.

Future work will take advantage of the continuity of the latent space, as well as the differentiable nature of GANs, to perform optimisation of certain morphological and electrochemical properties in order to discover improved electrode microstructures for batteries and fuel cells.

References

- [1] M. Weyland, P. A. Midgley, and J. M. Thomas, “Electron tomography of nanoparticle catalysts on porous supports: A new technique based on Rutherford scattering,” *Journal of Physical Chemistry B*, vol. 105, no. 33, pp. 7882–7886, 2001.
- [2] J. Méndez-Venegas and M. A. Díaz-Viera, “Geostatistical modeling of clay spatial distribution in siliciclastic rock samples using the plurigaussian simulation method,” *Geofísica Internacional*, vol. 52, no. 3, pp. 229–247, 2013.
- [3] P. Fantazzini, R. J. S. Brown, and G. C. Borgia, “Bone tissue and porous media: Common features and differences studied by NMR relaxation,” *Magnetic Resonance Imaging*, vol. 21, no. 3-4, pp. 227–234, 2003.
- [4] H. Moussaoui, R. K. Sharma, J. Debayle, Y. Gavet, G. Delette, and J. Laurencin, “Microstructural correlations for specific surface area and triple phase boundary length for composite electrodes of solid oxide cells,” *Journal of Power Sources*, vol. 412, no. November 2018, pp. 736–748, 2019.
- [5] S. J. Cooper, A. Bertei, D. P. Finegan, and N. P. Brandon, “Simulated impedance of diffusion in porous media,” *Electrochimica Acta*, vol. 251, pp. 681–689, 2017.
- [6] H. Moussaoui, J. Laurencin, Y. Gavet, G. Delette, M. Hubert, P. Cloetens, T. Le Bihan, and J. Debayle, “Stochastic geometrical modeling of solid oxide cells electrodes validated on 3D reconstructions,” *Computational Materials Science*, vol. 143, pp. 262–276, 2018.
- [7] L. Holzer, B. Iwanschitz, T. Hocker, B. Münch, M. Prestat, D. Wiedenmann, U. Vogt, P. Holtappels, J. Sfeir, A. Mai, and T. Graule, “Microstructure degradation of cermet anodes for solid oxide fuel cells: Quantification of nickel grain growth in dry and in humid atmospheres,” *Journal of Power Sources*, vol. 196, no. 3, pp. 1279–1294, 2011.
- [8] D. S. Eastwood, R. S. Bradley, F. Tariq, S. J. Cooper, O. O. Taiwo, J. Gelb, A. Merkle, D. J. Brett, N. P. Brandon, P. J. Withers, P. D. Lee, and P. R. Shearing, “The application of phase contrast X-ray techniques for imaging Li-ion battery electrodes,” *Nuclear Instruments and Methods in Physics Research*,

- Section B: Beam Interactions with Materials and Atoms*, vol. 324, pp. 118–123, 2014.
- [9] N. Ni, S. J. Cooper, R. Williams, N. Kemen, D. W. McComb, and S. J. Skinner, “Degradation of $(\text{La}_{0.6}\text{Sr}_{0.4})_{0.95}(\text{Co}_{0.2}\text{Fe}_{0.8})\text{O}_{3-\delta}$ Solid Oxide Fuel Cell Cathodes at the Nanometer Scale and below,” *ACS Applied Materials and Interfaces*, vol. 8, no. 27, pp. 17360–17370, 2016.
- [10] P. Pietsch and V. Wood, “X-Ray Tomography for Lithium Ion Battery Research: A Practical Guide,” *Annual Review of Materials Research*, vol. 47, no. 1, pp. 451–479, 2017.
- [11] J. A. Quiblier, “A new three-dimensional modeling technique for studying porous media,” *Journal of Colloid And Interface Science*, vol. 98, no. 1, pp. 84–102, 1984.
- [12] B. Lu and S. Torquato, “N-Point Probability Functions for a Lattice Model of Heterogeneous Media,” *Physical Review B*, vol. 42, no. 7, pp. 4453–4459, 1990.
- [13] C. L. Yeong and S. Torquato, “Reconstructing random media,” *Physical Review E - Statistical Physics, Plasmas, Fluids, and Related Interdisciplinary Topics*, vol. 57, no. 1, pp. 495–506, 1998.
- [14] C. L. Yeong and S. Torquato, “Reconstructing random media. II. Three-dimensional media from two-dimensional cuts,” *Physical Review E - Statistical Physics, Plasmas, Fluids, and Related Interdisciplinary Topics*, vol. 58, no. 1, pp. 224–233, 1998.
- [15] C. Manwart, S. Torquato, and R. Hilfer, “Stochastic reconstruction of sandstones,” *Physical Review E - Statistical Physics, Plasmas, Fluids, and Related Interdisciplinary Topics*, vol. 62, no. 1 B, pp. 893–899, 2000.
- [16] N. Sheehan and S. Torquato, “Generating microstructures with specified correlation functions,” *Journal of Applied Physics*, vol. 89, no. 1, pp. 53–60, 2001.
- [17] Y. Jiao, F. H. Stillinger, and S. Torquato, “Modeling heterogeneous materials via two-point correlation functions: Basic principles,” *Physical Review E - Statistical, Nonlinear, and Soft Matter Physics*, vol. 76, no. 3, pp. 1–37, 2007.

- [18] Y. Jiao, F. H. Stillinger, and S. Torquato, "Modeling heterogeneous materials via two-point correlation functions. II. Algorithmic details and applications," *Physical Review E - Statistical, Nonlinear, and Soft Matter Physics*, vol. 77, no. 3, pp. 1–35, 2008.
- [19] V. Sundararaghavan, "Reconstruction of three-dimensional anisotropic microstructures from two-dimensional micrographs imaged on orthogonal planes," *Integrating Materials and Manufacturing Innovation*, vol. 3, no. 1, pp. 1–11, 2014.
- [20] Y. Suzue, N. Shikazono, and N. Kasagi, "Micro modeling of solid oxide fuel cell anode based on stochastic reconstruction," *Journal of Power Sources*, vol. 184, no. 1, pp. 52–59, 2008.
- [21] A. Hasanabadi, M. Baniassadi, K. Abrinia, M. Safdari, and H. Garmestani, "3D microstructural reconstruction of heterogeneous materials from 2D cross sections: A modified phase-recovery algorithm," *Computational Materials Science*, vol. 111, pp. 107–115, 2016.
- [22] A. Hasanabadi, M. Baniassadi, K. Abrinia, M. Safdari, and H. Garmestani, "Optimization of solid oxide fuel cell cathodes using two-point correlation functions," *Computational Materials Science*, vol. 123, pp. 268–276, 2016.
- [23] H. Izadi, M. Baniassadi, A. Hasanabadi, B. Mehrgini, H. Memarian, H. Soltanian-Zadeh, and K. Abrinia, "Application of full set of two point correlation functions from a pair of 2D cut sections for 3D porous media reconstruction," *Journal of Petroleum Science and Engineering*, vol. 149, no. October 2016, pp. 789–800, 2017.
- [24] A. Hasanabadi, M. Baniassadi, K. Abrinia, M. Safdari, and H. Garmestani, "Optimal combining of microstructures using statistical correlation functions," *International Journal of Solids and Structures*, vol. 160, pp. 177–186, 2019.
- [25] M. Baniassadi, H. Garmestani, D. S. Li, S. Ahzi, M. Khaleel, and X. Sun, "Three-phase solid oxide fuel cell anode microstructure realization using two-point correlation functions," *Acta Materialia*, vol. 59, no. 1, pp. 30–43, 2011.

- [26] N. A. Siddique and F. Liu, "Process based reconstruction and simulation of a three-dimensional fuel cell catalyst layer," *Electrochimica Acta*, vol. 55, no. 19, pp. 5357–5366, 2010.
- [27] N. Siddique, A. Salehi, and F. Liu, "Stochastic reconstruction and electrical transport studies of porous cathode of Li-ion batteries," *Journal of Power Sources*, vol. 217, pp. 437–443, 2012.
- [28] A. Ali, X. Wen, K. Nandakumar, J. Luo, and K. T. Chuang, "Geometrical modeling of microstructure of solid oxide fuel cell composite electrodes," *Journal of Power Sources*, vol. 185, no. 2, pp. 961–966, 2008.
- [29] B. Kenney, M. Valdmanis, C. Baker, J. G. Pharoah, and K. Karan, "Computation of TPB length, surface area and pore size from numerical reconstruction of composite solid oxide fuel cell electrodes," *Journal of Power Sources*, vol. 189, no. 2, pp. 1051–1059, 2009.
- [30] Q. Cai, C. S. Adjiman, and N. P. Brandon, "Modelling the 3D microstructure and performance of solid oxide fuel cell electrodes: Computational parameters," *Electrochimica Acta*, vol. 56, no. 16, pp. 5804–5814, 2011.
- [31] A. Bertei, H. W. Choi, J. G. Pharoah, and C. Nicolella, "Percolating behavior of sintered random packings of spheres," *Powder Technology*, vol. 231, pp. 44–53, 2012.
- [32] G. Le Loc'h and A. Galli, "A. Truncated Plurigaussian method: theoretical and practical points of view.," *Proc. Geostatistics Int. Conf., Wollongong 96*, no. 1, pp. 211–222, 1997.
- [33] M. Neumann, M. Osenberg, A. Hilger, D. Franzen, T. Turek, I. Manke, and V. Schmidt, "On a pluri-Gaussian model for three-phase microstructures, with applications to 3D image data of gas-diffusion electrodes," *Computational Materials Science*, vol. 156, no. October 2018, pp. 325–331, 2019.
- [34] F. L. E. Usseglio-Viretta, A. Colclasure, A. N. Mistry, K. P. Y. Claver, F. Pouraghajan, D. P. Finegan, T. M. M. Heenan, D. Abraham, P. P. Mukherjee, D. Wheeler, P. Shearing, S. J. Cooper, and K. Smith, "Resolving the Discrepancy in Tortuosity Factor Estimation for Li-Ion Battery Electrodes through

- Micro-Macro Modeling and Experiment,” *Journal of The Electrochemical Society*, vol. 165, no. 14, pp. A3403–A3426, 2018.
- [35] B. L. Trembacki, A. N. Mistry, D. R. Noble, M. E. Ferraro, P. P. Mukherjee, and S. A. Roberts, “Editors’ Choice—Mesoscale Analysis of Conductive Binder Domain Morphology in Lithium-Ion Battery Electrodes,” *Journal of The Electrochemical Society*, vol. 165, no. 13, pp. E725–E736, 2018.
- [36] M. M. Forouzan, C. W. Chao, D. Bustamante, B. A. Mazzeo, and D. R. Wheeler, “Experiment and simulation of the fabrication process of lithium-ion battery cathodes for determining microstructure and mechanical properties,” *Journal of Power Sources*, vol. 312, pp. 172–183, 2016.
- [37] I. Srivastava, D. S. Bolintineanu, J. B. Lechman, and S. A. Roberts, “Controlling binder adhesion to impact electrode mesostructures and transport,” *ACS Applied Materials and Interfaces*, vol. 12, no. 31, pp. 34919–34930, 2020.
- [38] L. Mosser, O. Dubrule, and M. J. Blunt, “Reconstruction of three-dimensional porous media using generative adversarial neural networks,” *Physical Review E*, vol. 96, no. 4, 2017.
- [39] L. Mosser, O. Dubrule, and M. J. Blunt, “Stochastic Reconstruction of an Oolitic Limestone by Generative Adversarial Networks,” *Transport in Porous Media*, vol. 125, no. 1, pp. 81–103, 2018.
- [40] I. Goodfellow, J. Pouget-Abadie, M. Mirza, B. Xu, D. Warde-Farley, S. Ozair, A. Courville, and Y. Bengio, “Generative Adversarial Networks,” *pre-print*, pp. 1–9. arXiv:1406.2661 [stat.ML].
- [41] X. Li, Z. Yang, L. Catherine Brinson, A. Choudhary, A. Agrawal, and W. Chen, “A deep adversarial learning methodology for designing microstructural material systems,” *Proceedings of the ASME Design Engineering Technical Conference*, vol. 2B-2018, pp. 1–14, 2018.
- [42] I. Goodfellow, “NIPS 2016 tutorial: Generative adversarial networks,” *pre-print*, 2016. arXiv:1701.00160 [stat.ML].
- [43] Y. Lecun, Y. Bengio, and G. Hinton, “Deep learning,” *Nature*, vol. 521, no. 7553, pp. 436–444, 2015.
- [44] T. Hsu, W. K. Epting, R. Mahbub, N. T. Nuhfer, S. Bhattacharya, Y. Lei, H. M.

- Miller, P. R. Ohodnicki, K. R. Gerdes, H. W. Abernathy, G. A. Hackett, A. D. Rollett, M. De Graef, S. Litster, and P. A. Salvador, "Mesoscale characterization of local property distributions in heterogeneous electrodes," *Journal of Power Sources*, vol. 386, no. 14, pp. A3403–A3426, 2018.
- [45] S. C. Blair, P. A. Berge, and J. G. Berryman, "Two-Point Correlation Functions to Characterize Microgeometry and Estimate Permeabilities of Synthetic and Natural Sandstones," *Lawrence Livermore National Laboratory Report*, no. UC-403, pp. 1–31, 1993.
- [46] A. Radford, L. Metz, and S. Chintala, "Unsupervised representation learning with deep convolutional generative adversarial networks," *4th International Conference on Learning Representations, ICLR 2016 - Conference Track Proceedings*, pp. 1–16, 2016.
- [47] V. Dumoulin and F. Visin *pre-print*, pages = 1-31, title = A guide to convolution arithmetic for deep learning, url = <http://arxiv.org/abs/1603.07285>, year = 2016, note=arXiv:1603.07285 [stat.ML].
- [48] L. Mescheder, A. Geiger, and S. Nowozin, "Which training methods for GANs do actually converge?," *35th International Conference on Machine Learning, ICML 2018*, vol. 8, pp. 5589–5626, 2018.
- [49] D. P. Kingma and J. L. Ba, "Adam: A method for stochastic optimization," *3rd International Conference on Learning Representations, ICLR 2015 - Conference Track Proceedings*, pp. 1–15, 2015.
- [50] S. J. Cooper, A. Bertei, P. R. Shearing, J. A. Kilner, and N. P. Brandon, "Tau-Factor: An open-source application for calculating tortuosity factors from tomographic data," *SoftwareX*, vol. 5, pp. 203–210, 2016.
- [51] A. G. Journel and R. Froidevaux, "Anisotropic hole-effect modeling," *Journal of the International Association for Mathematical Geology*, vol. 14, no. 3, pp. 217–239, 1982.
- [52] M. Pyrcz and C. Deutsch, "The whole story on the hole effect," *Geostatistical Association of Australasia Newsletter 18*, vol. 18, no. March, p. 18, 2003.
- [53] M. Paganini, L. De Oliveira, and B. Nachman, "Accelerating Science with Generative Adversarial Networks: An Application to 3D Particle Showers in

- Multilayer Calorimeters,” *Physical Review Letters*, vol. 120, no. 4, pp. 1–6, 2018.
- [54] M. Heusel, H. Ramsauer, T. Unterthiner, B. Nessler, and S. Hochreiter, “GANs trained by a two time-scale update rule converge to a local Nash equilibrium,” *Advances in Neural Information Processing Systems*, vol. 2017-Decem, no. Nips, pp. 6627–6638, 2017.
- [55] S. Arora and Y. Zhang, “Do GANs actually learn the distribution? An empirical study,” *pre-*rpint**, pp. 1–11, 2017. arXiv:1706.08224 [cs.LG].
- [56] Z. Wang, Q. She, and T. E. Ward, “Generative adversarial networks: A survey and taxonomy,” *arXiv*, no. November, pp. 1–41, 2019.
- [57] M. Arjovsky, S. Chintala, and L. Bottou, “Real-time optimization meets bayesian optimization and derivative-free optimization: A tale of modifier adaptation,” *pre-print*, 2017. arXiv:1701.07875 [stat.ML].
- [58] I. Gulrajani, F. Ahmed, M. Arjovsky, V. Dumoulin, and A. Courville, “Improved Training of Wasserstein GANs,” *arXiv: 1704.00028*, 2017.
- [59] X. Mao, Q. Li, H. Xie, R. Y. Lau, Z. Wang, and S. P. Smolley, “Least Squares Generative Adversarial Networks,” *Proceedings of the IEEE International Conference on Computer Vision*, vol. 2017-October, pp. 2813–2821, 2017.
- [60] Y. Yoshida and T. Miyato, “Spectral Norm Regularization for Improving the Generalizability of Deep Learning,” *arXiv: 1705.10941*, 2017.
- [61] Y. Zhang, M. Yan, Y. Wan, Z. Jiao, Y. Chen, F. Chen, C. Xia, and M. Ni, “High-throughput 3D reconstruction of stochastic heterogeneous microstructures in energy storage materials,” *npj Computational Materials*, vol. 5, no. 1, 2019.
- [62] D. Zhang, A. Bertei, F. Tariq, N. Brandon, and Q. Cai, “Progress in 3D electrode microstructure modelling for fuel cells and batteries: transport and electrochemical performance,” *Progress in Energy*, vol. 1, no. 1, p. 012003, 2019.
- [63] A. W. Lees and S. F. Edwards, “The computer study of transport processes under extreme conditions,” *Journal of Physics C: Solid State Physics*, vol. 5, no. 15, pp. 1921–1928, 1972.

- [64] P. Henyš, L. Čapek, and J. Březina, “Comparison of current methods for implementing periodic boundary conditions in multi-scale homogenisation,” *European Journal of Mechanics, A/Solids*, vol. 78, no. July, p. 103825, 2019.
- [65] R. A. Yeh, C. Chen, T. Yian Lim, A. G. Schwing, M. Hasegawa-Johnson, and M. N. Do, “Semantic image inpainting with deep generative models,” *Proceedings - 30th IEEE Conference on Computer Vision and Pattern Recognition, CVPR 2017*, vol. 2017-Janua, pp. 6882–6890, 2017.
- [66] P. Isola, J. Y. Zhu, T. Zhou, and A. A. Efros, “Image-to-image translation with conditional adversarial networks,” *Proceedings - 30th IEEE Conference on Computer Vision and Pattern Recognition, CVPR 2017*, vol. 2017-Janua, pp. 5967–5976, 2017.

Chapter 6

Gaussian Processes and Bayesian optimisation for the design of microstructures with optimum properties

6.1 Abstract

The generation of multiphase porous electrode microstructures with optimum morphological and transport properties is essential in the design of improved electrochemical energy storage devices. This work presents a generation-optimisation closed-loop algorithm for the design of microstructures with optimum or customised properties. A deep convolutional Generative Adversarial Network (DCGAN)^{1,2} is implemented to generate synthetic three-phase three-dimensional images of a porous lithium ion battery cathode material. A Gaussian Process Regression is used as a surrogate model to correlate the latent space of the trained generator with the microstructural properties of the synthetic microstructures. A Bayesian optimisation is further implemented to optimise a set of properties as a function of the latent space of the generator. As a way of proving the generation-optimisation method, a set of functions were defined to performed an unconstrained maximisation of morphological properties (volume fraction, specific surface area) and transport properties (relative diffusivity). The results show the

ability to perform simultaneous maximisation of correlated properties (Specific surface area and relative diffusivity), as well as an optimisation of these properties constrained by constant values of volume fraction. A visualisation of the optimised latent space proves a correlation between this and the morphological properties, which leads to the fast generation of visually realistic microstructures with customised properties.

6.2 Introduction

Lithium-ion batteries (LIBs) constitute one of the leading technologies for electrochemical energy storage. Their large-scale implementation, particularly for electric vehicles, is expected to grow rapidly over the next decade to enable the electrification of transport systems. However, a series of technological challenges that lie within the electrodes at a micro-scale level still need to be addressed in order to guarantee LIBs with high energy and power densities, long cycling life, and good reliability. While adopting new chemistries for active materials is one approach to improving performance, this study will instead focus on the optimisation of the microstructure of the porous electrode.

Electrodes constitute the main sites where the electrochemical reactions coupled with transport processes occur within LIBs. They are composed of porous materials to maximise the active surface area but need to contain percolating paths to enable the ionic and electronic transport while maintaining sufficient mechanical integrity.^{3,4} Thus, the electrode microstructure significantly impacts the battery performance and the design of an optimum morphology is considered essential for the development of the next generation battery technologies.⁵ Some important steps for improving the battery performance involve enhancing the electronic and ionic transport within electrodes through conducting pathways, and achieving a high utilisation of the active material.⁶ Therefore, an understanding of these transport processes and microstructural properties in correlation to the complex micro-scale spatial arrangement is critical for the design of improved electrodes.

Previous works have performed comprehensive analyses of the physical and

electrochemical processes at the micro-scale level in order to rationalise the effect of the electrode morphology and microstructural properties in the battery performance.⁷ The electrode porosity, tortuosity and thickness have been considered as the main microstructural properties to analyse and optimise through computational modelling. High porosity and low tortuosity electrodes have been evidenced to impact the ionic conductivity by enabling a transport of lithium ions through the liquid electrolyte. Nonetheless, an increasing porosity would lead to a reduced volume fraction of the active material and thus a reduced energy density. Additionally, recent analyses of the tortuosity and effective electrical conductivity in Li-ion cathodes have proved the important role of the synthetic carbon-binder domain (CBD) in the electrochemical performance.^{8,9} Based on this, a set of mathematical correlations that can account for the interplay between microstructural properties must be considered in order to optimise the electrode morphology. Apart from micro-scale models, continuum modeling has been implemented to elucidate the optimum porosity, the effect of graded porosity, and the optimum effective diffusivity; however, these values are theoretical and result in models where the microstructure obtained is idealised.¹⁰

Although these works are insightful, a previous step that involves the quantification of the electrode spatial arrangement or geometry in correlation to its estimated microstructural properties (*i.e.* porosity, specific surface area, tortuosity) is critical in order to understand the microstructure-performance relationship as a closed-loop process.¹¹ The electrode morphology is determined by the synthesis techniques and therefore a set of parameters that define its spatial arrangement such as the interpenetrating percolating networks of the different phases would be directly correlated to its microstructural properties. Based on this, the ability to control the electrode morphology is crucial in order to perform an optimisation of the electrode microstructure. The key question lies in the existence of a mathematical function that can define the electrode spatial arrangement which can be manipulated based on a set of parameters in order to obtain ideal or user-specified properties that can maximise the performance. One pathway for analysing the microstructure-performance relation consists of the generation of synthetic electrodes by means of statistical and computational modelling. The generation of synthetic multiphase electrode microstructures

could provide an insight of the optimum morphology required for design high-performance LIBs electrodes.

A large body of work has been presented in the generation of synthetic microstructure for energy materials. Some authors have implemented statistical methods using a two-point correlation function to reconstruct three-dimensional microstructures of composite Solid Oxide Fuel Cell (SOFC) anodes.^{12,13} Alternative algorithms implement a sphere packing and growth technique to simulate the process of sintering used in the production of SOFC electrodes.¹⁴⁻¹⁷ In the area of Li-ion batteries, previous authors have performed particle-based simulations to correlate the fabrication process of electrodes to their respective microstructure.^{18,19} These physics-based models are able to predict the effect of the microstructure in transport properties; however, they have proved to be computationally expensive and specific to a particular type of electrode material.

Recent advances in deep learning have led to the implementation of generative models for the stochastic generation of porous media. Mosser et al. implemented a Generative Adversarial Network (GAN) to reconstruct the three-dimensional microstructure of two-phase synthetic and granular materials. Gayon-Lombardo et al.²⁰ extended this method for the generation of three-dimensional, three-phase electrodes: a Solid-Oxide Fuel Cell anode and a Li-ion cathode. These reconstructions proved to possess the same microstructural properties and two-point correlation function as the original tomographic data. In comparing the most common microstructure generation techniques, GANs are able to perform fast sampling of high-dimensional and intractable density functions without the need for an a priori model of the probability distribution function to be specified²¹. Thus, GANs proved to be an efficient method for generating realistic microstructures, where the trained generator constitutes a virtual representation of the real microstructure.

The objective of this work is to introduce a closed-loop generation-optimisation framework that can link the generation of synthetic microstructures with optimum user-specified properties. This work expands on the research of

Gayon-Lombardo et al.²⁰ and implements a GAN as a basis for the generation of optimised microstructure Li-ion cathode.

6.2.1 Generative Adversarial Networks

The concept of GANs was previously introduced in chapter 5.^{1,2} In this chapter the same concept was implemented, where both the generator $G_{\theta(G)}(\mathbf{z})$ and the discriminator $D_{\theta(D)}(\mathbf{x})$ are deep convolutional neural networks. A few modifications were implemented in the architecture and in the discriminator's loss function $J^{(D)}$, defined as:

$$J^{(D)} = J_{BCE}^{(D)} + J_{MSE}^{(D)} \quad (6.1)$$

In this work $J^{(D)}$ is composed of two terms, one that corresponds to the binary cross-entropy loss in a classifier between the discriminator's prediction and the real label, given by equation 6.2; and one additional term corresponding to the reconstruction loss between the real data \mathbf{x} and the generated data $G(\mathbf{z})$ in order to increase the resolution of the synthetic realisations, given by equation 6.3.

$$J_{BCE}^{(D)} = \mathbb{E}_{\mathbf{x} \sim p_{\text{data}}(\mathbf{x})} [\log (D(\mathbf{x}))] + \mathbb{E}_{\mathbf{z} \sim p_{\mathbf{z}}(\mathbf{z})} [\log (1 - D(G(\mathbf{z})))] \quad (6.2)$$

$$J_{MSE}^{(D)} = \frac{1}{N} \sum_{i=1}^N (\mathbf{x} - G(\mathbf{z}))^2 \quad (6.3)$$

Subsequently, the generator is trained to minimise its loss function corresponding to minimising the log-probability of the discriminator being correct:

$$J^{(G)} = \mathbb{E}_{\mathbf{z} \sim p_{\mathbf{z}}(\mathbf{z})} [\log (1 - D(G(\mathbf{z})))] \quad (6.4)$$

The solution to this optimisation problem is a Nash equilibrium² where each player achieves a local minimum, and the discriminator can no longer distinguish between real and synthetic data.

Recent works have explored the capabilities of the latent space \mathbf{z} of GANs and its correlation with the output image $G(\mathbf{z})$.^{22,23} By interpolating between pairs of \mathbf{z} vectors, the generator is able to produce semantically meaningful images and a smooth transition between each other.²² Moreover, linear arithmetic operations can be performed in the latent space of GANs which lead to meaningful transformations of images with visually different properties.²² It is therefore clear that the output image from the trained generator will be directly correlated to the input vector in the latent space. In terms of microstructural generation, any new microstructure obtained from a trained generator based on an input z from the latent space distribution (*i.e.* $z \sim \mathcal{N}(0, 1)$) would be visually different but will possess the same distribution of statistical and microstructural properties as the training set.^{20,21,24} The reason for it lies in the fact that the latent space used as input during training consists of a random normal distribution and therefore any generated microstructure would be obtained from that same distribution. In the case where the input latent vector of a trained generator is not a sample from a normal distribution, the generated microstructure would possess different microstructural properties (*i.e.* volume fractions, relative diffusivities, etc) from the training set, but the microstructure would remain visually realistic (*i.e.* visually indistinguishable from the real data in the training set). Based on this, an optimisation of the latent space can be performed in order to obtain a microstructure with a set of desired properties.²³ The process of correlating the latent vector with the microstructural properties consists of a two-way forward process: first the generation of the microstructure using a trained generator, and second the calculation of microstructural and transport properties using a physics-based model. Given that some of the physics-based simulations used to calculate the transport properties are expensive and cannot be backpropagated to the latent variables in a gradient-based optimisation, a surrogate model must be defined which correlates the input latent vector (\mathbf{z}) with the microstructural and transport properties of the generated microstructure $f(\mathbf{z})$. Using a similar approach to Li et al.²³, this work implements a Gaussian Process regression method as the surrogate model that maps the inputs \mathbf{z} and outputs $f(\mathbf{z})$.

6.2.2 Introduction to Gaussian Process regression

This section gives an introduction to Gaussian Process (GP) regression. GP regression was first proposed by O’Hagan and Kingman²⁵ and then popularized by Neal²⁶ and Ramussen and Williams²⁷. GPs are a generalisation of a multivariate Gaussian distribution to infinite dimensions. Formally, GP regression aims to model an unknown latent function $f(\mathbf{x})$ using noisy observations y of $f(\mathbf{x})$ defined as^{28,29}:

$$y = f(\mathbf{x}) + \epsilon, \quad \epsilon \sim \mathcal{N}(0, \sigma_\epsilon^2) \quad (6.5)$$

where $\mathbf{x} \in \mathbb{R}^n$ denote an arbitrary input vector and $\epsilon \in \mathbb{R}$ is Gaussian distributed measurement noise with zero mean and variance σ_ϵ^2 .^{27,30} A GP is able to perform a mapping from inputs \mathbf{x} to outputs $y \in \mathbb{R}$ by defining $\hat{f}(\mathbf{x})_{GP}$ as a surrogate distribution over functions to represent $f(\mathbf{x})$. The GP is fully specified by a mean function $m(\mathbf{x})$ and a covariance function $k(\mathbf{x}, \mathbf{x}')$:

$$\hat{f}(\mathbf{x})_{GP} \sim GP(m(\mathbf{x}), k(\mathbf{x}, \mathbf{x}')) \quad (6.6)$$

where:

$$m(\mathbf{x}) = \mathbb{E}[f(\mathbf{x})] \quad (6.7)$$

$$k(\mathbf{x}, \mathbf{x}') = \mathbb{E}[(f(\mathbf{x}) - m(\mathbf{x}))(f(\mathbf{x}') - m(\mathbf{x}'))^T] \quad (6.8)$$

Through the implementation of a GP, a regression based on a non-parametric model is performed. Instead of defining a parametric function $f(\mathbf{x}, \theta)$, and estimating the parameters $\theta \in \mathbb{R}^{n_\theta}$, it is assumed that the function $f(\mathbf{x})$ is a sample from a Gaussian Process as defined by equations 6.7 and 6.8.^{31,32} Based on the additive property of Gaussian distributions, the noisy observations y also follow a GP with the same mean but with a different covariance function to account for the measurement of noise:

$$y \sim GP(m(\mathbf{x}), k(\mathbf{x}, \mathbf{x}') + \sigma_\epsilon^2 \delta(\mathbf{x}, \mathbf{x}')) \quad (6.9)$$

where δ is known as the Kronecker-delta, where $\delta(\mathbf{x}, \mathbf{x}') = 1$ if $\mathbf{x} = \mathbf{x}'$, and else

$\delta(\mathbf{x}, \mathbf{x}') = 0$ Equations 6.6 and 6.9 define the prior of the function which would be updated based on input-output data observations. A zero-mean $m(\mathbf{x})$ is commonly used in Machine Learning³³⁻³⁵ and therefore implemented in this work. A squared-exponential (SE) covariance function is implemented in this work, which is a frequently applied stationary covariance^{25,27} defined by

$$k_{SE}(x_i, x_j) = \sigma_f^2 \exp\left(-\frac{1}{2\lambda_d^2}(x_i - x_j)^2\right) \quad (6.10)$$

where σ_f^2 and λ_d^2 correspond to the covariance function hyperparameters that control the y -scaling and x -scaling respectively. Equation 6.10 can be rewritten for multiple dimensions as

$$k_{SE}(\mathbf{x}_i, \mathbf{x}_j) = \sigma_f^2 \exp\left(-\frac{1}{2}(\mathbf{x}_i - \mathbf{x}_j)^T W (\mathbf{x}_i - \mathbf{x}_j)\right) \quad (6.11)$$

where $W = \text{diag}[w_1, \dots, w_D]$, where $w_d = 1/\lambda_d^2$

Assuming that N observations $\mathbf{y} = [y_1, \dots, y_N]^T$ are available at N different inputs $\mathbf{X} = [\mathbf{x}_1, \dots, \mathbf{x}_N]$ (where each of the elements in \mathbf{y} are scalars and \mathbf{y} corresponds to all N samples concatenated), the uncertainty of estimating N function values can be represented based on the prior from the mean and the covariance function of the vector $\mathbf{F} = [f(\mathbf{x}_1), \dots, f(\mathbf{x}_N)]^T$. This vector has a mean vector defined as $\mathbf{0}$ and a $N \times N$ covariance matrix defined as

$$\Sigma = [k(\mathbf{x}_i, \mathbf{x}_j)]_{N \times N} \quad (6.12)$$

From equation 6.12, the uncertainty of the observation matrix \mathbf{y} can be expressed in the same way as \mathbf{F} with a mean function of $\mathbf{0}$ and a covariance matrix defined as

$$\mathbf{K} = [k(\mathbf{x}_i, \mathbf{x}_j) + \sigma_\epsilon^2 \delta(\mathbf{x}_i, \mathbf{x}_j)]_{N \times N} \quad (6.13)$$

which can be reduced to:

$$\mathbf{K} = \Sigma + \sigma_\epsilon^2 \mathbf{I} \quad (6.14)$$

where σ_ϵ^2 constitutes the variance of Gaussian distributed perturbation noise

as given by equation 6.5.

Given a set of training data \mathbf{X} and \mathbf{y} , a GP is fully defined by the hyperparameters of the covariance function and the random noise of y in equation 6.14. Since these values are commonly unknown *a priori*, an important step in the Gaussian Process regression is the estimation of such hyperparameters. These hyperparameters are jointly denoted by the vector $\Theta = [w_1, \dots, w_D, \sigma_f^2, \sigma_\epsilon^2]$, and can be estimated by maximising the log-likelihood of the conditional probability density function (PDF) $p(\mathbf{y}|\mathbf{X}, \Theta)$. It is known that $\mathbf{y}|\mathbf{X}, \Theta \sim \mathcal{N}(\mathbf{0}, \mathbf{K})$, therefore the PDF is defined as

$$p(\mathbf{y}|\mathbf{X}, \Theta) = \frac{1}{(2\pi)^{n/2}(\det[\mathbf{K}])^{1/2}} \exp \left[-\frac{1}{2} \mathbf{Y}^T \mathbf{K}^{-1} \mathbf{y} \right] \quad (6.15)$$

To estimate the log-likelihood, the log function is implemented in equation 6.15 as

$$\log[p(\mathbf{y}|\mathbf{X}, \Theta)] = -\frac{n}{2} \log(2\pi) - \frac{1}{2} \log(\det[\mathbf{K}]) - \frac{1}{2} \mathbf{y}^T \mathbf{K}^{-1} \mathbf{y} \quad (6.16)$$

although hyperparameters Θ are not explicitly shown in equation 6.16, they are contained in \mathbf{K} (according to equation 6.14). A convenient way of maximising the log-likelihood is to minimise the negative log-likelihood (NLL)^{27,36} of equation 6.15, thus, the function to be minimised is the negative of equation 6.16, defined as

$$\mathcal{L}(\Theta) = -\log[p(\mathbf{y}|\mathbf{X}, \Theta)] \quad (6.17)$$

A non-linear optimisation algorithm can be implemented to obtain the optimum hyperparameters Θ that define the Gaussian Process:

$$\Theta^* \in \operatorname{argmin}_{\Theta} \mathcal{L}(\Theta) \quad (6.18)$$

Once the hyperparameters of the Gaussian Process have been determined based on the training data, predictions can be inferred at unknown input data \mathbf{x}_{new} by computing the conditional probability distribution of a Gaussian process

on data $\mathbf{X}, \mathbf{y}, \mathbf{x}_{\text{new}}$. It is previously established that the covariance of observations y are given by equation 6.14 and a mean function of $m(\mathbf{x}) = 0$ can be chosen. Hence, when a new observation \mathbf{x}_{new} occurs, the prediction y_{new} is conditioned to the observed training data as

$$\begin{bmatrix} \mathbf{y} \\ y_{\text{new}} \end{bmatrix} \sim \mathcal{N} \left(\begin{bmatrix} \mathbf{0} \\ 0 \end{bmatrix}, \begin{bmatrix} \mathbf{K} & \Sigma(\mathbf{X}, \mathbf{x}_{\text{new}}) \\ \Sigma(\mathbf{x}_{\text{new}}, \mathbf{X}) & \Sigma(\mathbf{x}_{\text{new}}, \mathbf{x}_{\text{new}}) \end{bmatrix} \right) \quad (6.19)$$

where

$$\Sigma(\mathbf{X}, \mathbf{x}_{\text{new}}) = [k(\mathbf{x}_1, \mathbf{x}_{\text{new}}), \dots, k(\mathbf{x}_n, \mathbf{x}_{\text{new}})]^T \quad (6.20)$$

The conditional probability of the prediction for the new observation $p(y_{\text{new}} | \mathbf{X}, \mathbf{y}, \mathbf{x}_{\text{new}})$ can therefore be obtained analytically by the conditional rules of Gaussian distributions as

$$y_{\text{new}} | \mathbf{X}, \mathbf{y}, \mathbf{x}_{\text{new}} \sim \mathcal{N}(\mu_{y_{\text{new}}}, \sigma_{y_{\text{new}}}^2) \quad (6.21)$$

where

$$\begin{aligned} \mu_{y_{\text{new}}} &= \mathbb{E}[y_{\text{new}} | \mathbf{X}, \mathbf{y}, \mathbf{x}_{\text{new}}] \\ &= \Sigma(\mathbf{x}_{\text{new}}, \mathbf{X}) [\Sigma(\mathbf{X}, \mathbf{X}) + \sigma_\epsilon^2 I]^{-1} \mathbf{y} \end{aligned} \quad (6.22)$$

$$\begin{aligned} \sigma_{y_{\text{new}}} &= \Sigma(\mathbf{x}_{\text{new}}, \mathbf{x}_{\text{new}}) \\ &\quad - \Sigma(\mathbf{x}_{\text{new}}, \mathbf{X}) [\Sigma(\mathbf{X}, \mathbf{X}) + \sigma_\epsilon^2 I]^{-1} \Sigma(\mathbf{X}, \mathbf{x}_{\text{new}}) \end{aligned} \quad (6.23)$$

This section has shown the implementation of GPs to map the correlation between a training set of inputs-outputs, in order to obtain predictions at arbitrary inputs. The procedure involves three steps:

- Select a mean and covariance function based on the prior knowledge of the function to model. In some cases, an explicit mean function is implemented in order to express the prior information of the expected form of the model.^{28,31,32} In this work, a zero mean is implemented.
- Perform a hyperparameter optimisation by minimising the negative log-likelihood using the training set.³⁶

- Make predictions of arbitrary inputs with equations 6.22 and 6.23, where $\mu_{y_{\text{new}}}$ represents the prediction and $\sigma_{y_{\text{new}}}$ represents the variance the corresponding uncertainty.³³

6.2.3 Bayesian Optimisation with Gaussian Processes

Gaussian Processes can be used as effective methods to model an objective function while taking uncertainty explicitly into account. This makes them ideal methods to be used in expensive **black-box** optimisation.²⁹ The GP regression framework not only provides an accurate prediction of unknown outputs, but also presents a measure for predicting uncertainty. This poses a significant advantage compared to commonly used black-box optimisation methods and makes the GP regression a powerful tool for derivative-free optimisation, both for single-objective optimisation^{29,37} and multi-objective optimisation^{33–35}. The optimisation problem to find the values of \mathbf{x} that minimise the function $f(\mathbf{x})$ is defined as

$$\begin{aligned} \min_{\mathbf{x} \in \mathcal{X}} \quad & f(\mathbf{x}) \\ \text{s.t.} \quad & x_i^{lb} \leq x_i \leq x_i^{ub} \end{aligned} \quad (6.24)$$

where $\mathbf{x} \in \mathbb{R}^{n_x} \rightarrow \mathbb{R}$, and x_i^{lb} and x_i^{ub} are the upper and lower bounds of \mathbf{x} . As stated above, the GP serves as a surrogate function defined as $\hat{f}(\mathbf{x})_{\text{GP}}$ to represent the objective function $f(\mathbf{x})$; thus, the new function to be optimised is $\hat{f}(\mathbf{x})_{\text{GP}}$. An initial GP is built with the training data of inputs \mathbf{x} and outputs \mathbf{y} . A non-linear optimisation approach is implemented to minimise $\hat{f}(\mathbf{x})_{\text{GP}}$ and obtain and estimation of the next point x_{new} . The real function $f(\mathbf{x})$ is evaluated at x_{new} and a new GP is built using the initial training set with updated values of x_{new} and $f(x_{\text{new}})$.^{38,39} This process is done until a convergence criterion is achieved. The Bayesian optimisation with GP algorithm is detailed below (Algorithm 1).

One of the main advantages of implementing this type of black-box optimisation method is that GPs do not need a full understanding of the complex mechanisms that take place within the electrode microstructure. Moreover, in comparing GPs with other proposed surrogate models such as artificial neural networks, GPs do not require large amounts of training data and therefore they are ideal for

Algorithm 1: Bayesian optimisation with Gaussian Processes

Initialisation: Obtain n_s initial observations \mathbf{X} and their evaluations at objective function $f(\mathbf{x})$. Build a GP with training set $\{\mathbf{X}, \mathbf{Y}\}$ to produce $\hat{f}(\mathbf{x})_{\mathcal{GP}}$. Set number of iterations N , set $n := 0$.

while $i \leq \text{termination criteria}$: **do**

1. Solve non-linear optimisation problem $\mathbf{x}_i^* := \operatorname{argmin}_{\mathbf{x} \in \mathcal{X}} \hat{f}(\mathbf{x})_{\mathcal{GP}}$
2. Evaluate the objective function f at point \mathbf{x}_i^* to calculate $y_i := f(\mathbf{x}_i^*) + \epsilon$
3. Add the new values \mathbf{x}_i^* and y_i to the training data of the GP
4. Update the GP with the new available data to model the surrogate function $\hat{f}(\mathbf{x})_{\mathcal{GP}}$
5. $i := i + 1$

end

computationally expensive black-box optimisation since they only need few evaluations.^{30,33} The complete process of coupling a GP as a surrogate model of the trained generator with a Bayesian optimisation approach for the generation of optimum electrodes is defined in section 6.3.

6.3 Method

6.3.1 Microstructural image data and pre-processing

The Li-ion battery cathode images were obtained from open-source nanotomography data which had already been segmented into their respective phases: particles of a ceramic active material (nickel manganese cobalt oxide – NMC 532), a conductive organic binder (polymer with carbon black) and pores. Details of the sample preparation, imaging, reconstruction, and segmentation approach used can found in⁸, and the specifications are shown in²⁰.

Approximately 13,000 overlapping sub-volumes were extracted from the original dataset using a sampling function with a stride of 8 voxels. The spatial dimensions of the cropped volumes were selected based on the average size of the largest structuring element. The sub-volume size was selected to guarantee that at least two structuring elements (*i.e.* particle size) could fit in one sub-volume⁴⁰. Once the sub-volumes were extracted from the large dataset in order to obtain the training set for the GAN, a one-hot encoding technique was implemented to the 8-bit greyscale images, as defined elsewhere²⁰

6.3.2 Closed-loop Generation-optimisation process

This section outlines the closed-loop algorithm for generating microstructures with optimum user-specified properties. This process consists of three integrated steps:

1. Train a GAN to obtain the generator as a virtual representation of the microstructure parametrised by θ and \mathbf{z} .²⁰
2. Create a training set $T = \{\mathbf{Z}, \mathbf{Y}\}$ consisting of a latent space (\mathbf{Z}) and its corresponding calculated microstructural and transport properties (\mathbf{Y}) and build a Gaussian Process based on this training set. To train the GPs, the inputs were scaled to lie between $[0, 1]$. The input scaling was chosen as a popular feature scaling procedure that have been shown to improve the prediction quality.⁴¹
3. Perform an iterative Bayesian optimisation process according to Algorithm 1 to obtain $\mathbf{z}_i^* := \operatorname{argmin}_{\mathbf{z} \in \mathcal{Z}} \hat{f}(\mathbf{Z})_{\mathcal{GP}}$

GAN training: The architecture of the GAN used for training is defined in 6.1, where both the discriminator and the generator are fully convolutional neural networks, as defined by Radford et al.⁴² The latent space of the Generator is given by a random normal distribution $z \sim \mathcal{N}(0, 1)$, where $z \in \mathbb{R}^{n_z \times l \times l \times l}$ and $l = 4$, therefore the total size of the input vector z is 64. The discriminator is composed of five convolutional layers, each followed by a batch normalisation. The first four layers use a leaky rectified linear unit (LeakyReLU) activation function and the last layer implements a sigmoid activation function. The generator is composed of five transposed convolutional layers⁴³ which expand the spatial dimensions in each step. Each layer is followed by a batch normalisation and all layers implement a ReLU activation function, except for the last layer which uses a Softmax function. The hyperparameters that define the GAN architecture were chosen as detailed in²⁰.

Table 6.1: Dimensionality of each layer in the GAN architecture for each porous material (layers, dimensions, optimiser, input image size, number of training samples)

Layer	Function	Input channels	Output channels	Spatial Kernel	Stride	Padding	Batch normalisation	Activation function
Discriminator								
D1	Conv3d	3	16	$4 \times 4 \times 4$	2	3	Yes	LeakyReLU
D2	Conv3d	16	32	$4 \times 4 \times 4$	2	2	Yes	LeakyReLU
D3	Conv3d	32	64	$4 \times 4 \times 4$	2	2	Yes	LeakyReLU
D4	Conv3d	64	128	$4 \times 4 \times 4$	2	2	Yes	LeakyReLU
D5	Conv3d	128	1	$6 \times 6 \times 6$	1	0	No	Sigmoid
Generator								
G1	ConvTransposed3d	1	512	$4 \times 4 \times 4$	2	2	Yes	ReLU
G2	ConvTransposed3d	512	256	$4 \times 4 \times 4$	2	2	Yes	ReLU
G3	ConvTransposed3d	256	128	$4 \times 4 \times 4$	2	2	Yes	ReLU
G4	ConvTransposed3d	128	64	$4 \times 4 \times 4$	2	2	Yes	ReLU
G5	ConvTransposed3d	64	3	$4 \times 4 \times 4$	2	3	No	Softmax

In order to overcome the instabilities commonly encountered during the GANs training, a one-sided label smoothing stabilisation was implemented². This method consists on reducing the label 1 corresponding to real images by a constant ε , such that the new label has the value of $1-\varepsilon$. For all cases in this work, ε has a value of 0.1. Additionally, a ratio of network optimisation for the generator and discriminator was set to 2 : 1, which means that the generator is updated twice while the discriminator is updated once at each optimisation step. A stochastic gradient descent is implemented for learning using the ADAM optimiser⁴⁴. The momentum constants are $\beta_1 = 0.5$, $\beta_2 = 0.999$ and the learning rate is 2×10^{-5} . All simulations are performed on a GPU (Nvidia TITAN

Xp) and the training process is limited to 72 epochs (c. 48 h).

GP training: As previously stated, the purpose of the Gaussian Process is to create a surrogate model $\hat{f}(\mathbf{z})_{GP}$ that can perform a mapping from the latent variables \mathbf{z} as parameters of design, and the generated microstructure $G(\mathbf{z})$ into the microstructural and transport properties $\mathbf{y} = f(G(\mathbf{z}))$, as shown in Figure 6.1. To create a surrogate model, a design of experiment based on a Latin Hypercube Sampling was performed. A total of 50 64-dimensional vectors (*i.e.* $1 \times 4 \times 4 \times 4$) were sampled in the \mathbf{z} space. With each of these vectors, a microstructure was generated using the previously trained generator, and subsequently its microstructural and transport properties were calculated using the open-source Matlab software TauFactor.⁴⁵ The training set for the GP was obtained from the 50 \mathbf{z} vectors and their respective microstructural properties \mathbf{y} as $T = \{\mathbf{Z}, \mathbf{Y}\}$.

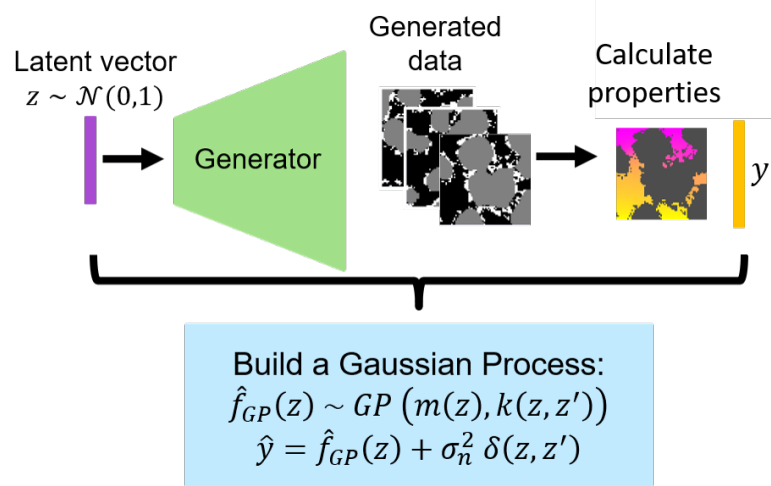


Figure 6.1: Gaussian Process as surrogate model $\hat{f}(\mathbf{x})_{GP}$ to map the correlation between the latent space \mathbf{z} and the estimated properties \mathbf{y}

The GP is fully defined by its hyperparameters $\Theta = [w_1, \dots, w_D, \sigma_f^2, \sigma_\epsilon^2]$. Since the hyperparameters are unknown *a priori*, they are estimated by calculating the NLL of the joint pdf, as detailed in equation 6.17. In order to avoid reaching a local minima, a multi-start search is performed by sampling five initial points determined by a Latin Hyper-cube Sampling (LHS). A gradient-based optimisation is performed for each of these points using the bounded (Sequential Least Squares Programming) SLSQP algorithm⁴⁶ and the values with the minimum NLL are chosen as the fitted hyperparameters Θ^* .

Bayesian optimisation: The optimisation problem is defined by the objective function $f(\mathbf{z})$ which represents the microstructural or transport property to be maximised as a function of the latent vector \mathbf{z} . It is common practice to represent a maximisation problem as the minimisation of the negative objective function, defined as

$$\begin{aligned} \mathbf{z}^* &= \operatorname{argmin}_{\mathbf{z} \in \mathcal{Z}} -f(\mathbf{z}) \\ &\text{s.t. } [-5, 5] \end{aligned} \quad (6.25)$$

where \mathbf{z} is bounded between $[-5, 5]$. The value of $f(\mathbf{z})$ is estimated by inserting \mathbf{z} into the trained generator, and calculating the microstructural or transport properties with a physics-based simulation. Since the microstructure-property problem is computationally expensive, an iterative sequential sampling is performed in which at each iteration a Gaussian Process is built to map $f(G(\mathbf{z}))$. A gradient-based optimisation with the SLSQP algorithm is performed over the GP inference equation (6.22) in order to obtain the new value of \mathbf{z}^* (equation 6.25).^{23,31,33,46} The surrogate objective function can be defined by the mean value of the GP prediction (*i.e.* $\hat{f}_{GP} := \mu_{GP}$), or an exploratory term that includes the variance can be added in order to avoid reaching local minimum (*e.g.* $\hat{f}_{GP} := \mu_{GP} - \alpha\sigma_{GP}$). In this work the latter is implemented, where the term α is a variable between 0 and 1.96, as defined by equation 6.26, to guarantee that the calculated values are within a confidence interval of 95%.³³

$$\alpha = 1.96 \cdot \left(1.0 - \frac{i}{i_{\max}}\right) \quad (6.26)$$

where i is the iteration number, and i_{\max} corresponds to the total number of iterations, in this case 500. Once \mathbf{z}^* was found at each iteration, \mathbf{y}^* is calculated with a physics-based model, and the new values of $\{\mathbf{z}, \mathbf{y}\}$ are added to the training set $T = \{\mathbf{Z}, \mathbf{Y}\}$. The GP is then updated with the new values of \mathbf{Z} and \mathbf{Y} and the new hyperparameters are calculated. For each property optimised, the maximum number of iterations were set to 500 as a stopping criteria. The integrated generation-optimisation loop is shown in figure 6.2.

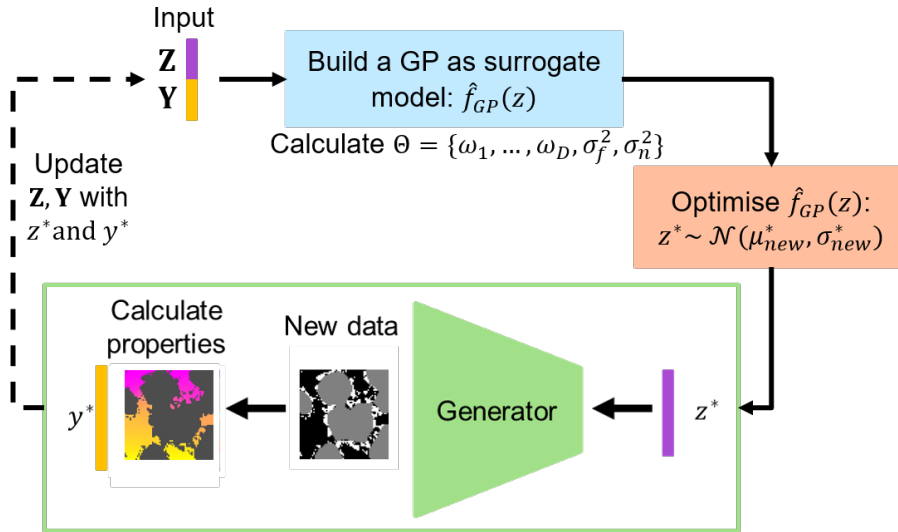


Figure 6.2: Closed-loop generation-optimisation process: implementation of a Bayesian optimisation algorithm to optimise the morphological and transport properties y of the generated microstructure as a function of the latent space z of the Generator.

6.3.3 Case study: Optimisation of a 3D Li-ion cathode

The objective of this work is the design of a Li-ion cathode with optimum user-specified microstructural and transport properties based on an open-source tomographic data of a Li-ion cathode synthesised using state-of-the-art methods⁸. The Li-ion cathode is composed of three phases: particles of a ceramic active material (nickel manganese cobalt oxide – NMC 532), a conductive organic binder (polymer with carbon black) and pores. Ideally, a Li-ion cathode would have a maximum relative diffusivity in the pore phase ($D_{\text{rel,pore}}$) with percolating paths that would enhance the liquid-state diffusion of Lithium ions. In this respect, the maximisation of the relative diffusivity in the pore phase along one of the three directions is of particular interest, since the transport of species is usually predominant along one direction (from the current collector to the separator). Additionally, a maximum specific surface area of the NMC phase (SSA_{NMC}) is desired to enhance the electrochemical reaction at the active sites and allow a sufficient utilisation of the NMC.

These properties, however, are correlated and therefore an optimisation of the microstructure is non-trivial and would require an interplay between these properties to be considered. For instance, an increase in ($D_{\text{rel,pore}}$) would

directly lead to an increase in (ϕ_{pore}) , and thus a decrease in (ϕ_{NMC}) , leading to a lower energy density. Based on this, an “improved microstructure” in terms of electrochemical performance would involve a trade-off between the available microstructural and transport properties. Nonetheless a complete analysis of microstructures with different properties, particularly an incremental analysis of one varying property keeping the others constant, is of interest to understand the effect of certain property in the electrode performance. It is therefore the purpose of this study to generate microstructures with a wide range of microstructural and transport properties to further produce databases of structures with specific desired properties. In this work, only the specific surface area and the relative diffusivity in the pore phase are chosen as properties to be optimised based on their known effect on the battery performance and their indirect correlation. Nonetheless it is important to point out that other microstructural properties, such as the volume fraction and conductivity of the CBD phase, are relevant to the battery performance and should be considered as future work. Additionally, it is worth mentioning that the optimisation of the properties is performed as a static process (*i.e.* time independent) and therefore the effect of these properties (*e.g.* maximised SSA_{NMC}) in degradation processes are not accounted for.

To prove the method of generation-optimisation of electrode microstructure, the following properties are maximised separately by defining a specific maximisation function for each case:

- Specific surface area of NMC phase (SSA_{NMC})
- Relative diffusivity of the pore phase ($D_{\text{rel,pore}}$)
- Relative diffusivity of the pore phase along the x direction ($D_{\text{rel,pore},x}$)
- Relative diffusivity of the pore phase ($D_{\text{rel,pore}}$) and Specific surface area of NMC phase (SSA_{NMC}) simultaneously.
- Specific surface area of the NMC phase (SSA_{NMC}) constrained by a constant phase volume fraction of the NMC phase ϕ_{NMC}
- Relative diffusivity of the pore phase ($D_{\text{rel,pore}}$) constrained by a constant porosity ϕ_{pore}

The following section shows the results of generating microstructure with

maximised or user-specified properties according to the method described in this section.

6.4 Results and Discussion

6.4.1 Optimisation of microstructural and transport properties

As a first step, a set of microstructural properties were maximised without constraints according to equation 6.25. This was performed in order to prove the concept of a closed-loop generation-optimisation algorithm along various properties essential for electrode design. Subsequently, a set of properties were optimised (*i.e.* $D_{\text{rel,b}}$ and SSA_{NMC}) by constraining the secondary effect on the other properties. Finally, a function is defined to generate microstructures with graded porosity along one direction, for microstructures of size 64^3 and 128^3 voxels. An analysis of the distribution of microstructural properties in the latent space of the generator is further performed in order to understand and visualise the existence of a correlation between these variables.

It must be pointed out that a full electrochemical model would be the ideal cost function to optimise. However, a three-dimensional pore-scale simulation is computationally expensive and beyond the scope of this work. For this reason, a variety of microstructural properties are implemented as proxy metrics to obtain improved microstructures more efficiently, and to demonstrate the capability of GPs to combine loss contributions.

Specific Surface Area of the NMC phase

The objective function to maximise the specific surface area of the NMC phase without constraints is defined as

$$f(\mathbf{z}) = SSA_{\text{NMC}} \quad (6.27)$$

The results of the maximisation process as a function of the number of iterations is shown in the inserted plot in figure 6.3. It can be seen that as the iterations increase, the specific surface area of the NMC phase also increases without reaching a maximum since the optimisation is unconstrained. As shown in the inserted plot, the iterative process is not smooth but rather oscillates significantly. The reason for this is the existence of the search term when updating

the Gaussian Process, which allows the exploration of further points within a trust region of 95%. From each of the explored points throughout the optimisation process, a set of microstructures can be generated, as shown in Figure 6.3, where 30 samples were generated from a latent vector z_i , where i corresponds to the iteration number. Each of these microstructures are unique, since z is different for each sample, but are visually similar given that their respective z is within the same region of the latent space, as will be shown in section 6.4.2, and therefore have similar properties. This assertion indicates that a set of values in the latent space is correlated with the properties of the generated microstructure. When the samples of z are obtained from a normal pdf, the properties are in the same region as the GAN training set. However, as the latent vector z is optimised and moves further from the normal distribution, microstructure with different properties can be generated.

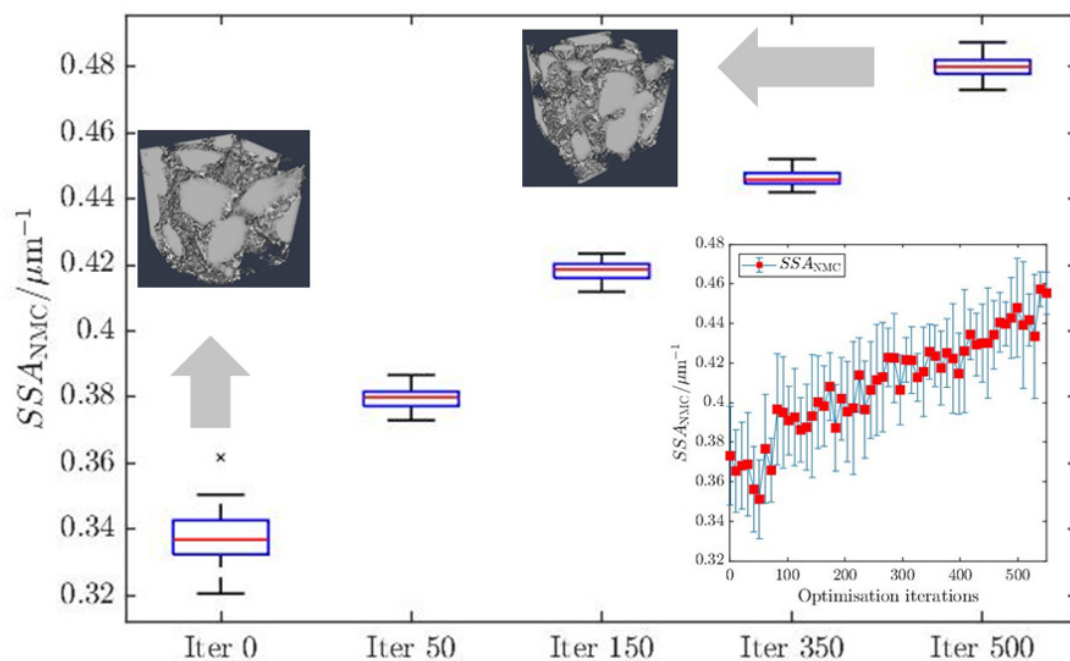


Figure 6.3: Estimated SSA of 30 generated samples at points 0, 50, 150, 350 and 500 during the maximisation process. The inserted figure shows the complete unconstrained maximisation of SSA of NMC phase for 500 iterations.

As previously stated, maximising the SSA of the active material, in this case the NMC phase, is of interest to ensure a high utilisation of the active material and

to enhance the electrochemical reaction. When an unconstrained optimisation is performed, the averaged properties of the particles do not change, as is reported in Table 6.2 for the mean particle diameter at each iteration, but the phase volume fraction of the NMC phase increases. This is shown by comparing the SSA and volume fraction of the NMC phase as a function of the number of iterations, shown in Figure 6.4. An increase in NMC loading would lead to a higher capacity, which is desirable for a “high energy” battery. However, as expected, when the NMC volume fraction increases, the pore volume fraction is reduced, leading to a reduced relative diffusivity in the pore phase $D_{\text{rel,pore}}$. This property would result in a reduced volume of percolating paths, causing an increased resistance due to a limited transport of Lithium ions through the liquid electrolyte. Therefore, an interplay between the effect of an enhanced specific surface area and a reduced relative diffusivity must be considered in the electrode design and will be further discussed in section 6.4.1.

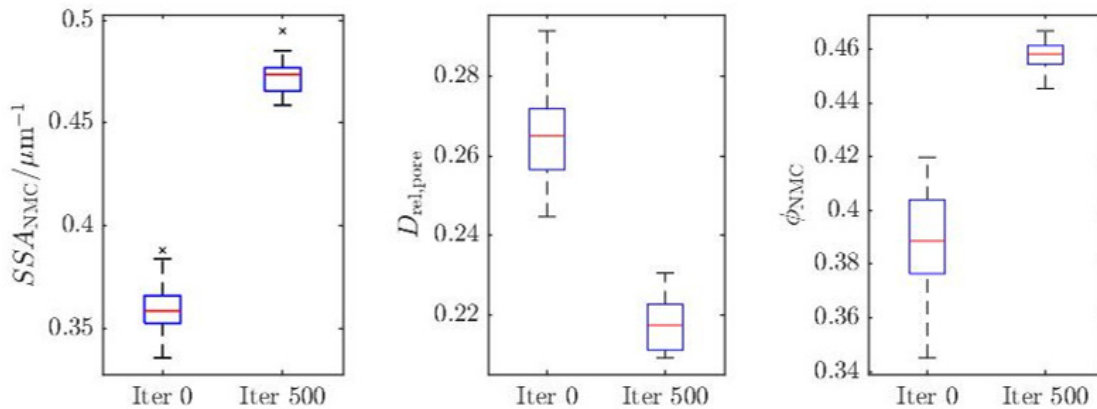


Figure 6.4: Comparison between the estimated SSA_{NMC} , $D_{\text{rel,pore}}$ and ϕ_{NMC} at iteration 0 and 500 for 30 generated samples

Although previous macro-homogeneous models have used mathematical correlations between the SSA_{NMC} and ϕ_{pore} , the applicability of these correlations is dependent on the type of microstructure and is based on idealised particle systems with a homogeneous particle size (d_p). An analysis of three different expressions proposed to estimate the SSA as a function of the porosity is performed to compare the estimated values using macro-homogeneous models and the SSA calculated over the generated microstructures, as can be seen in Figure 6.5. The equations used for comparison purposes are defined as:

- Packed particles:

$$SSA_{NMC} = \frac{6 \cdot (1 - \phi_{\text{pore}})}{d_p} \quad (6.28)$$

- Grains⁴⁷:

$$SSA_{NMC} = \frac{4.23 \cdot (1 - \phi_{\text{pore}})}{d_p} \quad (6.29)$$

- Li-ion modification¹⁰:

$$SSA_{NMC} = \frac{6 \cdot (1 - \phi_{\text{pore}} - \phi_{\text{CBD}})}{d_p} \quad (6.30)$$

Where d_p corresponds to the mean particle diameter, which was assigned the value of $6 \mu\text{m}$ based on Table 6.2.

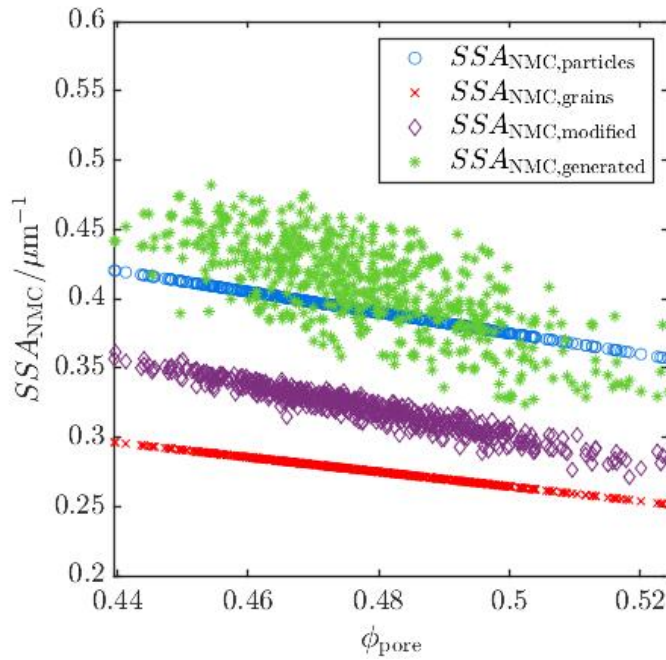


Figure 6.5: Estimated SSA_{NMC} as a function of ϕ_{pore} using different correlations compared to the image-based estimated values of the generated microstructures with different ϕ_{pore}

From Figure 6.5, it can be seen that even though for the four cases the SSA follows a negative slope with respect to the porosity, the values of SSA obtained with equations 6.29 and 6.30 is underestimated with respect to the generated ones in all cases. The values of SSA estimated with equation 6.28 for ideal packed particles is the closest one to the generated dataset; nonetheless, the variability

of the calculated SSA at a micro-scale level due to other microstructural factors apart from the porosity, is not captured with these macro-homogeneous models. Thus, the validity of these correlations can be assessed based on the generation of large amount of non-idealised synthetic microstructures with different properties.

Table 6.2: Equivalent diameter and sphericity of Li-ion microstructures samples during SSA_{NMC} unconstrained maximisation

Iteration	Equivalent diameter / μm	Sphericity
0	6.45	0.85
100	5.51	0.87
250	5.15	0.87
350	5.57	0.88
500	6.25	0.87

Relative diffusivity of the pore phase

As described previously, an improvement in the design of “high power” Li-ion electrodes would enable the fast transport of Lithium ions through the liquid electrolyte in the porous phase. Thus, a maximum relative diffusivity in the porous phase is desired to enhance the ionic transport. This unconstrained maximisation problem is defined by the objective function:

$$f(\mathbf{z}) = D_{\text{rel,pore}} = \frac{\phi_{\text{pore}}}{\tau} \quad (6.31)$$

The results of the unconstrained maximisation of D_{rel} of the pore phase are shown in from Figure 6.6.

The inserted 3D reconstructions show that the maximisation process changes the transport properties, however the resulting microstructures are visually indistinguishable from the training data. This is a property attributed to the generator since it is trained to recreate synthetic microstructures with the same probability distribution function as the real tomographic data. Comparing the SSA_{NMC} of the initial and optimised microstructures as given in Figure 6.7, it is seen that the SSA_{NMC} decreases as $D_{\text{rel,pore}}$ increased.

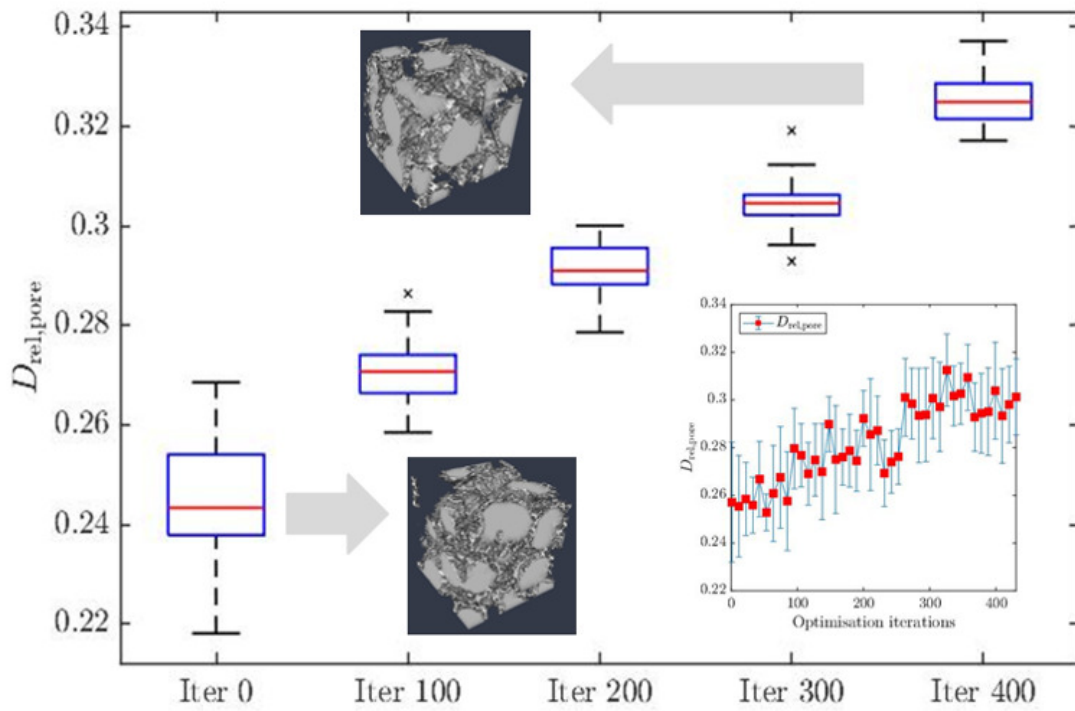


Figure 6.6: Estimated $D_{\text{rel,pore}}$ of 30 generated samples at each 100 points during the maximisation process. The inserted figure shows the complete unconstrained maximisation of $D_{\text{rel,pore}}$ for 400 iterations.

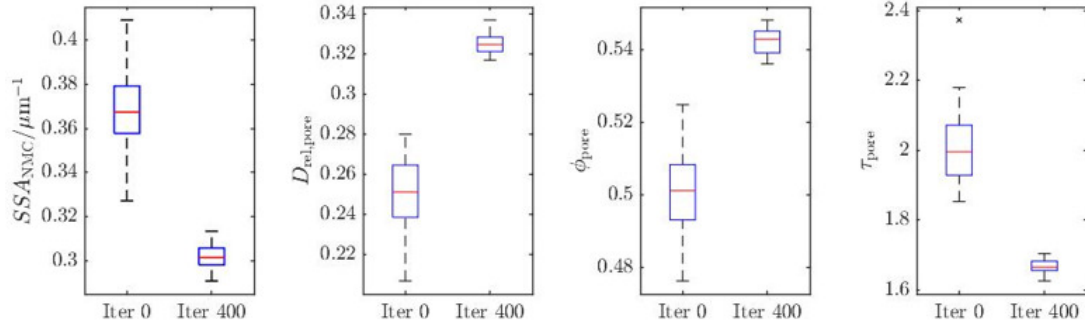


Figure 6.7: Comparison of the estimated SSA_{NMC} , $D_{\text{rel,pore}}$, ϕ_{pore} , and τ_{pore} for iteration 0 and 400 of the unconstrained maximisation process of $D_{\text{rel,pore}}$.

This inverse correlation between these two properties is expected and analysed in the previous section. Additionally, a maximisation of $D_{\text{rel,pore}}$ could be purely attributed to an increase in the pore volume fraction, however as it can be seen in Figure 6.7, in comparing the properties of the initial and the optimised microstructures after 400 iterations, not only is ϕ_{pore} increased, but also the tortuosity factor τ is reduced. This indicates that the configuration of the microstructure is manipulated through the optimisation of the latent space to

enable the existence of less tortuous paths that can reduce the resistance of the material towards an incoming diffusive flow.

These results show the existence of a strong correlation between the microstructural and transport properties and therefore highlight the need to implement constraints during the optimisation process. By considering the trade-off between the SSA of the NMC phase and the D_{rel} of the pore phase, a question arises whether an equilibrium exists for maximising these two properties simultaneously, thus enhancing both the electrochemical reaction and the fast transport of ions. The following section addresses this question.

Relative diffusivity of the pore phase and Specific Surface Area of the NMC phase

The results from the previous sections (6.4.1 and 6.4.1) proved that the microstructure can be manipulated in order to maximise the microstructural and transport properties that are known for increasing the cell performance. However, these properties are not independent and are strongly correlated. Although previous authors have presented mathematical functions to correlate the effect of tortuosity factor with porosity and SSA with porosity, these correlations present deviations for different microstructures (as proved in section 6.4.1)⁴. Therefore, in order to understand the effect of maximising mutually correlated properties, an objective function must be defined which performs an optimisation of the desired microstructural and transport properties while constraining the values of the correlated properties. For the purpose of this work, to obtain a microstructure with maximum values of SSA_{NMC} and $D_{rel,pore}$, both properties must be optimised simultaneously in the definition of $f(z)$. Based on this, the objective function is defined as

$$f(\mathbf{z}) = \beta \cdot D_{rel,pore,norm} + \gamma \cdot SSA_{NMC,norm} \quad (6.32)$$

where

$$D_{rel,pore,norm} = \frac{D_{rel,pore}}{D_{rel,pore,range}} \quad (6.33)$$

$$D_{rel,pore,range} = D_{rel,pore,max} - D_{rel,pore,min} \quad (6.34)$$

$$SSA_{\text{NMC, norm}} = \frac{SSA_{\text{NMC}}}{SSA_{\text{NMC, range}}} \quad (6.35)$$

$$SSA_{\text{NMC, range}} = SSA_{\text{NMC, max}} - SSA_{\text{NMC, min}} \quad (6.36)$$

By definition, $\beta, \gamma \in [0, \dots, 1]$ are coefficients that determine the weight of each property in the objective function. These two coefficients are related to each other by equation 6.37

$$\beta = 1 - \gamma \quad (6.37)$$

A sensitivity analysis was performed to evaluate the impact of each property in the objective function by varying the values of β and γ from $\gamma = \{0.25, 0.5, 0.75\}$. The results for each value of γ for an optimisation of 500 iterations are given in Figure 6.8.

Based on the assumption that both properties contribute equally to the maximisation of the objective function, it would be predicted that a microstructure with maximum SSA_{NMC} and $D_{\text{rel, pore}}$ simultaneously would be obtained by assigning the value of $\gamma = 0.5$. However, from the results in Figure 6.8, it is seen that a value of $\gamma = 0.5$ leads to an increase in SSA_{NMC} (positive slope) while keeping the values of $D_{\text{rel, pore}}$ almost constant (slope approx. 0). By reducing the value of γ to 0.25, the slope of the values of $D_{\text{rel, pore}}$ becomes positive and the slope of the values of SSA_{NMC} becomes negative. The fact that the slope of SSA_{NMC} is inverted indicates that a maximum in $f(\mathbf{z})$ where both properties present a positive slope would be found at a value of γ between 0.5 and 0.25. This analysis shows that the objective function is more sensitive towards a variation in the SSA_{NMC} than a variation in $D_{\text{rel, pore}}$, and therefore a small increase in the coefficient of SSA_{NMC} leads to a significant increase in the objective function. This is also indicative that there is a more direct correlation between the latent space of the generator and the SSA_{NMC} than with other properties. This finding is important to point out for future work where the latent space could be implemented as parameters of design of optimum microstructure.

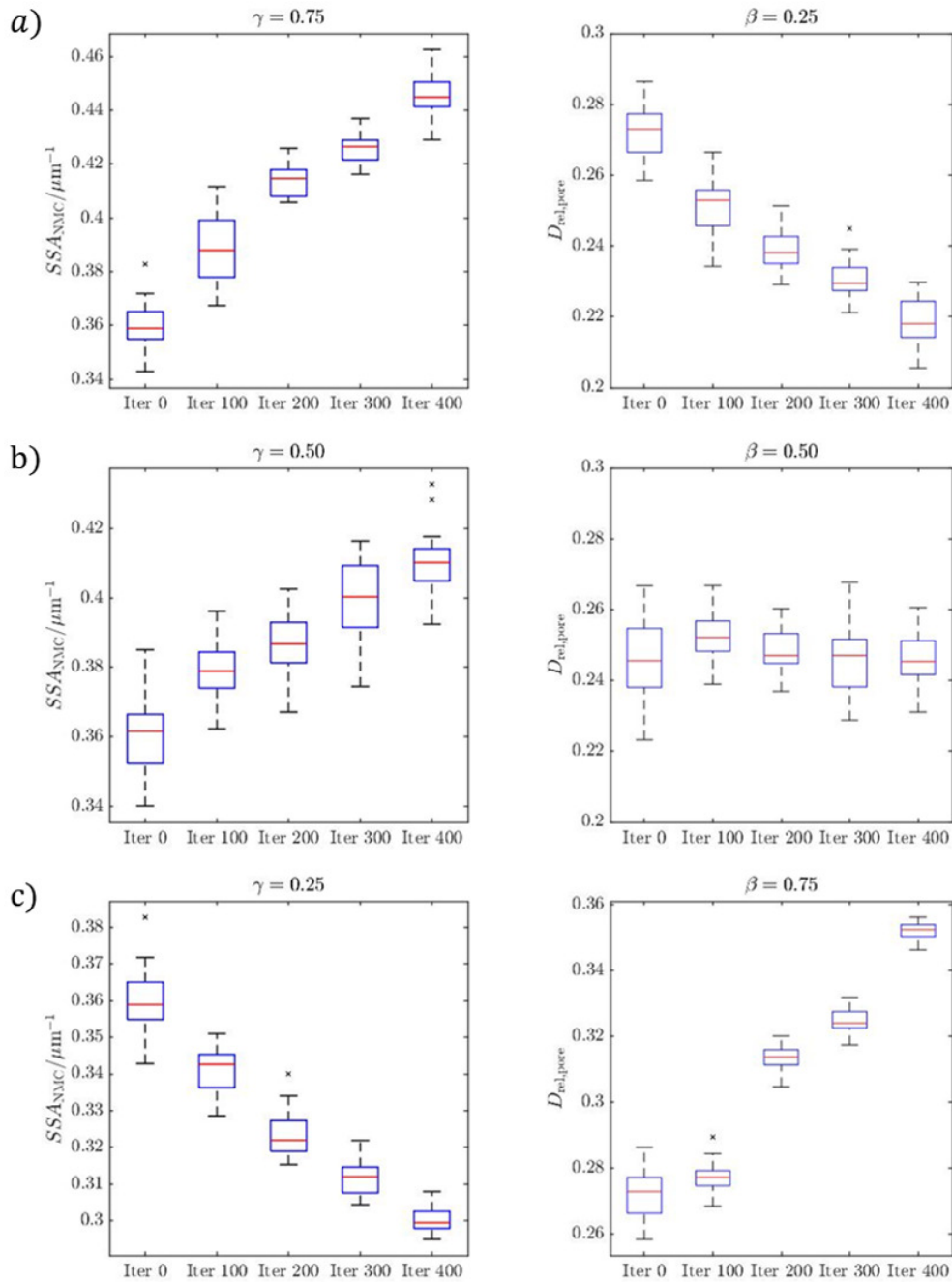


Figure 6.8: Results of estimated SSA_{NMC} and $D_{rel,pore}$ as a function of the iterations number for different values of β : a) $\beta = 0.25$, b) $\beta = 0.5$, c) $\beta = 0.75$

When analysing the other two cases where $\gamma = 0.75$ and 0.25 , it is important to point out that even though the correlation between the two properties is inverse, by manipulating the coefficient of each property in the objective function (*i.e.* β and γ) it is possible to obtain microstructures with a large improvement in a specific property (maximisation with positive slope) while constraining the decrease in the values of the correlated property. These results highlight the im-

portance of considering the trade-off between properties values when optimising and designing electrode microstructure.

Specific Surface Area of the NMC phase constrained by the NMC volume fraction

One pathway to obtain a maximum SSA_{NMC} is to increase the volume fraction of the NMC material (ϕ_{pore}). Although this is theoretically achievable and desired for a “high energy” battery, an increase in the NMC loading leads to a decrease in the porosity, and therefore a decrease in the $D_{\text{rel,pore}}$, which implies a reduction in the battery power. Therefore, in an attempt to balance the energy and power of the battery, it is desired to optimise the accessible capacity for a fixed total loading (*i.e.* fixed volume fraction of NMC material). Based on this, a maximisation of the SSA_{NMC} must be constrained to maintaining the volume fraction of the NMC material constant. Thus, the objective function to optimise is defined by

$$f(z) = \frac{SSA_{\text{NMC}}}{SSA_{\text{NMC,range}}} - \frac{\text{RMSE}(\phi_{\text{NMC}} - \phi_{\text{NMC,mean}})}{\phi_{\text{NMC,range}}} \quad (6.38)$$

where the second term is a penalisation term to keep the volume fraction constant, defined as

$$\text{RMSE} = \sqrt{\frac{\sum_{i=1}^N (\phi_{\text{NMC}_i} - \phi_{\text{NMC}_{\text{mean}}})^2}{N}} \quad (6.39)$$

Equation 6.39 corresponds to the Root-Mean-Squared Error (RMSE) of ϕ_{NMC_i} for $i = \{1, \dots, N\}$ where N constitutes the total number of samples, and $\phi_{\text{NMC}_{\text{mean}}}$ corresponds to the mean value of ϕ_{NMC} in the training set.

Previous authors have proposed an optimisation of the microstructure by decreasing the particle size to enable a higher specific surface area. These works however are based on idealised representations of the microstructure constituted by spherical particles which can be decreased according to an objective function. In this work the particle size is not a target of the objective function, but rather the result of optimising the SSA. The optimisation is performed directly over the architecture of the microstructure defined by the latent space, without targeting a

particular property.

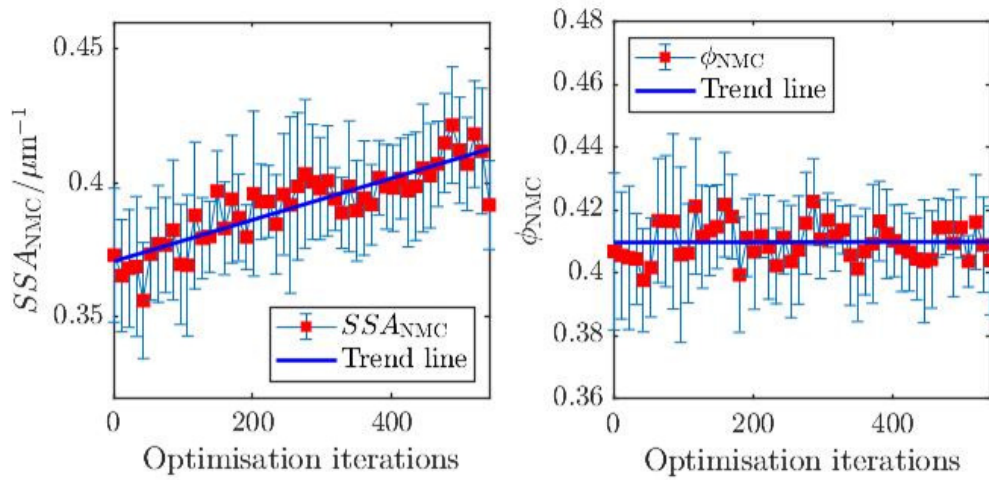


Figure 6.9: Results of estimated SSA_{NMC} and ϕ_{NMC} as a function of the iterations number for the SSA_{NMC} maximisation process constrained by a constant ϕ_{NMC} . The results show a confidence interval of 95%.

The results of the maximisation of the SSA_{NMC} constraining the NMC volume fraction are shown in Figure 6.9. These results show an increase in the SSA_{NMC} while the values of the ϕ_{NMC} remain constant. This proves that it is possible to maximise the specific surface area of microstructures without increasing the amount of NMC material, which can be experimentally difficult. By comparing the estimated average particle size and sphericity of the initial microstructure with the optimised microstructure reported in Table 6.3, it is shown that the mean particle size does not vary significantly. This implies that the maximisation of the SSA_{NMC} is not always related to the particle size or sphericity, but can be a result of a redistribution of the active particles in the given space, or a change in the roughness of the outer surface that lead to an increase in surface area. A change in roughness can be seen by the change in particle sphericity reported in Table 6.3. Additionally, even though the mean particle size remains constant throughout the optimisation, it is possible that the distribution of particle sizes changes, which could potentially lead to the generation of microstructures with a particular arrangement of particle sizes which enhances the specific surface area.

Table 6.3: Equivalent diameter and sphericity of Li-ion microstructures samples during SSA_{NMC} maximisation constraining ϕ_g

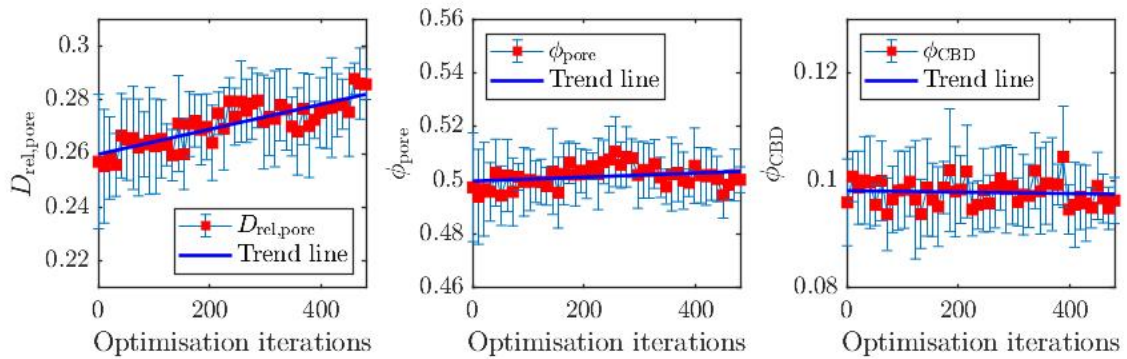
Iteration	Equivalent diameter / μm	Sphericity
0	5.31	0.88
100	6.13	0.85
200	7.03	0.81
300	5.73	0.83
500	6.43	0.81

Relative diffusivity of the pore phase constrained by the pore phase volume fraction

As previously stated, an unconstrained maximisation of the relative diffusivity in the pore phase ($D_{\text{rel,pore}}$) leads to an increase in the porosity of the system, which subsequently decreases the loading of active material. In this respect, a maximisation of the $D_{\text{rel,pore}}$ needs to be constrained by keeping the porosity constant. This is defined as

$$f(z) = \frac{D_{\text{rel,pore}}}{D_{\text{rel,pore,range}}} - \frac{\text{RMSE}(\phi_{\text{pore}} - \phi_{\text{pore,mean}})}{\phi_{\text{pore,range}}} \quad (6.40)$$

where the second term of the RHS of the equation corresponds to the RMSE of the porosity ϕ_{pore} calculated for each of the N generated samples.

**Figure 6.10:** Results of estimated $D_{\text{rel,pore}}$, ϕ_{pore} and ϕ_{CBD} as a function of the iterations number for the $D_{\text{rel,pore}}$ maximisation process constrained by a constant ϕ_{pore} . The results show a confidence interval of 95%.

The results of the increase in $D_{\text{rel,pore}}$ as a function of the number of iterations is shown in Figure 6.10. This shows that an increase in the $D_{\text{rel,pore}}$ is achieved after 500 iterations, while the ϕ_{pore} is kept constant. In comparing the constrained and unconstrained maximisation, the positive slope of the constrained iterative process is not as steep as the one for the unconstrained maximisation of $D_{\text{rel,pore}}$, shown in Figure 6.10. This proves the tight correlation between $D_{\text{rel,pore}}$ and ϕ_{pore} . Given that the ϕ_{pore} is constant, it is rationalised that the maximisation of the relative diffusivity is achieved by a decrease in the electrode tortuosity. This means that the latent space optimisation allows a restructuring of the microstructure which results in the opening of flow paths that enable the transport of lithium ions. An additional analysis of the effect of the CBD during the constrained optimisation is considered in this work. The purpose of the CBD is to provide mechanical integrity to the electrode and conduct electrons. Thus, a change in the CBD load would directly impact the conductivity of electrons. From figure 6.10 it is seen that a constraint in the porosity leads to a fixed volume fraction of the CBD (and by definition of volume fraction, the loading of active material ϕ_{NMC} is also constant).

Relative diffusivity of the pore phase along the x direction

A characterisation of the original microstructure shown elsewhere²⁰ indicates that the microstructure is isotropic and therefore all its properties are statistically the same along the three directions (through-plane and in-plane). Nonetheless, it is known that the transport of lithium ions during cycling is predominant along the through-plane direction which consists of the transport from the membrane to the current collector. Based on this, an improved relative diffusivity in the pore phase is desired along this direction of transport, and therefore a maximisation of the $D_{\text{rel,pore},x}$ is considered as the objective function, defined as

$$f(\mathbf{z}) = D_{\text{rel,pore},x} = \frac{\phi_{\text{b},x}}{\tau_x} \quad (6.41)$$

This equation does not constraint the increase of the $D_{\text{rel,pore}}$ along the other two directions, nonetheless it favours an increase in the direction to be maximised (*i.e.* x).

As seen in Figures 6.11 and 6.12, the $D_{\text{rel,pore}}$ along direction y and z remains

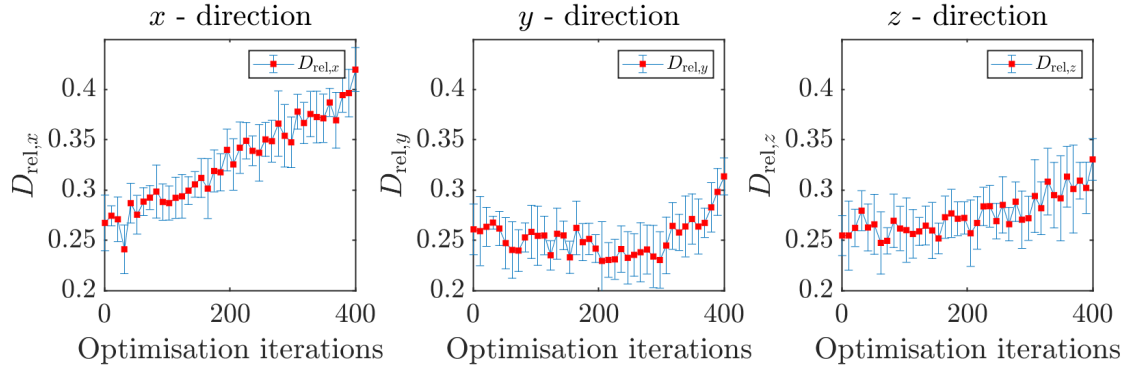


Figure 6.11: Results of the estimated $D_{\text{rel,pore}}$ as a function of the iterations number for the three directions x , y and z for the unconstrained maximisation of $D_{\text{rel,pore},x}$. The results show a confidence interval of 95%.

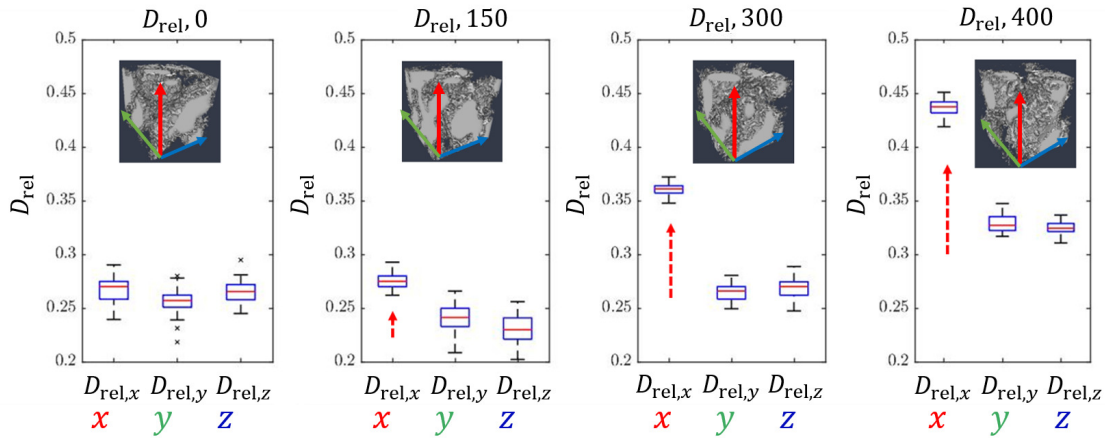


Figure 6.12: Results of estimated $D_{\text{rel,pore}}$ of 30 microstructure samples generated at four points during the unconstrained maximisation process of $D_{\text{rel,pore},x}$.

constant throughout all iterations, until iteration 300, where a further increase in the $D_{\text{rel,pore},x}$ imposes an increase in $D_{\text{rel,pore},y}$ and $D_{\text{rel,pore},z}$. In order to constrain the $D_{\text{rel,pore}}$ to be constant along y and z directions, a penalisation term for each direction is added to the objective function, as given by equation 6.42

$$f(\mathbf{z}) = D_{\text{rel,pore},x} - \text{RMSE}(D_{\text{rel,pore},y}, D_{\text{rel,pore},y_{\text{mean}}}) - \text{RMSE}(D_{\text{rel,pore},z}, D_{\text{rel,pore},z_{\text{mean}}}) \quad (6.42)$$

where

$$\text{RMSE} = \sqrt{\frac{\sum_{i=1}^N (D_{\text{rel,pore},y_i} - D_{\text{rel,pore},y_{\text{mean}}})^2}{N}} \quad (6.43)$$

Equation 6.43 constitutes the RMSE of $D_{\text{rel,pore},y_i}$ for $i = \{1, \dots, N\}$ where N constitutes the total number of samples, and $D_{\text{rel,pore},y_{\text{mean}}}$ corresponds to the mean value of $D_{\text{rel,pore},y}$ in the training set. Equation 6.43 is also applicable for z direction.

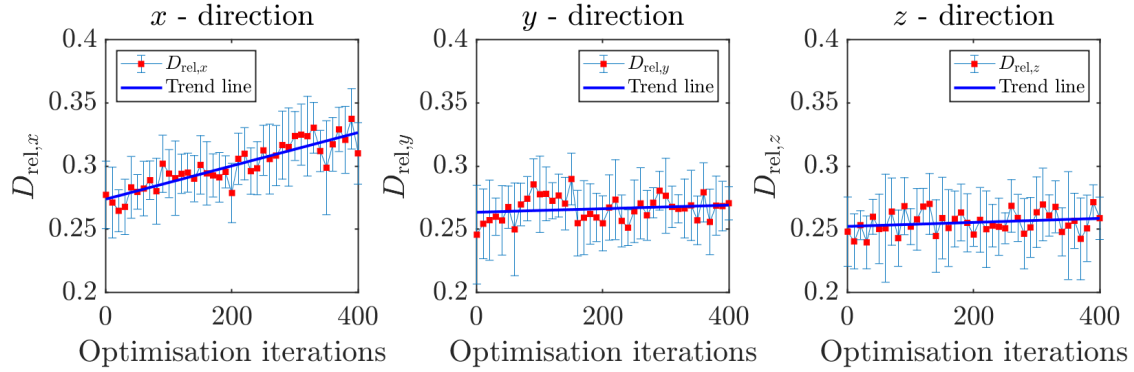


Figure 6.13: Results of the estimated $D_{\text{rel,pore}}$ as a function of the iterations number for the three directions x , y and z for the maximisation of $D_{\text{rel,pore},x}$ constrained by a constant value of $D_{\text{rel,pore},y}$ and $D_{\text{rel,pore},z}$. The results show a confidence interval of 95%

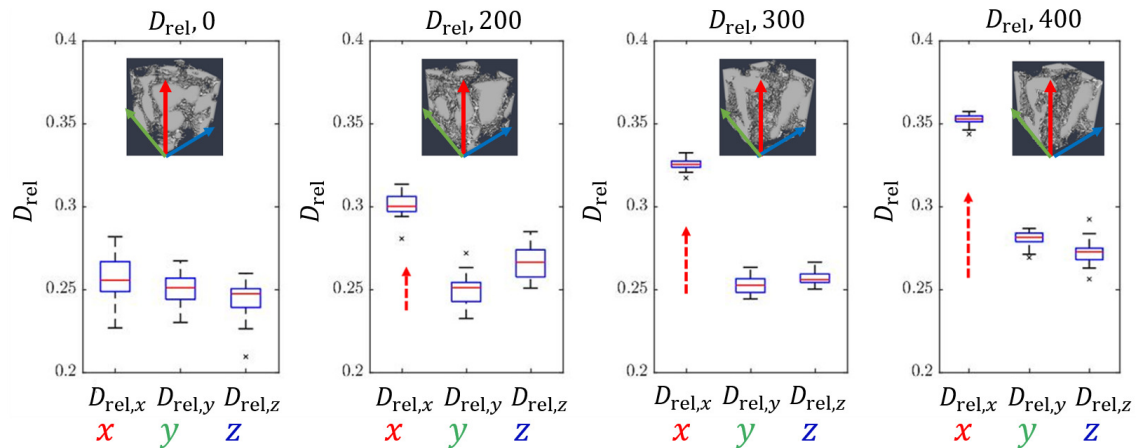


Figure 6.14: Results of estimated $D_{\text{rel,pore}}$ of 30 microstructure samples generated at four points during the maximisation process of $D_{\text{rel,pore},x}$ constrained by a constant value of $D_{\text{rel,pore},y}$ and $D_{\text{rel,pore},z}$.

The results from Figure 6.13 and 6.14 show that by imposing two penalisation terms in the objective function corresponding to the increase of the relative diffusivity in y and z , the maximisation of $D_{\text{rel,pore},x}$ is achieved while $D_{\text{rel,pore},y}$ and $D_{\text{rel,pore},z}$ are kept constant. In comparing Figure 6.11 and Figure 6.13, it is clear that the increase in $D_{\text{rel,pore},x}$ is not as steep when a penalisation terms is added in the other two directions. This proves the tight correlation between the properties

along each direction; however it also shows that the directionality of each property can be treated independently and does not necessarily change the properties along the other directions.

Graded porosity

Previous authors have shown an improved battery performance through the design of electrodes with graded porosity and graded particle size distribution⁷. This graded properties are achieved through a direct manipulation of the tomographic data by changing a specific set of voxels to increase or decrease the phase volume fraction. As an alternative method, this work proposes the implementation of the closed-loop generation optimisation approach for the generation of new microstructure with graded porosity or particle distribution. By implementing a target volume fraction at the inlet and outlet walls (*i.e.* 2D slices at the inlet and outlet of the $64 \times 64 \times 64$ microstructure) and defining a linear space between these points and the electrode length (*i.e.* 64 voxels), an objective function can be defined to fit the volume fraction of each image to the target volume fraction. This function is defined as

$$f(\mathbf{z}) = \text{RSME}(\phi_{p,i}, \phi_{\text{inspace},i}) \quad (6.44)$$

where p refers to the phase (*i.e.* pore, NMC or binder), and i corresponds to the size of the electrode length. In this case the total length in voxels is 64, which corresponds to the number of stacked 2D images obtained from tomographic data.

Figure 6.15 shows the initial and optimised volume fraction of the pore and NMC phases as a function of the electrode length. It can be seen that the initial image contained a random distribution of the phase volume fraction. After 30 iterations, the resulting volume fraction is graded along a positive or negative slope in the direction of the corresponding values of the linear space. These results show that an optimisation of the \mathbf{z} space not only leads to a change in the microstructural properties as homogenised values, but can also provide directionality to the properties. This can be implemented for any property by defining an objective function similar to equation 6.44.

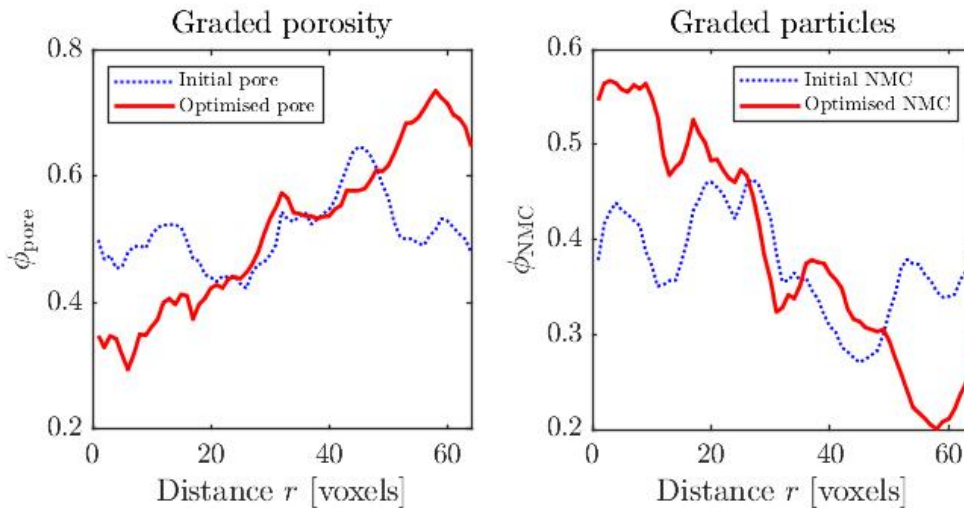


Figure 6.15: Porosity as a function of the electrode length along the direction to be optimised

Implementation of the method to a larger microstructure

The method described in section 6.3.2 was implemented to generate volumes of 64^3 voxels. Based on the fully convolutional architecture of the generator, microstructures of any size can be generated by increasing the size of the latent space. For instance, with a latent space of $1 \times 4 \times 4 \times 4 = 64$, a volume of 64^3 is generated; however, a latent space of dimensions $1 \times 6 \times 6 \times 6 = 216$ is required to generate a volume of 128^3 voxels. The inconvenience with this is the estimation of the covariance matrix \mathbf{K} (given by equation 6.16), and the inversion of this matrix to find the hyperparameters of the GP.

During the first iterations where the size of the training set is 50, the input \mathbf{X} has dimensions of 216×50 , and \mathbf{K} has dimensions of 50×50 . However, as the number of iterations increase, the estimation of the new covariance matrix becomes more expensive since \mathbf{X}_{new} includes all the previous data points and has dimensions of $216 \times n$, where n corresponds to the number of data points. The size of \mathbf{K} also increases at each time-step, with dimensions $n \times n$, and therefore the inversion process becomes more computationally expensive with each iteration. A solution was proposed by Roberts et al.⁴⁸ where the optimisation algorithm is modified and previous iterations are forgotten, leaving a matrix of constant size for each iteration. Nonetheless, given that the GP is updated at each iteration

with the search term α that involves the GP variance, after a number of iterations where the previous steps are forgotten the algorithm will search for the optimum in places previously explored which are no longer contained in the updated $\{\mathbf{Z}, \mathbf{Y}\}$. This is considered a disadvantage of the method in terms of efficiency and therefore a larger number of iterations is required to reach an maximum. Notwithstanding this inconveniences, to the author's knowledge the proposed method is the first one introduced for designing large microstructure with specified properties and of a size enough to contain the thickness of the entire electrode.

In order to demonstrate the implementation of this method to larger microstructures, a maximisation of the effective diffusivity in the pore phase is implemented for a volume of 128^3 voxels. The objective function is defined as equation 6.41. The results of the maximisation process for a maximum of 800 iterations is shown in Figure 6.16. These results prove the effectiveness of implementing the proposed closed-loop optimisation process for a large microstructure. From Figure 6.16 it is seen that the visually realistic microstructure with increased relative diffusivity in the pore phase is achieved. Moreover, a larger set of microstructures of the same size with different properties can be generated based on the optimisation process of the latent space. Thus, knowing the values of the vectors \mathbf{z} which are correlated to their respective values of $D_{\text{rel,pore}}$ is equivalent to encoding the large microstructures into a 64-digit "code" where the 128^3 microstructure can be rapidly generated (~ 3 seconds) with the generator. This allows a large amount of three-dimensional data to be saved in a computationally inexpensive manner.

6.4.2 Analysis and visualisation of the microstructural properties as a function of the latent space

Up until now, this work has proved that an optimisation of the latent vector (\mathbf{z}) of the generator as parameters of design can lead to the generation of microstructures ($G(\mathbf{z})$) with customised properties. However, a question arises whether the correlation of the latent space with the various microstructural properties can be visualised or further implemented for the generation of new microstructures. As an answer to this question and for visualisation purposes, the 64-dimensional latent space was reduced to a 2-dimensional space by implementing a Principal

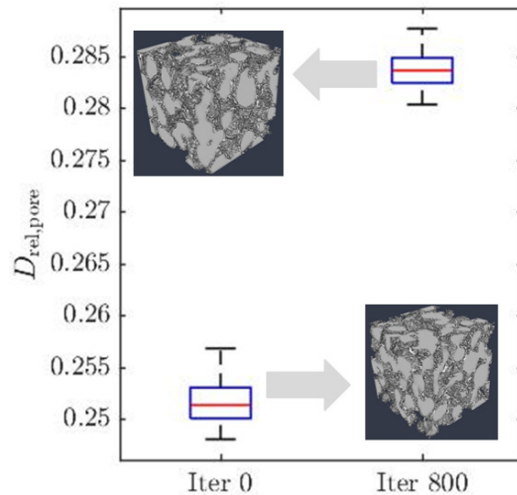


Figure 6.16: Unconstrained maximisation of the relative diffusivity of the pore phase $D_{\text{rel,pore}}$ for an image of size 128^3 voxels.

Component Analysis (PCA).

PCA is a feature extraction technique that reduces the inputs into a smaller dimensionality space. This method finds the directions of greatest variance in the data set, which means the lines that capture most information of the data, and projects each data point by its coordinates along each of these directions⁴⁹. Given a data set of n dimensions (*i.e.* $x^{(1)}, x^{(2)}, \dots, x^{(n)}$), the data is projected from an n -dimensional space to a p -dimensional space. From the standardised data, the covariance matrix is calculated, as described in equation 6.12. The eigenvalues (λ) of the covariance matrix are calculated, and the p largest eigenvalues ($\lambda_{i=1, \dots, p}$) are selected. The p eigenvectors associated with the p largest eigenvalues are called principal components. Finally the data is projected on the space of dimension p according to the principal components. The first principal component captures most of the information of the data, while the second component captures less information, and so on.⁴⁹

In this work, the 64-dimensional space is squeezed into two principal components, as shown in Figure 6.17. This dimensionality reduction process is a major task which could lead to uncorrelated data according to the microstructural properties since these are not considered in the dimensionality reduction process.

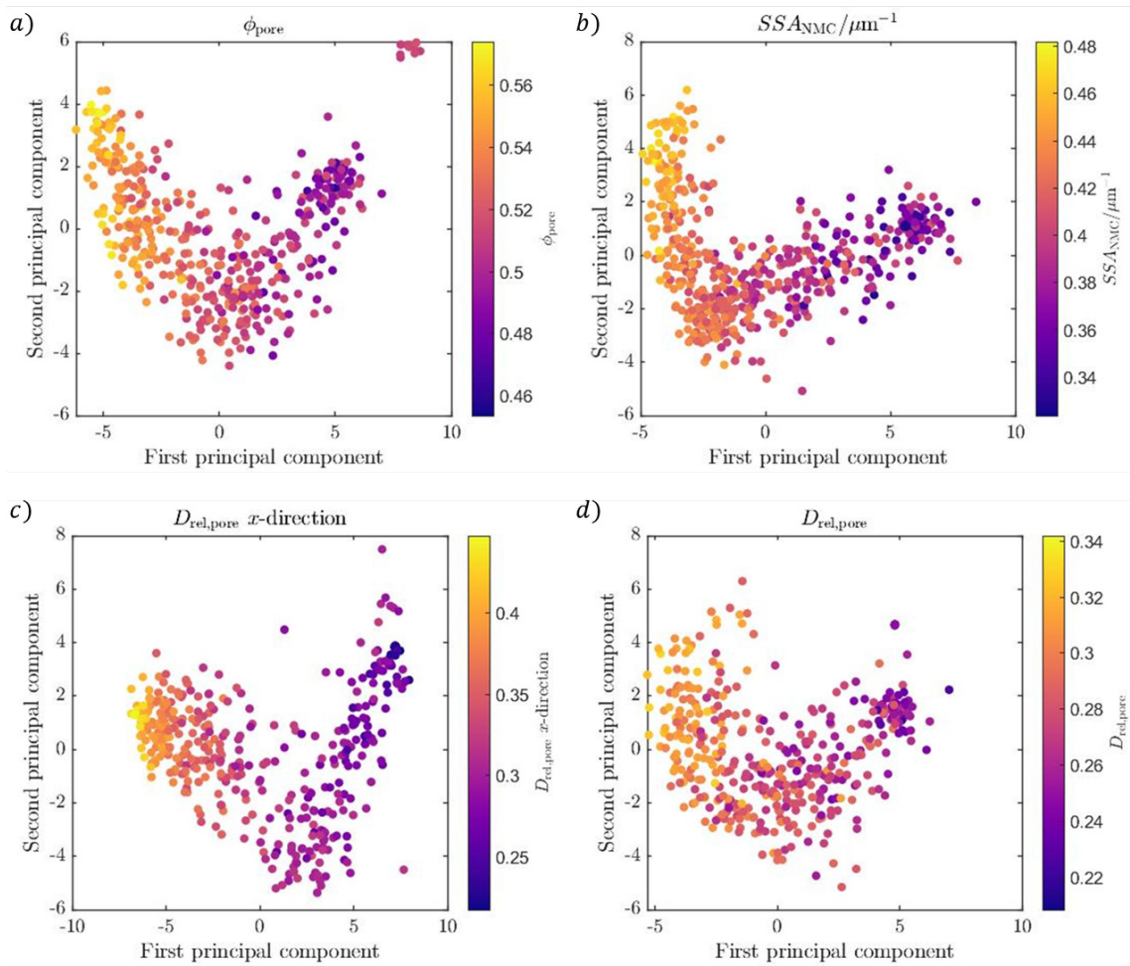


Figure 6.17: Two principal components of the 64-dimensional latent space as a function of different microstructural and transport properties: a) porosity (ϕ_{pore}), b) Specific surface area of the NMC phase (SSA_{NMC}), c) relative diffusivity of the pore phase along the x direction ($D_{rel,pore,x}$), d) relative diffusivity of the pore phase ($D_{rel,pore}$)

Nonetheless, in this case, it is clear that the two principal components of the latent space are related to the electrode's microstructural properties. Moreover, the implementation of PCA allows the creation of a space where the neighbouring principal components contain similar microstructural properties. Therefore, this 2D continuous space can be separated into regions of different properties, each of which is associated with a region in the 64-dimensional latent space, and an interpolation in the 2D space from one region to the other can be performed in order to obtain microstructures with different properties.

6.5 Conclusions

Exploring the effect of the latent space of GANs is one of the main topics of interest for the Machine Learning community. However, only a few selected works have implemented GANs for the stochastic reconstruction of microstructure. Thus, no previous work has performed a detailed analysis of the effect of the latent space of the generator in the resulting microstructural properties. This work introduces a method for analysing the latent space as optimisation parameters the electrode microstructure and implements this method for the design of microstructures of Li-ion cathodes with user-specified properties.

For the design of electrodes, it is essential to obtain a function that defines the geometric space and morphology of the microstructure. This work uses a trained deep-convolutional generator as such a function that captures the pdf that defines the microstructure. Based on this, an algorithm is introduced to perform a closed-loop generation-optimisation process to enable the generation of synthetic microstructure with optimum properties. It is demonstrated in this work that the implementation of a Gaussian Process (GP) regression is able to serve as a surrogate function that maps the latent space of the generator with the microstructural and transport properties of the generated microstructure. This process is key in the development of a closed-loop generation-optimisation process of images with desired optimum properties. Based on the existence of a GP, a Bayesian optimisation approach can be implemented for iteratively searching for an optimum latent space that generates microstructures with a particular set of properties.

It has been proved in this work that the method developed can be implemented for the unconstrained maximisation of properties such as SSA and relative diffusivity. Additionally, this work is able to perform a simultaneous optimisation of correlated properties such as SSA and relative diffusivity by defining an objective function that accounts for the trade-off between both properties. In a similar way, it is possible to maximise these properties while constraining the value of the phase volume fractions to be constant. This step is key for future work in which the optimisation of microstructural properties is correlated with

the experimental synthesis methods. To the author's knowledge, this is the first work that presents a methodology for defining a constrained function that can optimise only a desired set of microstructural properties. Based on this, the results of this work show the advantage of implementing this method due to its ability to perform constrained and unconstrained optimisation of various microstructural and transport properties. The effect of these improvements is expected to be quantified with a full electrochemical simulation over the generated microstructures; however this falls beyond the scope of this work and is recommended as future work.

It is important to point out that in the generation-optimisation process, an exploration of the microstructural design space was performed in terms of some morphological and transport properties. However, an "optimum microstructure" was not established since the optimality depends on the target or purpose of the electrode. As pointed out in section 6.4.1, a trade-off between certain properties must be taken into account to define which property would have a preferred weight over the other. In this context, it is worth mentioning that an optimum microstructure would be the one that delivers the best functional performance (high C rate, energy density, durability, etc.). Thus, as future work it is suggested to implement a full electrochemical simulation that can provide a metric of performance based on the generated microstructures and link this to the GP and Bayesian optimisation process. This metric is expected to provide an insight into which microstructural properties possess a higher impact on the performance in a closed-loop optimisation process.

An analysis of the correlation between the latent space and the output properties is performed by reducing its dimensions from a 64-dimensional space to a 2D space. These results show that the solution of the microstructure with the desired properties is not necessarily unique. Nonetheless, as can be seen from the correlation of the latent space plots with the output properties, microstructures with similar properties are located in areas close together, and an interpolation in this continuous optimised latent space allows the generation of microstructures with a large spectrum of properties.

Even though it has been shown in this work that the manipulation of the latent space leads to the generation of synthetic microstructures, this latent space possess no physical meaning. Thus, there is also a need to correlate experimental synthesis methods with microstructural and transport properties. A direct design of the microstructure based on experimental data requires a vast dataset, which in some cases is expensive. Correlating the latent space of a generative model with synthesis methods could lead to a fast detection of the optimum synthesis methods required to obtain improved electrodes.

References

- [1] I. Goodfellow, J. Pouget-Abadie, M. Mirza, B. Xu, D. Warde-Farley, S. Ozair, A. Courville, and Y. Bengio, “Generative Adversarial Networks,” *pre-print*, pp. 1–9. arXiv:1406.2661 [stat.ML].
- [2] I. Goodfellow, “NIPS 2016 tutorial: Generative adversarial networks,” *pre-print*, 2016. arXiv:1701.00160 [stat.ML].
- [3] H. Moussaoui, R. K. Sharma, J. Debayle, Y. Gavet, G. Delette, and J. Laurencin, “Microstructural correlations for specific surface area and triple phase boundary length for composite electrodes of solid oxide cells,” *Journal of Power Sources*, vol. 412, no. November 2018, pp. 736–748, 2019.
- [4] S. J. Cooper, A. Bertei, D. P. Finegan, and N. P. Brandon, “Simulated impedance of diffusion in porous media,” *Electrochimica Acta*, vol. 251, pp. 681–689, 2017.
- [5] H. Moussaoui, J. Laurencin, Y. Gavet, G. Delette, M. Hubert, P. Cloetens, T. Le Bihan, and J. Debayle, “Stochastic geometrical modeling of solid oxide cells electrodes validated on 3D reconstructions,” *Computational Materials Science*, vol. 143, pp. 262–276, 2018.
- [6] A. Bielefeld, D. A. Weber, and J. Janek, “Microstructural Modeling of Composite Cathodes for All-Solid-State Batteries,” *Journal of Physical Chemistry C*, vol. 123, no. 3, pp. 1626–1634, 2019.
- [7] X. Lu, A. Bertei, D. P. Finegan, C. Tan, S. R. Daemi, J. S. Weaving, K. B. O’Regan, T. M. Heenan, G. Hinds, E. Kendrick, D. J. Brett, and P. R. Shearing, “3D microstructure design of lithium-ion battery electrodes assisted by X-ray nano-computed tomography and modelling,” *Nature Communications*, vol. 11, no. 1, pp. 1–13, 2020.
- [8] F. L. E. Usseglio-Viretta, A. Colclasure, A. N. Mistry, K. P. Y. Claver, F. Pouraghajan, D. P. Finegan, T. M. M. Heenan, D. Abraham, P. P. Mukherjee, D. Wheeler, P. Shearing, S. J. Cooper, and K. Smith, “Resolving the Discrepancy in Tortuosity Factor Estimation for Li-Ion Battery Electrodes through Micro-Macro Modeling and Experiment,” *Journal of The Electrochemical Society*, vol. 165, no. 14, pp. A3403–A3426, 2018.

- [9] B. L. Trembacki, A. N. Mistry, D. R. Noble, M. E. Ferraro, P. P. Mukherjee, and S. A. Roberts, “Editors’ Choice—Mesoscale Analysis of Conductive Binder Domain Morphology in Lithium-Ion Battery Electrodes,” *Journal of The Electrochemical Society*, vol. 165, no. 13, pp. E725–E736, 2018.
- [10] B. Suthar, P. W. C. Northrop, D. Rife, and V. R. Subramanian, “Effect of Porosity, Thickness and Tortuosity on Capacity Fade of Anode,” *Journal of The Electrochemical Society*, vol. 162, no. 9, pp. A1708–A1717, 2015.
- [11] Y. Zhang, M. Yan, Y. Wan, Z. Jiao, Y. Chen, F. Chen, C. Xia, and M. Ni, “High-throughput 3D reconstruction of stochastic heterogeneous microstructures in energy storage materials,” *npj Computational Materials*, vol. 5, no. 1, 2019.
- [12] Y. Suzue, N. Shikazono, and N. Kasagi, “Micro modeling of solid oxide fuel cell anode based on stochastic reconstruction,” *Journal of Power Sources*, vol. 184, no. 1, pp. 52–59, 2008.
- [13] M. Baniassadi, H. Garmestani, D. S. Li, S. Ahzi, M. Khaleel, and X. Sun, “Three-phase solid oxide fuel cell anode microstructure realization using two-point correlation functions,” *Acta Materialia*, vol. 59, no. 1, pp. 30–43, 2011.
- [14] A. Ali, X. Wen, K. Nandakumar, J. Luo, and K. T. Chuang, “Geometrical modeling of microstructure of solid oxide fuel cell composite electrodes,” *Journal of Power Sources*, vol. 185, no. 2, pp. 961–966, 2008.
- [15] B. Kenney, M. Valdmanis, C. Baker, J. G. Pharoah, and K. Karan, “Computation of TPB length, surface area and pore size from numerical reconstruction of composite solid oxide fuel cell electrodes,” *Journal of Power Sources*, vol. 189, no. 2, pp. 1051–1059, 2009.
- [16] Q. Cai, C. S. Adjiman, and N. P. Brandon, “Modelling the 3D microstructure and performance of solid oxide fuel cell electrodes: Computational parameters,” *Electrochimica Acta*, vol. 56, no. 16, pp. 5804–5814, 2011.
- [17] A. Bertei, H. W. Choi, J. G. Pharoah, and C. Nicolella, “Percolating behavior of sintered random packings of spheres,” *Powder Technology*, vol. 231, pp. 44–53, 2012.
- [18] M. M. Forouzan, C. W. Chao, D. Bustamante, B. A. Mazzeo, and D. R.

- Wheeler, “Experiment and simulation of the fabrication process of lithium-ion battery cathodes for determining microstructure and mechanical properties,” *Journal of Power Sources*, vol. 312, pp. 172–183, 2016.
- [19] I. Srivastava, D. S. Bolintineanu, J. B. Lechman, and S. A. Roberts, “Controlling binder adhesion to impact electrode mesostructures and transport,” *ACS Applied Materials and Interfaces*, vol. 12, no. 31, pp. 34919–34930, 2020.
- [20] A. Gayon-Lombardo, L. Mosser, N. P. Brandon, and S. J. Cooper, “Pores for thought: generative adversarial networks for stochastic reconstruction of 3D multi-phase electrode microstructures with periodic boundaries,” *npj Computational Materials*, vol. 6, no. 1, pp. 1–11, 2020.
- [21] L. Mosser, O. Dubrule, and M. J. Blunt, “Stochastic Reconstruction of an Oolitic Limestone by Generative Adversarial Networks,” *Transport in Porous Media*, vol. 125, no. 1, pp. 81–103, 2018.
- [22] P. Bojanowski, A. Joulin, D. L. Paz, and A. Szlam, “Optimizing the latent space of generative networks,” *35th International Conference on Machine Learning, ICML 2018*, vol. 2, pp. 960–972, 2018.
- [23] X. Li, Z. Yang, L. Catherine Brinson, A. Choudhary, A. Agrawal, and W. Chen, “A deep adversarial learning methodology for designing microstructural material systems,” *Proceedings of the ASME Design Engineering Technical Conference*, vol. 2B-2018, pp. 1–14, 2018.
- [24] L. Mosser, O. Dubrule, and M. J. Blunt, “Reconstruction of three-dimensional porous media using generative adversarial neural networks,” *Physical Review E*, vol. 96, no. 4, 2017.
- [25] A. O’Hagan, “Curve Fitting and Optimal Design for Prediction,” *Journal of the Royal Statistical Society: Series B (Methodological)*, vol. 40, no. 1, pp. 1–24, 1978.
- [26] R. Neal, *Bayesian Learning for Neural Networks*. Springer Science & Business Media, 2012.
- [27] C. E. Rasmussen and C. K. Williams, *Gaussian Processes for Machine Learning*. Cambridge, MA, USA: MIT Press, 2006.

- [28] M. Ebden, “Gaussian Processes: A Quick Introduction,” *pre-print*, 2008. arXiv:1505.02965 [math.ST].
- [29] D. R. Jones, M. Schonlau, and W. J. Welch, “Efficient Global Optimization of Expensive Black-Box Functions,” *Journal of Global Optimization*, vol. 13, no. 4, pp. 455–492, 1998.
- [30] C. E. Rasmussen, *Evaluation of Gaussian Processes and other Methods for Non-Linear Regression*. PhD thesis, University of Toronto, 1997.
- [31] R. R. Richardson, M. A. Osborne, and D. A. Howey, “Gaussian process regression for forecasting battery state of health,” *Journal of Power Sources*, vol. 357, pp. 209–219, 2017.
- [32] R. R. Richardson, M. A. Osborne, and D. A. Howey, “Battery health prediction under generalized conditions using a Gaussian process transition model,” *Journal of Energy Storage*, vol. 23, no. April, pp. 320–328, 2019.
- [33] E. Bradford, A. M. Schweidtmann, D. Zhang, K. Jing, and E. A. del Rio-Chanona, “Dynamic modeling and optimization of sustainable algal production with uncertainty using multivariate Gaussian processes,” *Computers and Chemical Engineering*, vol. 118, pp. 143–158, 2018.
- [34] E. Bradford, L. Imsland, D. Zhang, and E. A. Del Rio Chanona, “Stochastic data-driven model predictive control using Gaussian processes,” *arXiv*, pp. 1027–1034, 2019.
- [35] E. Bradford, A. M. Schweidtmann, and A. Lapkin, “Efficient multiobjective optimization employing Gaussian processes, spectral sampling and a genetic algorithm,” *Journal of Global Optimization*, vol. 71, no. 2, pp. 407–438, 2018.
- [36] S. Sundararajan and S. Sathya Keerthi, “Predictive approaches for choosing hyperparameters in Gaussian Processes,” *Advances in Neural Information Processing Systems*, vol. 1118, pp. 631–637, 2000.
- [37] B. Shahriari, K. Swersky, Z. Wang, R. P. Adams, and N. De Freitas, “Taking the human out of the loop: A review of Bayesian optimization,” *Proceedings of the IEEE*, vol. 104, no. 1, pp. 148–175, 2016.
- [38] E. A. Del Rio Chanona, J. E. Alves Graciano, E. Bradford, and B. Chachuat,

- “Modifier-adaptation schemes employing Gaussian processes and trust regions for real-time optimization,” *IFAC-PapersOnLine*, vol. 52, no. 1, pp. 52–57, 2019.
- [39] E. A. del Rio-Chanona, P. Petsagkourakis, E. Bradford, J. E. A. Graciano, and B. Chachuat, “Real-time optimization meets bayesian optimization and derivative-free optimization: A tale of modifier adaptation,” *pre-print*, 2021. arXiv:2009.08819 [math.OC].
- [40] S. C. Blair, P. A. Berge, and J. G. Berryman, “Two-Point Correlation Functions to Characterize Microgeometry and Estimate Permeabilities of Synthetic and Natural Sandstones,” *Lawrence Livermore National Laboratory Report*, no. UC-403, pp. 1–31, 1993.
- [41] S. Aksoy and R. M. Haralick, “Feature normalization and likelihood-based similarity measures for image retrieval,” *Pattern Recognition Letters*, vol. 22, no. 5, pp. 563–582, 2001.
- [42] A. Radford, L. Metz, and S. Chintala, “Unsupervised representation learning with deep convolutional generative adversarial networks,” *4th International Conference on Learning Representations, ICLR 2016 - Conference Track Proceedings*, pp. 1–16, 2016.
- [43] V. Dumoulin and F. Visin *pre-print*, pages = 1-31, title = A guide to convolution arithmetic for deep learning, url = <http://arxiv.org/abs/1603.07285>, year = 2016, note=arXiv:1603.07285 [stat.ML].
- [44] D. P. Kingma and J. L. Ba, “Adam: A method for stochastic optimization,” *3rd International Conference on Learning Representations, ICLR 2015 - Conference Track Proceedings*, pp. 1–15, 2015.
- [45] S. J. Cooper, A. Bertei, P. R. Shearing, J. A. Kilner, and N. P. Brandon, “Tau-Factor: An open-source application for calculating tortuosity factors from tomographic data,” *SoftwareX*, vol. 5, pp. 203–210, 2016.
- [46] D. Kraft, “On Converting Optimal Control Problems into Nonlinear Programming Problems,” in *Computational Mathematical Programming. NATO ASI Series* (S. K., ed.), Berlin: Springer, 1985.
- [47] A. Rabbani and S. Jamshidi, “Specific surface and porosity relationship for

- sandstones for prediction of permeability,” *International Journal of Rock Mechanics and Mining Sciences*, vol. 71, pp. 25–32, 2014.
- [48] S. Roberts, M. Osborne, M. Ebden, S. Reece, N. Gibson, and S. Aigrain, “Gaussian processes for time-series modelling,” *Philosophical Transactions of The Royal Society*, no. A371:20110550, 2013.
- [49] G. Hinton and R. Salakhutdinov, “Reducing the Dimensionality of Data with Neural Networks,” *Science*, vol. 313, no. July, pp. 504–508, 2006.

Chapter 7

Conclusions and further work

The overall aim of this project was the characterisation and optimisation of electrode microstructures for energy storage devices. For this purpose, a series of computational techniques were implemented, which involved the development of multiphysics pore-scale models, the implementation of machine learning techniques and the use of Gaussian Processes coupled with Bayesian optimisation algorithms.

The specific objectives considered in this work were the following:

1. The development of a computationally inexpensive model based on a PNM to correlate the electrode morphology with the system performance.
2. The stochastic reconstruction of multi-phase three-dimensional electrode microstructures through the implementation of GANs.
3. The development of a closed-loop generation- optimisation algorithm for the design of electrode microstructures with customised properties.

The fulfilment of each of these objectives was described separately in Chapters 3 and 4 (item 1), Chapter 5 (items 2), Chapter 6 (items 3). The key outcomes from each chapter are summarised below.

7.1 Summary and conclusions

7.1.1 Chapter 3: A Pore Network Model for electrochemical energy storage devices

A computationally inexpensive model based on a PNM was introduced to simulate the coupled flow, mass and charge transport that occur within electrodes in electrochemical devices. This model is able to represent the concentration and current distributions inside the electrode and bridges the gap between volume-averaged continuum models and pore-scale direct numerical simulations.

The methodology was validated with a cubic hypothetical PNM to represent the anode of a VRFB. A comparison between the results obtained in this work and those reported in the literature for a continuum model under the same conditions prove that the model is able to produce similar results in terms of averaged electrode potentials and overpotentials. Nonetheless the present model is able to show microstructural details and provide insight into the effect of the microstructure in the electrode transport and reactive processes.

From this chapter it is concluded that an implementation of a hypothetical PNM that couples the flow, mass, reactive and electrophoretic transport is able to represent the transport processes that occur within the electrode at a pore-scale. This is a key step for understanding the microstructure-performance correlation from a forward perspective, since it provides an insight into the effect of some microstructural parameters, such as permeability and tortuosity, in the battery performance at various SOC.

7.1.2 Chapter 4: PNM implementation for various VRFB electrodes

The previously introduced PNM framework was implemented to simulate the transport processes in a VRFB anode over pore-networks extracted from XCT data of three different carbon-based electrodes: Toray 090, SGL 29AA, Freudenberg and ELAT-H cloth. The results show that in electrodes with large pore-size

diversity, the flow draws preferred paths that connect the largest pores across the electrode length where convection is predominant. Contrary to this case, the areas where convective flow is minimum are limited by mass transport as the movement of species is almost purely diffusive. This non-uniform flow leads to a non-uniform electrode utilisation, which results in the existence of “starved zones” where the pores are not constantly replenished with fresh electrolyte. This causes areas that discharge at a faster rate than the pores on routes with high convective flow.

This analysis proves the advantage of using a pore-scale model over a continuous volume-averaged one for representing with more detail the effects of transport processes in electrode utilisation. Based on this, it is reasonable to conclude that an analysis of the effect of electrode microstructure in mass transport processes is crucial for the design of RFBs with improved performance. These results represent the first visual showcase of how regions limited by low convective flow affect the rate of discharge in an electrode.

7.1.3 Chapter 5: Generative Adversarial Networks for the reconstruction of three-dimensional multi-phase electrode microstructure

This work presents a method for generating synthetic multi-phase three-dimensional microstructures through the implementation of DC-GANs. This method allows the model to represent the statistical and morphological properties of the real microstructure, which are captured in the weights of the trained generator networks.

The method was implemented for two datasets corresponding to a Li-ion cathode and a SOFC anode. A statistical comparison of the microstructural properties of 100 generated microstructures and 100 real sub-volumes showed excellent agreement between the two datasets. Two particular highlights of this work include the ability to generate arbitrarily large synthetic microstructural volumes and the generation of periodic boundaries, both of which are of high

interest to the electrochemical modelling community.

7.1.4 Chapter 6: Gaussian Processes and Bayesian optimisation for the design of microstructures with optimum properties

This work introduces a method for analysing the latent space of a GAN as parameters of design of the electrode microstructure of a Li-ion cathodes. This work uses a trained generator as a function that captures the pdf that defines the microstructure. Based on this, an algorithm is introduced to perform a closed-loop generation-optimisation process to enable the generation of synthetic microstructure with optimum properties. It is demonstrated in this work that the implementation of a Gaussian Process (GP) regression is able to serve as a surrogate function that maps the latent space of the generator with the microstructural properties of the generated microstructure. Based on the existence of a GP, a Bayesian optimisation approach can be implemented for iteratively searching for an optimum latent vector that generates microstructures with a particular set of properties.

The method developed in this work is implemented for the unconstrained maximisation of properties (*i.e.* specific surface area and relative diffusivity) as well as for the simultaneous optimisation of correlated properties. This is performed by defining an objective function that accounts for the trade-off between both properties. In a similar way, a maximisation of these properties is performed while constraining the value of the phase volume fractions to be constant, which constitutes a major step towards the generation of microstructures with optimum properties.

An analysis of the correlation between the latent space and the output properties is performed by reducing its dimensions from a 64-dimensional space to a 2D space. A correlation of the latent space plots with the output properties show that microstructures with similar properties are located in areas close together, and therefore an interpolation in this continuous optimised latent

space allows the generation of microstructures with a large spectrum of properties.

This work represents a major breakthrough in the generation of optimum electrode microstructure since it is able to capture the essence of the microstructure in a lower dimensionality function. Based on this fully defined function it is possible to manipulate and optimise the microstructural properties that are able to increase the electrode performance. In this way, this work provides for the first time an analysis of the microstructure-properties correlation from a forward and backward perspective, which is key for understanding the microstructure-performance correlation as a closed-loop process.

7.2 Further work

This work merges a series of computational techniques, commonly used in other scientific areas (*i.e.* geostatistics, machine learning, computer vision, etc), for the characterisation and optimisation of electrode microstructures. Thus, the present work hereby sets the basis for future opportunities in the area of electrode design and pore-scale modelling for the development of the next generation energy storage technologies.

1. From Chapters 3 and 4 the following steps are recommended as future work:
 - Implementing the PNM over XCT data of a REV to represent the complete electrode of a RFB, and implement a flow-through simulation of the whole cell, including the anode and cathode.
 - Couple the PNM extracted from XCT images with a continuum model that represents the flow through the channel in a RFB. Perform this study with different channel configurations to estimate the effect of the channel in the electrode utilisation and the transport processes within the electrode.
 - Implement a mathematical expression that involves a mass transfer coefficient to correlate the concentration at the bulk of the pore and at the pore surface as a correction to the mixed-cell method.
 - Explore the capabilities of extending the PNM algorithm for different

types of batteries, such as Li-ion batteries, and analyse the effect of changing the pore sizes during cycling due to degradation.

2. From Chapter 5, the following future work is recommended:

- Implement a modification of the vanilla-GAN divergence (*i.e.* Jensen-Shanon divergence) with a Wasserstein divergence to implement WGANs in order to avoid mode collapse during training and ensure a larger variability in the generated data.
- Perform a stochastic optimisation of the GAN hyperparameters to ensure the implementation of an optimised architecture.
- Use of the method described in this work for different types of electrodes, such as carbon-based electrodes.
- Extend the method presented in this work to the implementation of conditional GANs to include microstructural properties in the training set for the further generation of microstructures with different properties.

3. From Chapter 6, the following points are recommended for future work:

- The integration of experimental synthesis data in the training set to perform a correlation between the various synthesis methods with the output microstructural properties.
- Establish a correlation of the synthesis methods with the latent space to a) provide physical meaning to the latent space; b) allow the interpolation in the latent space to generate microstructures with real synthesis parameters; c) perform an optimisation in the latent space to generate optimum microstructures with their respective synthesis parameters.
- Develop a full electrochemical model that can predict the electrode performance and integrate it to the generation-optimisation algorithm.

7.3 Dissemination

7.3.1 Papers

A. Gayon-Lombardo, B. A. Simon, O. O. Taiwo, S. J. Neethling, N.P. Brandon. "A pore network model of porous electrodes in electrochemical devices." *Journal of*

Energy Storage, 24, pp. 100736, (2019).

<https://doi.org/10.1016/j.est.2019.04.010>

A. Gayon-Lombardo, L. Mosser, N. P. Brandon, S. J. Cooper. “Pores for thought: generative adversarial networks for stochastic reconstruction of 3D multi-phase electrode microstructures with periodic boundaries.” *npj Comput. Mater.* 6, 82, pp. 1-11 (2020). <https://doi.org/10.1038/s41524-020-0340-7>

7.3.2 Oral presentations

A. Gayon-Lombardo, L. Mosser, N. P. Brandon, S. J. Cooper. “Pores for thought: generative adversarial networks for stochastic reconstruction of 3D multi-phase electrode microstructures with periodic boundaries”, SE-lectrochem (2019)

A. Gayon-Lombardo, L. Mosser, N. P. Brandon, S. J. Cooper. “Pores for thought: generative adversarial networks for stochastic reconstruction of 3D multi-phase electrode microstructures with periodic boundaries”, 17th Symposium on Modeling and Experimental Validation of Electrochemical Energy Technologies - Modval (2020)

A. Gayon-Lombardo, L. Mosser, N. P. Brandon, S. J. Cooper. “Pores for thought: generative adversarial networks for stochastic reconstruction of 3D multi-phase electrode microstructures with periodic boundaries”, Machine Learning and batteries workshop MREX (2020)

A. Gayon-Lombardo, B. A. Simon, O. O. Taiwo, S. J. Neethling, N.P. Brandon. “A pore network model of porous electrodes in electrochemical devices”, PRiME meeting of The Electrochemical Society (2020)

A. Gayon-Lombardo, L. Mosser, N. P. Brandon, S. J. Cooper. “Pores for thought: generative adversarial networks for stochastic reconstruction of 3D multi-phase electrode microstructures with periodic boundaries”, PRiME meeting of The Electrochemical Society (2020)

7.3.3 Poster presentations

A. Gayon-Lombardo, B. A. Simon, O. O. Taiwo, S. J. Neethling, N.P. Brandon. “A pore network model of porous electrodes in electrochemical devices”, International Renewable Energy Storage Conference (2018)

A. Gayon-Lombardo, B. A. Simon, O. O. Taiwo, S. J. Neethling, N.P. Brandon. “A pore network model of porous electrodes in electrochemical devices”, UK Energy Storage Conference (2018)

A. Gayon-Lombardo, B. A. Simon, O. O. Taiwo, S. J. Neethling, N.P. Brandon. “A pore network model of porous electrodes in electrochemical devices”, 16th Symposium on Modeling and Experimental Validation of Electrochemical Energy Technologies - Modval (2019)

A. Gayon-Lombardo, L. Mosser, N. P. Brandon, S. J. Cooper. “Pores for thought: generative adversarial networks for stochastic reconstruction of 3D multi-phase electrode microstructures with periodic boundaries”, Oxford Battery Modelling Symposium (2020)

References

- [1] R. Gorte and J. Vohs, "Catalysis in solid oxide fuel cells.," *Annual review of chemical and biomolecular engineering*, vol. 2, pp. 9–30, 2011.
- [2] K. M. Abraham, "Prospects and limits of energy storage in batteries," *The Journal of Physical Chemistry Letters*, vol. 6, no. 5, pp. 830–844, 2015.
- [3] A. K. Rohit, K. P. Devi, and S. Rangnekar, "An overview of energy storage and its importance in indian renewable energy sector: Part i – technologies and comparison," *Journal of Energy Storage*, vol. 13, pp. 10–23, 2017.
- [4] M. Ji and Z. Wei, "A review of water management in polymer electrolyte membrane fuel cells," *Energies*, vol. 2, no. 4, pp. 1057–1106, 2009.
- [5] C. L. Yeong and S. Torquato, "Reconstructing random media. II. Three-dimensional media from two-dimensional cuts," *Physical Review E - Statistical Physics, Plasmas, Fluids, and Related Interdisciplinary Topics*, vol. 58, no. 1, pp. 224–233, 1998.
- [6] Y. Jiao, F. H. Stillinger, and S. Torquato, "Modeling heterogeneous materials via two-point correlation functions. II. Algorithmic details and applications," *Physical Review E - Statistical, Nonlinear, and Soft Matter Physics*, vol. 77, no. 3, pp. 1–35, 2008.
- [7] Y. Suzue, N. Shikazono, and N. Kasagi, "Micro modeling of solid oxide fuel cell anode based on stochastic reconstruction," *Journal of Power Sources*, vol. 184, no. 1, pp. 52–59, 2008.
- [8] A. Gayon Lombardo, B. A. Simon, O. Taiwo, S. J. Neethling, and N. P. Brandon, "A pore network model of porous electrodes in electrochemical devices," *Journal of Energy Storage*, vol. 24, p. 100736, 2019.

- [9] M. J. Blunt, *Multiphase Flow in Permeable Media: A Pore-Scale Perspective*. Cambridge: Cambridge University Press, 1 ed., 2017.
- [10] G. Qiu, A. S. Joshi, C. R. Dennison, K. W. Knehr, E. C. Kumbur, and Y. Sun, “3-D pore-scale resolved model for coupled species/charge/fluid transport in a vanadium redox flow battery,” *Electrochimica Acta*, vol. 64, pp. 46–64, mar 2012.
- [11] D. You, H. Zhang, and J. Chen, “A simple model for the vanadium redox battery,” *Electrochimica Acta*, vol. 54, no. 27, pp. 6827–6836, 2009.
- [12] J. T. Gostick, M. A. Ioannidis, M. W. Fowler, and M. D. Pritzker, “Pore network modeling of fibrous gas diffusion layers for polymer electrolyte membrane fuel cells,” *Journal of Power Sources*, vol. 173, pp. 277–290, nov 2007.
- [13] M. L. Perry and A. Z. Weber, “Advanced Redox-Flow Batteries: A Perspective,” *Journal of The Electrochemical Society*, vol. 163, no. 1, pp. A5064–A5067, 2016.
- [14] D. Rastler, “Electricity energy storage technology options: a white paper primer on applications, costs, and benefits,” 2010.
- [15] Department of Transport, “Decarbonising transport, Setting the Challenge,” tech. rep., Department of Transport, 2020.
- [16] Bloomberg NEF, “Battery Pack Prices Cited Below \$100/kWh for the First Time in 2020, While Market Average Sits at \$137/kWh,” 2020.
- [17] H. W. Wu, “A review of recent development: Transport and performance modeling of PEM fuel cells,” *Applied Energy*, vol. 165, pp. 81–106, 2016.
- [18] M. H. Chakrabarti, N. P. Brandon, S. A. Hajimolana, F. Tariq, V. Yufit, M. A. Hashim, M. A. Hussain, C. T. Low, and P. V. Aravind, “Application of carbon materials in redox flow batteries,” *Journal of Power Sources*, no. 253, pp. 150–166, 2014.
- [19] A. Gupta, J. H. Seo, X. Zhang, W. Du, A. M. Sastry, and W. Shyy, “Effective Transport Properties of LiMn₂O₄ Electrode via Particle-Scale Modeling,” *Journal of The Electrochemical Society*, vol. 158, no. 5, p. A487, 2011.
- [20] H. Moussaoui, J. Laurencin, Y. Gavet, G. Delette, M. Hubert, P. Cloetens,

- T. Le Bihan, and J. Debayle, “Stochastic geometrical modeling of solid oxide cells electrodes validated on 3D reconstructions,” *Computational Materials Science*, vol. 143, pp. 262–276, 2018.
- [21] G. Hinds and E. Brightman, “In situ mapping of electrode potential in a PEM fuel cell,” *Electrochemistry Communications*, vol. 17, no. 1, pp. 26–29, 2012.
- [22] Y. Zhang, M. Yan, Y. Wan, Z. Jiao, Y. Chen, F. Chen, C. Xia, and M. Ni, “High-throughput 3D reconstruction of stochastic heterogeneous microstructures in energy storage materials,” *npj Computational Materials*, vol. 5, no. 1, 2019.
- [23] S. J. Cooper, A. Bertei, D. P. Finegan, and N. P. Brandon, “Simulated impedance of diffusion in porous media,” *Electrochimica Acta*, vol. 251, pp. 681–689, 2017.
- [24] G. Qiu, C. R. Dennison, K. W. Knehr, E. C. Kumbur, and Y. Sun, “Pore-scale analysis of effects of electrode morphology and electrolyte flow conditions on performance of vanadium redox flow batteries,” *Journal of Power Sources*, vol. 219, pp. 223–234, 2012.
- [25] A. A. Shah, R. Tangirala, R. Singh, R. G. A. Wills, and F. C. Walsh, “A Dynamic Unit Cell Model for the All-Vanadium Flow Battery,” *Journal of The Electrochemical Society*, vol. 158, pp. A671–A677, jun 2011.
- [26] Y. A. Gandomi, D. S. Aaron, T. A. Zawodzinski, and M. M. Mench, “In Situ Potential Distribution Measurement and Validated Model for All-Vanadium Redox Flow Battery,” *Journal of The Electrochemical Society*, vol. 163, no. 1, pp. A5188–A5201, 2016.
- [27] J. Newman, “Optimization of Porosity and Thickness of a Battery Electrode by Means of a Reaction-Zone Model,” *Journal of The Electrochemical Society*, vol. 142, no. 1, pp. 97–101, 1995.
- [28] A. Gayon-Lombardo, L. Mosser, N. P. Brandon, and S. J. Cooper, “Pores for thought: generative adversarial networks for stochastic reconstruction of 3D multi-phase electrode microstructures with periodic boundaries,” *npj Computational Materials*, vol. 6, no. 1, pp. 1–11, 2020.

- [29] G. Matheron, *Random sets and integral geometry*. Wiley New York, 1975.
- [30] J. Serra, “The Boolean model and random sets,” *Computer Graphics and Image Processing*, vol. 12, no. 2, pp. 99–126, 1980.
- [31] D. Jeulin, “Random texture models for material structures,” *Statistics and Computing*, vol. 10, no. 1, pp. 121–132, 2000.
- [32] C. L. Yeong and S. Torquato, “Reconstructing random media,” *Physical Review E - Statistical Physics, Plasmas, Fluids, and Related Interdisciplinary Topics*, vol. 57, no. 1, pp. 495–506, 1998.
- [33] S. Torquato, *Random heterogeneous materials: microstructure and macroscopic properties*. Springer Science & Business Media, 1 ed., 2013.
- [34] P. A. Rikvold and G. Stell, “Porosity and specific surface for interpenetrable-sphere models of two-phase random media,” *The Journal of Chemical Physics*, vol. 82, no. 2, pp. 1014–1020, 1985.
- [35] B. Lu and S. Torquato, “N-Point Probability Functions for a Lattice Model of Heterogeneous Media,” *Physical Review B*, vol. 42, no. 7, pp. 4453–4459, 1990.
- [36] C. Manwart, S. Torquato, and R. Hilfer, “Stochastic reconstruction of sandstones,” *Physical Review E - Statistical Physics, Plasmas, Fluids, and Related Interdisciplinary Topics*, vol. 62, no. 1 B, pp. 893–899, 2000.
- [37] N. Sheehan and S. Torquato, “Generating microstructures with specified correlation functions,” *Journal of Applied Physics*, vol. 89, no. 1, pp. 53–60, 2001.
- [38] L. M. Pant, *Stochastic characterization and reconstruction of porous media*. PhD thesis, University of Alberta, 2016.
- [39] Y. Jiao, F. H. Stillinger, and S. Torquato, “Modeling heterogeneous materials via two-point correlation functions: Basic principles,” *Physical Review E - Statistical, Nonlinear, and Soft Matter Physics*, vol. 76, no. 3, pp. 1–37, 2007.
- [40] M. M. Forouzan, C. W. Chao, D. Bustamante, B. A. Mazzeo, and D. R. Wheeler, “Experiment and simulation of the fabrication process of lithium-

- ion battery cathodes for determining microstructure and mechanical properties,” *Journal of Power Sources*, vol. 312, pp. 172–183, 2016.
- [41] I. Srivastava, D. S. Bolintineanu, J. B. Lechman, and S. A. Roberts, “Controlling binder adhesion to impact electrode mesostructures and transport,” *ACS Applied Materials and Interfaces*, vol. 12, no. 31, pp. 34919–34930, 2020.
- [42] N. Siddique, A. Salehi, and F. Liu, “Stochastic reconstruction and electrical transport studies of porous cathode of Li-ion batteries,” *Journal of Power Sources*, vol. 217, pp. 437–443, 2012.
- [43] N. A. Siddique and F. Liu, “Process based reconstruction and simulation of a three-dimensional fuel cell catalyst layer,” *Electrochimica Acta*, vol. 55, no. 19, pp. 5357–5366, 2010.
- [44] S. P. S. Badwal, S. S. Giddey, C. Munnings, A. I. Bhatt, and A. F. Hollenkamp, “Emerging electrochemical energy conversion and storage technologies,” *Frontiers in Chemistry*, vol. 2, p. 79, 2014.
- [45] H. Moussaoui, R. K. Sharma, J. Debayle, Y. Gavet, G. Delette, and J. Laurencin, “Microstructural correlations for specific surface area and triple phase boundary length for composite electrodes of solid oxide cells,” *Journal of Power Sources*, vol. 412, no. November 2018, pp. 736–748, 2019.
- [46] X. Lu, A. Bertei, D. P. Finegan, C. Tan, S. R. Daemi, J. S. Weaving, K. B. O’Regan, T. M. Heenan, G. Hinds, E. Kendrick, D. J. Brett, and P. R. Shearing, “3D microstructure design of lithium-ion battery electrodes assisted by X-ray nano-computed tomography and modelling,” *Nature Communications*, vol. 11, no. 1, pp. 1–13, 2020.
- [47] N. Nitta, F. Wu, J. T. Lee, and G. Yushin, “Li-ion battery materials: present and future,” *Materials Today*, vol. 18, no. 5, pp. 252–264, 2015.
- [48] R. M. Darling and M. L. Perry, “The Influence of Electrode and Channel Configurations on Flow Battery Performance,” *Journal of The Electrochemical Society*, vol. 161, no. 9, pp. A1381–A1387, 2014.
- [49] M. Kazacos and M. Skyllas-Kazacos, “Performance Characteristics of Carbon

- Plastic Electrodes in the All-Vanadium Redox Cell,” *Journal of The Electrochemical Society*, vol. 136, no. 9, pp. 2759–2760, 1989.
- [50] J. T. Gostick, “Versatile and efficient pore network extraction method using marker-based watershed segmentation,” *Physical Review E*, vol. 96, no. 2, pp. 1–15, 2017.
- [51] Q. Xiong, T. G. Baychev, and A. P. Jivkov, “Review of pore network modelling of porous media: Experimental characterisations, network constructions and applications to reactive transport,” *Journal of Contaminant Hydrology*, vol. 192, pp. 101–117, 2016.
- [52] I. Goodfellow, J. Pouget-Abadie, M. Mirza, B. Xu, D. Warde-Farley, S. Ozair, A. Courville, and Y. Bengio, “Generative Adversarial Networks,” *pre-print*, pp. 1–9. arXiv:1406.2661 [stat.ML].
- [53] I. Goodfellow, “NIPS 2016 tutorial: Generative adversarial networks,” *pre-print*, 2016. arXiv:1701.00160 [stat.ML].
- [54] I. Goodfellow, Y. Bengio, and A. Courville, *Deep Learning*. Cambridge, MA, USA: MIT Press, 2016.
- [55] X. Li, Z. Yang, L. Catherine Brinson, A. Choudhary, A. Agrawal, and W. Chen, “A deep adversarial learning methodology for designing microstructural material systems,” *Proceedings of the ASME Design Engineering Technical Conference*, vol. 2B-2018, pp. 1–14, 2018.
- [56] C. E. Rasmussen and C. K. Williams, *Gaussian Processes for Machine Learning*. Cambridge, MA, USA: MIT Press, 2006.
- [57] C. E. Rasmussen, *Evaluation of Gaussian Processes and other Methods for Non-Linear Regression*. PhD thesis, University of Toronto, 1997.
- [58] E. A. Del Rio Chanona, J. E. Alves Graciano, E. Bradford, and B. Chachuat, “Modifier-adaptation schemes employing Gaussian processes and trust regions for real-time optimization,” *IFAC-PapersOnLine*, vol. 52, no. 1, pp. 52–57, 2019.
- [59] E. A. del Rio-Chanona, P. Petsagkourakis, E. Bradford, J. E. A. Graciano, and B. Chachuat, “Real-time optimization meets bayesian optimization

- and derivative-free optimization: A tale of modifier adaptation,” *pre-print*, 2021. arXiv:2009.08819 [math.OC].
- [60] M. Weyland, P. A. Midgley, and J. M. Thomas, “Electron tomography of nanoparticle catalysts on porous supports: A new technique based on Rutherford scattering,” *Journal of Physical Chemistry B*, vol. 105, no. 33, pp. 7882–7886, 2001.
- [61] J. Méndez-Venegas and M. A. Díaz-Viera, “Geostatistical modeling of clay spatial distribution in siliciclastic rock samples using the plurigaussian simulation method,” *Geofísica Internacional*, vol. 52, no. 3, pp. 229–247, 2013.
- [62] P. Fantazzini, R. J. S. Brown, and G. C. Borgia, “Bone tissue and porous media: Common features and differences studied by NMR relaxation,” *Magnetic Resonance Imaging*, vol. 21, no. 3-4, pp. 227–234, 2003.
- [63] G. Wei, C. Jia, J. Liu, and C. Yan, “Carbon felt supported carbon nanotubes catalysts composite electrode for vanadium redox flow battery application,” *Journal of Power Sources*, vol. 220, pp. 185–192, dec 2012.
- [64] A. Q. Su, N. F. Wang, S. Q. Liu, T. Wu, and S. Peng, “Modification of Carbon Paper Electrode via Hydrothermal Oxidation Applied in the Vanadium Redox Battery,” *Acta Phys. - Chim. Sin.*, vol. 28, no. 6, pp. 1387–1392, 2012.
- [65] B. Sun and M. Skyllas-Kazacos, “Modification of graphite electrode materials for vanadium redox flow battery application-I. Thermal treatment,” *Electrochimica Acta*, vol. 37, no. 7, pp. 1253–1260, 1992.
- [66] B. Chakrabarti, D. Nir, V. Yufit, F. Tariq, J. Rubio-Garcia, R. Maher, A. Kucerak, P. V. Aravind, and N. P. Brandon, “Performance Enhancement of Reduced Graphene Oxide-Modified Carbon Electrodes for Vanadium Redox-Flow Systems,” *ChemElectroChem*, vol. 4, pp. 194–200, jan 2017.
- [67] Z. He, Z. Chen, W. Meng, Y. Jiang, G. Cheng, L. Dai, and L. Wang, “Modified carbon cloth as positive electrode with high electrochemical performance for vanadium redox flow batteries,” *Journal of Energy Chemistry*, vol. 25, pp. 720–725, 2016.
- [68] X. L. Zhou, Y. K. Zeng, X. B. Zhu, L. Wei, and T. S. Zhao, “A high-

- performance dual-scale porous electrode for vanadium redox flow batteries,” *Journal of Power Sources*, vol. 325, pp. 329–336, 2016.
- [69] X. L. Zhou, T. S. Zhao, Y. K. Zeng, L. An, and L. Wei, “A highly permeable and enhanced surface area carbon-cloth electrode for vanadium redox flow batteries,” *Journal of Power Sources*, vol. 329, pp. 247–254, 2016.
- [70] M. Rebai and M. Prat, “Scale effect and two-phase flow in a thin hydrophobic porous layer. Application to water transport in gas diffusion layers of proton exchange membrane fuel cells,” *Journal of Power Sources*, vol. 192, no. 2, pp. 534–543, 2009.
- [71] X. Ke, J. I. D. Alexander, J. M. Prah, and R. F. Savinell, “Flow distribution and maximum current density studies in redox flow batteries with a single passage of the serpentine flow channel,” *Journal of Power Sources*, vol. 270, pp. 646–657, 2014.
- [72] X. Ke, J. I. D. Alexander, J. M. Prah, and R. F. Savinell, “A simple analytical model of coupled single flow channel over porous electrode in vanadium redox flow battery with serpentine flow channel,” *Journal of Power Sources*, vol. 288, pp. 308–313, 2015.
- [73] Q. Zheng, X. Li, Y. Cheng, G. Ning, F. Xing, and H. Zhang, “Development and perspective in vanadium flow battery modeling,” *Applied Energy*, vol. 132, pp. 254–266, 2014.
- [74] N. Pinjari, B. Kumar, A. Bhargav, and P. Ruch, “Effect of Electrode Properties on Performance of Miniaturized Vanadium Redox Flow Battery,” *IEEE*, vol. 3, p. 1040, 2017.
- [75] X. Li, “Modeling and simulation study of a metal free organic-inorganic aqueous flow battery with flow through electrode,” *Electrochimica Acta*, vol. 170, pp. 98–109, 2015.
- [76] A. A. Shah, M. J. Watt-Smith, and F. C. Walsh, “A dynamic performance model for redox-flow batteries involving soluble species,” *Electrochimica Acta*, vol. 53, no. 27, pp. 8087–8100, 2008.
- [77] X. Ma, H. Zhang, and F. Xing, “A three-dimensional model for negative half

- cell of the vanadium redox flow battery,” *Electrochimica Acta*, vol. 58, no. 1, pp. 238–246, 2011.
- [78] M. D. R. Kok, A. Khalifa, and J. T. Gostick, “Multiphysics Simulation of the Flow Battery Cathode: Cell Architecture and Electrode Optimization,” *Journal of The Electrochemical Society*, vol. 163, no. 7, pp. A1408–A1419, 2016.
- [79] Q. Xu, T. S. Zhao, and P. K. Leung, “Numerical investigations of flow field designs for vanadium redox flow batteries,” *Applied Energy*, vol. 105, pp. 47–56, 2013.
- [80] A. Tang, J. Bao, and M. Skyllas-Kazacos, “Studies on pressure losses and flow rate optimization in vanadium redox flow battery,” *Journal of Power Sources*, vol. 248, pp. 154–162, 2014.
- [81] I. M. Bayanov and R. Vanhaelst, “The numerical simulation of vanadium RedOx flow batteries,” *Journal of Mathematical Chemistry*, vol. 49, no. 9, pp. 2013–2031, 2011.
- [82] Q. Xu and T. S. Zhao, “Fundamental models for flow batteries,” *Progress in Energy and Combustion Science*, vol. 49, pp. 40–58, 2015.
- [83] K. Bromberger, J. Kaunert, and T. Smolinka, “A Model for All-Vanadium Redox Flow Batteries: Introducing Electrode-Compression Effects on Voltage Losses and Hydraulics,” *Energy Technology*, vol. 2, no. 1, pp. 64–76, 2014.
- [84] C. L. Chen, H. K. Yeoh, and M. H. Chakrabarti, “An enhancement to Vynnycky’s model for the all-vanadium redox flow battery,” *Electrochimica Acta*, vol. 120, pp. 167–179, 2014.
- [85] J. Houser, J. Clement, A. Pezeshki, and M. M. Mench, “Influence of architecture and material properties on vanadium redox flow battery performance,” *Journal of Power Sources*, vol. 302, pp. 369–377, 2016.
- [86] M. Vynnycky, “Analysis of a model for the operation of a vanadium redox battery,” *Energy*, vol. 36, no. 4, pp. 2242–2256, 2011.
- [87] X. Yang, Y. Mehmani, W. A. Perkins, A. Pasquali, M. Schönherr, K. Kim, M. Perego, M. L. Parks, N. Trask, M. T. Balhoff, M. C. Richmond, M. Geier, M. Krafczyk, L. S. Luo, A. M. Tartakovsky, and T. D. Scheibe, “Intercom-

- parison of 3D pore-scale flow and solute transport simulation methods,” *Advances in Water Resources*, vol. 95, pp. 176–189, 2016.
- [88] Z. Shi and X. Wang, “Comparison of Darcy’s Law, the Brinkman Equation, the Modified N-S Equation and the Pure Diffusion Equation in PEM Fuel Cell Modeling,” *Proceeding of the COMSOL Conference*, 2007.
- [89] F. A. Howes and S. Whitaker, “The spatial averaging theorem revisited,” *Chemical Engineering Science*, vol. 40, no. 8, pp. 1387–1392, 1985.
- [90] X. Ke, J. M. Prah, J. I. D. Alexander, and R. F. Savinell, “Redox flow batteries with serpentine flow fields: Distributions of electrolyte flow reactant penetration into the porous carbon electrodes and effects on performance,” *Journal of Power Sources*, vol. 384, no. February, pp. 295–302, 2018.
- [91] Q. Xu, T. S. Zhao, and C. Zhang, “Performance of a vanadium redox flow battery with and without flow fields,” *Electrochimica Acta*, vol. 142, pp. 61–67, 2014.
- [92] M. Parvazinia, V. Nassehi, R. J. Wakeman, and M. H. R. Ghoreishy, “Finite element modelling of flow through a porous medium between two parallel plates using the Brinkman equation,” *Transport in Porous Media*, vol. 63, no. 1, pp. 71–90, 2006.
- [93] P. C. Lichtner, “Continuum model for simultaneous chemical reactions and mass transport in hydrothermal systems,” *Geochimica et Cosmochimica Acta*, vol. 49, no. 3, pp. 779–800, 1985.
- [94] S. J. Cooper, A. Bertei, P. R. Shearing, J. A. Kilner, and N. P. Brandon, “TauFactor: An open-source application for calculating tortuosity factors from tomographic data,” *SoftwareX*, vol. 5, pp. 203–210, 2016.
- [95] D. F. Yule and W. R. Gardner, “Longitudinal and Transverse Dispersion Coefficients in Unsaturated Plainfield Sand,” *Water Resources Research*, vol. 14, no. 4, pp. 582–588, 1978.
- [96] S. Patankar, *Numerical Heat Transfer and Fluid Flow*. London: CRC Press Taylor & Francis Group, 2 ed., 1980.
- [97] M. A. Spaid and F. R. Phelan, “Lattice Boltzmann methods for modeling

- microscale flow in fibrous porous media,” *Physics of Fluids*, vol. 9, no. 9, pp. 2468–2474, 1997.
- [98] J. Monaghan, “Smoothed particle hydrodynamics,” *Annu. Rev. Astron. Astrophys.*, vol. 30, pp. 543–574, 1992.
- [99] M. El Hannach, J. Pauchet, and M. Prat, “Pore network modeling: Application to multiphase transport inside the cathode catalyst layer of proton exchange membrane fuel cell,” *Electrochimica Acta*, vol. 56, no. 28, pp. 10796–10808, 2011.
- [100] M. El Hannach, M. Prat, and J. Pauchet, “Pore network model of the cathode catalyst layer of proton exchange membrane fuel cells: Analysis of water management and electrical performance,” *International Journal of Hydrogen Energy*, vol. 37, no. 24, pp. 18996–19006, 2012.
- [101] R. Wu, Q. Liao, X. Zhu, and H. Wang, “Pore network modeling of cathode catalyst layer of proton exchange membrane fuel cell,” *International Journal of Hydrogen Energy*, vol. 37, no. 15, pp. 11255–11267, 2012.
- [102] J. Park, M. Matsubara, and X. Li, “Application of lattice Boltzmann method to a micro-scale flow simulation in the porous electrode of a PEM fuel cell,” *Journal of Power Sources*, vol. 173, no. 1, pp. 404–414, 2007.
- [103] Y. Hu, D. Li, S. Shu, and X. Niu, “Full Eulerian lattice Boltzmann model for conjugate heat transfer,” *Physical Review E - Statistical, Nonlinear, and Soft Matter Physics*, vol. 92, no. 6, 2015.
- [104] D. V. Patil, “Chapman-Enskog analysis for finite-volume formulation of lattice Boltzmann equation,” *Physica A: Statistical Mechanics and its Applications*, vol. 392, no. 12, pp. 2701–2712, 2013.
- [105] Y. Mehmani, M. Oostrom, and M. T. Balhoff, “A streamline splitting pore-network approach for computationally inexpensive and accurate simulation of transport in porous media,” *Water Resources Research*, vol. 50, pp. 2488–2517, 2014.
- [106] R. C. Acharya, S. E. A. T. M. Van der Zee, and A. Leijnse, “Transport modeling of nonlinearly adsorbing solutes in physically heterogeneous pore networks,” *Water Resources Research*, vol. 41, p. W02020, feb 2005.

- [107] Y. Mehmani, T. Sun, M. T. Balhoff, P. Eichhubl, and S. Bryant, “Multiblock Pore-Scale Modeling and Upscaling of Reactive Transport: Application to Carbon Sequestration,” *Transport in Porous Media*, vol. 95, no. 2, pp. 305–326, 2012.
- [108] J. Tansey and M. T. Balhoff, “Pore Network Modeling of Reactive Transport and Dissolution in Porous Media,” *Transport in Porous Media*, vol. 113, pp. 303–327, jun 2016.
- [109] M. Aghighi, M. A. Hoeh, W. Lehnert, G. Merle, and J. Gostick, “Simulation of a Full Fuel Cell Membrane Electrode Assembly Using Pore Network Modeling,” *Journal of The Electrochemical Society*, vol. 163, no. 5, pp. F384–F392, 2016.
- [110] L. Li, C. A. Peters, and M. A. Celia, “Upscaling geochemical reaction rates using pore-scale network modeling,” *Advances in Water Resources*, vol. 29, pp. 1351–1370, sep 2006.
- [111] R. C. Acharya, M. I. van Dijke, K. S. Sorbie, S. E. Van der Zee, and A. Leijnse, “Quantification of longitudinal dispersion by upscaling Brownian motion of tracer displacement in a 3D pore-scale network model,” *Advances in Water Resources*, vol. 30, no. 2, pp. 199–213, 2007.
- [112] D. Kim, C. A. Peters, and W. B. Lindquist, “Upscaling geochemical reaction rates accompanying acidic CO₂-saturated brine flow in sandstone aquifers,” *Water Resources Research*, vol. 47, no. 1, pp. 1–16, 2011.
- [113] A. Raof, H. M. Nick, S. M. Hassanizadeh, and C. J. Spiers, “PoreFlow: A complex pore-network model for simulation of reactive transport in variably saturated porous media,” *Computers and Geosciences*, vol. 61, pp. 160–174, 2013.
- [114] A. Raof, H. M. Nick, T. K. Wolterbeek, and C. J. Spiers, “Pore-scale modeling of reactive transport in wellbore cement under CO₂ storage conditions,” *International Journal of Greenhouse Gas Control*, vol. 11, no. SUPPL, pp. S67–S77, 2012.
- [115] L. Holzer, B. Iwanschitz, T. Hocker, B. Münch, M. Prestat, D. Wiedenmann, U. Vogt, P. Holtappels, J. Sfeir, A. Mai, and T. Graule, “Microstructure degra-

- dation of cermet anodes for solid oxide fuel cells: Quantification of nickel grain growth in dry and in humid atmospheres,” *Journal of Power Sources*, vol. 196, no. 3, pp. 1279–1294, 2011.
- [116] D. S. Eastwood, R. S. Bradley, F. Tariq, S. J. Cooper, O. O. Taiwo, J. Gelb, A. Merkle, D. J. Brett, N. P. Brandon, P. J. Withers, P. D. Lee, and P. R. Shearing, “The application of phase contrast X-ray techniques for imaging Li-ion battery electrodes,” *Nuclear Instruments and Methods in Physics Research, Section B: Beam Interactions with Materials and Atoms*, vol. 324, pp. 118–123, 2014.
- [117] N. Ni, S. J. Cooper, R. Williams, N. Kemen, D. W. McComb, and S. J. Skinner, “Degradation of $(\text{La}_{0.6}\text{Sr}_{0.4})_{0.95}(\text{Co}_{0.2}\text{Fe}_{0.8})\text{O}_{3-\delta}$ Solid Oxide Fuel Cell Cathodes at the Nanometer Scale and below,” *ACS Applied Materials and Interfaces*, vol. 8, no. 27, pp. 17360–17370, 2016.
- [118] P. Pietsch and V. Wood, “X-Ray Tomography for Lithium Ion Battery Research: A Practical Guide,” *Annual Review of Materials Research*, vol. 47, no. 1, pp. 451–479, 2017.
- [119] A. N. Diógenes, L. O. E. Dos Santos, C. P. Fernandes, A. C. Moreira, and C. R. Apolloni, “Porous Media Microstructure Reconstruction Using Pixel-Based and Object-Based Simulated Annealing – Comparison With Other Reconstruction Methods,” *Revista de Engenharia Térmica*, vol. 8, no. 2, p. 35, 2009.
- [120] P. M. Adler, C. G. Jacquin, and J. A. Quiblier, “Flow in simulated porous media,” *International Journal of Multiphase Flow*, vol. 16, no. 4, pp. 691–712, 1990.
- [121] Z. R. Liang, C. P. Fernandes, F. S. Magnani, and P. C. Philippi, “A reconstruction technique for three-dimensional porous media using image analysis and Fourier transforms,” *Journal of Petroleum Science and Engineering*, vol. 21, no. 3-4, pp. 273–283, 1998.
- [122] J. A. Quiblier, “A new three-dimensional modeling technique for studying porous media,” *Journal of Colloid And Interface Science*, vol. 98, no. 1, pp. 84–102, 1984.

- [123] M. Y. Joshi, *A class of stochastic models for porous media*. PhD thesis, University of Kansas, 1974.
- [124] P. Levitz, “Off-lattice reconstruction of porous media: Critical evaluation, geometrical confinement and molecular transport,” *Advances in Colloid and Interface Science*, vol. 76-77, pp. 71–106, 1998.
- [125] R. Hilfer, “Local Porosity Theory and Stochastic Reconstruction for Porous Media,” *Statistical Physics and Spatial Statistics*, pp. 203–241, 2000.
- [126] M. E. Kainourgiakis, E. S. Kikkinides, T. A. Steriotis, A. K. Stubos, K. P. Tzevelekos, and N. K. Kanellopoulos, “Structural and transport properties of alumina porous membranes from process-based and statistical reconstruction techniques,” *Journal of Colloid and Interface Science*, vol. 231, no. 1, pp. 158–167, 2000.
- [127] V. Sundararaghavan, “Reconstruction of three-dimensional anisotropic microstructures from two-dimensional micrographs imaged on orthogonal planes,” *Integrating Materials and Manufacturing Innovation*, vol. 3, no. 1, pp. 1–11, 2014.
- [128] A. Hasanabadi, M. Baniassadi, K. Abrinia, M. Safdari, and H. Garmestani, “3D microstructural reconstruction of heterogeneous materials from 2D cross sections: A modified phase-recovery algorithm,” *Computational Materials Science*, vol. 111, pp. 107–115, 2016.
- [129] A. Hasanabadi, M. Baniassadi, K. Abrinia, M. Safdari, and H. Garmestani, “Optimization of solid oxide fuel cell cathodes using two-point correlation functions,” *Computational Materials Science*, vol. 123, pp. 268–276, 2016.
- [130] H. Izadi, M. Baniassadi, A. Hasanabadi, B. Mehrgini, H. Memarian, H. Soltanian-Zadeh, and K. Abrinia, “Application of full set of two point correlation functions from a pair of 2D cut sections for 3D porous media reconstruction,” *Journal of Petroleum Science and Engineering*, vol. 149, no. October 2016, pp. 789–800, 2017.
- [131] A. Hasanabadi, M. Baniassadi, K. Abrinia, M. Safdari, and H. Garmestani, “Optimal combining of microstructures using statistical correlation func-

- tions,” *International Journal of Solids and Structures*, vol. 160, pp. 177–186, 2019.
- [132] M. Baniassadi, H. Garmestani, D. S. Li, S. Ahzi, M. Khaleel, and X. Sun, “Three-phase solid oxide fuel cell anode microstructure realization using two-point correlation functions,” *Acta Materialia*, vol. 59, no. 1, pp. 30–43, 2011.
- [133] M. Armstrong, A. Galli, H. Beucher, G. Le Loc’h, D. Renard, B. Doligez, R. Eschard, and G. F., *Plurigaussian simulations in geosciences*. Springer Science & Business Media, 1 ed., 2011.
- [134] L. Mosser, O. Dubrule, and M. J. Blunt, “Reconstruction of three-dimensional porous media using generative adversarial neural networks,” *Physical Review E*, vol. 96, no. 4, 2017.
- [135] G. Le Loc’h and A. Galli, “A. Truncated Plurigaussian method: theoretical and practical points of view,” *Proc. Geostatistics Int. Conf., Wollongong 96*, no. 1, pp. 211–222, 1997.
- [136] M. Neumann, M. Osenberg, A. Hilger, D. Franzen, T. Turek, I. Manke, and V. Schmidt, “On a pluri-Gaussian model for three-phase microstructures, with applications to 3D image data of gas-diffusion electrodes,” *Computational Materials Science*, vol. 156, no. October 2018, pp. 325–331, 2019.
- [137] A. Ali, X. Wen, K. Nandakumar, J. Luo, and K. T. Chuang, “Geometrical modeling of microstructure of solid oxide fuel cell composite electrodes,” *Journal of Power Sources*, vol. 185, no. 2, pp. 961–966, 2008.
- [138] B. Kenney, M. Valdmanis, C. Baker, J. G. Pharoah, and K. Karan, “Computation of TPB length, surface area and pore size from numerical reconstruction of composite solid oxide fuel cell electrodes,” *Journal of Power Sources*, vol. 189, no. 2, pp. 1051–1059, 2009.
- [139] Q. Cai, C. S. Adjiman, and N. P. Brandon, “Modelling the 3D microstructure and performance of solid oxide fuel cell electrodes: Computational parameters,” *Electrochimica Acta*, vol. 56, no. 16, pp. 5804–5814, 2011.
- [140] A. Bertei, H. W. Choi, J. G. Pharoah, and C. Nicolella, “Percolating behav-

- ior of sintered random packings of spheres,” *Powder Technology*, vol. 231, pp. 44–53, 2012.
- [141] F. L. E. Usseglio-Viretta, A. Colclasure, A. N. Mistry, K. P. Y. Claver, F. Pouraghajan, D. P. Finegan, T. M. M. Heenan, D. Abraham, P. P. Mukherjee, D. Wheeler, P. Shearing, S. J. Cooper, and K. Smith, “Resolving the Discrepancy in Tortuosity Factor Estimation for Li-Ion Battery Electrodes through Micro-Macro Modeling and Experiment,” *Journal of The Electrochemical Society*, vol. 165, no. 14, pp. A3403–A3426, 2018.
- [142] B. L. Trembacki, A. N. Mistry, D. R. Noble, M. E. Ferraro, P. P. Mukherjee, and S. A. Roberts, “Editors’ Choice—Mesoscale Analysis of Conductive Binder Domain Morphology in Lithium-Ion Battery Electrodes,” *Journal of The Electrochemical Society*, vol. 165, no. 13, pp. E725–E736, 2018.
- [143] L. Mosser, O. Dubrule, and M. J. Blunt, “Stochastic Reconstruction of an Oolitic Limestone by Generative Adversarial Networks,” *Transport in Porous Media*, vol. 125, no. 1, pp. 81–103, 2018.
- [144] T. Mitchell, *Machine learning*. Burr Ridge, IL: McGraw Hill, 1997.
- [145] A. Geron, *Hands-on machine learning with Scikit-Learn and TensorFlow: concepts, tools, and techniques to build intelligent systems*. Sebastopol, CA: O’Reilly Media, 2017.
- [146] F. Rosenblatt, “The Perceptron, a perceiving and recognizing automaton,” tech. rep., Cornell Aeronautical Laboratory, Inc, 1957.
- [147] K. Hornik, “Multilayer Feedforward Networks,” *Neural Networks*, vol. 2, pp. 359–366, 1989.
- [148] Y. Lecun, Y. Bengio, and G. Hinton, “Deep learning,” *Nature*, vol. 521, no. 7553, pp. 436–444, 2015.
- [149] D. E. Rumelhart, G. E. Hintont, and R. J. Williams, “Learning Representations by Back-Propagating Errors,” *Letters to Nature*, vol. 323, pp. 533–536, 1986.
- [150] Y. Lecun, “A Theoretical Framework for Back-Propagation,” *Proceedings of the 1988 Connectionist Models Summer School*, pp. 21–28, 1988.

- [151] Y. Lecun, L. Bottou, G. B. Orr, and K.-R. Muller, “Efficient BackProp,” in *Neural Networks: Tricks of the Trade. Lecture Notes in Computer Science* (M. G., G. Orr, and K. Müller, eds.), vol. 7700, Berlin, Heidelberg: Springer, 2012.
- [152] L. Bottou, “Large-Scale Machine Learning with Stochastic Gradient Descent,” *Proceedings of COMPSTAT’2010*, pp. 177–186, 2010.
- [153] B. A. Krizhevsky, I. Sutskever, and G. E. Hinton, “ImageNet Classification with Deep Convolutional Neural Networks,” *Communications of the ACM*, vol. 60, no. 6, pp. 84–90, 2017.
- [154] B. Frey, *Graphical models for machine learning and digital communication*. Cambridge, MA, USA: MIT Press, 1998.
- [155] G. Deco and W. Brauer, “Higher Order Statistical Decorrelation without Information Loss,” *Advances in Neural Information Processing Systems 7*, vol. c, pp. 247–254, 1995.
- [156] L. Dinh, J. Sohl-Dickstein, and S. Bengio, “Density estimation using real NVP,” *5th International Conference on Learning Representations, ICLR 2017 - Conference Track Proceedings*, 2017.
- [157] A. van den Oord, S. Dieleman, H. Zen, K. Simonyan, O. Vinyals, A. Graves, N. Kalchbrenner, A. Senior, and K. Kavukcuoglu, “WaveNet: A Generative Model for Raw Audio,” pp. 1–15, 2016.
- [158] D. P. Kingma and M. Welling, “Auto-encoding variational bayes,” *2nd International Conference on Learning Representations, ICLR 2014 - Conference Track Proceedings*, no. M1, pp. 1–14, 2014.
- [159] A. Radford, L. Metz, and S. Chintala, “Unsupervised representation learning with deep convolutional generative adversarial networks,” *4th International Conference on Learning Representations, ICLR 2016 - Conference Track Proceedings*, pp. 1–16, 2016.
- [160] J. T. Springenberg, A. Dosovitskiy, T. Brox, and M. Riedmiller, “Striving for simplicity: The all convolutional net,” *3rd International Conference on Learning Representations, ICLR 2015 - Workshop Track Proceedings*, pp. 1–14, 2015.
- [161] D. P. Kingma and J. L. Ba, “Adam: A method for stochastic optimization,”

- 3rd International Conference on Learning Representations, ICLR 2015 - Conference Track Proceedings*, pp. 1–15, 2015.
- [162] B. Bijeljic and M. J. Blunt, “Pore-scale modeling of transverse dispersion in porous media,” *Water Resources Research*, vol. 43, no. 12, pp. 1–8, 2007.
- [163] P. A. García-Salaberri, I. V. Zenyuk, A. D. Shum, G. Hwang, M. Vera, A. Z. Weber, and J. T. Gostick, “Analysis of representative elementary volume and through-plane regional characteristics of carbon-fiber papers: diffusivity, permeability and electrical/thermal conductivity,” *International Journal of Heat and Mass Transfer*, vol. 127, pp. 687–703, 2018.
- [164] R. Banerjee, N. Bevilacqua, L. Eifert, and R. Zeis, “Characterization of carbon felt electrodes for vanadium redox flow batteries – A pore network modeling approach,” *Journal of Energy Storage*, vol. 21, no. November 2018, pp. 163–171, 2019.
- [165] J. Gostick, M. Aghighi, J. Hinebaugh, T. Tranter, M. A. Hoeh, H. Day, B. Spellacy, M. H. Sharqawy, A. Bazylak, A. Burns, W. Lehnert, and A. Putz, “OpenPNM: A Pore Network Modeling Package,” *Computing in Science & Engineering*, vol. 18, pp. 60–74, jul 2016.
- [166] J. Newman and K. E. Rhomas-Alyea, *Electrochemical Systems*. Hoboken, New Jersey: John Wiley and Sons, Inc., 3 ed., 2004.
- [167] Z. Yang, J. Zhang, M. C. W. Kintner-Meyer, X. Lu, D. Choi, J. P. Lemmon, and J. Liu, “Electrochemical Energy Storage for Green Grid,” *Chemical Reviews*, vol. 111, no. 5, pp. 3577–3613, 2011.
- [168] IRENA, “IRENA, Renewable Energy Statistics 2018, Renewable Energy Statistics.” <http://www.irena.org/publications/2018/Jul/Renewable-Energy-Statistics-2018>, 2018. [Online; accessed 14-August-2018].
- [169] M. L. Perry, R. M. Darling, and R. Zaffou, “High Power Density Redox Flow Battery Cells,” *ECS Transactions*, vol. 53, no. 7, pp. 7–16, 2013.
- [170] U.S. DOE, “Grid Energy Storage,” 2013.
- [171] EASE, “Joint EASE/EERA recommendations for a European Energy Storage Technology Development Roadmap towards 2030,” 2018.

- [172] Y. Zhu and C. Huang, “An Improved Median Filtering Algorithm for Image Noise Reduction,” *Physics Procedia*, vol. 25, pp. 609–616, 2012.
- [173] A. Forner-Cuenca, E. E. Penn, A. M. Oliveira, and F. R. Brushett, “Exploring the Role of Electrode Microstructure on the Performance of Non-Aqueous Redox Flow Batteries,” *Journal of The Electrochemical Society*, vol. 166, no. 10, pp. A2230–A2241, 2019.
- [174] K. M. Tenny, A. Forner-Cuenca, Y.-M. Chiang, and F. R. Brushett, “Comparing Physical and Electrochemical Properties of Different Weave Patterns for Carbon Cloth Electrodes in Redox Flow Batteries,” *Journal of Electrochemical Energy Conversion and Storage*, vol. 17, no. 4, 2020.
- [175] T. Hsu, W. K. Epting, R. Mahbub, N. T. Nuhfer, S. Bhattacharya, Y. Lei, H. M. Miller, P. R. Ohodnicki, K. R. Gerdes, H. W. Abernathy, G. A. Hackett, A. D. Rollett, M. De Graef, S. Litster, and P. A. Salvador, “Mesoscale characterization of local property distributions in heterogeneous electrodes,” *Journal of Power Sources*, vol. 386, no. 14, pp. A3403–A3426, 2018.
- [176] S. C. Blair, P. A. Berge, and J. G. Berryman, “Two-Point Correlation Functions to Characterize Microgeometry and Estimate Permeabilities of Synthetic and Natural Sandstones,” *Lawrence Livermore National Laboratory Report*, no. UC-403, pp. 1–31, 1993.
- [177] V. Dumoulin and F. Visin *pre-print*, pages = 1-31, title = *A guide to convolution arithmetic for deep learning*, url = <http://arxiv.org/abs/1603.07285>, year = 2016, note=*arXiv:1603.07285 [stat.ML]*.
- [178] L. Mescheder, A. Geiger, and S. Nowozin, “Which training methods for GANs do actually converge?,” *35th International Conference on Machine Learning, ICML 2018*, vol. 8, pp. 5589–5626, 2018.
- [179] A. G. Journel and R. Froidevaux, “Anisotropic hole-effect modeling,” *Journal of the International Association for Mathematical Geology*, vol. 14, no. 3, pp. 217–239, 1982.
- [180] M. Pyrcz and C. Deutsch, “The whole story on the hole effect,” *Geostatistical Association of Australasia Newsletter 18*, vol. 18, no. March, p. 18, 2003.
- [181] M. Paganini, L. De Oliveira, and B. Nachman, “Accelerating Science with

- Generative Adversarial Networks: An Application to 3D Particle Showers in Multilayer Calorimeters,” *Physical Review Letters*, vol. 120, no. 4, pp. 1–6, 2018.
- [182] M. Heusel, H. Ramsauer, T. Unterthiner, B. Nessler, and S. Hochreiter, “GANs trained by a two time-scale update rule converge to a local Nash equilibrium,” *Advances in Neural Information Processing Systems*, vol. 2017-Decem, no. Nips, pp. 6627–6638, 2017.
- [183] S. Arora and Y. Zhang, “Do GANs actually learn the distribution? An empirical study,” *pre-rpint*, pp. 1–11, 2017. arXiv:1706.08224 [cs.LG].
- [184] Z. Wang, Q. She, and T. E. Ward, “Generative adversarial networks: A survey and taxonomy,” *arXiv*, no. November, pp. 1–41, 2019.
- [185] M. Arjovsky, S. Chintala, and L. Bottou, “Real-time optimization meets bayesian optimization and derivative-free optimization: A tale of modifier adaptation,” *pre-print*, 2017. arXiv:1701.07875 [stat.ML].
- [186] I. Gulrajani, F. Ahmed, M. Arjovsky, V. Dumoulin, and A. Courville, “Improved Training of Wasserstein GANs,” *arXiv: 1704.00028*, 2017.
- [187] X. Mao, Q. Li, H. Xie, R. Y. Lau, Z. Wang, and S. P. Smolley, “Least Squares Generative Adversarial Networks,” *Proceedings of the IEEE International Conference on Computer Vision*, vol. 2017-Octob, pp. 2813–2821, 2017.
- [188] Y. Yoshida and T. Miyato, “Spectral Norm Regularization for Improving the Generalizability of Deep Learning,” *arXiv: 1705.10941*, 2017.
- [189] D. Zhang, A. Bertei, F. Tariq, N. Brandon, and Q. Cai, “Progress in 3D electrode microstructure modelling for fuel cells and batteries: transport and electrochemical performance,” *Progress in Energy*, vol. 1, no. 1, p. 012003, 2019.
- [190] A. W. Lees and S. F. Edwards, “The computer study of transport processes under extreme conditions,” *Journal of Physics C: Solid State Physics*, vol. 5, no. 15, pp. 1921–1928, 1972.
- [191] P. Henyš, L. Čapek, and J. Březina, “Comparison of current methods for implementing periodic boundary conditions in multi-scale homogenisation,” *European Journal of Mechanics, A/Solids*, vol. 78, no. July, p. 103825, 2019.

- [192] R. A. Yeh, C. Chen, T. Yian Lim, A. G. Schwing, M. Hasegawa-Johnson, and M. N. Do, “Semantic image inpainting with deep generative models,” *Proceedings - 30th IEEE Conference on Computer Vision and Pattern Recognition, CVPR 2017*, vol. 2017-Janua, pp. 6882–6890, 2017.
- [193] P. Isola, J. Y. Zhu, T. Zhou, and A. A. Efros, “Image-to-image translation with conditional adversarial networks,” *Proceedings - 30th IEEE Conference on Computer Vision and Pattern Recognition, CVPR 2017*, vol. 2017-Janua, pp. 5967–5976, 2017.
- [194] A. Bielefeld, D. A. Weber, and J. Janek, “Microstructural Modeling of Composite Cathodes for All-Solid-State Batteries,” *Journal of Physical Chemistry C*, vol. 123, no. 3, pp. 1626–1634, 2019.
- [195] B. Suthar, P. W. C. Northrop, D. Rife, and V. R. Subramanian, “Effect of Porosity, Thickness and Tortuosity on Capacity Fade of Anode,” *Journal of The Electrochemical Society*, vol. 162, no. 9, pp. A1708–A1717, 2015.
- [196] P. Bojanowski, A. Joulin, D. L. Paz, and A. Szlam, “Optimizing the latent space of generative networks,” *35th International Conference on Machine Learning, ICML 2018*, vol. 2, pp. 960–972, 2018.
- [197] A. O’Hagan, “Curve Fitting and Optimal Design for Prediction,” *Journal of the Royal Statistical Society: Series B (Methodological)*, vol. 40, no. 1, pp. 1–24, 1978.
- [198] R. Neal, *Bayesian Learning for Neural Networks*. Springer Science & Business Media, 2012.
- [199] M. Ebden, “Gaussian Processes: A Quick Introduction,” *pre-print*, 2008. arXiv:1505.02965 [math.ST].
- [200] D. R. Jones, M. Schonlau, and W. J. Welch, “Efficient Global Optimization of Expensive Black-Box Functions,” *Journal of Global Optimization*, vol. 13, no. 4, pp. 455–492, 1998.
- [201] R. R. Richardson, M. A. Osborne, and D. A. Howey, “Gaussian process regression for forecasting battery state of health,” *Journal of Power Sources*, vol. 357, pp. 209–219, 2017.
- [202] R. R. Richardson, M. A. Osborne, and D. A. Howey, “Battery health pre-

- diction under generalized conditions using a Gaussian process transition model,” *Journal of Energy Storage*, vol. 23, no. April, pp. 320–328, 2019.
- [203] E. Bradford, A. M. Schweidtmann, D. Zhang, K. Jing, and E. A. del Rio-Chanona, “Dynamic modeling and optimization of sustainable algal production with uncertainty using multivariate Gaussian processes,” *Computers and Chemical Engineering*, vol. 118, pp. 143–158, 2018.
- [204] E. Bradford, L. Imsland, D. Zhang, and E. A. Del Rio Chanona, “Stochastic data-driven model predictive control using Gaussian processes,” *arXiv*, pp. 1027–1034, 2019.
- [205] E. Bradford, A. M. Schweidtmann, and A. Lapkin, “Efficient multiobjective optimization employing Gaussian processes, spectral sampling and a genetic algorithm,” *Journal of Global Optimization*, vol. 71, no. 2, pp. 407–438, 2018.
- [206] S. Sundararajan and S. Sathiya Keerthi, “Predictive approaches for choosing hyperparameters in Gaussian Processes,” *Advances in Neural Information Processing Systems*, vol. 1118, pp. 631–637, 2000.
- [207] B. Shahriari, K. Swersky, Z. Wang, R. P. Adams, and N. De Freitas, “Taking the human out of the loop: A review of Bayesian optimization,” *Proceedings of the IEEE*, vol. 104, no. 1, pp. 148–175, 2016.
- [208] S. Aksoy and R. M. Haralick, “Feature normalization and likelihood-based similarity measures for image retrieval,” *Pattern Recognition Letters*, vol. 22, no. 5, pp. 563–582, 2001.
- [209] D. Kraft, “On Converting Optimal Control Problems into Nonlinear Programming Problems,” in *Computational Mathematical Programming. NATO ASI Series* (S. K., ed.), Berlin: Springer, 1985.
- [210] A. Rabbani and S. Jamshidi, “Specific surface and porosity relationship for sandstones for prediction of permeability,” *International Journal of Rock Mechanics and Mining Sciences*, vol. 71, pp. 25–32, 2014.
- [211] S. Roberts, M. Osborne, M. Ebdon, S. Reece, N. Gibson, and S. Aigrain, “Gaussian processes for time-series modelling,” *Philosophical Transactions of The Royal Society*, no. A371:20110550, 2013.

- [212] G. Hinton and R. Salakhutdinov, "Reducing the Dimensionality of Data with Neural Networks," *Science*, vol. 313, no. July, pp. 504–508, 2006.

Appendix A

Flow chart of PNM iterative process

This chapter shows the flow chart that outlines the numerical algorithm implemented in the development of a Pore Network Model for electrochemical energy storage devices.

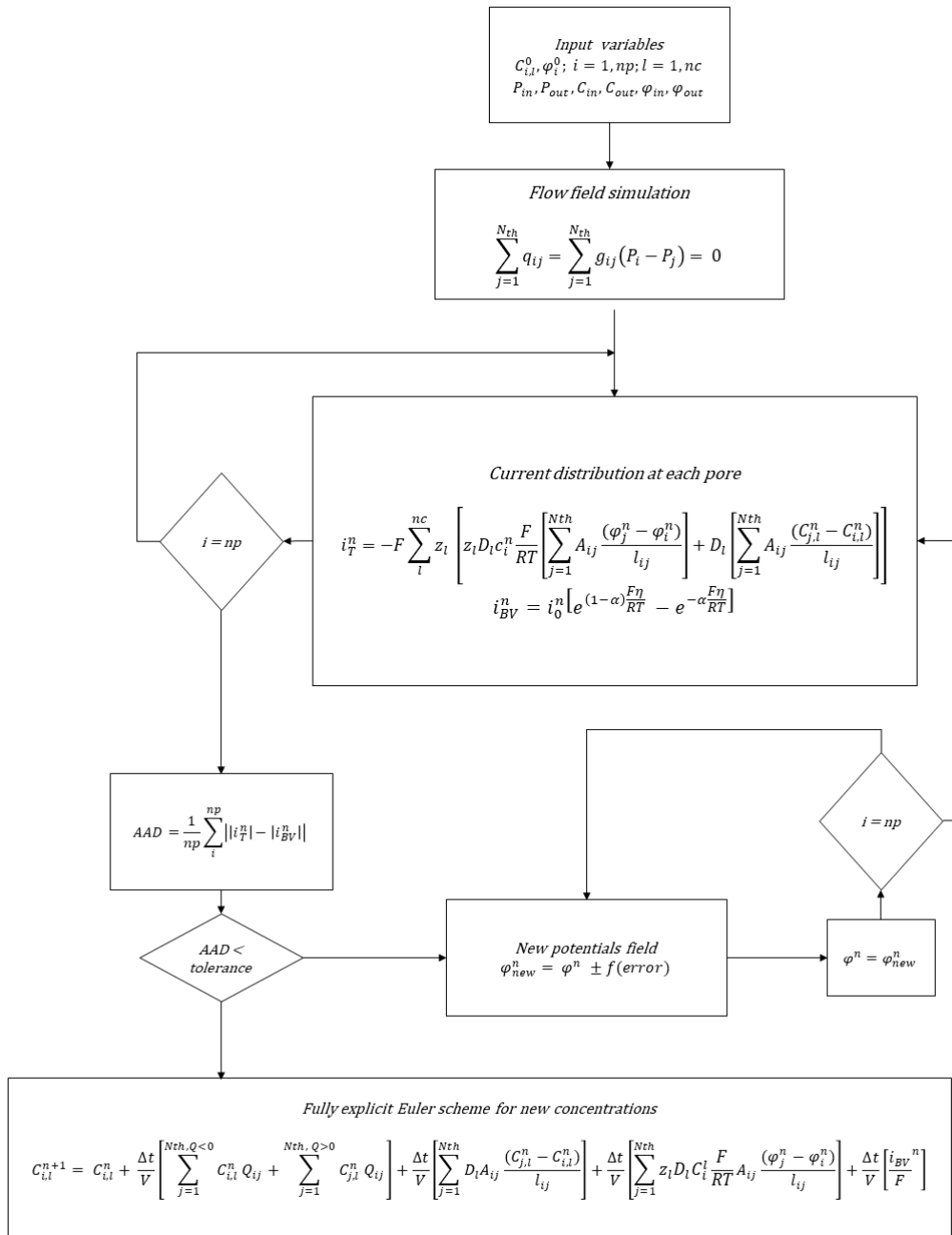


Figure A.1: Flow chart graphically outlining the numerical algorithm.

Appendix B

Publications

B.1 Publication 1

A. Gayon-Lombardo, B. A. Simon, O. O. Taiwo, S. J. Neethling, N.P. Brandon. “A pore network model of porous electrodes in electrochemical devices.” *Journal of Energy Storage*, 24, pp. 100736, (2019).

<https://doi.org/10.1016/j.est.2019.04.010>

Front page in figure B.1


B.2 Publication 2

A. Gayon-Lombardo, L. Mosser, N. P. Brandon, S. J. Cooper. “Pores for thought: generative adversarial networks for stochastic reconstruction of 3D multi-phase electrode microstructures with periodic boundaries. *npj Comput. Mater.* 6, 82, pp. 1-11, (2020).”

<https://doi.org/10.1038/s41524-020-0340-7>

Front page in figure B.2

Journal of Energy Storage 24 (2019) 100736




ELSEVIER

Contents lists available at ScienceDirect

Journal of Energy Storage


journal homepage: www.elsevier.com/locate/est



A pore network model of porous electrodes in electrochemical devices

Andrea Gayon Lombardo^a, Benedict A. Simon, Oluwadamilola Taiwo, Stephen J. Neethling, Nigel P. Brandon

Royal School of Mines, Department of Earth Science and Engineering, South Kensington Campus, Imperial College London, London SW7 2AZ, United Kingdom



ARTICLE INFO

Keywords:
Pore network model
Electrode microstructure
Pore-scale modelling
Electrochemical devices
X-ray computed tomography

ABSTRACT

A computationally efficient pore network model (PNM) has been developed to incorporate the transport and electrochemical phenomena occurring within porous electrodes. This PNM is validated on a synthetic cubic structure and subsequently run on a network obtained from X-ray computed tomography (X-CT) images of a sample of commercial porous carbon paper commonly used in electrochemical devices. The carbon paper's physical characteristics (pore-size distribution, permeability, porosity and electroactive surface area) are discussed. The concentration distribution of active species is examined considering solely the transient convective and diffusive transport processes initially, and subsequently is compared to the concentration of active species when migration and reactive transport factors are included.

The results show non-uniformity in the concentration and pressure distributions in the electrode when considering the pure convective/diffusive transport processes. The migration and reactive processes are subsequently considered and are shown to be influenced by the rate in which the convective/diffusive flow permeates the electrode. A uniform steady decline in volume-averaged state of charge is shown, followed by a pore-scale non-uniform current density and state of charge distribution upon discharge. These results were obtained on a standard single core workstation highlighting the benefits of using a computationally inexpensive model.

1. Introduction

Electrodes constitute one of the main components in electrochemical energy storage and energy conversion technologies as they represent the sites where the major transport and reactive mechanisms occur [1]. Due to their importance in energy storage systems, understanding the multi-transport processes that occur within electrodes is crucial in order to improve their durability, increase the active surface area and aid in the design of more optimum systems [2–4].

It has been shown experimentally that further improvements in the electrode structure at a pore-scale level will lead to an improved power density [5–8]. However, experimental trial and error is expensive, time consuming and physically laborious. Therefore, it has become of high interest to employ mathematical modelling and simulation techniques to optimise and investigate electrode microstructure.

Electrochemical impedance spectroscopy (EIS) and transition line modelling (TLM) are important tools commonly implemented to investigate characteristics of porous electrodes. EIS is widely used [9,10], and is experimentally performed by measuring the response of an electrochemical system upon application of small oscillating currents or

potentials with varying frequency. The response is an impedance, Z , which can be plotted in several ways (Nyquist, Bode, Lissajous). Impedance of porous electrodes has been studied by many researchers including Huang and Siptoni [9,11]. In both of these papers, an equivalent circuit model (ECM) is used to describe the theoretical impedance response of each component. De Levie pioneered TLM, a subset of ECMs – which focuses specifically on the impedance associated within a porous electrode infiltrated by liquid electrolyte [12]. The main utility of this type of modelling is in predicting the availability of the electrochemically accessible surface area (which is not necessarily the same as the physical surface area) – the configuration of the porous electrode (e.g. pore-to-pore connectivity) is therefore taken into account. These methods have been used as the foundation to explain the movement of ions through electrolyte within porous electrodes [13]. Meyers et al. presented another important extension of this application by using these principles to describe the impedance associated with spherical intercalation particle movement through porous electrode materials [14]. While impedance studies are vital to understanding the resistances within an electrode, these resistances can also be analysed by implementing the governing transport phenomena equations over the cell domain.

^a Corresponding author.
E-mail addresses: a.gayon-lombardo17@imperial.ac.uk (A. Gayon Lombardo), b.simon17@imperial.ac.uk (B.A. Simon), o.taiwo@imperial.ac.uk (O. Taiwo), s.neethling@imperial.ac.uk (S.J. Neethling), n.brandon@imperial.ac.uk (N.P. Brandon).

<https://doi.org/10.1016/j.est.2019.04.010>
Received 22 January 2019; Received in revised form 10 April 2019; Accepted 10 April 2019
Available online 16 May 2019
2352-152X/ © 2019 Elsevier Ltd. All rights reserved.

Figure B.1: Paper front page

ARTICLE OPEN



Pores for thought: generative adversarial networks for stochastic reconstruction of 3D multi-phase electrode microstructures with periodic boundaries

Andrea Gayon-Lombardo¹, Lukas Mosser², Nigel P. Brandon¹ and Samuel J. Cooper^{1,2}

The generation of multiphase porous electrode microstructures is a critical step in the optimisation of electrochemical energy storage devices. This work implements a deep convolutional generative adversarial network (DC-GAN) for generating realistic n-phase microstructural data. The same network architecture is successfully applied to two very different three-phase microstructures: A lithium-ion battery cathode and a solid oxide fuel cell anode. A comparison between the real and synthetic data is performed in terms of the morphological properties (volume fraction, specific surface area, triple-phase boundary) and transport properties (relative diffusivity), as well as the two-point correlation function. The results show excellent agreement between datasets and they are also visually indistinguishable. By modifying the input to the generator, we show that it is possible to generate microstructure with periodic boundaries in all three directions. This has the potential to significantly reduce the simulated volume required to be considered "representative" and therefore massively reduce the computational cost of the electrochemical simulations necessary to predict the performance of a particular microstructure during optimisation.

npj Computational Materials (2020)6:82; <https://doi.org/10.1038/s41524-020-0340-7>

INTRODUCTION

The geometrical properties of multiphase materials are of central importance to a wide variety of engineering disciplines. For example, the distribution of precious metal catalysts on porous supports; the structure of metallic phases and defects in high-performance alloys; the arrangement of sand, organic matter, and water in soil science; and the distribution of calcium, collagen and blood vessels in bone^{1–3}. In electrochemistry, whether we are considering batteries, fuel cells or supercapacitors, their electrodes are typically porous to maximise surface area but need to contain percolating paths for the transport of both electrons and ions, as well as maintaining sufficient mechanical integrity^{4,5}. Thus the microstructure of these electrodes significantly impacts their performance and their morphological optimisation is vital for developing the next generation of energy storage technologies⁶.

Recent improvements in 3D imaging techniques such as X-ray computed tomography (XCT) have allowed researchers to view the microstructure of porous materials at sufficient resolution to extract relevant metrics^{7–10}. However, a variety of challenges remain, including how to extract the key metrics or "essence" of an observed microstructural dataset such that synthetic volumes with equivalent properties can be generated, and how to modify specific attributes of this microstructural data without compromising its overall resemblance to the real material.

A wide variety of methods that consist of generating synthetic microstructure by numerical means have been developed to solve these challenges⁶. A statistical method for generating synthetic three-dimensional porous media based on distance correlation functions was introduced by Quiblier et al.¹¹. Following this work, Torquato et al. implemented a stochastic approach based on the n-point correlation functions for generating reconstructions of heterogeneous materials.^{12–16} Jiao et al.^{17,18} extended this method to present an isotropy-preserving algorithm to generate

realisations of materials from their two-point correlation functions (TPCF). Based on these previous works, the most widely used approach for reconstruction of microstructure implements statistical methods through the calculation of the TPCF^{2,19–24}.

In the area of energy materials, interest has recently surged for generating synthetic microstructure in order to aid the design of optimised electrodes. The three-phase nature of most electrochemical materials adds an extra level of complexity to their generation compared to two-phase materials. Suzue et al.²⁰ implemented a TPCF from a two-dimensional phase map to reconstruct a three-dimensional microstructure of a porous composite anode. Baniassadi et al.²⁵ extended this method by adding a combined Monte Carlo simulation with a kinetic growth model to generate three-phase realisations of a SOFC electrode. Alternative algorithms for reconstruction of porous electrodes have been inspired by their experimental fabrication techniques. A stochastic algorithm based on the process of nucleation and grain growth was developed by Siddique et al.²⁶ for reconstructing a three-dimensional fuel cell catalyst layer. This process was later implemented by Siddique et al.²⁷ to reconstruct a three-dimensional three-phase LiFePO₄ cathode. A common approach for generating synthetic microstructure of SOFC electrodes involves the random packing of initial spheres or "seeds" followed by the expansion of such spheres to simulate the sintering process^{28–31}. Moussaoui et al.⁶ implement a combined model based on sphere packing and truncated Gaussian random field to generate synthetic SOFC electrodes. Additional authors have implemented plurigaussian random fields to model the three-phase microstructure of SOFC electrodes and establish correlations between the microstructure and model parameters^{3,32,33}.

In the area of Li-ion batteries some authors have implemented computational models to adhere a synthetic carbon-binder domain (CBD) (usually hard to image) into XCT three-

¹Department of Earth Science and Engineering, Imperial College London, London SW7 2BP, UK. ²Earth Science Analytics ASA, Professor Olav Hanssens vei 7A, Stavanger 4021, Norge. ³Dyson School of Design Engineering, Imperial College London, London SW7 2DB, UK. ⁴email: samuel.cooper@imperial.ac.uk

Figure B.2: Paper front page